

Pertanika Journal of
**SCIENCE &
TECHNOLOGY**

JST

VOL. 25 (S) FEB. 2017

A special issue devoted to
Contemporary Issues Towards Smart Sustainable Engineering Solution

Guest Editors

**Siti Anom Ahmad, Ribhan Zafira Abdul Rahman, Wan Zuha Wan Hasan,
Mohd Amran Mohd Radzi, Suhaidi Shafie, Noor Izzri Abdul Wahab & Nashiren Farzilah Mailah**



PERTANIKA
JOURNALS

A scientific journal published by Universiti Putra Malaysia Press

Journal of Science & Technology

About the Journal

Overview

Pertanika Journal of Science & Technology (JST) is the official journal of Universiti Putra Malaysia published by UPM Press. It is an open-access online scientific journal which is free of charge. It publishes the scientific outputs. It neither accepts nor commissions third party content.

Recognized internationally as the leading peer-reviewed interdisciplinary journal devoted to the publication of original papers, it serves as a forum for practical approaches to improving quality in issues pertaining to science and engineering and its related fields.

JST is a **quarterly** (January, April, July and October) periodical that considers for publication original articles as per its scope. The journal publishes in **English** and it is open to authors around the world regardless of the nationality.

The Journal is available world-wide.

Aims and scope

Pertanika Journal of Science and Technology aims to provide a forum for high quality research related to science and engineering research. Areas relevant to the scope of the journal include: bioinformatics, bioscience, biotechnology and bio-molecular sciences, chemistry, computer science, ecology, engineering, engineering design, environmental control and management, mathematics and statistics, medicine and health sciences, nanotechnology, physics, safety and emergency management, and related fields of study.

History

Pertanika was founded in 1978. A decision was made in 1992 to streamline Pertanika into three journals as Journal of Tropical Agricultural Science, Journal of Science & Technology, and Journal of Social Sciences & Humanities to meet the need for specialised journals in areas of study aligned with the interdisciplinary strengths of the university.

After almost 25 years, as an interdisciplinary Journal of Science & Technology, the revamped journal now focuses on research in science and engineering and its related fields.

Goal of *Pertanika*

Our goal is to bring the highest quality research to the widest possible audience.

Quality

We aim for excellence, sustained by a responsible and professional approach to journal publishing. Submissions are guaranteed to receive a decision within 14 weeks. The elapsed time from submission to publication for the articles averages 5-6 months.

Abstracting and indexing of *Pertanika*

Pertanika is almost 40 years old; this accumulated knowledge has resulted in Pertanika JST being abstracted and indexed in SCOPUS (Elsevier), Thomson (ISI) Web of Knowledge [BIOSIS & CAB Abstracts], EBSCO & EBSCOhost, DOAJ, ERA, Cabell's Directories, Google Scholar, MyAIS, ISC & Rubriq (Journal Guide).

Future vision

We are continuously improving access to our journal archives, content, and research services. We have the drive to realise exciting new horizons that will benefit not only the academic community, but society itself.

Citing journal articles

The abbreviation for Pertanika Journal of Science & Technology is *Pertanika J. Sci. Technol.*

Publication policy

Pertanika policy prohibits an author from submitting the same manuscript for concurrent consideration by two or more publications. It prohibits as well publication of any manuscript that has already been published either in whole or substantial part elsewhere. It also does not permit publication of manuscript that has been published in full in Proceedings.

Code of Ethics

The Pertanika Journals and Universiti Putra Malaysia takes seriously the responsibility of all of its journal publications to reflect the highest in publication ethics. Thus all journals and journal editors are expected to abide by the Journal's codes of ethics. Refer to Pertanika's **Code of Ethics** for full details, or visit the Journal's web link at http://www.pertanika.upm.edu.my/code_of_ethics.php

International Standard Serial Number (ISSN)

An ISSN is an 8-digit code used to identify periodicals such as journals of all kinds and on all media—print and electronic. All Pertanika journals have ISSN as well as an e-ISSN.

Journal of Science & Technology: ISSN 0128-7680 (*Print*); ISSN 2231-8526 (*Online*).

Lag time

A decision on acceptance or rejection of a manuscript is reached in 3 to 4 months (average 14 weeks). The elapsed time from submission to publication for the articles averages 5-6 months.

Authorship

Authors are not permitted to add or remove any names from the authorship provided at the time of initial submission without the consent of the Journal's Chief Executive Editor.

Manuscript preparation

Refer to Pertanika's **INSTRUCTIONS TO AUTHORS** at the back of this journal.

Most scientific papers are prepared according to a format called IMRAD. The term represents the first letters of the words **I**ntroduction, **M**aterials and **M**ethods, **R**esults, **A**nd, **D**iscussion. IMRAD is simply a more 'defined' version of the "IBC" [Introduction, Body, Conclusion] format used for all academic writing. IMRAD indicates a pattern or format rather than a complete list of headings or components of research papers; the missing parts of a paper are: *Title, Authors, Keywords, Abstract, Conclusions, and References*. Additionally, some papers include Acknowledgments and Appendices.

The *Introduction* explains the scope and objective of the study in the light of current knowledge on the subject; the *Materials and Methods* describes how the study was conducted; the *Results* section reports what was found in the study; and the *Discussion* section explains meaning and significance of the results and provides suggestions for future directions of research. The manuscript must be prepared according to the Journal's **INSTRUCTIONS TO AUTHORS**.

Editorial process

Authors are notified with an acknowledgement containing a *Manuscript ID* on receipt of a manuscript, and upon the editorial decision regarding publication.

Pertanika follows a **double-blind peer-review** process. Manuscripts deemed suitable for publication are usually sent to reviewers. Authors are encouraged to suggest names of at least three potential reviewers at the time of submission of their manuscript to Pertanika, but the editors will make the final choice. The editors are not, however, bound by these suggestions.

Notification of the editorial decision is usually provided within ten to fourteen weeks from the receipt of manuscript. Publication of solicited manuscripts is not guaranteed. In most cases, manuscripts are accepted conditionally, pending an author's revision of the material.

As articles are double-blind reviewed, material that might identify authorship of the paper should be placed only on page 2 as described in the first-4 page format in Pertanika's **INSTRUCTIONS TO AUTHORS** given at the back of this journal.

The Journal's peer-review

In the peer-review process, three referees independently evaluate the scientific quality of the submitted manuscripts.

Peer reviewers are experts chosen by journal editors to provide written assessment of the **strengths** and **weaknesses** of written research, with the aim of improving the reporting of research and identifying the most appropriate and highest quality material for the journal.

Operating and review process

What happens to a manuscript once it is submitted to *Pertanika*? Typically, there are seven steps to the editorial review process:

1. The Journal's chief executive editor and the editorial board examine the paper to determine whether it is appropriate for the journal and should be reviewed. If not appropriate, the manuscript is rejected outright and the author is informed.
2. The chief executive editor sends the article-identifying information having been removed, to three reviewers. Typically, one of these is from the Journal's editorial board. Others are specialists in the subject matter represented by the article. The chief executive editor asks them to complete the review in three weeks.

Comments to authors are about the appropriateness and adequacy of the theoretical or conceptual framework, literature review, method, results and discussion, and conclusions. Reviewers often include suggestions for strengthening of the manuscript. Comments to the editor are in the nature of the significance of the work and its potential contribution to the literature.

3. The chief executive editor, in consultation with the editor-in-chief, examines the reviews and decides whether to reject the manuscript, invite the author(s) to revise and resubmit the manuscript, or seek additional reviews. Final acceptance or rejection rests with the Editor-in-Chief, who reserves the right to refuse any material for publication. In rare instances, the manuscript is accepted with almost no revision. Almost without exception, reviewers' comments (to the author) are forwarded to the author. If a revision is indicated, the editor provides guidelines for attending to the reviewers' suggestions and perhaps additional advice about revising the manuscript.
4. The authors decide whether and how to address the reviewers' comments and criticisms and the editor's concerns. The authors return a revised version of the paper to the chief executive editor along with specific information describing how they have answered the concerns of the reviewers and the editor, usually in a tabular form. The author(s) may also submit a rebuttal if there is a need especially when the author disagrees with certain comments provided by reviewer(s).

5. The chief executive editor sends the revised paper out for re-review. Typically, at least one of the original reviewers will be asked to examine the article.
6. When the reviewers have completed their work, the chief executive editor in consultation with the editorial board and the editor-in-chief examine their comments and decide whether the paper is ready to be published, needs another round of revisions, or should be rejected.
7. If the decision is to accept, an acceptance letter is sent to all the author(s), the paper is sent to the Press. The article should appear in print in approximately three months.

The Publisher ensures that the paper adheres to the correct style (in-text citations, the reference list, and tables are typical areas of concern, clarity, and grammar). The authors are asked to respond to any minor queries by the Publisher. Following these corrections, page proofs are mailed to the corresponding authors for their final approval. At this point, **only essential changes are accepted**. Finally, the article appears in the pages of the Journal and is posted on-line.



Pertanika Journal of
**SCIENCE
& TECHNOLOGY**

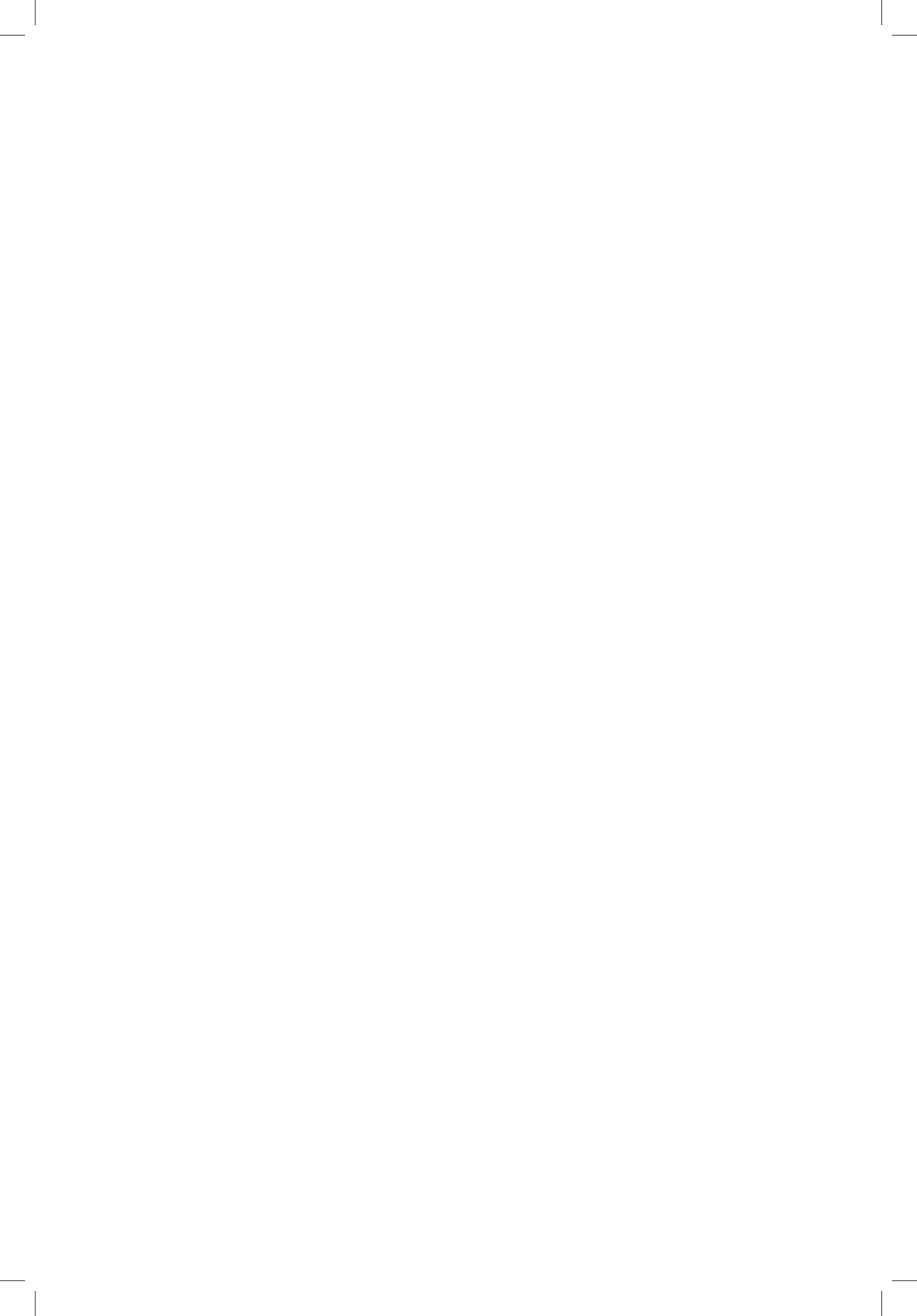
A special issue devoted to
Contemporary Issues Towards Smart Sustainable Engineering Solution

Vol. 25 (S) Feb. 2017
(Special Edition)

Guest Editors

Siti Anom Ahmad, Ribhan Zafira Abdul Rahman, Wan Zuha Wan Hasan,
Mohd Amran Mohd Radzi, Suhaidi Shafie, Noor Izzri Abdul Wahab & Nashiren Farzilah Mailah

A scientific journal published by Universiti Putra Malaysia Press



EDITOR-IN-CHIEF

Mohd Adzir Mahdi

Physics, Optical Communications

CHIEF EXECUTIVE EDITOR

Nayan Deep S. Kanwal

Environmental Issues – Landscape Plant Modelling Applications

UNIVERSITY PUBLICATIONS COMMITTEE

Mohd Azmi Mohd Lila, Chair

EDITORIAL STAFF

Journal Officers:

Kanagamalar Silvarajoo, *ScholarOne*

Lim Ee Leen, *ScholarOne*

Editorial Assistants:

Zulinaardawati Kamarudin

Florence Jiyom

COPY EDITORS

Doreen Dillah

Crescentia Morais

Pooja Terasha Stanslas

PRODUCTION STAFF

Pre-press Officer:

Kanagamalar Silvarajoo

Layout & Typeset:

Lilian Loh Kian Lin

WEBMASTER

Mohd Nazri Othman

PUBLICITY & PRESS RELEASE

Magdalene Pokar (*ResearchSEA*)

Florence Jiyom

EDITORIAL OFFICE

JOURNAL DIVISION

Office of the Deputy Vice Chancellor (R&I)

1st Floor, IDEA Tower II

UPM-MTDC Technology Centre

Universiti Putra Malaysia

43400 Serdang, Selangor Malaysia.

Gen Enq.: +603 8947 1622 | 1619 | 1616

E-mail: executive_editor.pertanika@upm.my

URL: <http://journals-id.upm.edu.my>

PUBLISHER

Kamariah Mohd Saidin

UPM Press

Universiti Putra Malaysia

43400 UPM, Serdang, Selangor, Malaysia.

Tel: +603 8946 8855, 8946 8854

Fax: +603 8941 6172

E-mail: penerbit@putra.upm.edu.my

URL: <http://penerbit.upm.edu.my>

EDITORIAL BOARD

2015-2017

Abdul Halim Shaari

Superconductivity and Magnetism, Universiti Putra Malaysia, Malaysia.

Adem Kilicman

Mathematical Sciences, Universiti Putra Malaysia, Malaysia.

Ahmad Makmom Abdullah

Ecophysiology and Air Pollution Modelling, Universiti Putra Malaysia, Malaysia.

Ali A. Moosavi-Movahedi

Biophysical Chemistry, University of Tehran, Tehran, Iran.

Amu Therwath

Oncology, Molecular Biology, Université Paris, France.

Angelina Chin

Mathematics, Group Theory and Generalisations, Ring Theory, University of Malaya, Malaysia.

Bassim H. Hameed

Chemical Engineering: Reaction Engineering, Environmental Catalysis & Adsorption, Universiti Sains Malaysia, Malaysia.

Biswa Mohan Biswal

Medical, Clinical Oncology, Radiotherapy, Universiti Sains Malaysia, Malaysia.

Christopher G. Jesudason

Mathematical Chemistry, Molecular Dynamics Simulations, Thermodynamics and General Physical Theory, University of Malaya, Malaysia.

Hari M. Srivastava

Mathematics and Statistics, University of Victoria, Canada.

Ivan D. Rukhlenko

Nonlinear Optics, Silicon Photonics, Plasmonics and Nanotechnology, Monash University, Australia.

Kaniraj R. Shenbaga

Geotechnical Engineering, Universiti Malaysia Sarawak, Malaysia.

Kanury Rao

Senior Scientist & Head, Immunology Group, International Center for Genetic Engineering and Biotechnology, Immunology, Infectious Disease Biology and System Biology, International Centre for Genetic Engineering & Biotechnology, New Delhi, India.

Karen Ann Crouse

Chemistry, Material Chemistry, Metal Complexes – Synthesis, Reactivity, Bioactivity, Universiti Putra Malaysia, Malaysia.

Ki-Hyung Kim

Computer and Wireless Sensor Networks, AIOU University, Korea.

Kunnawee Kanitpong

Transportation Engineering-Road Traffic Safety, Highway Materials and Construction, Asian Institute of Technology, Thailand.

Megat Mohd Hamdan

Megat Ahmad
Mechanical and Manufacturing Engineering, Universiti Pertahanan Nasional Malaysia, Malaysia.

Miralini Kandiah

Public Health Nutrition, Nutritional Epidemiology, UCSI University, Malaysia.

Mohamed Othman

Communication Technology and Network, Scientific Computing, Universiti Putra Malaysia, Malaysia.

Mohd. Ali Hassan

Bioprocess Engineering, Environmental Biotechnology, Universiti Putra Malaysia, Malaysia.

Mohd Sapuan Salit

Concurrent Engineering and Composite Materials, Universiti Putra Malaysia, Malaysia.

Narongrit Sombatsompop

Engineering & Technology: Materials and Polymer Research, King Mongkut's University of Technology Thonburi (KMUTT), Thailand.

Prakash C. Sinha

Physical Oceanography, Mathematical Modelling, Fluid Mechanics, Numerical Techniques, Universiti Malaysia Terengganu, Malaysia.

Rajinder Singh

Biotechnology, Biomolecular Sciences, Molecular Markers/ Genetic Mapping, Malaysia Palm Oil Board, Kajang, Malaysia.

Renuganth Varatharajoo

Engineering, Space System, Universiti Putra Malaysia, Malaysia.

Riyanto T. Bambang

Electrical Engineering, Control, Intelligent Systems & Robotics, Bandung Institute of Technology, Indonesia.

Sabira Khatun

Engineering, Computer Systems & Software Engineering, Applied Mathematics, Universiti Malaysia Pahang, Malaysia.

Shiv Dutt Gupta

Director, IHMR, Health Management, Public Health, Epidemiology, Chronic and Non-communicable Diseases, Indian Institute of Health Management Research, India.

Suan-Choo Cheah

Biotechnology, Plant Molecular Biology, Asiatic Centre for Genome Technology (ACGT), Kuala Lumpur, Malaysia.

Wagar Asrar

Engineering, Computational Fluid Dynamics, Experimental Aerodynamics, International Islamic University, Malaysia.

Wing Keong Ng

Aquaculture, Aquatic Animal Nutrition, Aqua Feed Technology, Universiti Sains Malaysia, Malaysia.

Yudi Samyudia

Chemical Engineering, Advanced Process Engineering, Curtin University of Technology, Malaysia.

INTERNATIONAL ADVISORY BOARD

2017-2019

Adarsh Sandhu

Editorial Consultant for Nature Nanotechnology and Contributing Writer for Nature Photonics, Physics, Magneto-resistive Semiconducting Magnetic Field Sensors, Nano-Bio-Magnetism, Magnetic Particle Colloids, Point of Care Diagnostics, Medical Physics, Scanning Hall Probe Microscopy, Synthesis and Application of Graphene, Electronics-inspired Interdisciplinary Research Institute (EIIRIS), Toyohashi University of Technology, Japan.

Graham Megson

Computer Science, The University of Westminster, U.K.

Kuan-Chong Ting

Agricultural and Biological Engineering, University of Illinois at Urbana-Champaign, USA.

Malin Premaratne

Advanced Computing and Simulation, Monash University, Australia.

Mohammed Ismail Elnaggar

Electrical Engineering, Ohio State University, USA.

Peter G. Alderson

Bioscience, The University of Nottingham, Malaysia Campus.

Peter J. Heggs

Chemical Engineering, University of Leeds, U.K.

Ravi Prakash

Vice Chancellor, JUIT, Mechanical Engineering, Machine Design, Biomedical and Materials Science, Jaypee University of Information Technology, India.

Said S.E.H. Elnashaie

Environmental and Sustainable Engineering, Penn. State University at Harrisburg, USA.

Suhash Chandra Dutta Roy

Electrical Engineering, Indian Institute of Technology (IIT) Delhi, India.

Vijay Arora

Quantum and Nano-Engineering Processes, Wilkes University, USA.

Yi Li

Chemistry, Photochemical Studies, Organic Compounds, Chemical Engineering, Chinese Academy of Sciences, Beijing, China.

ABSTRACTING/INDEXING

Pertanika is now over 35 years old; this accumulated knowledge has resulted the journals being indexed in SCOPUS (Elsevier), Thomson (ISI) Web of Knowledge [BIOSIS & CAB Abstracts], EBSCO, DOAJ, Google Scholar, AGRICOLA, ISC, Citefactor, Rubriq and MyAIS. JST is also indexed in ERA.



The publisher of *Pertanika* will not be responsible for the statements made by the authors in any articles published in the journal. Under no circumstances will the publisher of this publication be liable for any loss or damage caused by your reliance on the advice, opinion or information obtained either explicitly or implied through the contents of this publication.

All rights of reproduction are reserved in respect of all papers, articles, illustrations, etc., published in *Pertanika*. *Pertanika* provides free access to the full text of research articles for anyone, web-wide. It does not charge either its authors or author-institution for refereeing/publishing outgoing articles or user-institution for accessing incoming articles.

No material published in *Pertanika* may be reproduced or stored on microfilm or in electronic, optical or magnetic form without the written authorization of the Publisher.

Copyright © 2017 Universiti Putra Malaysia Press. All Rights Reserved.



Preface

We are very pleased to present this special issue of the *Pertanika Journal of Science and Technology (JST)*. This issue is a compilation of selected papers that were presented at the 2016 International Conference on Electrical and Electronic Technology (ICEETech2016), held on the 22nd to 26th August 2016 in Universiti Putra Malaysia. The ICEETech2016 was organised by Universiti Putra Malaysia, Kyushu Institute of Technology Japan and Prince of Songkla University, Thailand. Out of a total of **73** papers selected from this conference, 38 had been published in the previous issue, this issue consists of the remaining 35 papers. The selected papers were subjected to the usual peer reviewing process.

In line with the theme '*Inculcating Great Minds towards Smart Sustainable Engineering Solution*', the ICEETech2016 topics include but not limited to: Power System and Protection, Renewable & Sustainable Energy, High Voltage, Dielectric Insulation, Machine, Power Electronics, Energy Efficient Transportation Engineering, Robotic Automation, Control System and Signal Processing, Biomedical Engineering, Intelligent System, Sensor Technology, System-on-Chip, MEMS and NEMS, IC Packaging and Test and Nanoelectronics.

We would like to thank the contributors as well as the reviewers for their commitment and patience which made this JST ICEETech2016 a successful endeavour. It is hoped this publication would be an encouragement for researchers from around the world to be more active in publishing their research papers.

Our deepest gratitude belongs to Dr. Nayan Kanwal of the Journal Division, as well as the team of Editorial Office, *Pertanika*, Universiti Putra Malaysia with whom we have had a chance to interact and learn of some of the processes involved in the publication of this *Pertanika* Special Issue.

Guest Editors:

Siti Anom Ahmad (*Assoc. Prof. Dr.*)
Ribhan Zafira Abdul Rahman (*Dr.*)
Wan Zuha Wan Hasan (*Assoc. Prof. Dr.*)
Mohd Amran Mohd Radzi (*Assoc. Prof. Dr.*)
Suhaidi Shafie (*Assoc. Prof. Dr.*)
Noor Izzri Abdul Wahab (*Assoc. Prof. Dr.*)
Nashiren Farzilah Mailah (*Dr.*)

February 2017



Pertanika Journal of Science & Technology
Vol. 25 (S) Feb. 2017

Contents

Contemporary Issues Towards Smart Sustainable Engineering Solution	
Voltage Flicker Estimation Based on Pair of Inter-harmonics Analysis Method <i>Mohd Amran, Mohd Radzi, Zai Peng, Goh and Hashim, Hizam</i>	1
DC-link Capacitor Voltage Regulation with Effort-reduction Fuzzy Logic Control for Three-level Inverter-based Shunt Active Power Filter <i>Nashiren Farzilah, Mailah, Yap Hoon and Mohd Amran, Mohd Radzi</i>	11
The Response of a High Voltage Transformer with Various Geometries of Core Joint Design <i>Omar. SH. Alyozbaky, Maryam. M. Isa, Mohd Zainal Abidin Ab Kadir and Mahdi Izadi</i>	21
RF CMOS Switch Design Methodologies for Multiband Transceiver Applications <i>Veeraiyah Thangasamy, Vinesh Thiruchelvam, Shaiful Jahari Hashim and Noor Ain Kamsani</i>	29
Nonlinear Dynamic Inverse Controller Based in Field Oriented with SVPWM Current Control <i>Settar S. Keream, Ahmed N Abdalla and Mohd Razali Bin Daud</i>	37
Passive Damping Techniques with LCL Filter in Inverter-Grid Connected <i>Erum Pathan and Shamsul Aizam Zulkifli</i>	45
Distinct Position of Chaotic Pulse Trains Observed in Malaysia <i>Muhammad Noh Hamzah and Chandima Gomes</i>	53
Field Evaluation of Magnetic Actuator Driven Switchgear in Malaysia <i>Mohd Dzaki, Mohd Amir and Sanuri, Ishak</i>	61
Lightning Breakdown Voltages of Refined Bleached and Deodorised Palm Oil under Needle-plane Configuration <i>Norhafiz Azis, Yee Von Thien, Robiah Yunus and Zaini Yaakub</i>	69
Analysis of Air Humidity and Temperature for Post Lightning Circumstances <i>Sharifah Sakinah, Tuan Othman, Jasronita, Jasni and Mohd Nazim, Mohtar</i>	79

Development of Power Recovery Circuit for Bio-Implantable Stimulator <i>Mokhalad Khaleel Alghairi, Nasri Bin Sulaiman, Roslina Bt Mohd Sidek and Saad Mutashar</i>	87
Weakest Bus Frequency Identification of Power System via TFDI <i>Athraa Iessa, Noor Izzri Abdul Wahab and Norman Mariun</i>	97
An FFT Computation Minimisation for an FPGA-Based MCSA while Preserving Frequency Resolution <i>Marut Raksa, Thanaporn Likitjarernkul, Kiattisak Sengchuai, Nattha Jindapetch and Krerckchai Thongnoo</i>	105
Auto-Grasping Algorithm of Robot Gripper Based on Pressure Sensor Measurement <i>Ahmed M. M. Almassri, Chikamune Wada, W. Z. Wan Hasan and S. A. Ahmad¹</i>	113
A Programmable CMOS Delay Line for Wide Delay Range Generation and Duty-Cycle Adjustability <i>Bilal I. Abdulrazzaq, Izhal Abdul Halin, Lee Lini, Roslina M. Sidek and Nurul Amziah Md. Yunus</i>	123
Fuzzy-Controlled Humidity Variation by Silica Gel and Nitrogen Gas in an Atmospheric Chamber <i>Ali Ghahraei, Nurul Amziah Md Yunus, Izhal Abdul Halin and Nasri Sulaiman</i>	133
Assessment of Transformer Health Index Using Different Model <i>J. Jasni, A. Azmi, N. Azis, M. S. Yahaya and M. A. Talib</i>	143
Top-oil Temperature Model for Transformers based on Nonlinear Thermal Resistance, Lumped Capacitance and Thermal-electrical Analogy <i>M. H. Roslan, N. Azis, J. Jasni and Z. Ibrahim</i>	151
Effect of Moisture on Electrical Response of Sand and Clay under High Impulse Voltage Applications <i>Chun Lim, Siow, Mohd Syariffuddin, Johari and Chandima, Gomes</i>	161
Generation of Space Vector PWM by Using Arduino Uno <i>Nur Ashida Salim, Muhammad Azizi Kaprowi and Ahmad Asri Abd Samat</i>	171
Analysis of Ground Potential Distribution under Lightning Current Condition <i>Chandima Gomes and Riyadh Z. Sabry</i>	181
EFVD along Porcelain Insulator using the FEM <i>Kian Tsong Ho, Mahdi Izadi and Mohd Zainal Abidin Ab Kadir</i>	189

Metal Shape Detection and Evaluation using Giant Magneto Resistance System <i>Norhisam M., M. K. Roslan, Ishak A. and M. N. Hamidon</i>	197
Zero-Padding in DWT Satellite Image Compression <i>Suhaidi Shafie, Halah Saadoon Shihab, Fauzan Ahmad and A. R. Ramli</i>	205
Design of Readout Circuit for Piezoresistive Pressure Sensor Using Nodal Array Approach Reading Technique <i>W. Z. Wan Hasan , F. R. M. Rashidi, M. N. Hamidon and Y. Wahab</i>	215
Transparent Solar Cell Using Spin Coating and Screen Printing <i>A. A. F. Husain and W. Z. Wan Hasan</i>	225
Transmission Lines Modelling based on RLC Passive and Active Filter Design <i>Ahmed Qasim Turki, Nashiren Farzilah Mailah and Ahmed H. Sabry</i>	235
Modelling and Control of Standing Up and Sitting Down Manoeuver <i>A. J. Ishak, M. O. Tokhi, M. S. Al-Quraishi, D. M. Linares and S. K. Ali</i>	243
Silicon Nanowire Interface Circuit for DNA Detection <i>Kamilu Iman Usman, Mohd Nizar Hamidon, Siti Fatimah Abd Rahman and Guan Ling Sim</i>	251
Sensitivity Study of Graphene Nanoribbon with NH ₃ at Room Temperature <i>Mohd Nizar Hamidon, Guan Ling Sim and Kamilu Iman Usman</i>	259
Transformer Incipient Fault Identification Using Depolarisation Current Ratio Index Analysis Technique <i>Mohd Aizam Talib, Nor Asiah Muhamad and Zulkurnain Abdul Malek</i>	267
Tuberculosis Bacteria Counting Using Watershed Segmentation Technique <i>M. K. Hassan, N. F. H. Eko and S. Shafie</i>	275
Analysis of AC - to - DC Uncontrolled Converters Harmonics for Electric Vehicles Applications <i>Shaker M. Khudher, Ishak Bin Aris, Nashiren F. Mailah and R. K. Z. Sahbudin</i>	283
Investigating Insulator UV Signal Frequency Components as Potential Tools for Condition Monitoring of Ceramic Insulators <i>Saiful Mohammad Iezham Suhaimi, Nouruddeen Bashir, Nor Asiah Muhamad and Mohd Aizam Talib</i>	291
A Hermite Interpolated LUT for RF Power Amplifiers <i>Dinaagaren Selvadurai, Roslina M. Sidek, Khalid Al-Hussaini and Borhanuddin M. Ali</i>	299



Voltage Flicker Estimation Based on Pair of Inter-harmonics Analysis Method

Mohd Amran, Mohd Radzi, Zai Peng, Goh* and Hashim, Hizam

Department of Electrical and Electronic Engineering, Faculty of Engineering, Universiti Putra Malaysia, 43400 UPM, Serdang, Selangor, Malaysia

ABSTRACT

This paper presents a voltage flicker estimation based on a pair of inter-harmonics analysis method. The proposed algorithm is able to estimate flicker frequency and amplitude changes of a voltage waveform. The correlation of the pair of inter-harmonics, flicker frequency, and amplitude changes are presented and their formulas highlighted. Experimental results indicate the amplitude of pair of inter-harmonics can detect the voltage flicker. Furthermore, the experimental results are compared with the measurement results obtained by using the Fluke power analyzer (Pst).

Keywords: voltage flicker, inter-harmonics, FFT

INTRODUCTION

Nowadays, utilization of nonlinear loads with asymmetrical current-voltage characteristics such as arc motor drive and arc furnace creates voltage fluctuation to the power system (Grady & Santoso, 2001). Specifically, voltage fluctuation with certain frequency value is considered as voltage flicker (Tayjasant, Wencong, Chun, & Wilsun, 2005). Moreover,

unsteadiness light luminance may occur due to the aforementioned voltage flicker. Practically, International Electrotechnical Commission (IEC) flickermeter is introduced by IEC standard for voltage flicker severity measurement ("Electromagnetic compatibility (EMC) - Part 4-15: Testing and measurement techniques - Flickermeter - Functional and design specifications.", 2011). Instantaneous flicker sensation (P_{inst}), Short Term Perceptibility (P_{st}) and Long Term Perceptibility (P_{lt}) are the voltage flicker severity measurement's indicators which are covered by IEC flickermeter. Pst and Plt are referred to voltage flicker severity indicators under observation of 10 minutes and 2 hours respectively.

ARTICLE INFO

Article history:

Received: 24 August 2016

Accepted: 03 Jun 2017

E-mail addresses:

amranmr@upm.edu.my (Mohd Amran, Mohd Radzi),

zaiPeng5987@gmail.com (Zai Peng, Goh),

hhizam@upm.edu.my (Hashim, Hizam)

*Corresponding Author

Some of research works have been conducted to improve the accuracy of the IEC flickermeter (Virulkar & Aware, 2012) and voltage flicker mitigation have also been done by many researchers (Michel & de Preville, 2004; Routimo et al., 2008). Analysis on reducing the observation time of Pst (Tan & Ramachandaramurthy, 2012) has also been done by researchers. Interrelationship between inter-harmonics and voltage flicker has been investigated by many researchers too (Dahai, Wilsun, & Nassif, 2005; Keppler, Watson, Arrillaga, & Shiun, 2003; Langella, Liccardo, Marino, Testa, & Triggianese, 2007; Tayjasant et al., 2005; Wilsun, 2005). Voltage flicker detection has been proposed by many researchers such as atomic method (Ning, Linchuan, & Qingquan, 2012), wavelet Fourier transform (WeiHui & ShiPing, 2011), Chirp-z transform (Kang, Guo, Li, & Yan, 2010), and new modified S-transform algorithm (Huang, Xu, Shi, & Zhang, 2014). The atomic method is considered not practical since it needs a special voltage flicker dictionary which is generated by matching pursuits algorithm. The voltage flicker detection based on wavelet Fourier transform is mathematically considered cumbersome as the measured waveform needs to be filtered by wavelet transform, and then use a long window is required to identify the voltage flicker amplitude and flicker frequency. Other than that, the Chirp-z transform is only tested in simulation and it is not practical as the algorithm is not tested with noise condition. Then, the modified S-transform for voltage flicker detection algorithm is able to detect duration time of voltage flicker effectively but it cannot detect severity of voltage flicker.

Basically, there are some changes on the amplitudes of pair of inter-harmonics due to intrinsic characteristic of a voltage flicker waveform (Jing, Tayjasant, Wilsun, & Caixin, 2008). This proposed algorithm is able to estimate flicker frequency and amplitude changes in a voltage waveform based on pair of inter-harmonics analysis method. Firstly, amplitudes of pair of inter-harmonics are detected by signal processing method. Then, the amplitudes of particular inter-harmonics are substituted in the formulas that have been generated in this paper. Subsequently, the flicker frequency and amplitude changes of a voltage flicker waveform are detected and are compare with the flicker reference curve in order to detect the voltage flicker.

A number of signal processing algorithms based on different techniques for inter-harmonics detection such as Discrete Fourier Transform (DFT), Fast Fourier Transform (FFT), Short-Time Fourier transform (STFT) (Wright, 1999) and spectrogram (Abdullah, Peng, Ghani, & Jopri, 2014) have been reported over the past years (Coppola, Qian, Buso, Boroyevich, & Bell, 2008). The FFT is considered direct improvement of the DFT which is able to perform faster conversion from time to frequency domain, but number of samples must fulfil $2n$ where n is an integer number. Otherwise, operation of the FFT may lead to inaccurate result due to phenomena of aliasing (Hsiung-Cheng, 2008), leakage (Chang, Chen, Liu, & Wu, 2008), and picket fence effects (Chang et al., 2008). Meanwhile, STFT is considered improvement of the FFT as it is generated based on sliding FFT process. The sliding FFT is done by dividing the measurement signal into many small divisions and FFT is applied to these tiny divisions. Next, spectrogram is considered as squared magnitude of the STFT and the output of spectrogram are plotted in spectrograph. Subsequently, the STFT and spectrogram are considered mathematical burden due to many times of applying FFT. Therefore, directly using FFT is merited, to be utilized in the proposed algorithm due to its speed capability to convert time domain to frequency domain. The correlation between voltage flicker and inter-harmonics are presented in Section II.

Sections III discusses the background of the FFT. Section IV presents the proposed algorithm. The experiments are presented in Sections VI. Lastly, the conclusion is contained in Section VI.

CORRELATION BETWEEN INTER-HARMONICS AND VOLTAGE FLICKER

Basically, modulated waveform can occur following the appearance of inter-harmonics in a power system. The fluctuation frequency of the instantaneous voltage is considered as voltage flicker frequency. The voltage flicker frequency (Jing et al., 2008), flicker can be calculated by

$$f_{flicker} = |f_{IH} - f_f| \quad (1)$$

where, f_{IH} and f_f are considered as inter-harmonic frequency and fundamental frequency respectively of the power system. By considering a 50 Hz power system which consists of 3 Hz of voltage flicker frequency, then the related inter-harmonics are 47 Hz and 53 Hz. Essentially, the voltage flicker may occur due to pair of inter-harmonics (47 and 53 Hz together) or single inter-harmonic (47 or 53 Hz). In practical situation, voltage flicker waveform occurs mainly due to pair of inter-harmonics. Therefore, the derivation of formula for aforementioned situation is shown as follow (Zai Peng, Radzi, Hizam, & Abdul Wahab, 2015):

$$v_2(t) = \alpha_3 e^{j\omega_3 t} + \alpha_1 e^{j\omega_1 t} + \alpha_2 e^{j\omega_2 t} \quad (2)$$

$v_2(t)$, α_1 , and ω_1 are represented as the instantaneous voltage, fundamental amplitude, and angular frequency (fundamental) respectively. Meanwhile, α_2 , and ω_2 are symbolized as the first inter-harmonic amplitude, and its angular frequency. Next, α_3 , and ω_3 are represented as the second inter-harmonic amplitude, and its angular frequency respectively. The relationship of ω is assumed as $\omega_3 < \omega_1 < \omega_2$.

After that, the aforementioned instantaneous voltage becomes,

$$v_2(t) = e^{j\omega_1 t} (\alpha_1 + \alpha_2 e^{j(\omega_2 - \omega_1)t} + \alpha_3 e^{j(\omega_3 - \omega_1)t}) \quad (3)$$

$e^{j\omega_1 t}$ is represented as factorized exponential form of fundamental frequency. The amplitude is represented as $\alpha_1 + \alpha_2 e^{j(\omega_2 - \omega_1)t} + \alpha_3 e^{j(\omega_3 - \omega_1)t}$. Therefore, the amplitude can be calculated as following:

$$Amp_{-2H} = |\alpha_1 + \alpha_2 e^{j(\omega_2 - \omega_1)t} + \alpha_3 e^{j(\omega_3 - \omega_1)t}| \quad (4)$$

After the expansion,

$$Amp_{-2H} = \left| \begin{array}{l} \alpha_1 + \alpha_2 \cos(\omega_2 - \omega_1)t + j\alpha_2 \sin(\omega_2 - \omega_1)t \\ + \alpha_3 \cos(\omega_3 - \omega_1)t + j\alpha_3 \sin(\omega_3 - \omega_1)t \end{array} \right| \quad (5)$$

The calculation for the amplitude is as follow:

$$Amp_{2H} = \sqrt{\left[\frac{\alpha_1 + \alpha_2 \cos(\omega_2 - \omega_1)t}{\alpha_3 \cos(\omega_3 - \omega_1)t} \right]^2 + [\alpha_2 \sin(\omega_2 - \omega_1)t + \alpha_3 \sin(\omega_3 - \omega_1)t]^2} \quad (6)$$

Further elaboration is:

$$Amp_{2H} = \sqrt{\left[\frac{2\alpha_1\alpha_2 \cos(\omega_2 - \omega_1)t + 2\alpha_1\alpha_3 \cos(\omega_3 - \omega_1)t + 2\alpha_2\alpha_3 \cos(\omega_2 - \omega_1)t \cos(\omega_3 - \omega_1)t + \alpha_1^2 + \alpha_2^2 \cos^2(\omega_2 - \omega_1)t + \alpha_3^2 \cos^2(\omega_3 - \omega_1)t + \alpha_2^2 \sin^2(\omega_2 - \omega_1)t + 2\alpha_2\alpha_3 \sin(\omega_2 - \omega_1)t \sin(\omega_3 - \omega_1)t + \alpha_3^2 \sin^2(\omega_3 - \omega_1)t}{\alpha_3^2 \cos^2(\omega_3 - \omega_1)t} \right]} \quad (7)$$

Since

$$\omega_3 \text{ p } \omega_1 \text{ p } \omega_2 \text{ and } \omega_3 - \omega_1 = \omega_2 - \omega_1 \quad (8)$$

Then,

$$Amp_{2H} = \sqrt{\left[\frac{2\alpha_1\alpha_2 \cos(\omega_2 - \omega_1)t + 2\alpha_1\alpha_3 \cos(\omega_3 - \omega_1)t + 2\alpha_2\alpha_3 \cos^2(\omega_2 - \omega_1)t + \alpha_1^2 + \alpha_2^2 \cos^2(\omega_2 - \omega_1)t + \alpha_3^2 \cos^2(\omega_3 - \omega_1)t + \alpha_2^2 \sin^2(\omega_2 - \omega_1)t + 2\alpha_2\alpha_3 \sin^2(\omega_2 - \omega_1)t + \alpha_3^2 \sin^2(\omega_3 - \omega_1)t}{\alpha_3^2 \cos^2(\omega_3 - \omega_1)t} \right]} \quad (9)$$

By simplifying using trigonometry identity:

$$Amp_{2H} = \sqrt{[2\alpha_1\alpha_2 \cos(\omega_2 - \omega_1)t + 2\alpha_1\alpha_3 \cos(\omega_3 - \omega_1)t + 2\alpha_2\alpha_3 + \alpha_1^2 + \alpha_2^2 + \alpha_3^2]} \quad (10)$$

Therefore, the simplified version is:

$$Amp_{2H} = \sqrt{[2\alpha_1(\alpha_2 + \alpha_3) \cos(\omega_2 - \omega_1)t + 2\alpha_2\alpha_3 + \alpha_1^2 + \alpha_2^2 + \alpha_3^2]} \quad (11)$$

The maximum of the instantaneous voltage is:

$$Amp_{2H} \text{ max} = \sqrt{[2\alpha_1(\alpha_2 + \alpha_3)(1) + 2\alpha_2\alpha_3 + \alpha_1^2 + \alpha_2^2 + \alpha_3^2]} \quad (12)$$

The minimum of the instantaneous voltage is:

$$Amp_{2H} \text{ min} = \sqrt{[2\alpha_1(\alpha_2 + \alpha_3)(-1) + 2\alpha_2\alpha_3 + \alpha_1^2 + \alpha_2^2 + \alpha_3^2]} \quad (13)$$

The substitution of the $\cos(\omega_2 - \omega_1)t$ to 1 and -1 is for calculating the maximum and minimum values of the instantaneous voltage respectively. Figure 1 shows voltage flicker waveform for 50 Hz voltage supply with presence of pair of inter-harmonics, in which 47 Hz (ω_3) and 53 Hz (ω_2) with amplitude of 0.1 p.u. (α_3) and 0.2 p.u. (α_2) respectively. The maximum and minimum values of the instantaneous voltage in Figure 1(b) are 1.3 and 0.7 p.u respectively. Assuming the amplitudes of α_3 , α_1 and α_2 are determined to be 0.1, 1 and 0.2 p.u. respectively Eq. (12) and

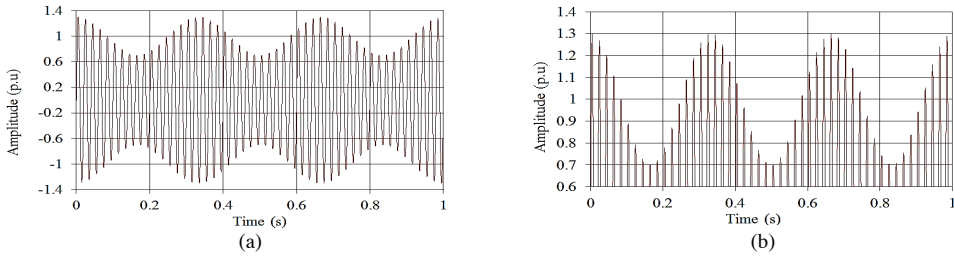


Figure 1. Voltage flicker waveform caused by pair of inter-harmonics: (a) zoom-out version, and (b) zoom-in version

eq. (13) is used to calculate the maximum and minimum values of the instantaneous voltage, which are 1.3 and 0.7 p.u. respectively. To evaluate severity of the voltage flicker, relative fluctuation voltage ($\Delta v/v$) has to be calculated based on the following formula:

$$\Delta v/v = \frac{Amp_{2H \cdot \max} - Amp_{2H \cdot \min}}{\alpha_1} \times 100 \quad (14)$$

For Figure 1, $\Delta v/v$ is 60%. Again, the amplitudes of fundamental (α_1) and two inter-harmonics (α_2 and α_3) are the key values to identify $\Delta v/v$.

To summarize, a generated voltage flicker may produce significant effect on the amplitudes of a pair of inter-harmonics (Jing et al., 2008). The amplitudes of fundamental (α_1) and pair of inter-harmonics (α_2 and α_3) is found to be crucial in order to identify $\Delta v/v$ and is discussed in the next section.

BACKGROUND OF FFT

Based on standard IEC 61000-4-7, the general formula for FFT is

$$X(k) = \sum_{n=1}^{N-1} x(n)e^{-j\omega_k n} \quad (15)$$

where,

$$\omega_k = \frac{2\pi k}{N} \quad (16)$$

N is number of samples in time domain; k is number of samples in frequency domain (Bin number returned by FFT); x is data in time domain and X is data in frequency domain. Since

$$e^{-j\omega_k n} = \cos\left(\frac{2\pi kn}{N}\right) - j\sin\left(\frac{2\pi kn}{N}\right) \quad (17)$$

Then, the output of the FFT in frequency domain is

$$X(k) = \sum_{n=1}^{N-1} \left[x(n)\cos\left(\frac{2\pi kn}{N}\right) - jx(n)\sin\left(\frac{2\pi kn}{N}\right) \right] \quad (18)$$

It can be written as

$$X(k) = \sum_{n=1}^{N-1} [real - j_imaginary] \tag{19}$$

After that, the amplitude and phase values of the desired signal can be extracted via following equation:

$$A = \sqrt{real^2 + imaginary^2} \tag{20}$$

$$\theta = \tan^{-1} \frac{imaginary}{real} \tag{21}$$

Based on previous works, optimized sampling frequency for FFT is 12.8k Hz (Leelajindakraierk & Chompoo-Inwai, 2012; Yamada, 2013) for detecting signal with fundamental frequency of 50 Hz. Specifically, the frequency resolution (eq. (22)) is needed for this proposed algorithm is 0.1. Therefore, the window size is 128k samples (12.8k/0.1). Consequently, 10s is needed for processing a single output data.

$$Frequency_resolution = \frac{Sampling_frequency}{Window_size} \tag{22}$$

PROPOSED ALGORITHM

As discussed earlier, the amplitudes of pair of inter-harmonics and fundamental frequency are the key values to determine the voltage flicker. Principally, FFT is utilized as the amplitudes detector due to its advantages as mentioned in the introduction section. The particular amplitudes' values are substituted into eq. (12) and eq. (13) to determine the maximum and minimum values of the fluctuation voltage and the relative fluctuation voltage ($\Delta v/v$) calculated via eq. (14). The voltage flicker can be detected by comparing $\Delta v/v$ with voltage flicker reference curve. Specifically, voltage flicker is detected when then $\Delta v/v$ is positioned above the flicker reference curve (Figure 3) and vice versa. The voltage flicker reference curve is generated based on IEC standard (Albistur, Aravena, Moran, & Espinoza, 2014). The block diagram of the proposed algorithm is shown in Figure 2.

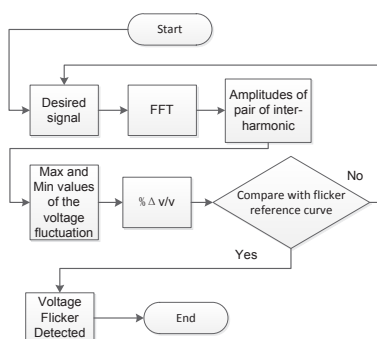


Figure 2. VBlock diagram of the proposed algorithm

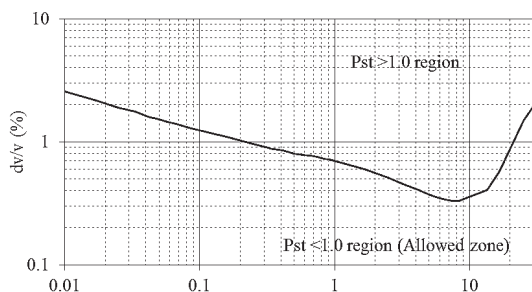


Figure 3. Voltage flicker reference curve

EXPERIMENTAL RESULTS

Figure 4 shows the experimental setup to perform this proposed algorithm. Programmable AC source model 6590 is utilized as voltage flicker waveform generator for this experimental setup. Furthermore, several voltage flicker waveforms are considered in this experimental work for further evaluating robustness of the proposed algorithm. The benchmarking tool used is Fluke power analyzer (P_{st}). Data acquisition is assessed using differential probe Gw Instek GDP_025 and Ni USB 6212. Sampling frequency of 12,800 Hz is utilized for this experimental work. The window width is 128k samples. Therefore, 10 seconds are needed for single experimental data. Finally, the data is exported to Matlab Simulink to further be analysed by the proposed algorithm as shown in Figure 2.

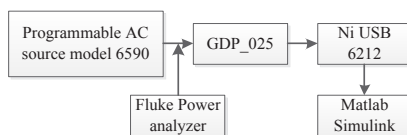


Figure 4. Configuration block for the experimental work

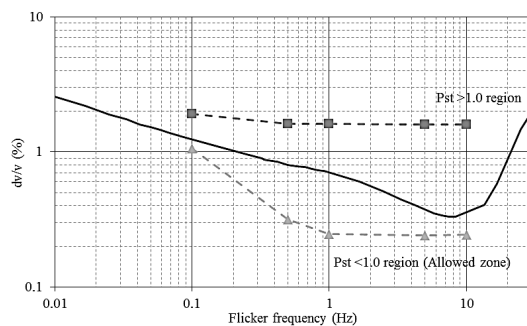


Figure 5. Data analysis for the experimental work

The programmable AC source is supplied by a voltage (rms) of 240 V and the aforementioned voltage waveform is interrupted by various envelope pulse levels which are generated by the programmable AC source too. Two types of envelope pulses level voltage (rms) are utilized in this experimental setup, which are 239.5 and 237 V. In addition, single envelope pulse level is programmed with various pulse frequencies such as 0.1, 0.5, 1, 5 and 10 Hz. Subsequently, 10 sets of experimental data are used for testing. Table 1 is a summary of the data analysis related to this experimental work. FFT is utilized to capture and analyse the voltage flicker waveform generated by the programmable AC source and the maximum, minimum and relative fluctuation voltages are generated by substituting the outputs of the FFT to eq. (12), eq. (13) and eq. (14) accordingly. The voltage flicker is detected, when the value of relative fluctuation voltage (eq. (14)) is located above the flicker reference curve (Figure 5). The Fluke power analyzer (P_{st}) is utilized for benchmarking purposes where the voltage flicker is detected when the P_{st} is greater than 1. The voltage flicker is successfully detected via the proposed algorithm, which is compared with the Fluke power analyzer (P_{st}) to ensure 100% detection accuracy.

Table 1
Summary of data analysis for the proposed algorithm (Experimental)

Pulse level (Vrms)	Pulse frequency/ Flicker frequency (Hz)	Number of test	FFT			Calculation by proposed algorithm				FLUKE		Detection Accuracy (%)
			50 Hz- Pulse frequency	50 Hz	50 Hz+ Pulse frequency	Max (Vpeak)	Min (Vpeak)	% $\Delta v/v$	Flicker detection	(P _{st})	Flicker detection (Pst>1)	
239.50	0.10	1	1.03	336.90	0.77	338.70	335.10	1.07	No	0.16	No	100
237.00		2	1.65	335.10	1.56	338.31	331.89	1.92	Yes	1.05	Yes	100
239.50	0.50	3	0.27	336.90	0.26	337.43	336.37	0.32	No	0.23	No	100
237.00		4	1.42	335.10	1.28	337.80	332.40	1.61	Yes	1.53	Yes	100
239.50	1.00	5	0.14	336.90	0.28	337.31	336.49	0.25	No	0.26	No	100
237.00		6	1.33	335.10	1.37	337.80	332.40	1.61	Yes	1.78	Yes	100
239.50	5.00	7	0.19	336.90	0.21	337.30	336.50	0.24	No	0.45	No	100
237.00		8	1.30	335.10	1.38	337.78	332.42	1.60	Yes	3.02	Yes	100
239.50	10.00	9	0.22	336.90	0.19	337.31	336.49	0.24	No	0.65	No	100
237.00		10	1.35	335.10	1.34	337.79	332.41	1.60	Yes	4.36	Yes	100

CONCLUSION

This paper has presented voltage flicker detection based on pair of inter-harmonics analysis method. The amplitudes of pair of inter-harmonics and fundamental frequency are shown to be the key values for determining the voltage flicker. The amplitude of the aforementioned inter-harmonics was substituted into the formula that have been derived in this paper accordingly. Subsequently, The voltage flicker can be detected when the relative fluctuation voltage is located above with the flicker reference curve. According to experimental results, the amplitudes of pair of inter-harmonics are able to detect the voltage flicker. The experimental results were compared with those obtained by using the Fluke power analyzer (P_{st}).

ACKNOWLEDGEMENT

This work was supported by the Putra Grouped Initiative Grant Scheme under Universiti Putra Malaysia (GP-IPB/2013/9412102), and Exploratory Research Gant Scheme under Ministry of Education, Malaysia (ERGS/1-2013/5527141).

REFERENCES

- Abdullah, A. R., Peng, G. Z., Ghani, S. A., & Jopri, M. H. (2014, March 24-25). A new vector draft method for harmonic source detection at point of common coupling. In *Power Engineering and Optimization Conference (PEOCO), 2014 IEEE 8th International*.
- Albistur, C. F., Aravena, P. A., Moran, L. A., & Espinoza, J. R. (2014). A Simple Predictive Method to Estimate Flicker. *IEEE Transactions on Industry Applications*, 50(3), 2150-2155.
- Chang, G. W., Chen, C. I., Liu, Y. J., & Wu, M. C. (2008). Measuring power system harmonics and interharmonics by an improved fast Fourier transform-based algorithm. *IET Generation, Transmission and Distribution*, 2(2), 193-201.

- Coppola, L., Qian, L., Buso, S., Boroyevich, D., & Bell, A. (2008). Wavelet Transform as an Alternative to the Short-Time Fourier Transform for the Study of Conducted Noise in Power Electronics. *IEEE Transactions on Industrial Electronics*, 55(2), 880-887.
- Dahai, Z., Wilsun, X., & Nassif, A. (2005, May 1-4). Flicker source identification by interharmonic power direction. *Canadian Conference on Electrical and Computer Engineering*, 2005.
- Electromagnetic compatibility (EMC) - Part 4-15: Testing and measurement techniques - Flickermeter - Functional and design specifications. IEC 61000-4-152011.
- Goh, Z. P., Radzi, M. A. M., Hizam, H., & Abdul W. N. I. (2015). A Simple Predictive Method of Critical Flicker Detection for Human Healthy Precaution. *Mathematical Problems in Engineering*, 2015.
- Grady, W. M., & Santoso, S. (2001). Understanding Power System Harmonics. *IEEE Power Engineering Review*, 21(11), 8-11.
- Hsiung, C. L. (2008). Inter-Harmonic Identification Using Group-Harmonic Weighting Approach Based on the FFT. *IEEE Transactions on Power Electronics*, 23(3), 1309-1319.
- Huang, Y. H., Xu, J. J., Shi, H., & Zhang, Y. S. (2014, May 31 2014-June 2 2014). Effective voltage flicker detection approach based on a new modified S-transform algorithm. *Control and Decision Conference (2014 CCDC), The 26th Chinese*.
- Jing, Y., Tayjasanant, T., Wilsun, X., & Caixin, S. (2008). Characterizing Voltage Fluctuations Caused by a Pair of Interharmonics. *IEEE Transactions on Power Delivery*, 23(1), 319-327.
- Kang, W., Guo, J., Li, H., & Yan, X. (2010, 28-31 March 2010). Voltage Flicker Detection Based on Chirp-z Transform. In *Power and Energy Engineering Conference (APPEEC), 2010 Asia-Pacific*.
- Keppler, T., Watson, N. R., Arrillaga, J., & Shiun, Chen. (2003). Theoretical assessment of light flicker caused by sub- and interharmonic frequencies. *IEEE Transactions on Power Delivery*, 18(1), 329-333.
- Langella, R., Liccardo, F., Marino, P., Testa, A., & Triggianese, M. (2007, May 21-23). On the Assessment of Light Flicker due to the Interharmonic Distortion Produced by Wind Turbines. *International Conference on Clean Electrical Power, 2007. ICCEP '07*.
- Leelajindakrairek, E. J. S. C. M., & Chompoo-Inwai, C. C. (2012, 12-14 Dec. 2012). Optimal technique for total harmonic distortion detection and estimation for smart meter. *IPEC, 2012 Conference on Power and Energy*.
- Michel, D., & de Preville, G. (2004, 31 March-2 April 2004). Mixed topology for flicker mitigation. *Power Electronics, Machines and Drives, 2004. (PEMD 2004). Second International Conference on (Conf. Publ. No. 498)*.
- Ning, W., Linchuan, L., & Qingquan, J. (2012, 21-24 May 2012). Detection of voltage flicker based on atomic method. *Innovative Smart Grid Technologies - Asia (ISGT Asia), 2012 IEEE*.
- Routimo, M., Makinen, A., Salo, M., Seesvuori, R., Kiviranta, J., & Tuusa, H. (2008). Flicker Mitigation With a Hybrid Compensator. *IEEE Transactions on Industry Applications*, 44(4), 1227-1238.
- Tan, R. H. G., & Ramachandaramurthy, V. K. (2012, June 6-7). Tolerance analysis of flicker Pst short term perceptibility assessment for one minute observation time. In *Power Engineering and Optimization Conference (PEDCO) Melaka, Malaysia, 2012 Ieee International*.

- Tayjasant, T., Wencong, W., Chun, L., & Wilsun, X. (2005). Interharmonic-flicker curves. *IEEE Transactions on Power Delivery*, 20(2), 1017-1024.
- Virulkar, V. B., & Aware, M. V. (2012, 25-28 Oct. 2012). Power system flicker analysis, modeling and prototype implementation. *IECON 2012 - 38th Annual Conference on IEEE Industrial Electronics Society*.
- WeiHui, Z., & ShiPing, S. (2011, September 16-18). Voltage flicker detection based on wavelet fourier transform. *International Conference on Electrical and Control Engineering (ICECE), 2011*.
- Wilsun, X. (2005, June 12-16). Deficiency of the IEC flicker meter for measuring interharmonic-caused voltage flickers. *Power Engineering Society General Meeting, 2005. IEEE*.
- Wright, P. S. (1999). Short-time Fourier transforms and Wigner-Ville distributions applied to the calibration of power frequency harmonic analyzers. *IEEE Transactions on Instrumentation and Measurement*, 48(2), 475-478.
- Yamada, T. (2013). High-Accuracy Estimations of Frequency, Amplitude, and Phase With a Modified DFT for Asynchronous Sampling. *IEEE Transactions on Instrumentation and Measurement*, 62(6), 1428-1435.



DC-link Capacitor Voltage Regulation with Effort-reduction Fuzzy Logic Control for Three-level Inverter-based Shunt Active Power Filter

Nashiren Farzilah, Mailah, Yap Hoon* and Mohd Amran, Mohd Radzi

Department of Electrical and Electronic Engineering, Faculty of Engineering, Universiti Putra Malaysia, 43400 UPM, Serdang, Selangor, Malaysia

ABSTRACT

Shunt active power filter (SAPF) is the most effective solution for current harmonics. In its controller, DC-link capacitor voltage regulation algorithm with either proportional-integral (PI) or fuzzy logic control (FLC) technique has played a significant role in maintaining a constant DC voltage across all the DC-link capacitors. However, PI technique performs poorly with high overshoot and significant time delay under dynamic state conditions, as its parameters are difficult to be tuned without requiring complete knowledge of the designated system. Although FLC technique has been developed to overcome limitations of PI technique, it is mostly developed with high complexity thereby increases computational burden of the designed controller. This paper presents a fuzzy-based DC-link capacitor voltage regulation algorithm with reduced computational efforts to enhance performance of three-phase three-level neutral-point diode clamped (NPC) inverter-based SAPF in overall DC-link voltage regulation. The proposed method is called effort-reduction FLC technique. The proposed algorithm is developed and evaluated in MATLAB-Simulink. Moreover, conventional algorithm with PI technique is tested for comparison purposes. Simulation results have confirmed improvement achieved by the proposed algorithm in comparison to the conventional algorithm.

Keywords: Active power filter, current harmonics, DC-link voltage control, fuzzy logic control (FLC), multilevel inverter

ARTICLE INFO

Article history:

Received: 24 August 2016

Accepted: 03 Jun 2017

E-mail addresses:

nashiren@upm.edu.my (Nashiren Farzilah Mailah),

davidhoon0304@hotmail.com (Yap Hoon),

amranmr@upm.edu.my (Mohd Amran Mohd Radzi)

*Corresponding Author

INTRODUCTION

High current harmonics resulting from intensive use of nonlinear loads such as power converters and adjustable speed drives is recognized as a major issue for a power system. The presence of current harmonics not only degrades overall system efficiency

by worsening its power factor (PF) performance, but it also causes other associated problems such as equipment overheating, failures of sensitive devices and capacitor blowing (Dai & Dai, 2008; Kale & Ozdemir, 2005a). It is compulsory to minimize the harmonics level of a power system. Shunt-typed active power filter (SAPF) is the most effective solution to current harmonics, where all the undesired current components are eliminated by injecting opposition current (simply known as injection current) back to the polluted power system. In addition, it also provides reactive power compensation meant for improving PF performances (Jain & Gupta, 2014; Kale & Ozdemir, 2005b).

Most of the established SAPFs employ a standard two-level inverter topology in their design. However, three-level inverters which have been reported to be more advantageous than traditional two-level inverters in term of output voltage quality and power losses are accepted as better alternatives (Hoon et al., 2016a, 2016b). The performance of SAPF in current harmonics mitigation is dependent on the performance of its controller. Specifically, its controller consists of harmonics extraction, DC-link capacitor voltage regulation and switching (current control) algorithms. The DC-link capacitor voltage regulation algorithm plays an important role in maintaining a constant overall DC-link voltage for a typical inverter-based SAPF. The DC-link voltage must be maintained at a level high enough to ensure successful generation of injection current. Moreover, in a three-level neutral-point diode clamped (NPC) inverter, voltage across the two splitting DC-link capacitors has to equally be maintained as half of the overall DC-link voltage so that a balanced injection current can be generated to properly mitigate the current harmonics.

The overall DC-link voltage is often regulated by manipulating the voltage error resulting from the difference between the actual overall DC-Link voltage and its reference voltage counterpart to estimate an output, which is assumed to be the main control signal for regulating DC-link voltage. Traditionally, the voltage error manipulation and control signal estimation processes are done with a proportional-integral (PI) controller (Afghoul & Krim, 2012; Jain et al., 2002; Karuppanan & Mahapatra, 2010, 2012; Suresh et al., 2012) due to its simple implementation features. However, it performs poorly with large overshoot (Afghoul & Krim, 2012; Jain et al., 2002; Suresh et al., 2012) and serious time delay (Afghoul & Krim, 2012; Jain et al., 2002; Karuppanan & Mahapatra, 2010, 2012) under dynamic state conditions. Moreover, the performance of PI controller is strictly dependent on its tuned proportional gain and integral gain parameters which are normally obtained through a tedious heuristic approach. Besides, the tuning process can be difficult as SAPF does not possess a precise linear mathematical model which is needed to accurately tune the gain parameters of PI controller (Jain et al., 2002; Karuppanan & Mahapatra, 2012).

Further improvement based on artificial intelligence (AI) technique using fuzzy logic controller (FLC) is employed to overcome limitations of PI controller. By incorporating advantages of FLCs the performance of SAPF in DC-link voltage regulation was significantly improved (Afghoul & Krim, 2012; Jain et al., 2002; Karuppanan & Mahapatra, 2010, 2012). Basically, FLC is an adaptive mechanism which is capable of approximating a function based on simple linguistic control (if-then) rules (Belaidi et al., 2012; Suresh et al., 2012;

Zainuri et al., 2016). As a result, it is able to work effectively with imprecise inputs, handle nonlinear system with parameter variations, and is possible to be designed without knowing the exact mathematical model of the system (Belaidi et al., 2012; Karuppanan & Mahapatra, 2010, 2012; Mikkili & Panda, 2012; Zainuri et al., 2016). However, the FLC technique that is used is implemented with high complexity: 7×7 fuzzy membership functions (MFs) with 49 control rules (Afghoul & Krim, 2012; Belaidi et al., 2012; Jain et al., 2002; Karuppanan & Mahapatra, 2010, 2012; Mikkili & Panda, 2012; Suresh et al., 2012), and imposes great computational burden to the controller. Lower numbers of fuzzy MFs and control rules have never been considered as they are reported to be incapable of maintaining the overall DC-link voltage constant (Mikkili & Panda, 2012).

This paper presents a DC-link capacitor voltage regulation algorithm with effort-reduction FLC technique to efficiently control the overall DC-link voltage of three-phase three-level NPC inverter-based SAPF. The proposed effort-reduction FLC technique is developed by considering a reduced amount of fuzzy MFs and control rules, thereby reducing both design efforts and computational burden of the designed controller. The design concept and effectiveness of the proposed algorithm are verified using MATLAB-Simulink. The paper is organized as follows. In Section 2, the proposed SAPF with control strategies is described. Section 3 provides detailed descriptions on the proposed algorithm. The simulation findings are presented, and discussed in Section 4 showing improvements achieved by the proposed algorithm in comparison to the conventional algorithm. A brief summary is provided at the end of the paper, highlighting significant contributions of this work.

SHUNT ACTIVE POWER FILTER (SAPF) WITH CONTROL STRATEGIES

The proposed three-phase three-level NPC inverter-based SAPF system and its control strategies are shown in Figure 1. The control strategies compose of harmonics extraction, DC-link capacitor voltage regulation, synchronizer, neutral-point voltage deviation control, and switching control algorithms.

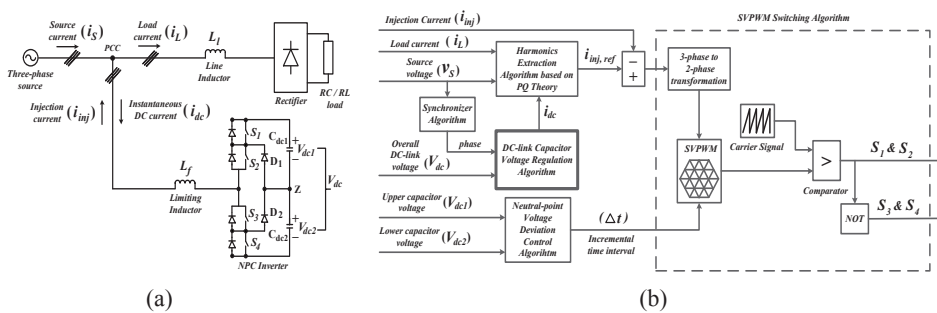


Figure 1. The proposed three-phase three-level NPC inverter-based SAPF: (a) circuit diagram, and (b) control strategies

The main focus of this paper is on the DC-link capacitor voltage regulation algorithm. From the literature, in order to ensure proper generation of injection current i_{injs} , the overall DC-link voltage V_{dc} is set according to the following requirement (Khadem et al., 2014)

$$v_s < v_{SAPF_max} \leq 2v_s \quad (1)$$

$$V_{dc} = 2v_{SAPF_max} \quad (2)$$

where v_s represents the source voltage, and v_{SAPF_max} represents the maximum output voltage of SAPF.

The minimum capacitance value C_{dc} for each capacitor can be calculated as follows (Yao & Green, 2005)

$$C_{dc} \geq \frac{\left| \int_0^t i_{inj} dt \right|}{4\Delta V_{max}} \quad (3)$$

where i_{inj} represents the injection current, and ΔV_{max} represents the maximum voltage ripple allowed on DC-link capacitors.

For the purpose of the harmonics extraction algorithm, instantaneous power (PQ) theory (Belaidi et al., 2012; Hoon et al., 2016b) is used. Meanwhile, a synchronizer is employed to provide referencing signal to the DC-link capacitor voltage regulation algorithm. Furthermore, voltage balancing of splitting DC-link capacitors is achieved via neutral-point voltage deviation control algorithm (Bhalodi & Agarwal, 2010). Finally, the switching control is accomplished through 25 kHz Space Vector PWM (SVPWM) switching algorithm (Bhalodi & Agarwal, 2010).

PROPOSED DC-LINK CAPACITOR VOLTAGE REGULATION ALGORITHM

Below details of the conventional algorithm utilizing the PI technique is presented. This is followed with a presentation of the proposed algorithm with effort-reduction FLC technique.

Conventional DC-Link Capacitor Voltage Regulation Algorithm with PI Technique

Generally, the overall DC-link voltage is regulated by controlling the real power drawn by SAPF throughout its switching operation. The voltage regulation process is considered to have accomplished when the real power drawn by the SAPF is made equal to its switching losses. To ensure proper function of SAPF the magnitude of the generated reference current must be adjusted by manipulating the variable known as instantaneous DC current i_{dc} (refer to Figure 1). which is generated based on the difference between overall DC-link voltage and its desired reference voltage counterpart, so that a precise amount of real power can be drawn by SAPF, to compensate its potential losses.

As mentioned in Section 1, PI technique is the most widely utilized technique in the area of DC-link capacitor voltage regulation. Based on this technique, the voltage error resulting from the difference between overall DC-link voltage V_{dc} ($V_{dc1} + V_{dc2}$) and its reference voltage

$V_{dc1,ref}$ is directly manipulated by a PI controller to approximate the required amplitude I_{dc} of control signal i_{dc} . The control approach can be summarized as (5). The control signal i_{dc} is made available by multiplying I_{dc} with the reference angle delivered by a synchronizer.

$$E(k) = V_{dc,ref}(k) - (V_{dc1}(k) + V_{dc2}(k)) \quad (4)$$

$$I_{dc} = E (K_p + K_i \int dk) \quad (5)$$

Figure 2 shows the control structure of conventional DC-link capacitor voltage regulation algorithm with PI technique. Meanwhile, the minimum value of the design parameters used in the PI technique can be obtained as follows (Hoon et al., 2016a; Zainuri et al., 2016)

$$K_p \geq C_{dc} \xi \omega \quad (6)$$

$$K_i \geq C_{dc} \omega / 2 \quad (7)$$

where K_p is the proportional gain, K_i is the integrator gain, C_{dc} is the capacitance value of each splitting capacitor, ξ is the damping factor fixed at 0.707, and ω is the angular frequency.

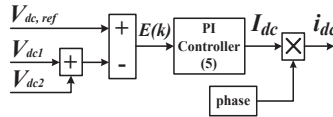


Figure 2. Control structure of conventional DC-link capacitor voltage regulation algorithm with PI technique

Proposed DC-Link Capacitor Voltage Regulation Algorithm with Effort-Reduction FLC Technique

The control structure of DC-link capacitor voltage regulation algorithm with effort-reduction FLC technique is shown in Figure 3(a). In this algorithm, FLC is employed to eliminate the reliance on PI controller. The FLC technique employed performs by using voltage error $E(k)$ and change of voltage error $CE(k)$ with sample time k given in (4) and (8) respectively to approximate the required amplitude I_{dc} .

$$CE(k) = E(k) - E(k-1) \quad (8)$$

Generally, FLC operation involves four processes, starting with fuzzification, followed by fuzzy rule base and inference interpretation, and end with defuzzification. During fuzzification, the formulated numerical $E(k)$ and $CE(k)$ variables are converted into their corresponding linguistic representation, according to their respective fuzzy MFs. All input conditions will be processed by Mamdani-style fuzzy inference mechanism (Jain et al., 2002; Karuppanan &

Mahapatra, 2012; Suresh et al., 2012; Zainuri et al., 2016) to generate the most appropriate fuzzified I_{dc} output value according to the designed fuzzy rule base table which composes a collection of simple linguistic “If X and Y, Then Z” control rules. The generated fuzzified I_{dc} value is converted back to its corresponding numerical value via the defuzzification process. Most FLC techniques use the famous centroid of area (COA) defuzzification method (Suresh et al., 2012; Zainuri et al., 2016) as it provides a good average feature in determining the best output result. The normalized fuzzy MFs and rule base for proposed effort-reduction FLC technique are shown in Figure 3(b) and Table 1 respectively.

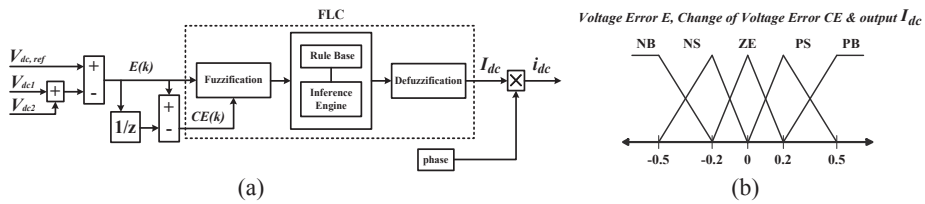


Figure 3. Proposed DC-link capacitor voltage regulation algorithm with effort-reduction FLC technique: (a) Control structure, and (b) Normalized fuzzy membership functions

Table 1
Fuzzy rule base for effort-reduction FLC technique

CE_k	$E(k)$				
	NB	NS	ZE	PS	PB
NB	NB	NB	NB	NS	ZE
NS	NB	NB	NS	ZE	PS
ZE	NB	NS	ZE	PS	PB
PS	NS	ZE	PS	PB	PB
PB	ZE	PS	PB	PB	PB

The fuzzy sets were selected according to the degree of voltage error $E(k)$ which may occur throughout the operation of SAPF. The selected fuzzy sets must possess certain sensitivity (level of fuzziness) which is sufficient enough to represent all the voltage error conditions. Low number of fuzzy sets may be insufficient to describe the characteristics of a signal. In contrast, large number of fuzzy sets provides much better results but high amount of fuzzy MFs and control rules are difficult to be developed.

In this study rather than relying on the complex FLC technique (7×7 fuzzy MFs with 49 control rules) which has widely been accepted as the best FLC design in the area of DC-link capacitor voltage regulation (Afghoul & Krim, 2012; Belaidi et al., 2012; Jain et al., 2002; Karuppanan & Mahapatra, 2010, 2012; Mikkili & Panda, 2012; Suresh et al., 2012), the effort-reduction FLC technique was developed by considering a reduced amount of fuzzy MFs and control rules: 5×5 fuzzy MFs with 25 control rules.

Our proposed effort-reduction FLC technique has also considered a combination of triangular and trapezoidal MFs. These types of fuzzy MFs are famous for their simple implementation features together with minimal computational efforts (Belaidi et al., 2012; Hoon et al., 2016a; Jain et al., 2002; Karuppanan & Mahapatra, 2012; Suresh et al., 2012). With utilization of the selected 5×5 fuzzy MFs in the proposed effort-reduction FLC technique, the overall DC-link voltage can constantly be maintained at desired value.

SIMULATION RESULTS

The three-phase three-level NPC inverter-based SAPF utilizing the proposed algorithm is simulated and evaluated in MATLAB-Simulink. The main specifications of the proposed SAPF are tabulated in Table 2. Simulation work is conducted under both steady and dynamic state conditions which involve two types of nonlinear loads. The first nonlinear load is constructed using a three-phase uncontrolled bridge rectifier feeding a 20 Ω resistor and 2200 μF capacitor connected in parallel (capacitive). The second nonlinear load is developed using similar rectifier feeding a series connected 50 Ω resistor and 50 mH inductor (inductive). Furthermore, to evaluate dynamic behaviour of the proposed algorithm, two dynamic state conditions can be created: capacitive to inductive load change and inductive to capacitive load change. However, due to limitation of pages, this work only considers dynamic state condition of capacitive to inductive load. Besides, evaluation under single dynamic state condition is good enough to evaluate the dynamic behaviour of the proposed algorithm. The conventional algorithm with PI technique was also tested for comparison purposes.

Table 2
Design specifications for SAPF

Parameter	Value
Voltage source	400 Vrms, 50 Hz
DC-link capacitor	3300 μF (each)
DC-link reference voltage	880 V
Limiting inductor	5 mH
Switching frequency	25 kHz

The simulation results of SAPF with effort-reduction FLC technique which include three-phase source voltage v_s , load current i_L , injection current i_{inj} , and source current i_s , for both nonlinear loads are shown in Figure 4. Meanwhile, THD values of source current i_s (phase A) before and after connecting the SAPF are summarized in Table 3. The findings clearly show that the THD values have been reduced to a level complying with the limit of 5 % set by IEEE Standard 519-2014 (IEEE, 2014). Moreover, SAPF with effort-reduction FLC technique has shown better harmonics mitigation performance as compared to PI technique. Furthermore, it can be observed that the mitigated source current i_s is working in phase with the source voltage v_s , thereby achieving almost unity power factor.

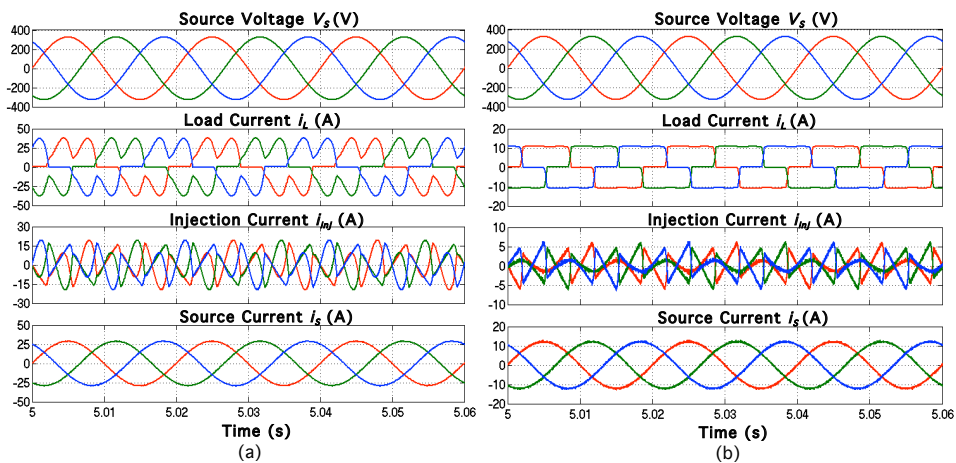


Figure 4. Simulation results of SAPF with effort-reduction FLC technique which include three-phase source voltage v_s , load current v_L , injection current i_{inj} and source current i_s for (a) capacitive, and (b) inductive loads

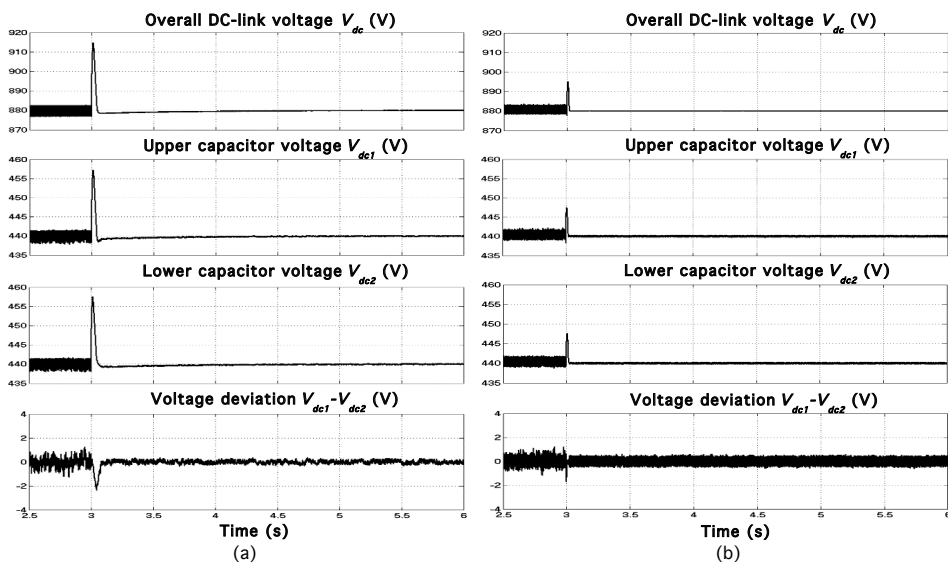


Figure 5. Simulation results of SAPF which include overall DC-link voltage V_{dc} , splitting DC-link capacitor voltages (V_{dc1} and V_{dc2}) and neutral-point voltage deviation ($V_{dc1} - V_{dc2}$) for dynamic state condition of capacitive to inductive load obtained using (a) conventional PI, and (b) proposed effort-reduction FLC techniques

Figure 5 shows the simulation results of SAPF which cover overall DC-link voltage V_{dc} , splitting DC-link capacitor voltages (V_{dc1} and V_{dc2}), and neutral-point voltage deviation ($V_{dc1} - V_{dc2}$) for dynamic state condition of capacitive to inductive load. Meanwhile, the performance of SAPF in term of overall DC-link voltage regulation is summarized in Table 3. From the findings, it is clear that the conventional algorithm with PI technique performs poorly with overshoot of 35 V, undershoot of 2 V, and response time of 1.50 s. In contrast, the proposed

algorithm with effort-reduction FLC technique performs outstandingly with overshoot of 15 V, undershoot of 0 V, and response time of 0.05 s. Therefore, in terms of overall DC-link voltage regulation, the proposed algorithm with effort-reduction FLC technique shows superior dynamic performance by achieving a response time of 30 times faster than the conventional algorithm with PI technique. In addition, it is clear that voltage across both splitting DC-link capacitors are successfully maintained as half of the overall DC-link voltage with minimum neutral-point voltage deviation and thus proving successful control of all DC voltages at their respective desired values.

Table 3
Overall performance comparison of both DC-link voltage regulation algorithms

DC-link voltage regulation algorithm	THD of Phase A Source Current i_s (%)		Dynamic Performance (Capacitive to Inductive)	
	Capacitive	Inductive	Overshoot/Undershoot (V)	Response Time (s)
N/A	43.03	27.43	N/A	N/A
			Before Connecting SAPF	
			After Connecting SAPF	
PI technique	1.21	1.66	35 V (Overshoot) 2 V(Undershoot)	1.50 s
Effort-reduction FLC technique	1.19	1.63	15 V (Overshoot) 0 V(Undershoot)	0.05 s

CONCLUSION

This paper has successfully demonstrated a DC-link capacitor voltage regulation algorithm with effort-reduction FLC technique for three-phase three-level NPC inverter-based SAPF. The proposed algorithm with effort-reduction FLC technique provides an insight into developing a much simpler yet effective fuzzy-based algorithm for controlling the overall DC-link voltage of a typical inverter-based SAPF which was previously only achievable using complex fuzzy-based algorithm. The algorithm complexity is reduced by considering a reduced amount fuzzy MFs and control rules in controller design. As a result, the proposed algorithm is proven to provide successful control of overall DC-link voltage with superior dynamic performances. Low overshoot, no undershoot, and fast response time clearly show the advantages of proposed algorithm over the conventional algorithm especially in dealing with dynamic state condition.

REFERENCES

- Afghoul, H., & Krim, F. (2012). Comparison between PI and fuzzy DPC control of a shunt active power filter. *IEEE International Energy Conference and Exhibition* (p. 146-151). Florence.
- Belaidi, R., Haddouche, A., & Guendouz, H. (2012). Fuzzy Logic Controller Based Three-Phase Shunt Active Power Filter for Compensating Harmonics and Reactive Power under Unbalanced Mains Voltages. *Energy Procedia*, 18, 560-570.

- Bhalodi, K.H., & Agarwal, P. (2010). Space Vector Modulation with DC-Link Voltage Balancing Control for Three-Level Inverters. *ACEEE International Journal on Communication*, 1(1), 14-18.
- Dai, Y., & Dai, W. (2008). Harmonic and Reactive Power Compensation with Artificial Neural Network Technology. In *7th World Congress on Intelligent Control and Automation* (p. 9001-9006). Chongqing.
- Hoon, Y., Radzi, M. A. M., Hassan, M. K., & Mailah, N. F. (2016a). DC-Link Capacitor Voltage Regulation for Three-Phase Three-Level Inverter-Based Shunt Active Power Filter with Inverted Error Deviation Control. *Energies*, 9(7), 533.
- Hoon, Y., Radzi, M. A. M., Hassan, M. K., & Mailah, N. F. (2016b). Enhanced Instantaneous Power Theory with Average Algorithm for Indirect Current Controlled Three-Level Inverter-Based Shunt Active Power Filter under Dynamic State Conditions. *Mathematical Problems in Engineering, Article ID 9682512*, 12 pages.
- IEEE. (2014). IEEE Recommended Practice and Requirement for Harmonic Control in Electric Power Systems. *IEEE Std 519-2014 (Revision of IEEE Std 519-1992)* (p. 1-29).
- Jain, N., & Gupta, A. (2014). Comparison between Two Compensation Current Control Methods of Shunt Active Power Filter. *International Journal of Engineering Research and General Science*, 2(5), 603-615.
- Jain, S. K., Agrawal, P., & Gupta, H. O. (2002). Fuzzy logic controlled shunt active power filter for power quality improvement. *IEE Proceedings of Electric Power Applications*, 149(5), 317-328.
- Kale, M., & Ozdemir, E. (2005a). An adaptive hysteresis band current controller for shunt active power filter. *Electric Power Systems Research*, 73(2), 113-119.
- Kale, M., & Ozdemir, E. (2005b). Harmonic and reactive power compensation with shunt active power filter under non-ideal mains voltage. *Electric Power Systems Research*, 74(3), 363-370.
- Karuppanan, P., & Mahapatra, K. K. (2010). PI, PID and Fuzzy logic controller for Reactive Power and Harmonic Compensation. *ACEEE International Journal on Electrical and Power Engineering*, 1(3), 54-58.
- Karuppanan, P., & Mahapatra, K.K. (2012). PI and fuzzy logic controllers for shunt active power filter - A report. *ISA Transaction*, 51(1), 163-169.
- Khadem, S. K., Basu, M., & Conlon, M. F. (2014). Harmonic power compensation capacity of shunt active power filter and its relationship with design parameters. *IET Power Electronics*, 7(2), 418-430.
- Mikkili, S., & Panda, A. K. (2012). Simulation and real-time implementation of shunt active filter id-iq control strategy for mitigation of harmonics with different fuzzy membership functions. *IET Power Electronics*, 5(9), 1856-1872.
- Suresh, Y., Panda, A. K., & Suresh, M. (2012). Real-time implementation of adaptive fuzzy hysteresis-band current control technique for shunt active power filter. *IET Power Electronics*, 5(7), 1188-1195.
- Yao, J., & Green, T. (2005). DC-link capacitors sizing for three-level neutral-point-clamped inverters in four-wire distributed generation systems. In *International Conference on Future Power Systems* (p. 1-5). Amsterdam.
- Zainuri, M. A. A. M., Radzi, M. A. M., Soh, A. C., Mariun, N., & Rahim, N. A. (2016). DC-link capacitor voltage control for single-phase shunt active power filter with step size error cancellation in self-charging algorithm. *IET Power Electronics*, 9(2), 323-335.



The Response of a High Voltage Transformer with Various Geometries of Core Joint Design

Omar. SH. Alyozbaky^{1,2*}, Maryam. M. Isa¹, Mohd Zainal Abidin Ab Kadir¹ and Mahdi Izadi¹

¹Centre for Electromagnetic and Lightning Protection Research (CELP), Faculty of Engineering, Universiti Putra Malaysia, 43400 UPM, Serdang, Selangor, Malaysia

²Department of Electrical Engineering, Faculty of Engineering, University of Mosul, Iraq

ABSTRACT

The core losses in a three phase transformer can be significantly reduced by improving the core joint geometry. The researchers were applied numerous types of T-joint designs in order to reach the optimum design that can be used in three phase transformer to reduction the losses. Two types of T-joint design are presented in this paper; T-joint with 90° butt-lap design and T-joint with 45° mitered design. A 3-phase distribution transformer was simulated in 3D using Ansys Maxwell software. The core loss for a three-leg three phase transformer rated 1000 KVA and the flux density distribution are investigated. The simulation results show the core losses were increased up to 3% and the flux density was increased to reach more than 22% flux density become higher when using T-joint with 90° butt-lap design as compared with T-joint with 45° mitered design.

Keywords: Core loss, power transformer, joints design, flux distribution

INTRODUCTION

No-load losses are also called iron or core losses. The three main components of no-load

losses are eddy currents, hysteresis and stray losses. Hysteresis describes the memory of a magnetic material. More force is necessary to demagnetise a magnetic material since the magnetic domains in the material resist realignment. Eddy current losses are small circulating currents in the core material. The steel core is a conductor that carries an alternating magnetic field, which induces circulating currents in the core. Many papers, books, reports and standards have been published on new models of transformers which ensure low losses (Amoairalis, Tsili,

ARTICLE INFO

Article history:

Received: 24 August 2016

Accepted: 03 Jun 2017

E-mail addresses:

O.Sh.Alyozbaky@gmail.com (Omar. SH. Alyozbaky),

maryam@upm.edu.my (Maryam. M. Isa),

mzk@upm.edu.my (Mohd Zainal Abidin Ab Kadir),

aryaphase@yahoo.com (Mahdi Izadi)

*Corresponding Author

& Kladas, 2009). The most recognised contributors of core loss performance in power and distribution transformers are firstly the iron losses of the core material (Valkovic, 1982) and secondly the additional losses caused by the global redistribution of the core flux in the different regions of the core (Mechler & Girgis, 1998; A. J Moses & Thomas, 1973). It is therefore important to obtain a better understanding of the magnetic flux behaviour in stacked transformer cores (Mechler & Girgis, 1998). Other studies have looked at the effect of the T-joint design on the flux distribution in the core and the additional losses caused by this joint in 3-phase 3-limb cores (Moses & Thomas, 1973; Moses, Thomas, & Thompson, 1972; Valkovic, 1982). Increasingly important in the transformer industry to reduce the core losses and improve the estimation techniques right from the design stage (Daut & Moses, 1990; Loffler, Booth, Pfützner, Bengtsson, & Gramm, 1995; Nakata, Takahashi, & Kawase, 1982). Several studies in this area in the literature have been reported over the past few decades (Du et al., 2010; Elleuch & Poloujadoff, 1998; Girgis, Te Nijenhuis, Gramm, & Wrethag, 1998; Moses, 1998; TeNyenhuis, Girgis, & Mechler, 2000).

The flux path in the T-joint area is very complex. A sinusoidal supply is provided to the core transformer by the windings. The change in direction of the supply can overcome the air gap distance, and the two processes cause the flux to pass through from the joint area. Circulation and rotation flux appears in this area with every change in the flux direction because the flux has the same properties as the supply. The middle limb is connected to the top and bottom yoke, and this joint is called a T-joint. The T-joint is considered to be the spine of the transformer core because it provides mechanical support for the core and most of the flux flows through the T-joint connection. Cores are typically made from cold-rolled, grain-orientated silicon steel laminations. The effects of materials on the behaviour of a three-phase three-core leg in a power transformer has been investigated under different operating conditions in (Alyozbaky, Kadir, Izadi, Gomes, & Azis, 2016). A third component of core loss is the eddy current or hysteresis phenomena, or stray, extra or anomalous loss. The finite element method (FEM) has been extensively employed in the prediction of no-load losses prediction problem. It has been previously shown that harmonics circulate in individual laminations in the limbs and yokes. Other studies (A.J. Moses & Thomas, 1974) have explored the local flux distribution in transformer cores as a function of joint design and its relevance for power loss and noise. FEM has been used extensively to study transformer joint air gaps, although this information does not appear to be applied in circuit models. In earlier research (Thomas, 1975) experiments to determine the flux paths and flux transfer mechanisms in the T-joints of three phase transformer cores had been performed. Third harmonic flux circulation similar to that observed previously (Basak & Higgs, 1982) in three limb cores has been observed in both core geometries.

Thus, changing the design of the T-joint of a core transformer is still an important factor, especially when this issue is reflected in its impact on the core losses and potential improvement of the core performance. In this paper a three-leg three-phase distribution transformer rated 1000KVA is simulated in 3D using Ansys Maxwell Software. The main objective is to present the relationship between the geometry of the T-joint with 90° butt-lap design, T-joint with 45° mitered design, the core loss issue and the correlation between the flux density and core loss of different T-joint designs.

METHOD

In this work the transformer core was built from grain orientated silicon steel (CRGO) 3% silicon, 97% iron which has saturation point around 2 Tesla. Two models of a T-joint design for the core transformer were compared and modelled in the Ansys Maxwell software, namely T-joint with 90° butt-lap design and T-joint with 45° mitered design. The simulation for the 3-D design using the Ansys Maxwell software was based on the common geometry model of a three phase transformer. The relevant data of the transformer was rated power 1MVA, 11/0.433KV, 50Hz. The height of the core is 900mm, width 1030mm and depth 243mm. The operation flux density for this core is 1.56T, the primary winding 16 turns and simulated as cylindrical shapes to reduce the running time for simulation. Figure 1 shows the sketch of the transformer for T-joint with 90° butt-lap design and T-joint with 45° mitered design.

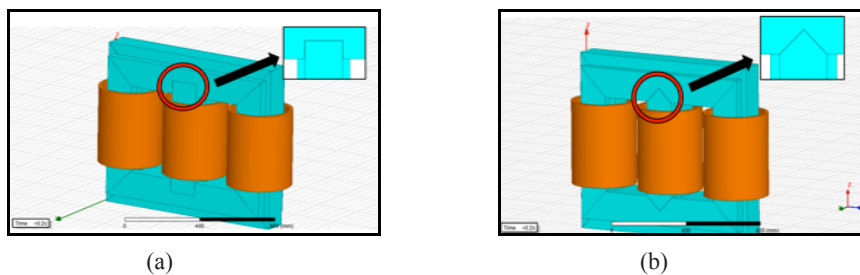


Figure 1. The core design (a) T-joints with 90° butt-lap, (b) T-joints with 45° mitered

RESULTS AND DISCUSSION

The flux density and core losses consider the main concern of this study. To compare the different types of T-joint geometries of the transformer core, primary windings has been set to provide a flux density of around 1.56 T in the limbs. However, to achieve the main goal of comparing the different geometries of the T-joints, it is necessary to compare the flux density, and the core loss should be on the same level of voltage. The region between the core and winding is filled with transformer oil. Each winding is connected to a voltage terminal that has been excited by a sinusoidal supply.

As a results the geometrical design of the T-joint of the core improves the core losses. Figure 2 shows the core losses for the T-joint with 90° butt-lap design and T-joint with 45° mitered design. It appears the core loss was reduced as average and maximum values when compare between the design of the T-joint with 90° butt-lap design and the T-joint with 45° mitered design.

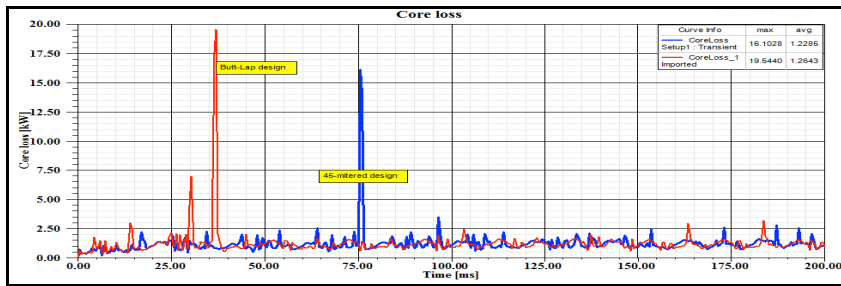


Figure 2. Core losses for different designs of T-joint

Furthermore, the main flux density which distributed on the transformer core with T-joint with 90° butt-lap design and T-joint with 45° mitered design is shown in Figure 3. By comparing the distribution of the flux density in the core geometry, although all the cores were excited using the same voltage level, in the case of butt-lap design, the flux density reached to 2.335 Tesla while decrease to 1.81T when the T-joint design was used T-joints with 45° mitred. The reason of that, the behaviour of movement for flux density was dissimilar because the shape of these joints was different. An efficient core can be built if manufactured using a T-joint with 45°mitered. In addition, from the results show that the saturation phenomena in the core transformer can be overcome.

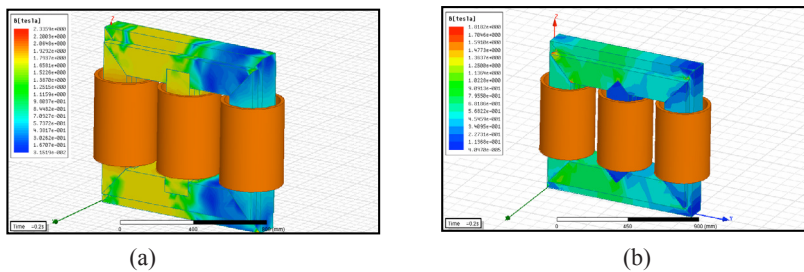


Figure 3. Flux distribution in the core (a) T-joints with 90° Butt-lap, (b) T-joints with 45° mitered

The behaviour of the flux density in the joint areas such as rotating and circulating flux and the effects of angles in T-joint with 90° butt-lap design led to magnetic flux tend to deviation in this area. The distortion and deviation of the flux density and localised losses in the T-joints is due to the core gaps across the core stack. The over stacking, limited area, gaps and corners in the T-joint with 90° butt-lap design are considered major reasons for increase in core losses and push the core to reach to the saturated condition. An improvement in the core loss is due to its effect on the flux path in the core. The flux density distribution in the T-joint area for different designs appears in Figure 4. It is noted there is an increase in the flux density along the path of flux, especially in the gaps and in the angles.

Response Transformer in the Different Joint Design

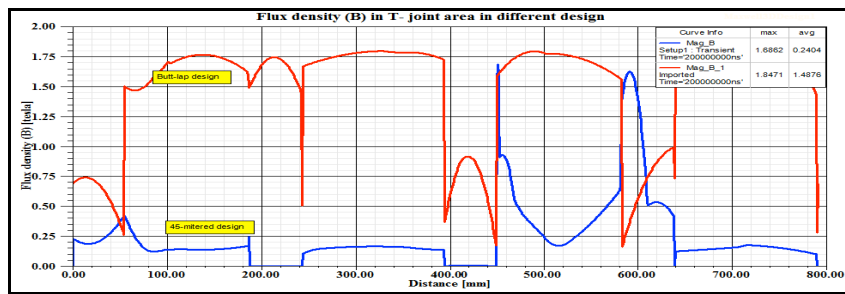


Figure 4. Flux distribution in the T-joint area for both designs

This deviation of the magnetic flux lines with respect to the rolling direction generates localised losses areas with higher flux density and therefore increased losses. At the maximum values of the flux density about 1.84 T and 1.68 T on joints with 90° butt-lap and T-joints with 45° mitred respectively. There is more than a 9.5 % increase in the flux density in the T-joint area when using T-joints with 90° butt-lap, while it is clear from Figure 4 that the average value of the flux density is better more value when using the T-joints with 45° mitred design. The T-joint section is very important as a case study because it is the main joint between the yoke and the limb. The flux path from the top yoke to the middle limb for different T-joint designs is presented in Figure 5. It is noticeable that the behaviour of the flux density is more complicated in the gaps which appear between the laminations when assembling the core during manufacture. It is about 1.9 T in the gap area while it is 1.07 T when using T-joints with 90° butt-lap and T-joints with 45° mitred respectively.

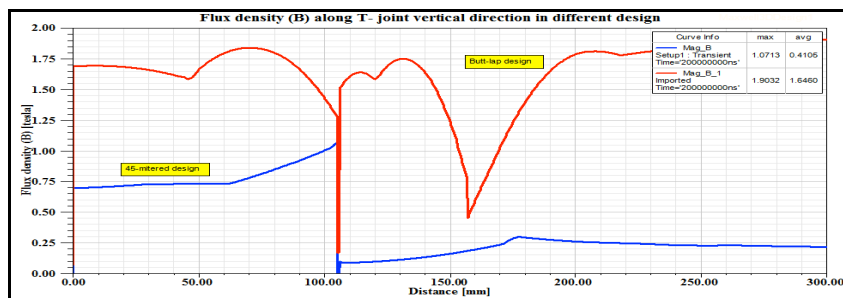


Figure 5. Flux density path from the top yoke to the middle limb for both designs

Figure 6 illustrates the behaviour of the flux density in the gap. The decrease in the amount of flux density in the gap area it is good sign especially in the edges for designers and researchers because that means the losses in this area have been reduced.

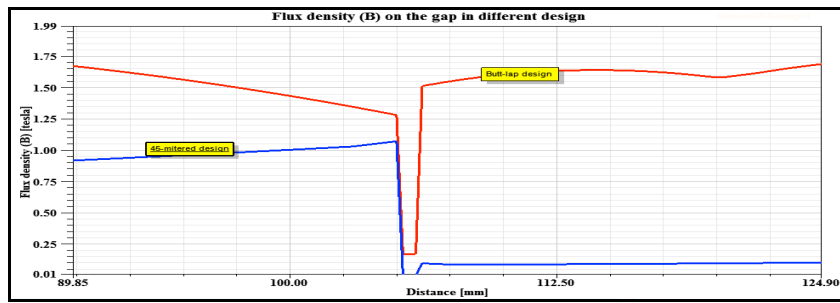


Figure 6. The behaviour of flux density in the gap between Top yoke with middle limb for different T-joint designs

The flux density is increased and caused to localized losses due to the distorted flux distribution in the T-joint regions (due to core gaps) across the core stack. The saturation phenomenon, one of the important point in transformer core performances. This study showed butt-lap joint design core reach to the saturation point of work within no-load. While the 45° mitred it appeared more efficient on this point. For the flux densities in overall the core it is exceeded the allowable limit of flux, the value reached to 2.33 T when used T-joint with butt-lap while in 45° mitred T-joint design it is still acceptable within the boundaries, the value reached to 1.81 T.

Thus the butt lap T-joint design is closest to the undesirable case of the saturation phenomena. The relationship between the core loss and flux density seems clear. As a result, each has an impact on the other. When the flux density increases in the T-joint section, the core loss is shown to increase concurrently. Simulated results of the transformer core in different joint designs are shown in Table 1.

Table 1
Difference between the values of Flux densities in T-joint with 90° butt-lap design and T-joint with 45° mitred design

Type of joint	Area test	Max (B)T	Average (B)T	Core loss
butt-lap design	Vertical distance in T-joint	1.9	1.64	
	Horizontal distance in T-joint	1.946	1.347	
	Around the T-joint area	1.84	1.48	
	All the core	2.33		
45° mitred design	Vertical distance in T-joint	1.07	0.14	
	Horizontal distance in T-joint	0.655	0.365	
	Around the T-joint area	1.68	0.24	
	All the core	1.81		

Generally, to complete the picture and to determine the effect of the geometry of the T-joint design on the flux density distribution in the T-joint area, a 3D simulation of the flux density for different T-joint designs was developed and illustrated in Figure 7. From the figure, it can be observed that the flux density for the T-joint with 90° butt-lap design has a higher value from T-joint with 45° mitered design.

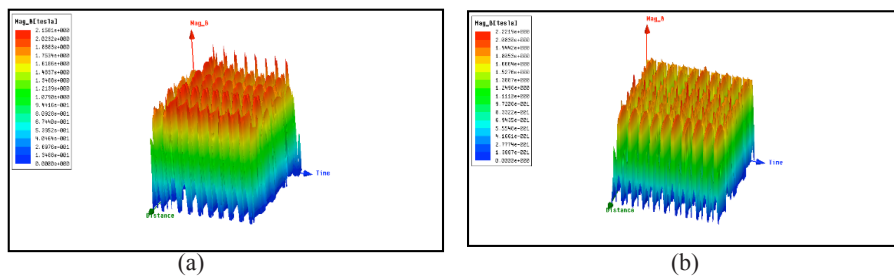


Figure 7. 3D flux density in the T-joint area for different design (a) T-joints with 90° butt-lap, (b) T-joints with 45° mitered

CONCLUSION

The flux distribution of two types of T-joint designs and the correlation between the geometry of the T-joint design and core loss was presented. The flexibility of the proposed model for a three-leg three phase transformer core that deals with the distribution of flux density in the core part, especially in the joint area highlighted. The losses of the core using a butt-lap design for the T-joint is 3% higher than the core using a 45°-mitered T-joint design are also shown. The 3D simulation model can be used to study transient operations and steady state operations. The flux density increases by up to 22 % when the T-joint with 90° butt-lap core design was used. Our results show that the overall performances for the T-joint with 45° mitered core design is better than for T-joint with 90° butt-lap core design.

ACKNOWLEDGEMENTS

The authors wish to thank the Centre for Electromagnetic and Lightning Protection Research (CELP), Electrical and Electronic Engineering Department, Universiti Putra Malaysia, Malaysia, for supporting this study. The main author would also like to thank The Ministry of Higher Education and Scientific Researches and Mosul University, College of Engineering, electric department for the scholarship.

REFERENCES

- Alyozbaky, O. S. A., Kadir, M. Z. A. A., Izadi, M., Gomes, C., & Azis, N. Bin. (2016). The Behaviour of Three phase Three- leg 11KV Transformer core type design Under sinusoidal and non-sinusoidal operating conditions for different core materials. In *10th International Power Engineering and Optimization Conference (PEOCO 2016) 26th March 2016, Shah Alam, Malaysia*.

- Amoiralis, E. I., Tsili, M. A., & Kladas, A. G. (2009). Transformer design and optimization: A literature survey. *IEEE Transactions on Power Delivery*, 24(4), 1999–2024.
- Basak, A., & Higgs, C. (1982). Flux distribution in three phase transformer cores with various T-joint geometries. *IEEE Transactions on Magnetics*, 18(2), 670–673.
- Daut, I., & Moses, A. J. (1990). Some Effects of Core Building on Localised Losses and Flux Distribution in a Three-Phase. *IEEE Transactions on Magnetics*, 26(5), 2002–2004.
- Du, Y., Cheng, Z., Zhao, Z., Fan, Y., Liu, L., Zhang, J., & Wang, J. (2010). Magnetic flux and iron loss modeling at laminated core joints in power transformers. *IEEE Transactions on Applied Superconductivity*, 20(3), 1878–1882.
- Elleuch, M., & Poloujadoff, M. (1998). New transformer model including joint air gaps and lamination anisotropy. *IEEE Transactions on Magnetics*, 34(5 pt 2), 3701–3711.
- Girgis, R. S., te Nijenhuis, E. G., Gramm, K., & Wrethag, J. E. (1998). Experimental investigations on effect of core production attributes on transformer core loss performance. *IEEE Transactions on Power Delivery*, 13(2), 526–531.
- Loffler, F., Booth, T., Pfützner, H., Bengtsson, C., & Gramm, K. (1995). Relevance of step-lap joints for magnetic characteristics of transformer cores. *IEE Proceedings - Electric Power Applications*, 142(6), 371–378.
- Mechler, G. F., & Girgis, R. S. (1998). Calculation of Spatial Loss Distribution in Stacked Power and Distribution transformer Cores. *IEEE Transactions on Power Delivery*, 13(2), 532–537.
- Moses, A. J. (1998). Comparison of transformer loss prediction from computed and measured flux density distribution. *IEEE Transactions on Magnetics*, 34(4 PART 1), 1186–1188.
- Moses, A. J., & Thomas, B. (1973). The spatial variation of localized power loss in two practical transformer T-joints. *IEEE Transactions on Magnetics*, 9(4), 655–659.
- Moses, A. J., & Thomas, B. (1974). Problems in the design of power transformers. *IEEE Transactions on Magnetics*, 10(2), 148–150.
- Moses, A. J., Thomas, B., & Thompson, E. (1972). Power Loss and Flux Density Distributions in the T-Joint . of a Three Phase Transformer Core. *IEEE Transactions on Magnetics*, MAG-8(4), 785–790.
- Nakata, T., Takahashi, N., & Kawase, Y. (1982). Magnetic performance of step-lap joints in distribution transformer cores. *IEEE Transactions on Magnetics*, 18(6), 1055–1057.
- TeNyenhuis, E. G., Girgis, R. S., & Mechler, G. F. (2000). Other factors contributing to the core loss performance of power and distribution transformers. *2000 Power Engineering Society Summer Meeting (Cat. No.00CH37134)*, 4(4), 648–653.
- Thomas, B. (1975). Flux Paths and Flux Transfer Mechanism in the T Joints of Three Phase Transformer Cores. *IEEE Transactions on Magnetics*, MAG-11(1), 65–71.
- Valkovic, Z. (1982). Influence of transformer core design on power losses. *IEEE Transactions on Magnetics*, 18(2), 801–804.



RF CMOS Switch Design Methodologies for Multiband Transceiver Applications

Veeraiyah Thangasamy^{1*}, Vinesh Thiruchelvam¹, Shaiful Jahari Hashim² and Noor Ain Kamsani²

¹School of Engineering, Asia Pacific University of Technology and Innovation, 57000, Kuala Lumpur, Malaysia

²Faculty of Engineering, Universiti Putra Malaysia, 43400 UPM, Serdang, Selangor, Malaysia

ABSTRACT

Multimode multiband connectivity has become a de-facto requirement for smartphones with 3G WCDMA/4G LTE applications. In transceivers, multiband operation is achieved by selecting an output from two or more signal path targeting for a specific frequency range in parallel or by using switched capacitor/inductor. In this paper, design methodology of 280nm CMOS switch is presented. Design optimization of RF CMOS switch is presented which is deciding proper selection of CMOS transistor parameters and switch size as per external circuit parameters. The CMOS switch of a 5-transistor stack with $W/L=1200\mu\text{m}/280\text{nm}$ provides insertion loss $< 0.6\text{dB}$ and isolation loss $>14\text{dB}$. The switches designed when implemented in a multiband power amplifier (PA) exhibits 36dB gain at 1900MHz high-band and 34.5dB gain at 900MHz low-band with 27.5dBm peak power at both bands. The switch design methodologies presented in this paper should be of use in designing various blocks in emerging multiband transceiver applications.

Keywords: CMOS RF switch, insertion loss, isolation loss, multiband power amplifier, Long Term Evolution (LTE)

INTRODUCTION

Wireless communication is evolving at a very fast rate and the smartphone devices need to be able to connect to more than one band of frequency (Moon, 2015; Cheng & Young, 2011) in order to support global roaming facilities. Transformer matching or LC matching is usually used in PA design at LTE operational frequencies. In order to achieve matching at a particular band frequency band,

ARTICLE INFO

Article history:

Received: 24 August 2016

Accepted: 03 Jun 2017

E-mail addresses:

veeraiyah@gmail.com (Veeraiyah Thangasamy),

dr.vinesh@apu.edu.my (Vinesh Thiruchelvam),

sjh@upm.edu.my (Shaiful Jahari Hashim),

nkamsani@upm.edu.my (Noor Ain Kamsani)

*Corresponding Author

the capacitor that is parallel to the transformer inductor or the capacitor in the LC matching network is tuned. For example, a tunable multiband PA was demonstrated by Ali et al. (2010) using BST (barium-strontium-titanate) varactor based tuning at frequencies from 1.7GHz to 2.2GHz; a multiband PA by Neo et al. (2006) using silicon-on-glass varactor diode for tuning was realized; a multiband PA using four number of MEMS switches was realised by Fukuda et al. (2006); and Kang et al. (2013) reported an MB PA that uses PIN diode switches. A multiband PA in the GaAs heterojunction-bipolar transistor (HBT) is presented by Lee et al. (2015), in which the input and output matching networks are tuned to achieve multiband operation.

In the above works, BST and MEMS-based tuning cannot be realised in CMOS process and PIN diode is not available in most of the standard CMOS PDK. Therefore, transformer matching with switches or LC matching with switches is used in the CMOS based PA design. However, the parasitic of the CMOS transistor switch degrades the gain and linearity of the PA, and hence optimum design of the switch is very essential. There are a few works reported on CMOS switch design (Yeh et al., 2006; Min & Rebeiz, 2007; Li et al., 2008) for transmit/receive (T/R) application associated with connecting antenna to the transmit and receive path. However, design of CMOS switches for individual multiband RF modules that is efficient is needed.

In this paper, the design methodologies of CMOS switch for minimum insertion and maximum isolation losses is presented. The designed switches are then integrated in a multiband PA design and its performance examined.

METHODOLOGY

CMOS Switch Design

In general, a transistor can be considered as a parasitic capacitor when it is in the OFF state and as a resistor when it is in the ON state as shown in Figure 1. The parasitic diode between the bulk and drain terminals is forward-biased during the negative half cycle of the ac signal; and similarly, the parasitic diode between the bulk and source terminals is forward-biased during the positive half cycle of the ac signal. Thus, in the OFF state of the transistor, the conduction of current through the parasitic diodes greatly affects the output power and linearity when used in PA application. Therefore, in this design, the bulk of the transistor is connected to the substrate (ground) through a resistor value of 10k Ω to control leakage current. In addition, the transistors should be stacked (let the number of series connected transistor be defined as stack length) in such a way that the voltage distributed across the parasitic capacitors is less than the “turn-on” voltage of the diodes. Moreover, when the transistor is ON, its resistance R_{on} should be as small as possible to achieve high gain and high output power. Therefore, an optimum design of CMOS switch becomes essential.

Investigations of the transistor ON state resistance and OFF state capacitance in the Silterra (Kedah, Kulim, Malaysia) 280nm CMOS transistor is taken here for the optimum switch design. Transient analysis was performed using Cadence simulation and the transistor ON state resistance calculated using Ohm's law (i.e. V_{DS}/I_{DS}). To determine the OFF state

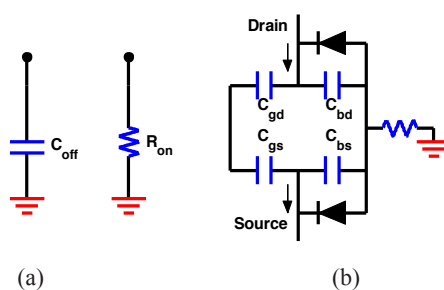


Figure 1. CMOS transistor-based switch implementation (a) transistor equivalent in the OFF and ON state (b) simplified equivalent model of a parasitic transistor

capacitance, transient analysis was performed and the power consumed by the switch was determined using the *integ* function available in the Cadence Spectre calculator, and then the capacitance estimated from the relation $P=C \times V^2 \times f$.

Figure 2(a) shows the ON state resistance of the switch with respect to the changes in the width of the transistor and its respective stack length; from which it is understood that increasing the transistor width will decrease the ON state resistance of the transistor. As such, if the CMOS switch in the circuit requires handling high current then the switch design should opt for larger transistor size. Moreover, as seen from the Figure 2(a), the resistance increases with higher stack length because the resistance of each transistor that is being stacked in series will be added to the total ON state resistance.

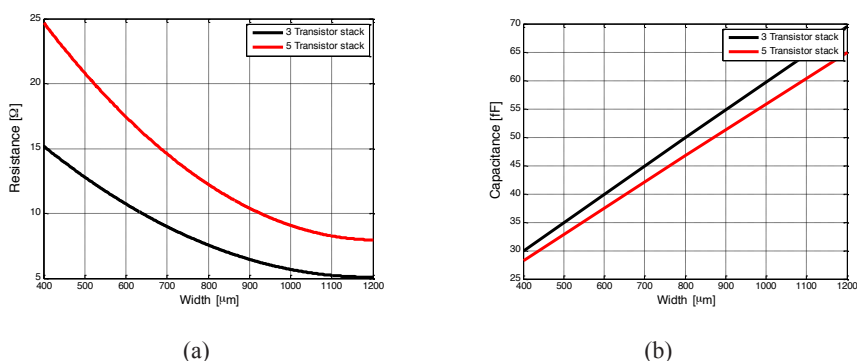


Figure 2. (a) ON state resistance, and (b) OFF state capacitance of the switch versus transistor width

On the other hand, Figure 2(b) shows the OFF state capacitance of the switch with respect to transistor width and transistor stack length; from which it is understood that increasing the transistor width will increase the transistor OFF state capacitance linearly. As such, if the external circuit capacitance value is high then the switch design should opt for smaller size transistor provided current through the switch is not constrained. If the current is constrained to a certain value, then the design should opt for increasing the stack length. Moreover, as seen

from the Figure 2(b), the capacitance decreases when the stack length increases, because of the reduced series capacitance of the transistors in the stack.

Figure 3(a) shows the ON state resistance of the switch with respect to the transistor stack length and the transistor width; from which it is clear, as expected, that increasing the stack length increases the transistor ON state resistance. Therefore, when the switch is designed to handle high voltage, then high stack length should be used so as to distribute the voltage across the parasitic diodes to be less than its ‘turn-on’ voltage. For 280nm CMOS transistor, the V_{DS} of less than 3V will keep the diodes ‘turn-off’. Therefore, for every V_{DS} increment by 3V the stack length should be increased by one transistor.

Similarly, on the other hand, Figure 3(b) shows the OFF state capacitance of the switch with respect to the transistor stack length and the transistor width. The capacitance decreases rather slowly for an increase in stack length but rapidly decreases for the decrease in transistor width. To have a good isolation in the OFF state, the reactance of switch parasitic capacitance should be higher than the external circuit capacitance. That is $X_{C_{off}} \gg X_C$ or $C_{off} \ll C$; where C is the external circuit capacitance and C_{off} is the switch OFF state parasitic capacitance.

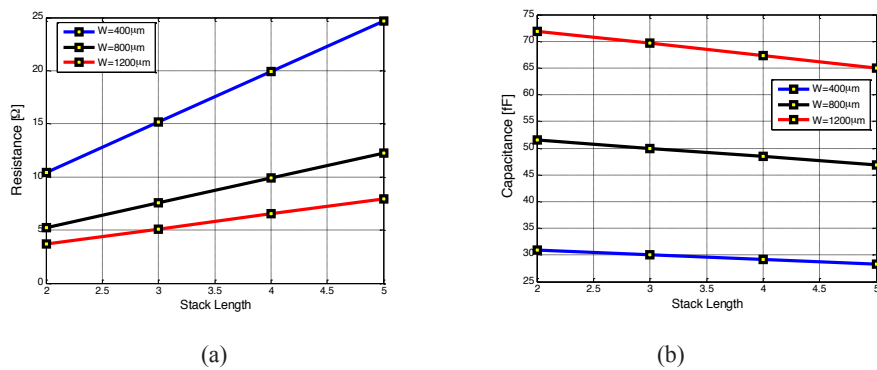


Figure 3. (a) ON state resistance, and (b) OFF state capacitance of the switch versus transistor stack length

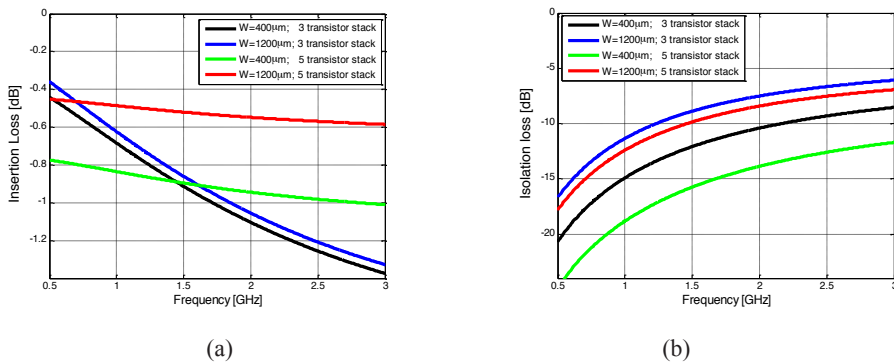


Figure 4. (a) Insertion loss (when the transistor in ON), and (b) Isolation loss (when the transistor OFF) of the switch against frequency

Figure 4(a) shows the insertion loss of the switch as a function of frequency. For a good switch the insertion loss has to be a minimum. It can be seen from the figure that the insertion loss increases with frequency. The loss can be minimised by increasing the transistor width for a fixed stack length; and/or by increasing the stack length for a fixed transistor width. Insertion loss of 0.4-0.6dB is nominal in a standard CMOS process (Kidwai et al., 2009). A 5-transistor stack with $W=1200\mu\text{m}$ in Silterra CMOS offers a loss of $\sim 0.5\text{dB}$ at the LTE operational band of frequencies, as such, it is found to be the optimum choice for the switch design. Similarly, Figure 4(b) shows the isolation loss of the switch as a function of frequency. For a good switch the isolation loss has to be a maximum. It can be seen from the figure; the isolation loss decreases with frequency. The loss can be maximized by decreasing the transistor width for a fixed stack length; and/or by increasing the stack length for a fixed transistor width.

Based on the above investigation, the switch design analysis can be summarised as in Figure 5. The transistor width is directly proportional to the current requirement of the switch and inversely proportional with the external capacitance (C_s) that the switch should be connected to. Therefore, the choice of transistor width depends on the right balance between current through the switch and the external capacitance value. When the requirement of current through the switch is fixed, then one should consider increase or decrease the stack length based on the external capacitance. Similarly, for a fixed external capacitor value we should increase or decrease the transistor width based on the requirement of current through the switch. The stack length should also increase with external node voltage (V_s) as shown in Figure 5. Thus, the correct choice of transistor width and stack length will provide minimum loss during ON state and maximum (isolation) impedance in OFF state leading to optimum circuit performance.

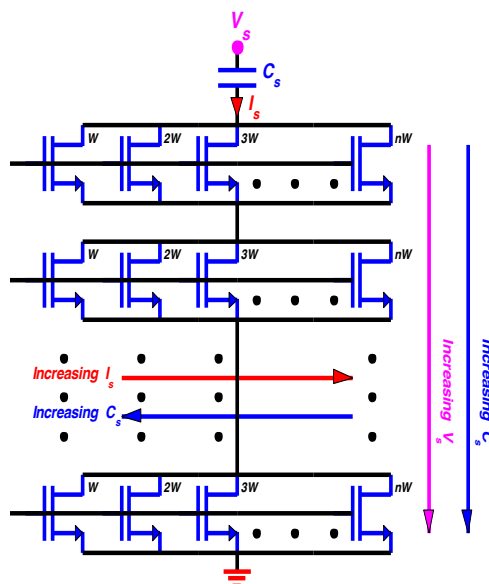


Figure 5. Switch implementation using stacked transistor array (shows how the transistor width and stack length changes with changes in circuit voltage, current and capacitor value)

Multiband PA Design using CMOS Switch

To evaluate the performance of the CMOS switch designed as per methodologies explained above, a multiband PA (Thangasamy et al., 2016) is designed as shown in Figure 6. Supply voltage of 3.3V is applied for the power stage and 1.2V for the driver stage. Switches S1, S2 and S3 are the CMOS switches designed to switch the PA operation from one operating band in to another band. The switches connect the capacitors C11, C31 and C51 in parallel with fixed capacitors C1, C3 and C5, respectively and thus the PA operating band is shifted. The schematic of switches S1, S2 and S3 is shown in Figure 7; whereby S1 is designed with two transistor stack with $W/L = (10\mu\text{m} \times 20)/280\text{nm}$ for each transistor, S2 is three transistor stack with size of each transistor $W/L = (10\mu\text{m} \times 50)/280\text{nm}$, and the switch S3 is designed with 5 transistor stack with size of each transistor $W/L = (10\mu\text{m} \times 60 \times 2)/280\text{nm}$.

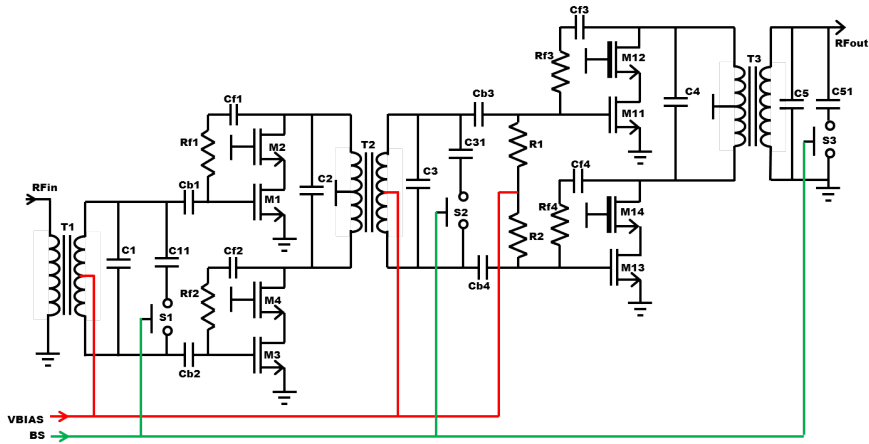


Figure 6. Circuit schematic of multiband PA with CMOS Switch

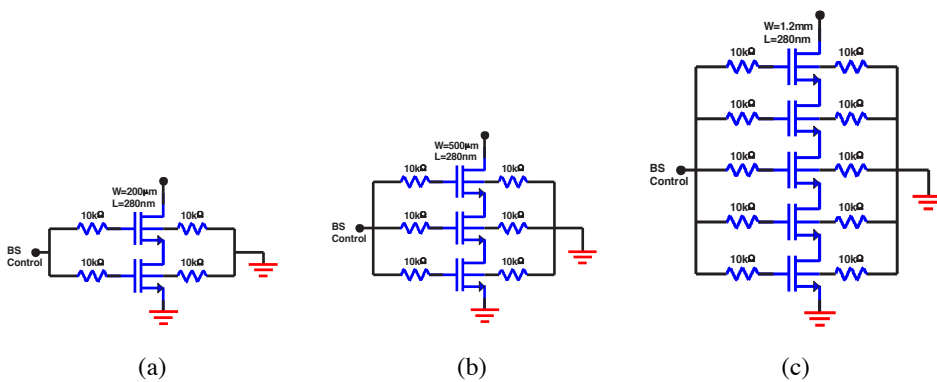


Figure 7. Schematic of (a) switch S1 with two transistor stack and $W/L = 200\mu\text{m}/280\text{nm}$ (b) switch S2 with three transistor stack and $W/L = 500\mu\text{m}/280\text{nm}$ (c) switch S3 with five transistor stack and $W/L = 1.2\text{mm}/280\text{nm}$

Here it can be seen that the switch S1 is used at the input stage, S2 is used at the intermediate stage, and S3 is used at the output stage of the PA. During simulation, at peak output power, the voltage across S1 swing around 1V, voltage across S2 swing around 4V, and voltage across S3 swing around 10V. As such, the transistor stack size is proportionally increased as shown in Figure 7. Moreover, at peak output power, the current through S1 is about 10mA, current through S2 is about 70mA, and that through S3 is about 150mA; as such, the transistor W/L ratio is proportionally increased for S1 through S3 as shown in Figure 7.

RESULTS AND DISCUSSION

The performance of the multiband PA with integrated switches has been evaluated and the simulated gain is shown in Figure 8(a). When the switches S1, S2 and S3 are OFF then the PA responds for 1.2GHz to 2.7GHz frequency band; and when the switches are ON the PA operation shifts to 820MHz to 920MHz band. Between the two gains there is a difference of nearly 1.5dB which is due to the insertion losses of the three switches. Similarly, the achieved P_{out} versus P_{in} performance of the multiband PA with integrated switches is shown in Figure 8(b).

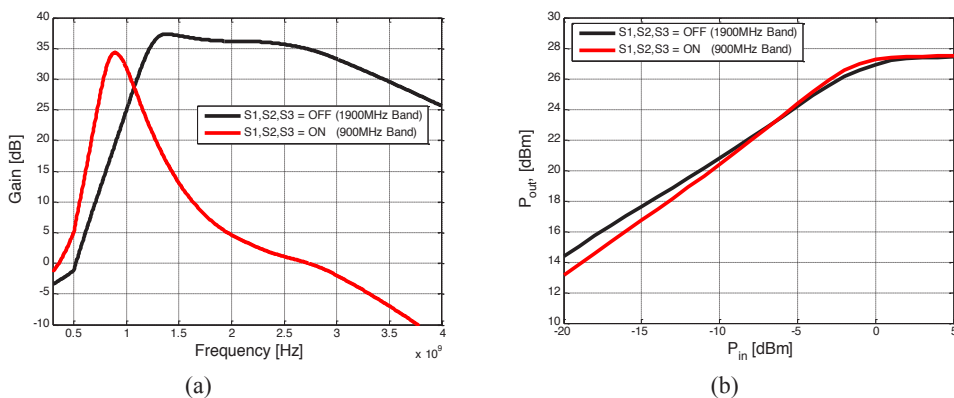


Figure 8. (a) S-parameter results, and (b) Pout versus Pin characteristics of multiband PA

When the switches S1, S2 and S3 are OFF then the PA has P1dB of 26dBm with maximum power at 27.5dBm; and when the switches are ON the PA has P1dB of 27dBm with maximum power at 27.5dBm. Between the powers there is a difference of nearly 1dBm in the low power region which is due to loss in the switch; however, in the high-power region these two powers are almost same. Thus, the optimum design of CMOS switch enables the multiband PA to deliver optimum power output and optimum gain in either band of operations.

CONCLUSION

Following the growing need for multiband RF modules efficient design of CMOS switches has become important. In this paper, we presented the design methodologies of CMOS switches in view of getting minimum insertion loss and maximum isolation loss as need for the switches in multiband RF module design applications. The switches designed on integration into a

multiband power amplifier exhibits good gain and output power performance both in ON state and OFF state of the switch. The switch design methodologies presented here should be useful in CMOS based multiband circuitry applications.

REFERENCES

- Ali, F., Lourandakis, E., Gloeckler, R., Abt, K., Fischer, G., & Weigel, R. (2010). Tunable Multiband Power Amplifier using Thin-Film BST Varactors for 4G Handheld Applications. In *IEEE Radio and Wireless Symposium* (pp. 236–239). New Orleans, LA, USA.
- Cheng, N., & Young, J. P. (2011). Challenges and Requirements of Multimode Multiband Power Amplifiers for Mobile Applications. In *IEEE Compound Semiconductor Integrated Circuit Symposium* (pp. 1–4). Waikoloa, Hawaii, USA. <http://doi.org/10.1109/CSICS.2011.6062432>
- Fukuda, A., Okazaki, H., & Narahashi, S. (2006). A Novel Compact Reconfigurable Quad-band Power Amplifier Employing RF-MEMS Switches. In *European Microwave Conference* (pp. 344–347). Manchester, USA.
- Kang, S., Kim, U., Kwon, Y., & Kim, J. (2013). A Multi-mode Multi-band Reconfigurable Power Amplifier for Low Band GSM/UMTS Handset Applications. In *IEEE Topical Conference on Power Amplifiers for Wireless and Radio Applications* (pp. 16–18). Santa Clara, CA, USA.
- Kidwai, A. A., Fu, C., Jensen, J. C., & Taylor, S. S. (2009). A Fully Integrated Ultra-Low Insertion Loss T/R Switch for 802.11b/g/n Application in 90nm CMOS Process. *IEEE Journal of Solid-State Circuits*, 44(5), 1352–1360.
- Lee, G., Jung, J., & Song, J.-I. (2015). A Multiband Power Amplifier With a Reconfigurable Output-Matching Network for 10-MHz BW LTE Mobile Phone Applications. *IEEE Transactions on Circuits and Systems II: Express Briefs*, 62(6), 558–562.
- Li, Q., Zhang, Y. P., Yeo, K. S., & Lim, W. M. (2008). 16.6- and 28-GHz Fully Integrated CMOS RF Switches With Improved Body Floating. *IEEE Transactions on Microwave Theory and Techniques*, 56(2), 339–345. <http://doi.org/10.1109/TMTT.2007.914364>
- Min, B. W., & Rebeiz, G. M. (2007). Ka-band Low-loss and High-isolation 0.13 μ m CMOS SPST/SPDT Switches using High Substrate Resistance. In *IEEE Radio Frequency Integrated Circuits Symposium* (pp. 569–572). Honolulu, Hawaii. <http://doi.org/10.1109/RFIC.2007.380948>
- Moon, H. (2015). A Low-Power Amplitude Modulator for Quad-Band GSM / EDGE Polar Transmitter in a 65nm CMOS Process. *Indian Journal of Science and Technology*, 8(26), 1–7. <http://doi.org/10.17485/ijst/2015/v8i26/84647>
- Neo, W. C. E., Lin, Y., Liu, X., Vreede, L. C. N. De, Larson, L. E., Spirito, M., ... Nanver, L. K. (2006). Adaptive Multi-Band Multi-Mode Power Amplifier Using Integrated Varactor-Based Tunable Matching Networks. *IEEE Journal of Solid-State Circuits*, 41(9), 2166–2176.
- Thangasamy, V., Kamsani, N. A., Hamidon, M. N., Hashim, S. J., Yusoff, Z., & Bukhori, M. F. (2017). Digital-Controlled Multimode Multiband Power Amplifier with Multiple Gated Transistor. *IETE Technical Review*, 34(1), 48–57. <http://doi.org/10.1080/02564602.2016.1141079>
- Yeh, M., Tsai, Z., Liu, R., Lin, K.-Y., Chang, Y.-T., & Wang, H. (2006). Design and Analysis for a Miniature CMOS SPDT Switch using Body-floating Technique. *IEEE Transactions on Microwave Theory and Techniques*, 54(1), 31–39. <http://doi.org/10.1109/APMC.2009.5384261>



Nonlinear Dynamic Inverse Controller Based in Field Oriented with SVPWM Current Control

Settar S. Keream^{1,2*}, Ahmed N Abdalla² and Mohd Razali Bin Daud

¹College of Engineering, University of Anbar, Iraq

²University Malaysia Pahang, Malaysia

ABSTRACT

A new Nonlinear Dynamic Inverse (NDI) method is proposed to minimise the ripple torque in an induction motor. This method is based on field oriented with space vector pulse width modulation (SVPWM). The nonlinear dynamic inverse controller cancelled a non-desirable response of the induction motor and enhancing the performance. This cancellation attempts by careful nonlinear algebraic equations. First, a mathematical model of induction motor and decoupling between two inputs have achieved. Then the desired new dynamic is derived from implementing the proposed nonlinear dynamic inverse controller (NDIC) technique that reserves some benefits such as fast torque control, minimum ripple torque, and fast speed response. Also, the proposed method significantly reduced the torque ripple which is the major concerns of the classical hysteresis-based in direct torque control (DTC) and feedback linearization control (FLC) scheme and have an effect on the stator current distortion. Finally, the simulation results with MATLAB/Simulink achieved for a 2-hp induction motor (IM) drive. The results are verification proved that the proposed (NDI-SVPWM) system achieves smaller torque ripple about 0.4% and faster torque response than the conventional SVM-based on proportional integral (PI-DTC) method.

Keywords: Dynamic inverse, induction motor, ripple torque

ARTICLE INFO

Article history:

Received: 24 August 2016

Accepted: 03 Jun 2017

E-mail addresses:

settar_msc@yahoo.com;

pee13003@stude.upm.edu.my (Settar S. Keream),

ahmed@upm.edu.my (Ahmed N Abdalla),

mrzali@upm.edu.my (Mohd Razali Bin Daud)

*Corresponding Author

INTRODUCTION

Decreasing the ripple torque in the induction motor is a concern for many researchers because of its role in induction motor (IM) performance. Switching frequency varies with operating conditions and high torque ripple are two main problems of direct torque control (DTC) drives. As a result, induction motor (IM)'s which are robustness, low price, reliability and free maintenance, are used in industrial applications for a large scale.

A direct torque control (DTC) with a simple flux regulation is presented in (Alsofyani and Idris 2016) for induction motor (IM) to improve torque and speed estimations at zero - and low -speed regions. In this system, in closed-loop speed control, the rotor speed feedback was estimated by extended Kalman filter based on real-time computation. However, a constant switching frequency controller (CSFC) was used due to the modest building of DTC-CSFC, small sampling time, hence significant control bandwidth was possible. Choi et al., (2016) presented a feedback which linearized direct torque control, and this control is with flux ripples for IPMSM drives and reduced torque. In this paper, the others succeed in reduction the torque and flux ripples to approximate (4-5) % with fast response to speed and torque varying conditions during the simulation process for uncertainties for some of the parameters. There is some difference between the simulation and experimental results. (Vafaie, Mirzaeian Dehkordi et al. 2016), proposed a new predictable DTC method via a voltage vector which has an optimal phase. This approach can improve the classical DTC's dynamic reaction as well as decrease torque ripples and flux ripples. By using space-vector modulation, which has five segments, the voltage vector that obtained the fixed frequency of switching was synthesized

This paper proposes a nonlinear dynamic inverse NDI technique to an induction motor. This method is used to minimize the ripple torque based on field-oriented current control with SVM. To apply the proposed NDI-SVPWM scheme, the decoupled dynamic model of an IM is first introduced by defining the two states (i.e., the stator flux and speed). The nonlinear dynamic inverse is applied to the nonlinear IM model to obtain an equivalent linearized model and then utilizing the linear control theory. The desired stator flux and rotor speed are adjusted with proportional integral derivative (PID) controller to get minimum allowed ripple torque with fast response. Consequently, the proposed method can significantly lessen the torque ripple which is the major weaknesses of the classical hysteresis-based DTC scheme. Simulation and investigations are carried out via MATLAB/Simulink of a 2-hp IM drive to confirm the performance of the proposed NDI-SVPWM scheme. Results indicate that the proposed NDI-SVPWM scheme realizes faster and low ripple torque of about 0.4%. Simulated results also confirm that the proposed method reduces the torque ripple effectively while improving the dynamic response of the traditional DTC and FLC methods, robust control under 100% parameter uncertainty. The proposed method helps to cancel undesired the behavior of induction motors caused by huge ripple torque and the instability of working under low speed and variable torque. After cancellation process by NDIC apply the desired input by a set of PID controller to get minimum allowed ripple torque with fast response.

Nonlinear Dynamic Inverse Controller

DI is a controller synthesis technique to cancel and replace deficient or undesirable dynamics with designer-specified desirable dynamics.

A tail-sitter vertical take-off and landing (VTOL) were used a hover flight attitude controller in the micro aerial vehicle (MAV) was presented by (Jin, Bifeng et al. 2015). Considering the aggravation affectability and nonlinear dynamics of the VTOL MAV, applying L1 versatile control hypothesis for augmenting the baseline dynamic inversion controller. The L1 versatile growth follows up on the evaluating, angular dynamics and compensating uncertainty in the

time-varying with fast adjustment rate and appropriate time-delay margin. The design of a self-scheduled current controller for doubly fed induction machines was presented by (Tien, Scherer et al. 2016) . The outline depended on the structure of straight parameter-shifting frameworks where the mechanical angular rate was thought to be a quantifiable time-changing parameter.

Current Control

Consider the field-oriented model of the induction motor (Boukas and Habetler 2004).

$$f(\dot{x}) = f(x) + B(x)u$$

$$f(x) = \begin{bmatrix} k\varphi_{rd}i_{sq} - \frac{f}{J}\Omega - \frac{T_L}{J} \\ -\alpha\varphi_{rd} + \alpha m_{sr}i_{sd} \\ p\Omega + \alpha m_{sr}\frac{i_{sq}}{\varphi_{rd}} \\ \alpha\beta\varphi_{rd} + \alpha m_{sr}\frac{i_{sq}^2}{\varphi_{rd}} + p\Omega i_{sq} - \epsilon i_{sd} \\ p\beta\Omega\varphi_{rd} - \alpha m_{sr}\frac{i_{sd}i_{sq}}{\varphi_{rd}} - p\Omega i_{sd} - \epsilon i_{sq} \end{bmatrix}, \quad B(x) = \begin{bmatrix} 0 & 0 \\ 0 & 0 \\ 0 & 0 \\ \frac{1}{\sigma L_s} & 0 \\ 0 & \frac{1}{\sigma L_s} \end{bmatrix}, \quad u = \begin{bmatrix} V_{sd} \\ V_{sq} \end{bmatrix} \quad (1)$$

$$x = [\Omega, \varphi_{rd}, \theta_{rf}, i_{sd}, i_{sq}], \quad \varphi_{rd} = \sqrt{\varphi_{r\alpha}^2 + \varphi_{r\beta}^2}, \quad \theta_{rf} = \tan^{-1}\left(\frac{\varphi_{r\beta}}{\varphi_{r\alpha}}\right)$$

This model is field-oriented, and its frame (synchronous) is (d,q), where d stands for direct axis and q for the quadrature-axis. These are the axes of the rotor flux, which in this case is aligned with the direct axis, while the quadrature-axis component is zero.

Assume PID (proportional plus integral and derivative) current loops of the following form:

$$V_{sd} = k_{dp}(i_{sd}^* - i_{sd}) + k_{di} \int (i_{sd}^* - i_{sd}) dt + k_{dd} \frac{d}{dt}(i_{sd}^* - i_{sd}) \quad (2)$$

$$V_{sq} = k_{qp}(i_{sq}^* - i_{sq}) + k_{qi} \int (i_{sq}^* - i_{sq}) dt + k_{qd} \frac{d}{dt}(i_{sq}^* - i_{sq}) \quad (3)$$

Where the symbol * denotes command inputs. For fast PID loops, we can assume the following:

$$i_{sd} = i_{sd}^* \quad (4)$$

$$i_{sq} = i_{sq}^*$$

A very realistic assumption, considering the performance of modern microprocessors and power electronics, which can achieve closed-loop control with a period of a few microseconds. Thus, the voltage-fed model (1) is reduced to the current-controlled field-oriented induction motor model, which is

$$\frac{d}{dt} \begin{bmatrix} \omega_r \\ \varphi_{rd} \\ \theta_{rf} \end{bmatrix} = \begin{bmatrix} \mu\varphi_{rd}i_{sq}^* - \frac{f}{J}\omega_r - \frac{T_L}{J} \\ -\alpha\varphi_{rd} + \alpha m_{sr}i_{sd}^* \\ p\omega_r + \alpha m_{sr}\frac{i_{sq}^*}{\varphi_{rd}} \end{bmatrix} \quad (5)$$

Speed Control in Stator-Oriented Model

This section deals with the application of the command matching control strategy to the stator-oriented induction motor model (Boukas and Habetler, 2004). The method is studied in depth for the current-fed field oriented control in the next section, which forms the main theoretic result of the current research. System (5) can be expressed in a more compact form as follows

$$\dot{x} = f(x) + B(x).u(t) \tag{6}$$

With output: $y = C(x)$

Where $x = [\Omega \ \varphi_{rd} \ \theta_{rd}]^T$ is the system state, $u(t)$ is the input vectors, $C(x) = [\Omega \ \varphi_{rd}]^T$, and $f(x)$, $B(x)$ appropriate functions of the following form

$$f(x) = \begin{bmatrix} -\frac{f}{j}\Omega - \frac{T_L}{j} \\ -\alpha\varphi_{rd} \\ p\Omega \end{bmatrix}, \quad B(x) = \begin{bmatrix} 0 & k\varphi_{rd} \\ \alpha m_{sr} & 0 \\ 0 & \frac{\alpha m_{sr}}{\varphi_{rd}} \end{bmatrix} \tag{7}$$

The system (6) is divided into two subsystems: (7) which contain the disturbance (load torque), and (8).

$$\dot{\Omega} = k\varphi_{rd} i_{sq}^* - \frac{f}{j}\Omega - \frac{T_L}{j} \tag{8}$$

While (9) is formed from the last two equations of (4). It is expressed in compact form as

$$\dot{x}_1 = f_1(x) + B_1(x).u(t) \tag{9}$$

$y = C(x)$

Where $x_1 = [\varphi_{rd} \ \theta_{rd}]^T$ is the system state, $u(t)$ is the input vectors, $C(x) = [\Omega \ \varphi_{rd}]^T$, and $f_1(x)$, $B_1(x)$ appropriate functions of the following form

$$f_1(x) = \begin{bmatrix} -\alpha\varphi_{rd} \\ p\Omega \end{bmatrix}, \quad B_1(x) = \begin{bmatrix} \alpha m_{sr} & 0 \\ 0 & \frac{\alpha m_{sr}}{\varphi_{rd}} \end{bmatrix} \tag{10}$$

The influence of the controlled subsystem (9) on (8) will be seen later when we form the closed-loop system from these two subsystems. Subsystem (10) is merely the last two equations of (7). At this point, the objective is to find an appropriate control input function $u(t)$, to achieve input-output decoupling (i.e. $y = u^*$) where u^* is the external command vector (φ_{rd}^* , Ω^* are the input commands for the rotor flux and the rotor mechanical speed, respectively).

$$u(t) = g_1^{-1}(x)[\dot{x}_1 - f_1(x) + u^* - c(x)] \tag{11}$$

Feeding (11) into (9) results in input-output decoupling

$$y(t) = u^* \tag{12}$$

The controller (11) is shown below regarding motor parameters to reveal its implementation simplicity:

$$I_{sd_des}^* = \frac{1}{\alpha m_{sr}} \left[\left(\frac{d\varphi_{rd}}{dt} + \alpha \varphi_{rd} \right) + (\varphi_{rd}^* - \varphi_{rd}) \right] \tag{13}$$

$$I_{sq_des}^* = \frac{\varphi_{rd}}{\alpha m_{sr}} \left[\left(\frac{d\theta_{rf}}{dt} - p\Omega \right) + (\Omega^* - \Omega) \right]$$

Nonlinear Dynamic Inverse for Induction Motor

In this section, a more common approach (Settar S. Keream 2014) is presented for the dynamic inverse of the current fed motor model (1). The last two relations of the field-oriented motor model (1), which represent the dynamics of the stator windings, are:

$$\frac{d}{dt} \begin{bmatrix} i_{sd} \\ i_{sq} \end{bmatrix} = \begin{bmatrix} \alpha\beta\varphi_{rd} + \alpha m_{sr} \frac{i_{sq}^2}{\varphi_{rd}} + p\Omega i_{sq} - \epsilon i_{sd} \\ p\beta\Omega\varphi_{rd} - \alpha m_{sr} \frac{i_{sd} i_{sq}}{\varphi_{rd}} - p\Omega i_{sd} - \epsilon i_{sq} \end{bmatrix} + \frac{1}{\sigma L_s} \begin{bmatrix} v_{sd} \\ v_{sq} \end{bmatrix} \tag{14}$$

We need to find appropriate input $v=[v_{sd}, v_{sq}]^T$ to cancel the nonlinearities of the system (14). The controller is of the form:

$$v = \delta(x) + \zeta(x)u \tag{15}$$

Where x is the full state vector of the motor model (1) and $u=[u_{sd}, u_{sq}]^T$ external input vector. Consider the following choices for the functions of (15)

$$\delta(x) = \sigma L_s \begin{bmatrix} -\alpha\beta\varphi_{rd} - \alpha m_{sr} \frac{i_{sq}^2}{\varphi_{rd}} - p\Omega i_{sq} + \epsilon i_{sd} \\ -p\beta\Omega\varphi_{rd} + \alpha m_{sr} \frac{i_{sd} i_{sq}}{\varphi_{rd}} + p\Omega i_{sd} + \epsilon i_{sq} \end{bmatrix}, \zeta(x) = 1 \tag{16}$$

Applying the controller (15), (16) to system (14) results in:

$$\frac{d}{dt} \begin{bmatrix} i_{sd} \\ i_{sq} \end{bmatrix} = \begin{bmatrix} u_{sd} \\ u_{sq} \end{bmatrix} \tag{17}$$

Flux Estimator

The additional feature of the estimator, in this case, is the extraction of the flux magnitude and flux angle derivatives (φ_{rd} , θ_{rf}). The estimator equations have to be numerically solved during the control process (Leonhard 2001). For a fast control Digital Signal Processor (DSP)

this is a typical task. Numerical methods used for their solution are studied. The estimator relations follow

$$\frac{d}{dt} \begin{bmatrix} \hat{\varphi}_{rd} \\ \hat{\theta}_{rf} \end{bmatrix} = \begin{bmatrix} -\alpha \hat{\varphi}_{rd} + \alpha m_{sr} i_{sd} \\ p\omega_r + \alpha m_{sr} \frac{i_{sq}}{\hat{\varphi}_{rd}} \end{bmatrix} \quad (18)$$

Where the ‘‘hat’’ symbol indicates estimated quantities. The percentage ripple torque calculation is attempt by (Aghili, Buehler et al. 1998)

$$R\% = \frac{T_{max} - T_{min}}{T_{ss}} \times 100 \quad (19)$$

Where R% is the percentage ripple torque, T_{max} is the maximum torque, T_{min} is the minimum torque, T_{ss} is the steady state torque at a specific time.

Simulation Results and Discussion

Figure 1 explained the dynamic inverse controllers as in (15). Figure 2 illustrates the line output voltage of the inverter that provides AC to the induction motor that is controlled to the performance of the induction motor and achieved the desired response such as speed and torque. The fast response of rotor speed of the induction motor is shown in Figure3, at time 0.12 second the speed is stable at 40 Rad/Sec as desired. The torque response is showing in Figure4, the magnitude of input load torque is varied from (0.4-0.8) N.m to test the behaviour of the output torque response. Figure 5 is the zooming of the Figure 4 at a certain time to explain the shape of the ripple torque and calculated the ripple torque percentage (19) (which about 0.4%).

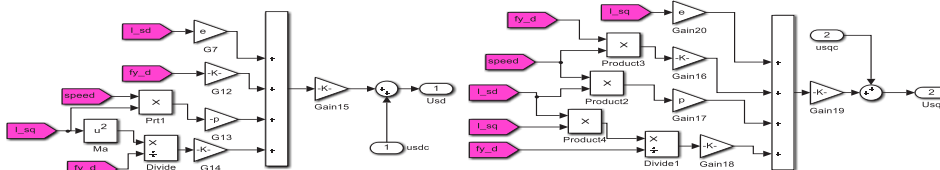


Figure 1. Block diagram of the dynamic inverse

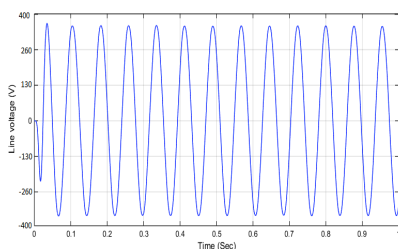


Figure 2. Output line voltage of the inverter

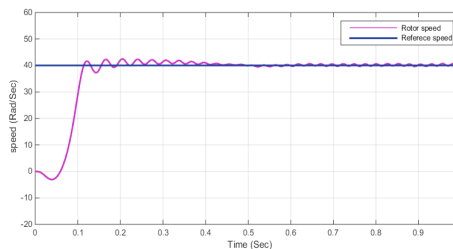


Figure 3. Rotor speed response with reference speed

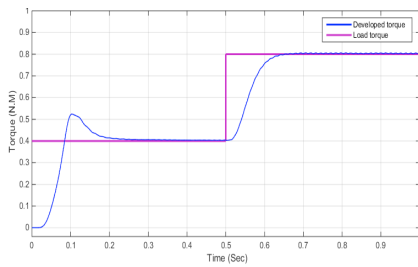


Figure 4. Developed torque response with variable load torque

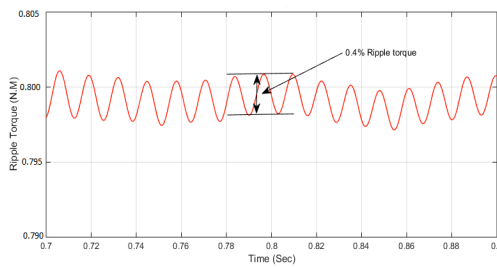


Figure 5. Ripple torque zooming for a given moment

Figure 6 and 7 illustrate the behavior of the rotor speed and torque under 100% uncertainty in stator resistance and rotor resistance and 20% uncertainty in mutual inductance.

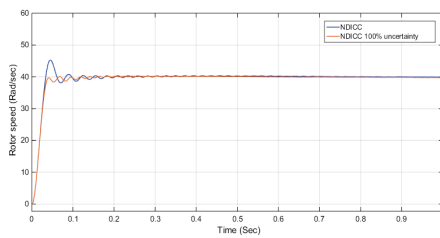


Figure 6. Rotor speed response with and without 100% uncertainty

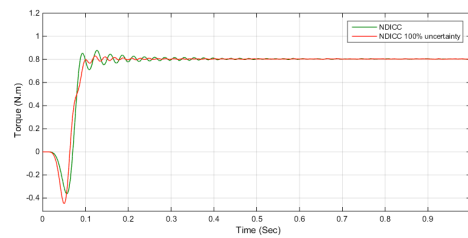


Figure 7. Torque response with and without 100% uncertainty

The three phase induction motor parameters are: Rated voltage 380 V, Power 2hp, Frequency 60Hz, Friction factor 0.0001 (N.m.s), Stator resistance and inductance (3.05Ω, 0.243H), Rotor resistance and inductance (2.12Ω, 0.306H), Mutual inductance 0.225H, Inertia 0.0005 (kg.m²), Pole pairs 2.

CONCLUSION

This paper introduces a nonlinear dynamic inverse controller (NDI) that is applied on induction motor based in SVPWM to minimise the ripple torque. It shows the variation in torque magnitude (0.4-0.8) N.m does not have a harmful effect on the speed response stability through operation time. The results confirm that the proposed method is both robust and does not depend on induction motor parameters.

REFERENCES

- Aghili, F., Buehler, M., & Hollerbach, J. M. (1998, October). Torque ripple minimization in direct-drive systems. In *IROS* (pp. 794-799).
- Alsofyani, I. M., & Idris, N. R. N. (2016). Simple Flux Regulation for Improving State Estimation at Very Low and Zero Speed of a Speed Sensorless Direct Torque Control of an Induction Motor. *IEEE Transactions on Power Electronics*, 31(4), 3027-3035.

- Boukas, T. K., & Habetler, T. G. (2004). High-performance induction motor speed control using exact feedback linearization with state and state derivative feedback. *IEEE Transactions on Power Electronics*, 19(4), 1022-1028.
- Choi, Y. S., Choi, H. H., & Jung, J. W. (2016). Feedback linearization direct torque control with reduced torque and flux ripples for IPMSM drives. *IEEE Transactions on Power Electronics*, 31(5), 3728-3737.
- Jin, W., Bifeng, S., Liguang, W., & Wei, T. (2015). L 1 Adaptive Dynamic Inversion Controller for an X-wing Tail-sitter MAV in Hover Flight. *Procedia Engineering*, 99, 969-974.
- Leonhard, W. (2001). *Control of electrical drives*. Springer Science & Business Media.
- Settar, S., Keream, A. N. A., Ghoni, R., Daud, M. R., & Al Mashhadany, Y. (2014). Robust Dynamic Inverse Controller For Spacecraft Mode. *International Journal of Scientific Research (IJSR)*, 3(5), 113-117.
- Tien, H. N., Scherer, C. W., Scherpen, J., & Muller, V. (2016). Linear Parameter Varying Control of Doubly Fed Induction Machines. *Industrial Electronics, IEEE Transactions on*, 63(1), 216-224.
- Vafaie, M. H., Dehkordi, B. M., Moallem, P., & Kiyoumars, A. (2016). A New Predictive Direct Torque Control Method for Improving Both Steady-State and Transient-State Operations of the PMSM. *IEEE Transactions on Power Electronics*, 31(5), 3738-3753.
- Zhang, B. Y., & Morton, B. (1998). Robustness analysis of dynamic inversion control laws applied to nonlinear aircraft pitch-axis models. *Nonlinear Analysis: Theory, Methods and Applications*, 32(4), 501-532.

Passive Damping Techniques with LCL Filter in Inverter-Grid Connected

Erum Pathan* and Shamsul Aizam Zulkifli*

Faculty of Electrical and Electronic Engineering, Universiti Tun Hussein Onn Malaysia, 86400 Parit Raja, Batu Pahat, Johor, Malaysia

ABSTRACT

In this paper, the challenge of harmonic injection mitigation becomes critical with the massive use of inverters in electrical distribution systems that has been discussed and analyzed. Currently, between the inverter and the grid, L, LC or LCL filters is often used to mitigate the current harmonic. Further, filter connection in both delta-to-star or star-to-delta transformer for state space model of LC filter couplings with impedance is obtained in this paper and it also talked about the different passive damping techniques that been used to suppress the resonance effect on the filter. The effect of series and parallel damping resistor techniques that impact filtering and stability are also been analyzed and discussed. At the end, the simulation results show that LCL filter with parallel damping resistor achieves best performance compared on those for L, LC, or LCL with series damping resistor while at the same time enhancing the smoothness of the signal output while at the same time reducing the percentage of total harmonic distortion between inverter-grid connection.

Keywords: Series Damping Resistor (SDR), Parallel Damping Resistor (PDR), Voltage Source Inverter (VSI)

INTRODUCTION

The voltage source converters (VSCs) have become an essential part of many prime

movers and appliances when connecting to the grid (Liu et al, 2009). Traditionally VSCs are connected with an inductor L, in order to reduce the switching frequency ripple current, although many topologies can be found in the literature incorporating only L-type filter (Akagi, 1996; Bolsens et al., 2006; Teodorescu et al, 2004). However, it is well-known that such an output filter may not be sufficient to meet power quality standards given in IEEE 519 or IEC 61000-3-2 (Twining

ARTICLE INFO

Article history:

Received: 24 August 2016

Accepted: 03 Jun 2017

E-mail addresses:

erumasad79@gmail.com (Erum Pathan),

aizam@uthm.edu.my;

s.aizam@yahoo.com.my (Shamsul Aizam Zulkifli)

*Corresponding Author

et al., 2003), because of the existing high-current ripple due to the Pulse Width Modulation (PWM) of the inverter. To further reduce the effect of thus PWM harmonics, more complex output filter can be used, such as an inductance capacitance (LC) or inductance capacitance inductance (LCL) topologies suggested in (Shen et al., 2008; Shanxu et al., 2010; Wang et al., 2003). Although, LCL filter may reduce costs and improve dynamic response, but a small inductor value is necessary to achieve the required performance in reducing the switching harmonics in comparison with L or LC filter. Particularly, in large power system where the frequency is low, whereby the advantages of LCL filter are more evident.

As known, LCL filter needs smaller inductance value compared to L-type filter for the same performance in harmonic suppression, where it is used in high-power and low-frequency current source controlled in grid-connected converters (Wu et al., 2013 a; Pena-Alzola et al., 2013a). However, LCL filter parameters design is not only related to the switching frequency or ripple attenuation but also related to the performance of the grid-current control loop (Kroutikova et al., 2007). In (Liserre et al., 2005; Julean et al., 2009) a detailed design procedure of an LCL filter was presented. According to the requirements of current ripple tolerance, voltage drop, resonance frequency, reactive power rate, and losses are needed to be considered before the LCL filter parameters can be designed.

In (Renzhong et al., 2013) the L, LC, and LCL filters have been compared and showed that the LCL filter give an excellent harmonic suppression capability, while at the mean time the LCL filter generates a significant resonance peaks that effect the system stability. Therefore, a damping technique must be introduced in order to improve the peak of the system. There are many passive and active methods are been proposed in order to satisfy the system stability requirements. In order to suppress LCL filters resonance, passive methods (Wu et al., 2013) are easier and cheaper to implement. The basic types of passive damping methods are described in (Wu et al., 2013c; Julean, 2009b) where Passive elements like resistor, inductor and capacitor are placed by using different combinations. However, it is really ambitious to trade-off losses and filter performance.

This paper presents a state-space model of LC filter coupling with impedances in star and delta connected capacitors will be discussed in Section 2. Then the effective passive damping methods will be presented in Section 3. At the end, the simulation result will prove that the LCL filter achieves the best performance, indicated the impacts on the stability and filtering property from the parallel resistor or series resistor will discuss in Section 4. Finally, this paper will be concluded in Section 5.

STATE-SPACE MODELS OF LC FILTER AND COUPLING IMPEDANCE IN STAR AND DELTA CONNECTED CAPACITORS

The LC filter and coupling impedance with Y and Δ connected capacitors are illustrated in Figure 1(a, b), where L_i is the inverter-side inductor L_c is the coupling grid-side inductor, C_f is a capacitor with a series R_f damping resistor, R_i and R_c are inductors resistances, V_{in} is an inverter output and V_{eg} as system output or grid side voltage. Other then that, I_{ia} , I_{ib} , I_{ic} , V_{ia} , V_{ib} , V_{ic} are per phase voltage and current of inverter side inductance whereas, I_{ga} , I_{gb} , I_{gc} , V_{ga} , V_{gb} , V_{gc} are per phase system output side voltage and current.

The selection of the inductor and capacitor involve some design consideration due to the dynamic effect that needs to be consider for low-frequency harmonics and the effect of the inductance if a transformer is been used to connect the inverter with the grid as shown in Figure 1 .How to design the output filter circuit is out of the scope of this paper but the reader can find the detailed of this filter in (Julean, 2009c).

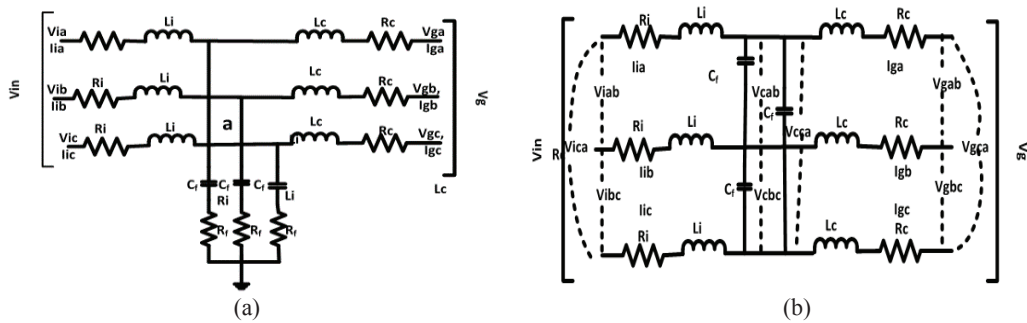


Figure 1(a, b). LC Filter and Coupling Impedance star and delta connected capacitors

The equations describing the phase a, b and c of the filter in star and delta connected is tabulated in Table 1.

Table 1
Star and delta connected parameters equations

Star connected capacitor equations	Delta connected equations
$\frac{dv_{c\phi}}{dt} = \frac{1}{C_{f\phi}} i_{i\phi} - \frac{1}{C_{f\phi}} i_{g\phi}$	$v_{ca} + v_{cb} + v_{cc} = 0, \frac{dv_{c\phi}}{dt} = \frac{1}{3C_f} i_{i\phi ab} - \frac{1}{3C_f} i_{g\phi ab}$
$\frac{di_{i\phi}}{dt} = \frac{1}{L_{i\phi}} v_{i\phi} - \frac{R_{1\phi} + R_{f\phi}}{L_{i\phi}} i_{i\phi} - \frac{v_{c\phi}}{L_{i\phi}} + \frac{R_{f\phi}}{L_{i\phi}} i_{g\phi}$	$\frac{dv_{c\phi a}}{dt} = \frac{1}{3C_{f\phi}} i_{i\phi ab} - \frac{1}{3C_{f\phi}} i_{g\phi ab}$
$\frac{di_{g\phi}}{dt} = \frac{1}{L_{c\phi}} v_{c\phi} + \frac{R_{f\phi}}{L_{c\phi}} i_{i\phi} - \frac{R_{c\phi} + R_{f\phi}}{L_{c\phi}} i_{g\phi} - \frac{V_{g\phi}}{L_{c\phi}}$	$\frac{di_{i\phi ab}}{dt} = \frac{1}{L_{1\phi}} v_{i\phi ab} - \frac{R_{1\phi} + R_{f\phi}}{L_{1\phi}} i_{i\phi ab} - \frac{v_{c\phi}}{L_{1\phi}} + \frac{R_{f\phi}}{L_{1\phi}} i_{g\phi ab}$
<p>here , $\phi = a , b , c$ (three phase system)</p>	$\frac{di_{g\phi ab}}{dt} = \frac{1}{L_{c\phi}} v_{i\phi ab} + \frac{R_{f\phi}}{L_{c\phi}} i_{i\phi ab} - \frac{R_{c\phi} + R_{f\phi}}{L_{c\phi}} i_{g\phi ab} - \frac{V_{g\phi ab}}{L_{c\phi}}$

In delta connected equations, $i_{i\phi ab} = i_{i\phi a} - i_{i\phi b}$, $i_{g\phi ab} = i_{g\phi a} - i_{g\phi b}$ where $\phi =$ phases A, B and C, with the general state space equation is given as follows:

$$\dot{x} = Ax + Bu \tag{1}$$

Whereas the state space representation of the equations for star and delta connected system are given in equation (2) and (3) respectively:

$$\begin{bmatrix} V_{c\phi} \\ i_{i\phi} \\ i_{g\phi} \end{bmatrix}_{9 \times 1} = \begin{bmatrix} I[0]_{3 \times 3} & I\left[\frac{1}{C_{r\phi}}\right]_{3 \times 3} & I\left[-\frac{1}{C_{r\phi}}\right]_{3 \times 3} \\ I\left[-\frac{1}{L_{1\phi}}\right]_{3 \times 3} & I\left[\frac{R_{1\phi}+R_{f\phi}}{L_{1\phi}}\right]_{3 \times 3} & I\left[\frac{R_{f\phi}}{L_{1\phi}}\right]_{3 \times 3} \\ I\left[\frac{1}{L_{c\phi}}\right]_{3 \times 3} & I\left[\frac{R_{f\phi}}{L_{c\phi}}\right]_{3 \times 3} & I\left[-\frac{R_{c\phi}+R_{f\phi}}{L_{c\phi}}\right]_{3 \times 3} \end{bmatrix}_{3 \times 3 \times 9 \times 9} \begin{bmatrix} V_{c\phi} \\ i_{i\phi} \\ i_{g\phi} \end{bmatrix}_{9 \times 1} + \begin{bmatrix} I\left[\frac{1}{L_{1\phi}}\right]_{3 \times 3} & I[0]_{3 \times 3} \\ I[0]_{3 \times 3} & I\left[-\frac{1}{L_{c\phi}}\right]_{3 \times 3} \end{bmatrix}_{6 \times 6} \begin{bmatrix} I[V_{iA}]_{3 \times 3} \\ I[V_{gA}]_{3 \times 3} \end{bmatrix}_{6 \times 1} \quad (2)$$

$$\begin{bmatrix} V_{c\phi} \\ i_{i\phi ab} \\ i_{g\phi ab} \end{bmatrix}_{9 \times 1} = \begin{bmatrix} I[0]_{3 \times 3} & I\left[\frac{1}{3C_{r\phi}}\right]_{3 \times 3} & I\left[-\frac{1}{3C_{r\phi}}\right]_{3 \times 3} \\ I\left[\frac{1}{L_{1\phi}}\right]_{3 \times 3} & I\left[-\frac{R_{1\phi}+R_{f\phi}}{L_{1\phi}}\right]_{3 \times 3} & I\left[\frac{R_{f\phi}}{L_{1\phi}}\right]_{3 \times 3} \\ I\left[\frac{1}{L_{c\phi}}\right]_{3 \times 3} & I\left[\frac{R_{f\phi}}{L_{c\phi}}\right]_{3 \times 3} & I\left[-\frac{R_{c\phi}+R_{f\phi}}{L_{c\phi}}\right]_{3 \times 3} \end{bmatrix}_{3 \times 3 \times 9 \times 9} \begin{bmatrix} V_{c\phi} \\ i_{i\phi ab} \\ i_{g\phi ab} \end{bmatrix}_{9 \times 1} + \begin{bmatrix} I\left[\frac{1}{L_{1\phi}}\right]_{3 \times 3} & I[0]_{3 \times 3} \\ I[0]_{3 \times 3} & I\left[-\frac{1}{L_{c\phi}}\right]_{3 \times 3} \end{bmatrix}_{6 \times 6} \begin{bmatrix} V_{i\phi ab} \\ V_{g\phi ab} \end{bmatrix}_{6 \times 1} \quad (3)$$

PASSIVE DAMPING METHODS

In LCL filter, the resonance effect can produce instabilities at the inverter output especially if some harmonic voltage/current is closed to resonant frequency (Pena-Alzola et al., 2013 b). To attenuate the possible resonances caused by the high-order power filter, whether at LC or at LCL filter, it is where an additional element which is a passive damping or active damping schemes should be adopted (Wu et al., 2013 d). In view of the suppleness and the cost, it mainly deals with LCL filter hardware circuit itself, so that sometimes the passive damping method is more attractive than the active damping. Notice that, bandwidth is always limited so that for certain frequencies active damping may not be able to actuate. Nevertheless, it is a challenge to balance the power losses or to have the satisfactory damping effect and to have the harmonic attenuation when selecting the damping parameters for a high order power filter (Wu et al., 2013 e). Passive damping is achieved by adding a resistance in series or in parallel with the capacitance as presented in next subsections.

R_d-series and parallel Damped LCL filter

The aim of using damping is to reduce the Q-factor at the characteristic resonance frequency. It is often easy to achieve by inserting a resistor in parallel or series with the capacitor as illustrated in Figure 2(a) and (b) respectively.

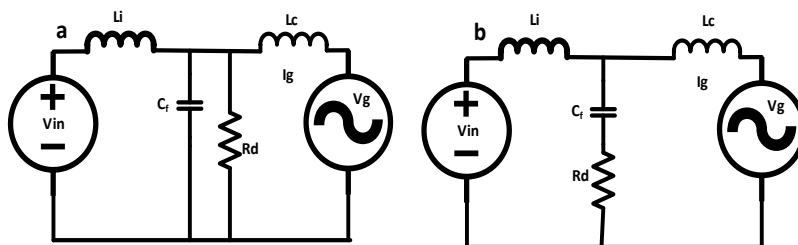


Figure 2. (a) damping R_d in parallel with C_f ; (b) damping R_d in series with C_f

The R_d -damped LCL filter is been inserted to avoid the resonance phenomenon. The equation for resonant frequency is given in equation (4)

$$f_r = \frac{1}{2\pi} \sqrt{\frac{L_i + L_c}{L_i L_c C_f}} \quad (4)$$

where f_r is resonant frequency, L_i is the inverter-side inductor, L_c is the coupling grid-side inductor, R_d is a damping resistor. It can be seen that, the R_d parameters is not consider in the Equation 4, where it does not affect the resonance of f_r (Wu et al., 2013 f).

The LCL filter transfer functions at line side current and inverter input voltage in a grid-connected mode of operation with series and parallel damping resistance are given in Equations 5 and 6 respectively. From the transfer functions, by analyzing those equations, larger series resistance values can give better damping or lower Q-factor, as can be seen from the transfer functions after damping are;

$$\frac{i_g}{V_{in}} = \frac{R_d C_f S + 1}{S^3 L_i L_c C_f + R_d C_f (L_i + L_c) S^2 + (L_i + L_c) S} \quad (5)$$

$$\frac{i_g}{V_{in}} = \frac{R_d}{S^3 L_i L_c C_f R_d + L_i L_c S^2 + (L_i + L_c) R_d S} \quad (6)$$

where the Q factor is proportional to R_d . If the selection of R_d is too big, the attenuation will be reduced which caused a harmonics problem to the LCL filter. However a higher R_d value can increase the losses at low frequency. In this case, as a hypothesis, this method cannot be used for higher power rating in the level of hundreds of kW or MW. For good filtering purposes, both parallel and series damping are suitable to be applied, but the question is to find out which one is better. The parallel and series resistor are described in Equation (7).

$$X_{series} = R_d + \frac{1}{C_f S} \quad , \quad X_{parallel} = \frac{R_d}{C_f R_d S + 1} \quad (7)$$

Due to the fact that the value of the series resistor is larger than the parallel resistor, the current that flows in series contain high-frequency harmonic current flow through capacitance compared in the parallel one. Therefore, the filter has a better effect of suppressing the high-frequency components. The spectrum characteristics are shown in Figure 3 (a, b) and the above approach was further proved and verified in simulation environment using MATLAB software.

SIMULATION RESULTS

Matlab/Simulink power system toolbox software was used to simulate the proposed approach. The designed LCL filter of the grid-connected inverter was simulated. and the calculated parameters is shown in Table 2.

In this paper, the simulation for LCL filter with series and parallel damping resistance are compared with the effect of both damping techniques. The presented simulation results are obtained for the harmonic current, voltage waveform for with and without damping techniques, as illustrated in following figures.

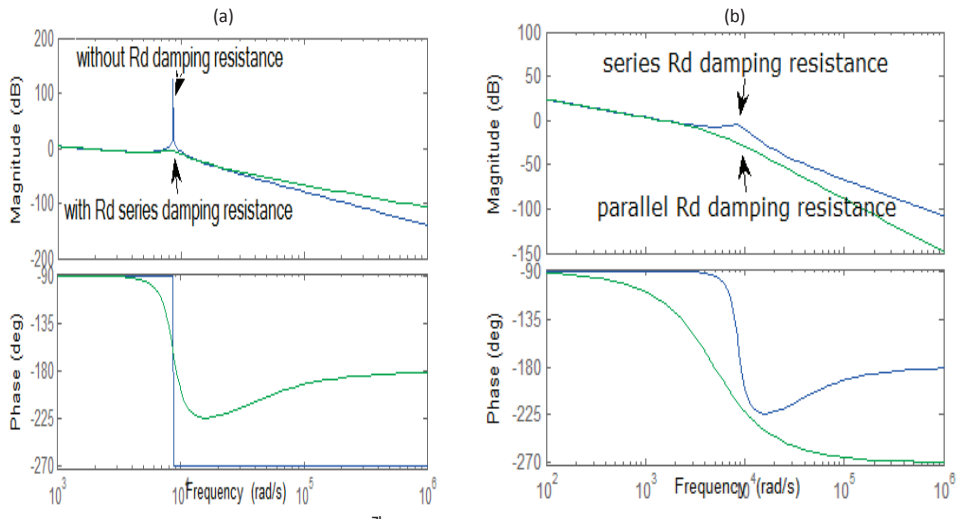


Figure 3. (a): Frequency response of $\frac{i_g}{V_{in}}$ with and without series R_d ; (b) series and parallel damping

Table 2
System parameters

Parameters	Value
V (Voltage)	240/415 V
f (Frequency)	50 Hz
P (Rated power)	1 kW
F_s (Switching frequency)	3 kHz
L_1	530 uH
L_2	143 uH
C_f	118 uF
R_d	0.3 ohm

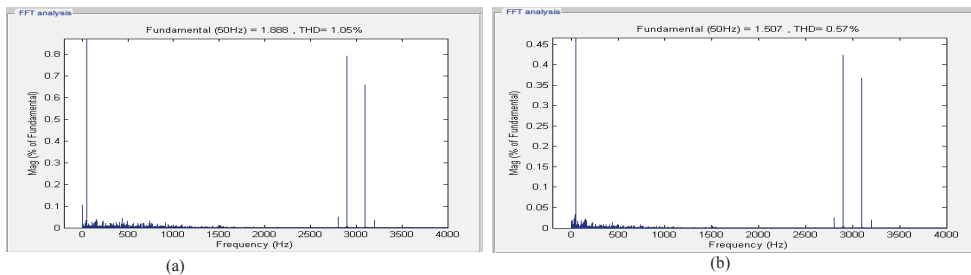


Figure 4. (a ,b): Harmonic waveform of LCL filter by (a) series damping (b) parallel damping resistance

Figure 4 (a) shows the THD is about 1.05% when series damping resistance is connected with LCL filter whereas in Figure 4. (b) is illustrated that THD of 0.57% is observed when damping resistance is connected in parallel with LCL filter. It is proved that, the parallel

resistance is the most effected arrangement at the inverter-grid connection where the R_d will help to increase the time constant of the filter.

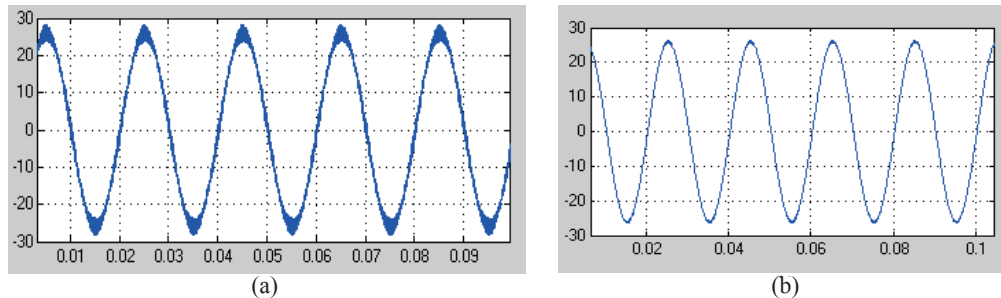


Figure 5. Current waveform (a) LCL filtering (b) with R_d +LCL filtering

The current output waveform without damping resistance gives high THD due to non quality signal that is effected on the inductor-capacitor respond which is illustrated in Figure 5(a). However, current waveform after filtering by LCL filter with the combination of the R_d has improve the quality of the signal as shown in Figure 5(b). This quality signal is necessary for the DSP process whereby it can affect the bit signal generated on the analog digital converter sensor in order to have a efficient power transfer between the inverter to the grid that will be discussed in next paper.

CONCLUSION

As a conclusion, this paper has investigated series and parallel resistive passive damping techniques in LCL filter for inverter-grid connection for star-delta and delta-star connection. The different damping methods are evaluated by showing the improve THD percentage with small bandgap of the bode plots between with or without damping resistor. As shows, the parallel resistance gives significant improvement to the quality of the signal. All features indicated that a better design can be obtained by using parallel connected damping techniques in LCL filter rather than series connection, especially for small and medium voltage source inverters connected to the grid.

ACKNOWLEDGEMENT

Authors gratefully acknowledge the support of Universiti Tun Hussein Onn Malaysia (UTHM) RAGS (R037) and Power and Renewable Energy Team (PaREnT), FKEE, UTHM to undertake this research activity.

REFERENCES

Akagi, H. (1996). New trends in active filters for power conditioning. *IEEE transactions on Industry applications*, 32(6), 1312-1322.

- Bolsens, B., De Brabandere, K., Van den Keybus, J., Driesen, J., & Belmans, R. (2004, June). Model-based Generation of low distortion currents in grid-coupled PWM-inverters using an LCL output filter. In *IEEE 35th Annual Power Electronics Specialists Conference, 2004. PESC 04. 2004* (Vol. 6, pp. 4616-4622). IEEE.
- Dahono, P. A. (2002). A control method to damp oscillation in the input LC filter. In *Power Electronics Specialists Conference, 2002. Pesc 02. 2002 IEEE 33rd Annual* (Vol. 4, pp. 1630-1635). IEEE.
- Julean, A. (2009). *Active damping of LCL filter resonance in grid connected Applications*. Aalborg Universitet Dinamarca, Dissertação de mestrado.
- Kroutikova, N., & Green, T. C. (2007). State-space model of grid-connected inverters under Current control Mode. *IET Electric Power Applications, 1*(3), 329-338.
- Liserre, M., Blaabjerg, F., & Hansen, S. (2005). Design and control of an LCL-filter-based Three-phase active Rectifier. *IEEE Transactions on Industry Applications, 41*(5), 1281-1291.
- Liu, F., Zha, X., Zhou, Y., & Duan, S. (2009, May). Design and research on parameter of LCL Filter in three-phase Grid-connected inverter. In *Power Electronics and Motion Control Conference, 2009. IPEMC'09. IEEE 6th International* (pp. 2174-2177). IEEE.
- Pena-Alzola, R., Liserre, M., Blaabjerg, F., Sebastián, R., Dannehl, J., & Fuchs, F. W. (2013). Analysis of the Passive damping losses in LCL-filter-based grid converters. *IEEE Transactions on Power Electronics, 28*(6), 2642-2646.
- Renzhong, X., Lie, X., Junjun, Z., & Jie, D. (2013). Design and research on the LCL filter in three-phase PV grid- Connected inverters. *International Journal of Computer and Electrical Engineering, 5*(3), 322.
- Rockhill, A. A., Liserre, M., Teodorescu, R., & Rodriguez, P. (2011). Grid-filter design for a Multimegawatt Medium- voltage voltage-source inverter. *IEEE Transactions on Industrial Electronics, 58*(4), 1205-1217.
- Shanxu, L. F. Z. X. D. (2010). Design and Research on Parameter of LCL Filter in Three-Phase Grid-Connected Inverter [J]. *Transactions of China Electro technical Society, 3*, 020.
- Shen, G., Xu, D., Cao, L., & Zhu, X. (2008). An improved control strategy for grid-connected Voltage source Inverters with an LCL filter. *IEEE Transactions on Power Electronics, 23*(4), 1899-1906.
- Teodorescu, R., Blaabjerg, F., Borup, U., & Liserre, M. (2004). A new control structure for grid -Connected LCL PV Inverters with zero steady-state error and selective harmonic compensation. In *Applied Power Electronics Conference and Exposition, 2004. APEC'04* (Vol. 1, pp. 580-586).
- Twining, E., & Holmes, D. G. (2003). Grid current regulation of a three-phase voltage source Inverter with an LCL Input filter. *IEEE Transactions on Power Electronics, 18*(3), 888-895.
- Wang, T. C., Ye, Z., Sinha, G., & Yuan, X. (2003, June). Output filter design for a grid - Interconnected three-phase inverter. *IEEE 34th Annual In Power Electronics Specialist Conference* (Vol. 2, pp.779-784). IEEE.
- Wu, W., He, Y., Tang, T., & Blaabjerg, F. (2013). A new design method for the passive damped LCL and LLCL filter-based single-phase grid-tied inverter. *IEEE Transactions on Industrial Electronics, 60*(10), 4339-4350.



Distinct Position of Chaotic Pulse Trains Observed in Malaysia

Muhammad Noh Hamzah^{1*} and Chandima Gomes

¹Centre for Electromagnetic and Lightning Protection Research (CELP), Faculty of Engineering, Universiti Putra Malaysia, 43400, UPM Serdang, Selangor, Malaysia

ABSTRACT

This paper presents the chaotic pulse train (CPT) waveforms of the vertical electric field generated by lightning observed in Malaysia. Focusing on the position where these electric field changes occur in a number of cloud to ground (CG) flashes, these CPTs were detected in different ways of occurrences, durations, intensities and amplitudes. Seventy-six chaotic pulse trains were found in this study from a sum of 172 CG flash records from three thunderstorm days. The fast field antenna was employed to do the field measurements. As opposed to the typical occurrence of chaotic pulse trains prior to subsequent strokes as reported in the literature, this study has found chaotic pulse trains occurring in different places along the CG electric field waveforms.

Keywords: Preliminary breakdown pulses, return stroke, chaotic pulse trains, electric field change, Position

INTRODUCTION

Before the emergence of a return stroke (RS) in a CG lightning strike, lightning activity must occur in order for the RS to take place. These lightning activities may be from the stepped leaders, dart leaders or dart stepped

leaders depending on the order of the RS that is being initiated (Schonland & Collens, 1934, Schonland et al., 1935, Qie et al., 2002). However, latter findings show an unusual occurrence of a lightning physical process which is disordered and rare in trait can also take place before subsequent strokes in place of dart leaders. They are referred to as CPTs or chaotic leaders to describe this type of lightning activity (Rakov & Uman, 1990, Gomes et al., 2004, Mäkelä et al., 2007, Hill et al., 2012, Zhang et al., 2014a). Figure 1 shows an example of a CPT that occurs prior to a RS, its fine structure resembling pulses that are erratic and irregular unlike other types of pulses.

ARTICLE INFO

Article history:

Received: 24 August 2016

Accepted: 03 Jun 2017

E-mail addresses:

muhammadnoh@gmail.com;

muhammad587@yahoo.com (Muhammad Noh Hamzah)

chandima@upm.edu.my;

chandima.gomes@hotmail.com (Chandima Gomes)

*Corresponding Author

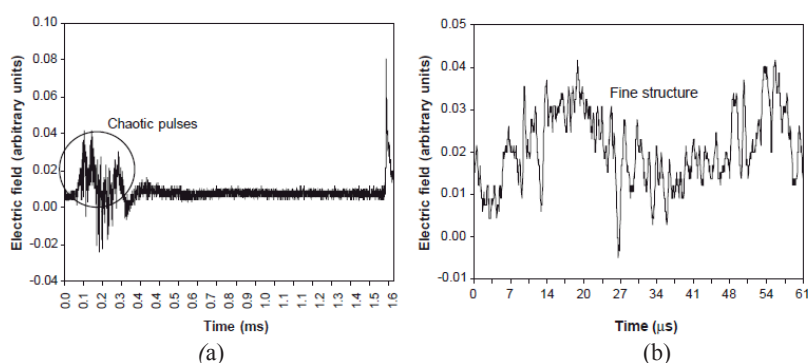


Figure 1. a) CPT that Occurs About 1 ms before a RS; b) The fine structure of the CPT in a) (Gomes et al. 2004)

CPTs are a kind of lightning activity that occur predominantly before the advent of a subsequent stroke. In nature, they are similar to the preliminary breakdown pulses (PBP) and pulse bursts, being more erratic and irregular without any kind of order (Gomes et al., 2004). CPTs commonly occur prior to a subsequent negative return stroke or between RSs. There is little evidence of them in the literature commencing before a first return stroke by reason of the preliminary breakdown and stepped leader pulses being present. While reports of CPTs appearing prior to the first return stroke and after the final return stroke can be found in the literature (Zhang et al., 2014b), they are nevertheless rare. For the case of CPTs appearing prior to a first return stroke, they do not occur whenever there are PBP trains (Zhang et al., 2014b). These occurrences can be seen in Figure 2 where CPTs are denoted by their respective locations. CPTs were also found to be occurring solely, with no association to return strokes that happens in cloud flashes that are free from RSs (Gomes et al., 2004). CPTs that have been found in the literature more specifically relate to those with cloud flashes or negative RSs. Hence, they are most probably a cloud event since CPTs can appear almost anywhere with other kinds of lightning activity. There are no reports of CPTs or chaotic leaders occurring with positive RSs. It is necessary to conduct measurements of the lightning vertical electric fields in order to have an adequate understanding of the chaotic pulse trains.

METHODOLOGY

The vertical electric field measurements were done for May, June and October 2013 at Universiti Putra Malaysia (UPM). The measurement site has a geographical coordinate of 2°59'19.9"N latitude and 101°43'29.8"E longitude and situated in Serdang, Selangor area, which is located in Central-West Peninsular Malaysia and close to the straits of Malacca. The measuring site is a large open space approximately 86 m above sea level. Malaysia generally has a tropical climate with maximum monsoon rain occurring from October to November due to southwest monsoon and intermonsoon periods which affects the Selangor area.

The measuring system that was used to measure the electric fields in this study is similar to Ibrahim et al. (2011). The physical height of the parallel plate antenna that was used for the measurement is 1.85 m from the ground. The LH0033 Electronic Buffer Amplifier with the

Distinct Position of Chaotic Pulse Trains in Malaysia

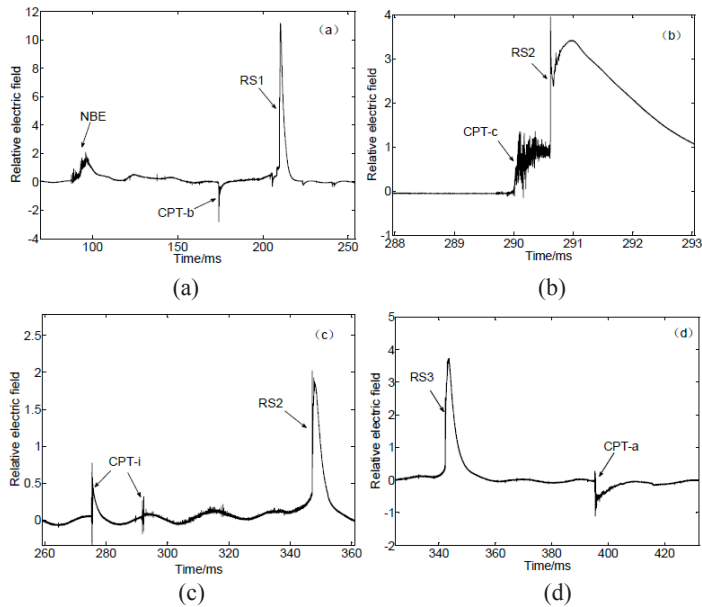


Figure 2. a) A CPT prior to a 1st RS denoted by CPT-b; b) A CPT prior to a SS denoted by CPT-c; c) CPTs prior to a SS with some duration denoted by CPT-i; d) A CPT that occurs after the final RS denoted by CPT-a (Zhang et al., 2014b)

circuitry was used to isolate the high input impedance of the antenna and offer enough power to drive the signal from antenna to the oscilloscope through the coaxial cable. A RG58 coaxial cable was used to connect the parallel plate to the buffer electronic and then to the Tektronix MS04032 oscilloscope where the lengths of the cables are 1 m and 25 m respectively. 50 MS/s (Mega samples per second) sampling rate was set or time resolution of 20 ns with the total length of recorded waveforms being 20 ms per division with a total of 200 ms window frame. The trigger level was set at 200 mV and post-trigger time of 60 ms. A 17 ms decay time constant was set to the buffer. A figure representing the basic needs of the electric field measurement is shown in Figure 3 where r is the distance of a lightning flash to the measurement site.

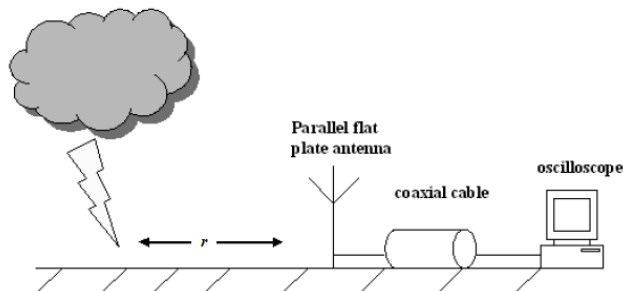


Figure 3. A representation of the measurement setup (Ahmad, 2011)

RESULTS AND DISCUSSIONS

The position of chaotic pulse trains found in this study can be categorized into three parts. The first are ones that occur in isolation or are not seemingly attached to a return stroke or any other kind of lightning activity. These chaotic pulse trains occur at more than an average of 20 ms before or after a lightning activity such as preliminary breakdown pulses and return strokes where 10 of them were found to be occurring in this study. Figure 4 shows a CPT of this nature that occurred after some time after the first return stroke. It is likely that these kinds of chaotic pulse trains are associated to cloud flashes as found in Gomes et al. (2004) as cloud flashes were also found to be occurring with CG flashes in this work. The second type of CPT occurs prior to return strokes which is the usual case as reported in Gomes et al. (2004), Mäkelä et al. (2007) and Lan et al. (2011). The criterion is taken that a CPT must occur within the range of 0 to 10 ms on average for it to be classified of this type. Figure 5 shows this kind of CPT found in this study occurring just before a RS. 42 of them were found in this study that is the highest amount found in comparison to other kinds of CPTs. A more distinct and unusual type of chaotic pulse train occurrence are ones that occur right after or are embedded with return strokes after the peak of the particular stroke which is the third type. These kinds of occurrences have never yet been reported in the literature to the best of this author's knowledge and can be considered new where 24 occurrences were found. Figure 6 summarizes all of the findings. It can be seen that chaotic pulse trains that precede return strokes has the highest amount followed by ones that occur right after or embedded with return strokes and in isolation.

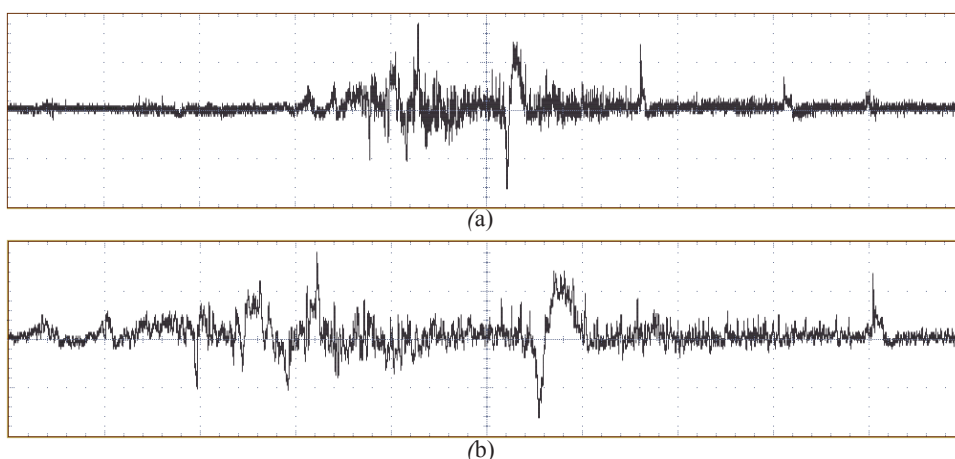


Figure 4. Isolated CPT of Flash ID TEK0056 with a Timeframe of 100 μ s per Division; b) Isolated CPT with a Timeframe of 40 μ s per Division

A number of CPTs were found to occur in sequences for the isolated and right after or embedded types. This implies that CPTs can occur several times in a flash as reported by Ahmad et al. (2014) where a series of two to three CPTs were detected. Every CPT found occurred after PBPs except twelve of them. This is highly unusual considering their position of occurrence. However, CPTs do occur before the advent of the first return stroke as found in Zhang et al. (2014b) but was identified as a very unusual event. It was also a unique event

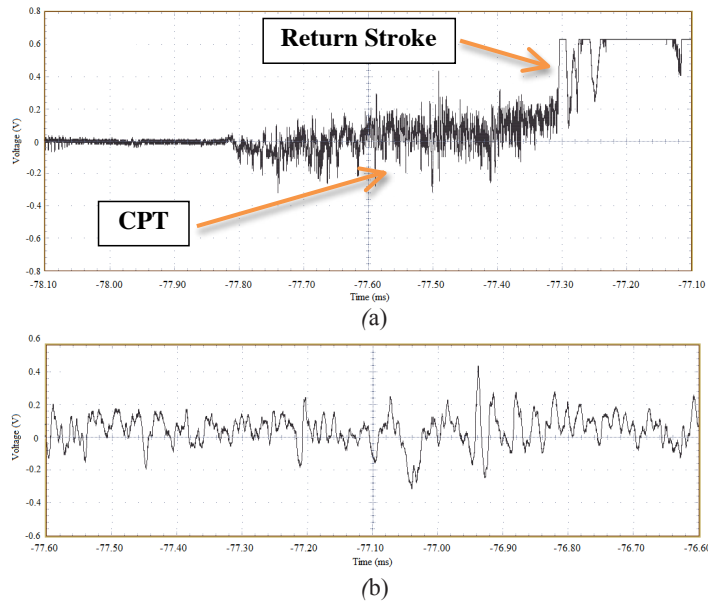


Figure 5. a) CPT of Flash ID TEK0052 with a Timeframe of 20 ms per Division; b) Part of its fine structure with a Timeframe of 10 μ s per Division

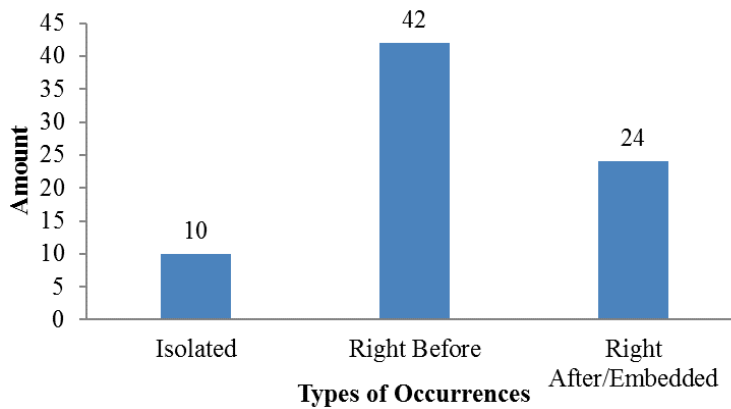


Figure 6. Types of Chaotic Pulse Train Occurrences and their Respective Numbers

because it was a flash without a PBP. This evidently shows that CPTs are more inclined to occur after PBPs and first return strokes which is usually the case despite the unusual occurrences of CPTs found in this study. This is in accordance with the studies found in Gomes et al. (2004), Mäkelä et al. (2007) and Lan et al. (2011). CPTs found in these studies show that those which occur after PBP and first return strokes are the most dominant. An example of two embedded chaotic pulse trains occurring after a return stroke can be seen in Figure 7(a) where Figures 7(b) and Figures 7(c) show their respective fine structures. This example is one of many found in the study. CPTs of this nature were found to be lower in number and duration in comparison to CPTs that occur prior to RSs. A total of three CPTs occurred with this particular RS with two of the embedded displayed in the figure.

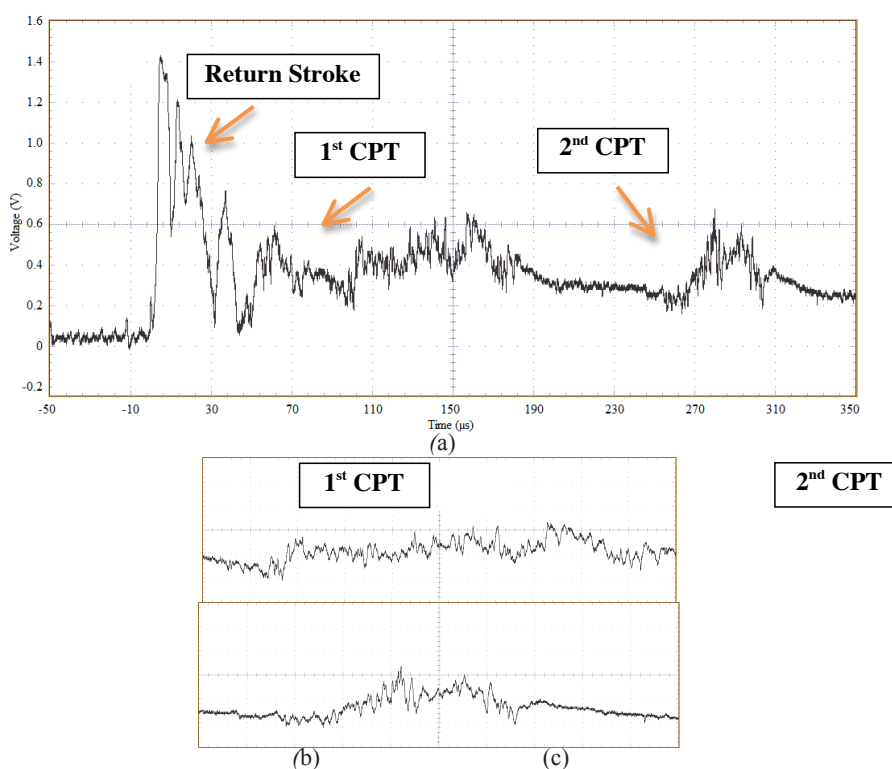


Figure 7. (a) Return Stroke of Flash ID TEK0072 with a Timeframe of 40 μ s per Division; b) Embedded CPT-1 a Timeframe of 10 μ s per Division; c) Embedded CPT-2 Timeframe of 10 μ s per Division

CONCLUSION

It is found that CPTs occur with PBPs and RSs almost anywhere in a CG lightning electric field waveform in the Central-West part of Malaysia. The dominant feature of CPTs is that they precede RSs as demonstrated by the findings of the CPT in this study and in the literature. However, the number of CPTs that are embedded or might occur right after RSs shows an apparent number more than those of isolated in nature. This new type of CPT incidents has not been reported and can therefore be considered as a new finding in terms of the position of an occurrence of a CPT.

Since results from only an electric field measurement cannot explain the physical mechanism and nature of CPTs, discussion is limited as maybe discerned from (Lan et al . 2011) the conclusion suggesting CPTs remains a debatable lightning process. Since CPTs are different from other kinds of lightning activity they may be coming from an unknown physical lightning mechanism. Hence, this study aims to fulfil that purpose. This kind of analysis was also done to view CPTs in light of a perspective that has never been accomplished before. By that, this also paves way for more kinds analyses to be explored in the future for more comprehension of the lightning activities. Ultimately, this paper has shown that the CPTs can occur embedding itself with RSs or occur right after RS. This is a distinct feature of the CPT in terms of its position that has never been reported before

REFERENCES

- Ahmad, M., Esa, M., Johari, D., Ismail, M., Cooray, V., Ahmad, M., & Ismail, M. (2014). Chaotic pulse train in cloud-to-ground and cloud flashes of tropical thunderstorms. In *2014 International Conference On Lightning Protection (ICLP)*. (pp. 808-809). Shanghai, China.
- Ahmad, N. A. (2011). *Broadband and HF radiation from cloud flashes and narrow bipolar pulses*. (Doctoral dissertation). Uppsala: Acta Universitatis Upsaliensis.
- Gomes, C., Cooray, V., Fernando, M., Montano, R., & Sonnadara, U. (2004). Characteristics of chaotic pulse trains generated by lightning flashes. *Journal Of Atmospheric And Solar-Terrestrial Physics*, *66*(18), 1733-1743.
- Hill, J. D., Uman, M. A., Jordan, D. M., Dwyer, J. R., & Rassoul, H. (2012). "Chaotic" dart leaders in triggered lightning: Electric fields, X-rays, and source locations. *Journal of Geophysical Research: Atmospheres*, *117*(D3).
- Ibrahim, W. I., Ghazali, M. R., Ghani, S. A., & Malek, Z. A. (2011). Measurement of vertical Electric fields from lightning flashes using parallel plate antenna. In *International Conference On Electrical, Control And Computer Engineering 2011 (INECCE)*. (pp. 466-471). Pahang, Malaysia.
- Lan, Y., Zhang, Y. J., Dong, W. S., Lu, W. T., Liu, H. Y., & Zheng, D. (2011). Broadband analysis of chaotic pulse trains generated by negative cloud-to-ground lightning discharge. *Journal of Geophysical Research: Atmospheres*, *116*(D17).
- Mäkelä, J. S., Edirisinghe, M., Fernando, M., Montaña, R., & Cooray, V. (2007). HF radiation emitted by chaotic leader processes. *Journal of Atmospheric and Solar-Terrestrial Physics*, *69*(6), 707-720.
- Qie, X., Yu, Y., Guo, C., Laroche, P., Zhang, G., & Zhang, Q. (2002). Some features of stepped and dart-stepped leaders near the ground in natural negative cloud-to-ground lightning discharges. *Annales Geophysicae*, *20*, 863-870.
- Rakov, V. A., & Uman, M. A. (1990). Some properties of negative cloud-to-ground lightning flashes versus stroke order. *Journal of Geophysical Research: Atmospheres*, *95*(D5), 5447-5453.
- Schonland, B. F. J., & Collens, H. (1934). Progressive Lightning. In *Proceedings of the Royal Society A: Mathematical, Physical and Engineering Sciences*, *143*(850), 654-674.
- Schonland, B. F. J., Malan, D. J., & Collens, H. (1935). Progressive Lightning II. In *Proceedings of The Royal Society A: Mathematical, Physical And Engineering Sciences*, *152*(877), 595-625.
- Zhang, Y., Li, C., Zhang, Y., Lu, W., & Zheng, D. (2014a). Research on chaotic leader in cloud-to-ground lightning. In *XV International Conference on Atmospheric Electricity*. Norman, Oklahoma, U.S.A.
- Zhang, Y., Zhang, Y., Zhou, W., Lu, W., Zheng, D., & Liu, H. (2014b). Study on occurrence regularity of CPT Discharge Event in Negative Ground Lightning. In *XV International Conference on Atmospheric Electricity*. Norman, Oklahoma, U.S.A.



Field Evaluation of Magnetic Actuator Driven Switchgear in Malaysia

Mohd Dzaki, Mohd Amir* and Sanuri, Ishak

Distribution Unit, TNB Research Sdn Bhd, Kajang, Malaysia

ABSTRACT

Magnetic actuator driven switchgear is a new medium voltage switchgear technology. In this switchgear, the conventional spring mechanism which is used to operate the circuit breaker is replaced with a magnetic actuator mechanism. The suitability of this technology in the Malaysian utility network specifically in highly loaded areas with frequent switching was assessed via a field evaluation. Preliminary results indicated that magnetic actuator driven switchgear perform commendably on the safety aspect, on-site performance monitoring and online diagnostic test results. However, there are several concerns that need to be addressed such as the ease of installation, substation system requirements, high life cycle cost and reliability of components, before this technology can be used widely.

Keywords: Magnetic actuator, medium voltage switchgear, condition monitoring, life cycle

INTRODUCTION

All the medium voltage switchgears in Malaysia achieve tripping and closing operations of the circuit breaker with the conventional mechanical spring and latch mechanism. However, several models of

switchgear which use the spring mechanism suffer from the so-called sluggishness issue, in which the circuit breaker failed to trip within the allocated time. This is caused by the hardening of lubrication (i.e. grease) as the circuit breaker can remain idle for long periods. The impact of which can cause a large number of consumers being affected when there is a breakdown (Muttalib & Amir, 2010).

One way to resolve this issue is to replace the conventional spring mechanism with switchgears that use magnetic actuator as the primary operating mechanism. Magnetic actuators use changes in the direction and force of magnetic fields to move or control

ARTICLE INFO

Article history:

Received: 24 August 2016

Accepted: 03 Jun 2017

E-mail addresses:

dzaki.amir@tnbr.edu.my (Mohd Dzaki, Mohd Amir),

sanuri.ishak@tnbr.com.my (Sanuri, Ishaki)

*Corresponding Author

a mechanical system (Jiles, 1998). Figure 1 shows a typical implementation of the magnetic actuator mechanism in medium voltage switchgears. In switchgears, electromagnets and permanent magnets are used together to provide the operating energy for the movement of the circuit breaker contacts as well as the essential bi-stable characteristic for both close and open conditions. A single moving part can replace the hundreds moving parts contained in a conventional switchgear spring mechanism (Lane, 1998). Therefore, the magnetic actuator mechanism has the advantages of increasing reliability by reducing mechanical parts count, smaller size and no longer need to maintain the mechanical parts compared to the conventional spring mechanism.

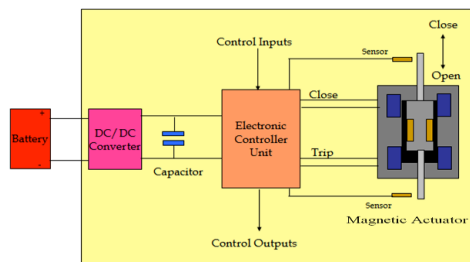


Figure 1. The magnetic actuator components which is used to operate the circuit breaker. This mechanism replaces the conventional spring mechanism

M Amir et al. (2013) performed a study to assess crucial areas for the reliable operation of the switchgears not covered in switchgear type tests. The study evaluated the major components of the magnetic actuator mechanism which are the magnetic actuator itself, electronic controller unit and capacitor, the performance of the switchgear panel as a whole as well as comparative analysis with the conventional spring mechanism via laboratory tests and finite element simulation.

M Amir et al. (2013) concluded that based on the laboratory test and simulation results, the magnetic actuator mechanism can be a viable alternative to spring mechanism. However, a field trial in an actual substation is required to study the performance in actual utility application.

The objective of this study is to determine the suitability and practicality of using magnetic actuator driven switchgear.

METHODOLOGY

In this field evaluation, five panels of magnetic actuator driven switchgear were installed in an actual substation. The configuration of the panels is as follows:

- 2 incomer panels
- 2 outgoing panels
- 1 bus-section panel

Figure 2 shows the single line diagram of the installed switchgears while Figure 3 is a photo of the actual installation on-site. The following activities were performed during the field evaluation:

- Site selection
- On-site performance monitoring
- Technical and financial assessment

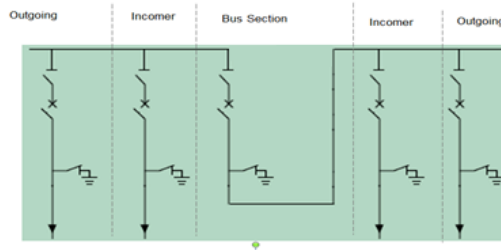


Figure 2. Single line diagram of the installed switchgears consisting of two incomer panels, two outgoing panels and one bus-section panel



Figure 3. Installation of the magnetic actuator driven switchgear in the trial site

Site selection

Correct site selection is necessary in order to arrive at an accurate representation of the long-term switchgear performance during field evaluation. The following criteria were used in determining the most suitable site for this field evaluation:

- Frequent switching operation: to assess the capability and reliability of the magnetic actuator during switching operations.
- High current loading: to test the switchgear up to its full current rating.
- Highly polluted: to determine the effect of environment to the switchgear.
- Network: the substation must have proper back up plan any failure happens during this field evaluation

- **Connectivity:** The substation must be connected to the regional control centre in order to allow online switchgear control and performance monitoring

A substation in an urban industrial area in the State of Selangor was selected as the location for this field evaluation as it met all the criteria listed above.

On-site performance monitoring

This activity was performed to assess the performance of the magnetic actuator driven switchgear during the six-month field evaluation period. The monitoring consists of two major parts which are:

1. **Online diagnostic tests.** There are three online diagnostic tests which are performed during the field evaluation period. These are thermography inspection and ultrasonic scanning. Thermography inspection was performed to determine the existence the hot spots especially in the contact parts of the switchgear. Ultrasonic scanning was performed to determine the insulation condition specifically the existence of partial discharge. All these tests were performed monthly during the field evaluation.
In addition, a partial discharge monitor was installed during the first and sixth month of the field evaluation. This equipment monitors the switchgear to determine the presence of partial discharge. The partial discharge detection method is by measuring the transient earth voltage (TEV). Trending analysis was then performed on the data obtained from the diagnostic tests to determine any signs of deterioration of the condition of the switchgear.
2. **Switchgear performance assessment.** Apart from the diagnostic tests, the performance of the switchgear when switching operation was performed was also collected. The sources of the data were data from the regional control centre as well as feedback from the operators.

Technical and financial assessment

This was performed to determine the suitability of using the magnetic actuator driven switchgear via two major aspects:

1. **Technical assessment.** The areas studied in technical evaluation include compliance to existing technical specifications and standard practice, ease of installation, ease of operation and maintenance, component reliability and safety aspect.
2. **Financial assessment.** For this purpose, the total life cycle cost of the magnetic actuator driven switchgear was calculated and compared to the life cycle cost of the existing air insulated switchgear with conventional spring mechanism. The life cycle cost consists of the purchase cost, installation cost, operation cost, condition monitoring cost, periodic maintenance cost, breakdown maintenance cost, spare parts cost and disposal cost (Loo, Y. H., et al. 2010).

RESULTS AND DISCUSSIONS

Online diagnostic tests

Table 1 below shows the limits used to interpret the results of the online diagnostic tests. The limits are based on the standard condition based maintenance interpretation guidelines used by TNB Distribution Division (TNB, 2013).

Table 1
Interpretation of the online diagnostic tests

Diagnostic test	Measurement	Results	Condition
Thermography	Temperature difference with ambient temperature	1 – 4°C	Normal
	Ultrasonic reading	5 – 9°C	Intermediate
	TEV magnitude	10 -14°C	Serious
		> 15°C	Critical
Ultrasound		0dB	Normal
		> 1dB	Serious / Critical
TEV		< 15dB	Normal
		16 – 25dB	Intermediate
		26 – 35dB	Serious
		> 35dB	Critical

The online diagnostic test results obtained during the field evaluation are in Table 2 below:

Table 2
Online diagnostic test results during the field evaluation

Diagnostic test	Month 1	Month 2	Month 3	Month 4	Month 5	Month 6
Thermography (Highest temperature difference in °C)	3	2	2	3	2	2
Highest ultrasonic reading (dB)	0	0	0	0	0	0
Highest TEV reading (dB)	13	-	-	-	-	12

Based on online diagnostic test results, no defects were detected in the condition of the switchgears within the field trial period. In addition, the measurements are consistent for all data points. This indicates that there is no significant deterioration of the insulation and conductor components of the switchgear.

Switchgear performance assessment

The magnetic actuator driven switchgear was able to perform within the specified limits during switching operations. No problem was reported during the field evaluation period.

Technical assessment

The assessment of the technical aspects of the magnetic actuator driven switchgear are as follows:

1. **Compliance to existing technical specifications and standard practice.** There were several minor non-compliances to the standard practice which were detected during the Product Inspection tests by the certified Quality Inspector. All of these non-compliances were rectified prior to installation and commissioning.
2. **Ease of installation.** Difficulties were encountered by the cable jointers when cable jointing was performed during installation. This was caused by the arrangement of the cable bushings which was from front to back compared to the conventional arrangement from left to right. Figure 4 overleaf shows the illustration of the cable bushing arrangement as seen from the top view of the switchgear panels of both the magnetic actuator driven switchgear as well as the switchgear with conventional spring mechanism. In addition, the cable bushing height for the red phase in the outgoing panels was lower than 500mm causing further difficulty during cable jointing as 3 core cables were used in the outgoing panels.

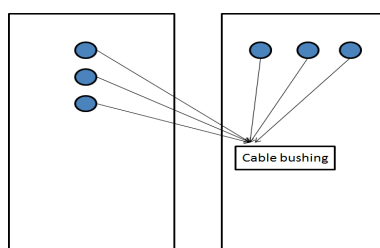


Figure 4. Cable bushing arrangement in the magnetic actuator driven switchgear (left) and air insulated switchgear with conventional spring mechanism (right)

3. **Ease of operation and maintenance.** Due to the fixed implementation of the circuit breaker, total shutdown is required when maintenance work and offline diagnostic tests are done on the circuit breaker. This is problematic especially during breakdown maintenance where only one panel is damaged but nevertheless requiring the whole substation to be taken offline. To deal with this problem, a the switchgear component arrangement needs to be redesigned whereby a three-position disconnecter for isolating and earthing purposes is used in lieu of separate isolator and earthing switch. This change will allow the circuit breaker to be fully isolated from the busbar.

4. **Component reliability.** Jin et al. (2005) reported that the lifetime of electronic components of the magnetic actuator mechanism, such as the electronic controller unit and the capacitor, are dependent on the operating temperature. An increase in the operating temperature beyond the recommended maximum temperature of 40°C will severely diminish the lifetime of the components. Based on the temperature measurement during the field evaluation, the ambient temperature can go beyond this maximum temperature.
5. **Safety.** As the circuit breaker in the magnetic actuator driven switchgear are in fixed implementation rather than the in a withdrawable truck, accidents during rack-in and rack-out operation are totally prevented.

Financial assessment

A qualitative analysis on the life cycle cost components is shown in Table 3 below:

Table 3
Qualitative analysis on the life cycle cost components

Cost component	Impact of the cost component to the overall life cycle cost	Cost comparison with air insulated switchgear with spring mechanism
Purchase	High	At least 2.5 times higher
Installation	Low	Same
Operation	Low	Same
Condition monitoring	Low	Same
Periodic maintenance	Medium	Lower as grease maintenance of the spring mechanism is not required (i.e. shorter shutdown duration)
Breakdown maintenance	Medium	Higher as total shutdown is required even if only one panel is affected.
Spare parts	Medium	Higher as more expensive components are used.
Disposal	Medium	Same

Based on the life cycle cost analysis, the total cost of owning the magnetic actuator driven switchgear is much higher compared to the traditional switchgear. This is due to the higher purchase price, breakdown maintenance cost and spare parts.

CONCLUSION

Preliminary results indicated that magnetic actuator driven switchgear perform commendably on the safety aspect, on-site performance monitoring and online diagnostic test results. However, concerns such as difficulties during cable installation, need for total shutdown of the substation when performing diagnostic tests and circuit breaker maintenance, higher initial purchase

price, and life span of the magnetic actuator mechanism need to be addressed. A review of the design needs to be made by manufacturers of this technology before they are widely adopted by utility suppliers.

ACKNOWLEDGEMENT

The authors would like to thank Tenaga Nasional Berhad for the funding of this research project.

REFERENCES

- Amir, M. D. M., Toh, K. B., & Muttalib, E. S. A. (2013, January). Evaluation of magnetic actuator driven switchgears in TNB. In *Electricity Distribution (CIRED 2013), 22nd International Conference and Exhibition on* (pp. 1-4). IET.
- Jiles, D. C. (1998). *Introduction to Magnetism and Magnetic Materials* (2nd Ed.). CRC Press.
- Jin, T., Xiong, Z., & Wang, P. (2005), Minimize system failure rate considering variations of electronic components lifetime data [PCB design for reliability]. In *Proceedings of 2005 International Conference on Asian Green Electronics, 2005. AGECE*. (pp. 129-134).
- Lane, S. E. (1999). Switchgear developments. *Transactions-Institute of Marine Engineers-Series C-*, 111(6), 39-46.
- Loo, Y. H., Yaw, C. T., Hashim, A. H., Mohamad, A. M., Faizah, M. K., & Noormala, A. (2010, June 23-24). Development of Switchgear Life Cycle Cost Analysis Software. In *4th International Power Engineering and Optimization Conf. (PEOCO2010)*. Shah Alam, Selangor, Malaysia.
- Muttalib, E. S. A., & Amir, M. D. M. (2010). *Root Cause Analysis of 11kV and 33kV Breaker Sluggishness and Remedial Measures in TNB*. T & D Asset Management Workshop, CIRED Malaysia, Session 3 Paper 16.
- TNB. (2013). *Condition Based Maintenance Manual for PPU*. Tenaga Nasional Berhad.



Lightning Breakdown Voltages of Refined Bleached and Deodorised Palm Oil under Needle-plane Configuration

Norhafiz Azis¹, Yee Von Thien^{1*}, Robiah Yunus² and Zaini Yaakub³

¹Centre for Electromagnetic and Lightning Protection Research (CELP), Faculty of Engineering, Universiti Putra Malaysia, 43400 Serdang, Selangor, Malaysia

²Department of Chemical and Environmental Engineering, Faculty of Engineering, Universiti Putra Malaysia, 43400 Serdang, Selangor, Malaysia

³Hyrax Oil Sdn. Bhd, Lot 4937 Batu 5 1/2, Jalan Meru, Mukim Kapar, 41050 Klang, Selangor, Malaysia

ABSTRACT

In recent years, vegetable oil such as Palm Oil (PO) has been identified as a potential alternative dielectric insulating fluid for transformers. It is biodegradable, non-toxic and has high flash and fire points. In this paper, a study on the positive lightning impulse breakdown voltages of PO under non-uniform field is carried out. The testing was carried out using needle-plane electrodes configuration at gap distances of 25 mm and 50 mm. Rising voltage, 1 and 3 shots per step testing methods were used and 3 types of Refined Bleach and Deodorized Palm Oil (RBDPO) and Mineral Oil (MO) were examined. It was found there is no significant effect on the breakdown voltages of all samples. The breakdown voltages of all RBDPO at 50% probability are comparable with MO. At 1% probability and gap distance of 50 mm, the breakdown voltages of all RBDPO are lower than MO.

Keywords: Lightning breakdown voltage, non-uniform field, palm oil, transformers

INTRODUCTION

Oil filled transformers form the majority type of transformers in high voltage power

system networks (Nynas Ab, 2004). The conventional dielectric insulating fluid used in transformers is Mineral Oil (MO) (Nynas Ab, 2004). However, MO is not -biodegradable, non-renewable, and has low flash points. Due to the increasing concern for the environment vegetable oils have been proposed as dielectric insulating fluid in transformers. Extensive studies had been carried out previously on different types of vegetable oils and used in small and medium transformers (Cigre, 2010; Hopkinson et al., 2006; Rycroft et al., 2014).

ARTICLE INFO

Article history:

Received: 24 August 2016

Accepted: 03 Jun 2017

E-mail addresses:

norhafiz@upm.edu.my (Norhafiz Azis),
yvonne.thien@gmail.com (Yee Von Thien),
robiah@upm.edu.my Robiah Yunus,
zaini@hyraxoil.com (Zaini Yaakub)

*Corresponding Author

Palm Oil (PO) is one of vegetable oil considered for transformers application. It is easily available in Indonesia and Malaysia (Agriculture, 2015) where it is used in food preparation and lubricants, biodiesel and biofuel (Mekhilefa et al., 2011; Reddy et al., 2014). Generally, PO is classified under the natural ester family and consists of glycerol and fatty acids which are known as triglycerides (Cigre, 2010). It contains an almost balanced mixture of saturated and unsaturated fatty acids (Cigre, 2010).

Studies too had been done to examine the lightning breakdown characteristics of PO under non-uniform field (Thien et al., 2014; Thien et al., 2015; Thien et al., 2016b; Vukovic et al., 2011). The point-plane or point-sphere configurations create non-uniform field which can be used to simulate the imperfections that could occur in transformers. Therefore, the lightning breakdown voltages of dielectric insulating fluids under non-uniform field are important as the parameter for transformers design (Thien et al., 2016a). It was found that based on needle-sphere electrodes configuration, the lightning breakdown voltages of PO were comparable to MO under positive polarity (Thien et al., 2014; Thien et al., 2015; Thien et al., 2016b). This paper investigates the lightning impulse breakdown voltages of 3 types of Refined Bleached and Deodorized Palm Oil (RBDPO) based on needle-plane electrodes configuration. The first section of the paper examines the effect of the rising voltage, 1 and 3 shots per step testing methods on the positive lightning breakdown voltages of the RBDPO. Next, the breakdown voltages of RBDPO at 1% and 50% probability obtained based on rising voltage, 1 shot per step method are computed by Weibull and normal distributions and compared with MO.

EXPERIMENTAL DESCRIPTION

Investigated samples

Three samples of RBDPO and 1 sample of MO were examined. The compositions of saturated/unsaturated fats and vitamins of the RBDPO are given in Table 1. RBDPOB has the highest quantity vitamin E followed by RBDPOA and RBDPOC while only RBDPOC has vitamin A.

Table 1
Fat, vitamin E/A contents of RBDPO

Contents	Samples		
	RBDPOA	RBDPOB	RBDPOC
Saturated fat (g)	44.4	43.0	45.4
Poly-unsaturated fat (g)	12.2	14.0	11.6
Mono-unsaturated fat (g)	43.3	43.0	43.0
Vitamin E (mg)	50.0	75.0	4.4
Vitamin A (μ g)	-	-	264

Test setups

The lightning breakdown voltage tests of all samples were carried out using needle-plane electrodes as shown in Figure 1. The tip radius curvature of the needle electrode was 50 ± 5 μ m while the diameter of the plane electrode was 200 mm with an edge radius of 3 mm. The

oils were filled in a cubic transparent Perspex test cell with an internal volume of 10 litres. All tests were carried out at gap distances of 25 mm and 50 mm. Standard positive lightning impulse of 1.2/50 μ s was delivered by the impulse generator with maximum voltage of 420 kV.

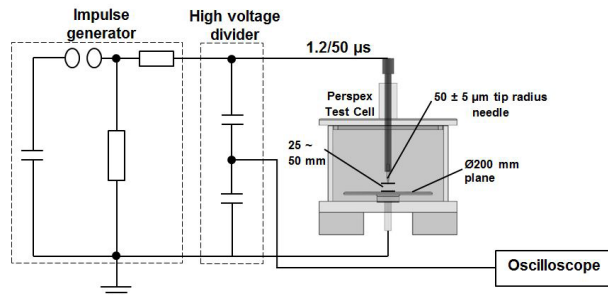


Figure 1. Test configuration for the lightning impulse

Testing methods

All measurements were carried out based on rising voltage method. The initial voltages were set at 70 kV and 140 kV respectively for both gap distances of 25 mm and 50 mm. The voltage increment was set to 10 kV.

The first test consisted of 5 breakdown voltages data for each sample based on the 1 shot per step method according to IEC 60897 and 3 shots per step method according to ASTM 3300 (IEC 60897, 1987; ASTM 3300, 2012). The testing was repeated after standing time intervals of 3 to 5 minutes. This set of data was obtained in order to compare the differences between both methods stated in IEC 60897 and ASTM 3300. The second test consisted of 15 breakdown voltages data for each sample at 1 shot per step method and the analysis on the breakdown voltages at 1% and 50% probabilities was carried out based on Weibull and normal distributions.

RESULT AND ANALYSIS OF DATA

Rising voltage – 1 shot per step and 3 shots per step

The 50% lightning breakdown voltages for all RBDPO and MO based on 1 shot per step are shown in Figure 2(a). At gap distance of 25mm, MO shows the highest breakdown voltage followed by RBDPOB, RBDPOA and RBDPOC with values of 98.0 kV, 96.4 kV, 95.7 kV and 95.1 kV. The same pattern is observed at gap distance of 50 mm where MO has the highest breakdown voltages with a value of 184.6 kV. For RBDPO, the highest breakdown voltage is RBDPOB followed by RBDPOC and RBDPOA with values of 165.0 kV, 163.4 kV and 162.9 kV respectively.

Figure 2(b) shows the 50% lightning breakdown voltages for all RBDPO and MO based on 3 shots per step method. The same pattern is observed as in rising voltage 1 shot per step method where the highest breakdown voltage is MO with values of 93.3 kV and 175.1 kV at gap distances of 25 mm and 50 mm respectively. At gap distance of 25 mm, the breakdown voltages of RBDPOA and RBDPOB are comparable to MO with a value of 92.9 kV. The breakdown

voltage of RBDPOC is slightly lower than RBDPOA and RBDPOB with a value of 92.2 kV. While at gap distance of 50 mm, RBDPOB has the highest breakdown voltage followed by RBDPOA and RBDPOC with values of 162.7 kV, 159.0 kV and 157.6 kV respectively.

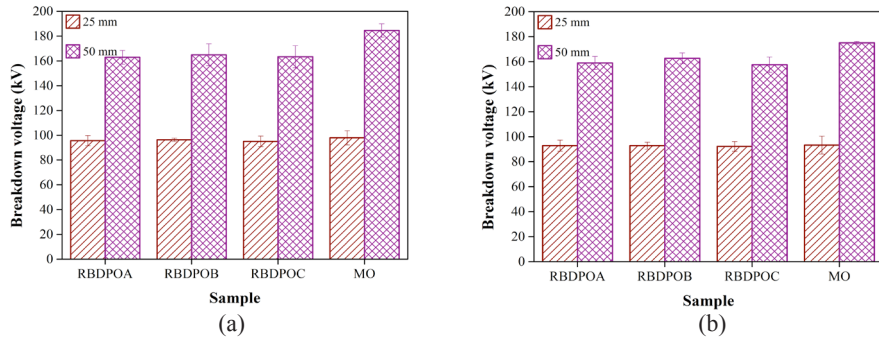


Figure 2. 50% breakdown voltages of all samples based on rising voltage (a) 1 shot per step; (b) 3 shots per step

Analysis results

It was found that the 50% lightning breakdown voltages of all samples obtained by 1 shot per step method are slightly higher than 3 shots per step method as shown in Figure 3(a) and 3(b). The highest percentages of differences are between 1% and 5% at both gap distances of 25 mm and 50 mm. Since both 1 shot per step and 3 shots per step methods show similar results, rising voltage 1shot per step method are recommended after considered their technical operations and times consumed for results obtained.

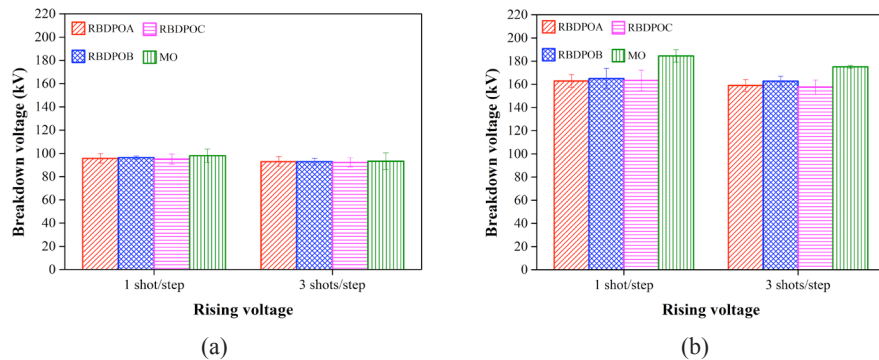


Figure 3. Comparison between 50% breakdown voltages obtained based on 1 and 3 shots per step methods of all samples at gap distances of (a) 25 mm; (b) 50 mm

Table 2 shows the breakdown voltages for all samples and the percentage of difference between the RBDPO samples and MO. Taking MO as a benchmark, it was found that the breakdown voltages of all RBDPO are comparable to MO where the highest percentage of difference is less than 3% at gap distance of 25 mm under both 1 and 3 shots per step methods. At gap distance of 50 mm, the differences between all RBDPO and MO are slightly high where

the highest percentages of differences are around 11.7% and 10% for both 1 and 3 shots per step methods respectively. Among all the RBDPO, RBDPOB has the closest breakdown voltage with MO with percentage of difference less than 10% at both gap distances. Thus, based on the results obtained, the possibility to replace MO with RBDPO is high.

Table 3 shows the average velocities of all samples that were determined based on the gap distance over the time to breakdown recorded for each breakdown event. The average velocities of all RBDPO are slightly slower than MO at gap distance of 25 mm but faster than MO at gap distance of 50 mm. At gap distance of 25 mm, the average velocities for all RBDPO are the same while at gap distance of 50 mm, the average velocity of the RBDPOA is the highest followed by RBDPOB and RBDPOC.

Table 2
Breakdown voltages using rising voltage 1 shot/step and 3 shots/step testing method at gap distances of 25 mm and 50 mm

Sample	Breakdown voltages at gap distance 25 mm (kV)			
	1 shot/step	% difference between RBDPO and MO	3 shots /step	% difference between RBDPO and MO
RBDPOA	95.7	2.3	92.9	0.5
RBDPOB	96.4	1.7	92.9	0.4
RBDPOC	95.1	3.0	92.2	1.2
MO	98.0	-	93.3	-
Sample	Breakdown voltages at gap distance 50 mm (kV)			
	1 shot/step	% difference between RBDPO and MO	3 shots /step	% difference between RBDPO and MO
RBDPOA	162.9	11.7	159.0	9.2
RBDPOB	165.0	10.6	162.7	7.1
RBDPOC	163.4	11.4	157.6	10.0
MO	184.6	-	175.1	-

Table 3
Average velocity of all samples

Sample	Velocity (km/s) at gap distance 25 mm		Velocity (km/s) at gap distance 50 mm	
	1 shot/step	3 shots/step	1 shot /step	3 shots /step
RBDPOA	1.5	1.5	4.2	4.3
RBDPOB	1.5	1.5	2.8	2.7
RBDPOC	1.5	1.6	2.8	2.3
MO	1.8	1.9	2.0	2.0

Lightning withstand voltages

Weibull distribution is commonly used to fit all the breakdown data of electrical insulation. The cumulative distribution function for Weibull distribution is given by Equation 1 (Liu, 2011).

$$F(x) = 1 - e^{-\left(\frac{x}{\alpha}\right)^\beta} \tag{1}$$

Where α and β are scale and shape parameters, while x represents the measured breakdown data.

Based on its shape and scale parameters, the withstand voltage can be calculated. Other common distribution that is used to analyse the breakdown data of electrical insulation is normal distribution. The probability function is given by Equation 2.

$$F(x) = \frac{1}{\sigma\sqrt{2\pi}} \exp\left(-\frac{1}{2}\left(\frac{x-\mu}{\sigma}\right)^2\right) \tag{2}$$

Where μ and σ are mean and standard deviation parameters, while x is the measured breakdown data.

According to the normal distribution, the withstand voltage can be determined based on mean and standard deviation. The Weibull and normal fittings for all samples can be seen in Figure 4(a), 4(b), 5(a) and 5(b). At gap distance of 25 mm, both Weibull and normal distributions can represent the all samples quite well. There is however, a slight deviation of both Weibull and normal fittings at gap distance of 50 mm.

The breakdown voltages at 1% and 50% probabilities for both Weibull and normal distributions are shown in Table 4. At gap distance of 25 mm, MO has a slightly lower

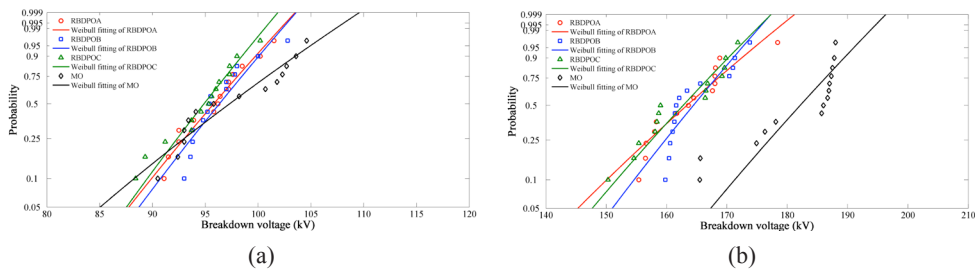


Figure 4. Weibull probability fittings of all samples at gap distances of (a) 25 mm; (b) 50 mm

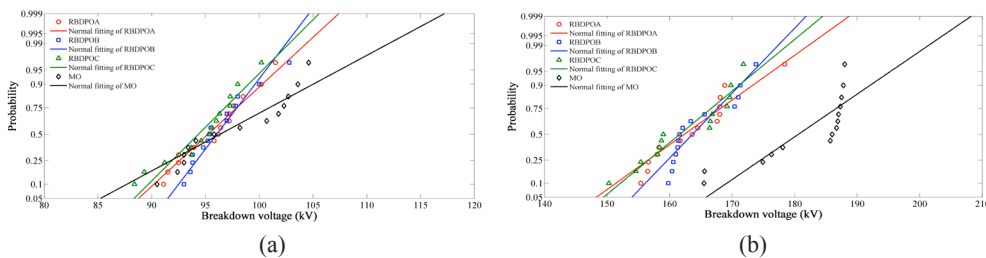


Figure 5. Normal probability fittings of all samples at gap distances of (a) 25 mm; (b) 50 mm

Table 4
Breakdown voltages of all samples at 1% and 50% breakdown probabilities

Sample	Breakdown probability	Breakdown voltage at gap distances (kV)			
		25 mm	50 mm	25 mm	50 mm
		W.D	N.D	W.D	N.D
RBDPOA	1%	83.1	86.1	135.0	142.5
	50%	95.8	95.2	163.4	162.3
RBDPOB	1%	84.3	89.6	143.2	150.0
	50%	96.3	96.0	164.4	163.6
RBDPOC	1%	83.2	85.9	139.0	144.4
	50%	94.9	94.3	162.7	161.6
MO	1%	78.2	80.6	158.6	159.8
	50%	97.3	96.3	182.1	180.6

* W.D – Weibull distribution and N.D – Normal distribution

breakdown voltage at 1% probability than all RBDPO where the highest percentages of differences are 7.8% and 6.8% for both Weibull and normal distributions. At gap distance of 50 mm, MO has the highest breakdown voltage at 1% probability voltage where the highest percentages of differences with all RBDPO are 15% and 10.8% for both Weibull and normal distributions. The breakdown voltages of all RBDPO at 50% probability are slightly lower than MO where the highest percentages of differences are 10.6% and 10.5% at both gap distances. The difference of the breakdown voltages among all RBDPO at 1% and 50% probabilities are quite small where the percentage of differences are between 0.2% and 5% at both gap distances. It is observed that at 1% probability, the breakdown voltages of all samples based on normal distribution are higher than Weibull distribution. However, at 50% probability, the breakdown voltages based on normal distribution are lower than Weibull distribution. Both normal and Weibull distribution show similar breakdown voltages results, Weibull distribution is recommended since it was commonly used in most of the previous studies.

CONCLUSION

Under the current needle-plane configuration, the positive lightning breakdown voltages of all RBDPO are slightly lower than MO at both gap distances of 25 mm and 50 mm. The range of the percentages of differences between all RBDPO and MO is between 1% and 11.7%. The composition of the saturated/unsaturated fats and vitamins of the RBDPO show no significant effect on the lightning breakdown voltages where the highest percentages of difference among all RBDPO samples are less than 2.3%. There is also no significant effect between 1 and 3 shots per step methods on the breakdown voltages of all samples where the range of the percentages of differences is between 1% and 5%. Considering the technical operation and time consumed for results obtained, rising voltage 1 shot/step is commonly used. It is also observed that the average velocities of all samples increase as the gap distance increases. Based on the Weibull and normal distributions analyses, it was found that the percentages of differences for the breakdown voltages at 1% probability between all RBDPO and MO can be up to 15%.

ACKNOWLEDGEMENT

The authors would like to thank Ministry of Education and Universiti Putra Malaysia for the funding under FRGS scheme (03-02-13-1280FR), (03-02-13-1279FR), Putra IPM and IPB schemes (GP-IPM/2013/9401500), (GP-IPB/2014/9440801). Special thanks to Hyrax Oil Sdn. Bhd and Malaysia Transformer Manufacturing Sdn. Bhd. for technical support.

REFERENCES

- Aditama, S. (2005). Dielectric properties of palm oils as liquid insulating materials: effects of fat content. In *International Symposium on Electrical Insulating Materials (ISEIM 2005)* (Vol. 91, p. 91-94).
- Agriculture, Department United States (USDA). (2015). *Oilseeds: World Markets and Trade*. United States.
- ASTM 3300. (2012). *Standard Test Method for Dielectric Breakdown Voltage of Insulating Oils of Petroleum Origin Under Impulse Conditions*. United States.
- Azis, N., Jasni, J., Ab Kadir, M. Z. A., & Mohtar, M. N. (2014). Suitability of palm based oil as dielectric insulating fluid in transformers. *Journal of Electrical Engineering and Technology*, 9(2), 662-669.
- Cigre, A2-35. (2010). *Experiences in Service with New Insulating Liquids*. United Kingdom.
- Hopkinson, P., Dix, L., McShane, C. P., Moore, H. R., Moore, S., Murphy, J., Prevost, T., & Smith, S. D. (2006). Progress Report on Natural Esters for Distribution and Power Transformers. In *IEEE PES Transmission and Distribution Conference and Exhibition* (p. 15-17).
- IEC 60897 (1987). *Methods for the determination of the lightning impulse breakdown voltage of insulating liquids*. International Electrotechnical Commission.
- Kiasatina, K., Kamarol, M., Zuhilmey, M., & Arief, Y. A. (2011). Breakdown characteristics of RBDPO and soybean oil mixture for transformer application. In *International Conference on Electrical, Control and Computer Engineering (INECCE)* (p. 219-222).
- Liu, Q. (2011). *Electrical Performance Of Ester Liquids Under Impulse Voltage For Application In Power Transformers*. The University of Manchester.
- Mekhilefa, S., Sigaa, S., & Saidurb, R. (2011). A review on palm oil biodiesel as a source of renewable fuel. *Renewable and Sustainable Energy Reviews*, 15(4), 1937-1949.
- Nynas AB. (2004). *Transformer oil handbook*. Sweden.
- Rajab, A., Suwarno, & Aminuddin, S. (2009). Properties of RBDPO Oleum as a candidate of palm based-transformer insulating liquid. In *International Conference on Electrical Engineering and Informatics, ICEEI* (p. 548-552).
- Reddy, K. S. V., Kabra, N., Kunchum, U., & Vijayakumar, T. (2014). Experimental Investigation on Usage of Palm Oil as a Lubricant to Substitute Mineral Oil in CI Engines. *Chinese Journal of Engineering*, 2014(2014), 1-5.
- Rycroft, Mike, & Publishers, EE. (2014). *Vegetable oil as insulating fluid for transformers*. Energize. South Africa.
- Suwarno, F. S., Suhariadi, I., & Imsak, L. (2003, June). Study on the characteristics of palm oil and it's derivatives as liquid insulating materials. In *7th International Conference on Properties and Applications of Dielectric Materials* (vol.492, p. 495-498).

- Thien, Y. V., Azis, N., Jasni, J., Ab Kadir, M. Z. A., Yunus, R., Ishak, M. T., & Yaakub, Z. (2016b). Evaluation on the Lightning Breakdown Voltages of Palm Oil and Coconut oil under Non-uniform Field at Small Gap Distances. *Journal of Electrical Engineering and Technology*, 11(1), 184-191.
- Thien, Y. V., Azis, N., Jasni, J., Ab Kadir, M. Z. A., Yunus, R., Ishak, M. T., & Yaakub, Z. (2014). Investigation on the lightning breakdown voltage of Palm Oil and Coconut Oil under non-uniform field. In *IEEE International Conference on Power and Energy (PECon)* (p. 1-4). IEEE.
- Thien, Y. V., Azis, N., Jasni, J., Ab Kadir, M. Z. A., Yunus, R., Ishak, M. T., & Yaakub, Z. (2016a). The effect of polarity on the lightning breakdown voltages of palm oil and coconut oil under a non-uniform field for transformers application. *Industrial Crops and Products*, 89, 250-256.
- Thien, Y. V., Azis, N., Jasni, J., Kadir, M. Z. A. Ab, Yunus, R., Ishak, M. T., & Hamzah, N. R. (2015). A Study on the Lightning Impulse Breakdown Voltages of Palm Oil and Coconut Oil by Different Methods. *Applied Mechanics and Materials*, 793, 9-13.
- Vukovic, D., Tenbohlen, S., Harthun, J., Perrier, C., & Fink, H. (2011). Breakdown strength of vegetable-based oils under AC and lightning impulse voltages. In *IEEE International Conference on Dielectric Liquids (ICDL)* (p. 1-4). IEEE.





Analysis of Air Humidity and Temperature for Post Lightning Circumstances

Sharifah Sakinah, Tuan Othman^{1*}, Jasronita, Jasni¹ and Mohd Nazim, Mohtar¹

¹Department of Electric and Electronic Engineering, Faculty of Engineering, Universiti Putra Malaysia, 43400 Serdang, Malaysia

ABSTRACT

Lightning is a natural phenomenon that generates a high electric field during thunderstorm. It has been reported that lightning strikes amid storms can occur around 100 times per second. The atmospheric electric field is an imperative parameter during a thunderstorm. Therefore, monitoring the electric field and its parameters is the best way for local lightning forecast. The electric field monitoring data can validate the accuracy of weather prediction in a local area from meteorology department or by using equipment specially designed to measure this electric field that exists when the phenomenon of lightning occurs. In this paper, the relationship between lightning, air humidity and temperature is discussed to understand the post lightning effect on these electric parameters. Additionally, the characteristics of the parameters are observed and analysed.

Keywords: Lightning, humidity, temperature, atmospheric electric field

INTRODUCTION

An atmospheric electric field is one of the most important parameters of a thunderstorm and every time a thunderstorm approaches, it is often accompanied by lightning whereby the

atmospheric electric field lights up (Bo, Bihua & Taichang, 2007). Typically, thunderstorms are linked to lightning whereby the latter generates electric discharge with high voltage. It is a transient discharge of static electricity which serves to re-create the electrostatic symmetry within a thunderstorm situation (Mohamed & Lee, 2006; Gan & Li, 2010; Oh, Pang & Chua, 2010). Atmospheric electric field is generated by the difference between ionosphere and ground that happens during fair weather in the order of 300kV (Price, 2002). During a thunderstorm, its strength near the ground can hit standards of 15 kV/m

ARTICLE INFO

Article history:

Received: 24 August 2016

Accepted: 03 Jun 2017

E-mail addresses:

shsakinah.to@gmail.com (Sharifah Sakinah, Tuan Othman),

jas@upm.edu.my (Jasronita, Jasni),

nazim@upm.edu.my (Mohd Nazim, Mohtar)

*Corresponding Author

and shows quick varieties described by short pulses identified with lightning. The measurement of atmospheric electric field is known widely as an analytic instrument for many applications. By observing atmospheric electric field in the high intensity and high frequency ranges, it is possible to analyse the polarity, intensity and number of thunderstorm discharges (Xie, Zhang, Liu & Kai, 2011). Studies have shown that the expansion of atmospheric electric field in fair weather can be one of the indicators of presence of aerosol in the air or the atmosphere in general (Sheftel, Chernyshev & Chernysheva, 1994). Atmospheric electric field varieties are created because of the electric charge generation and the movement into a thunderstorm. During the thunderstorm and lightning, changes of magnitude and polarity of the atmospheric electric field occur. On cloud electric field estimations, it is possible to know the total thunderstorm duration, the distinctive thunderstorm stages and some lightning parameters, for example, lightning location and transfer charge (Aranguren, Delgadillo, Vargas, Perez & Torres, 2006). Lightning is just like a static electricity that happens because of the attraction between positive and negative charges in atmosphere (Srinivasan & Gu, 2006). During a thunderstorm, the moisture of air is changeable. The humidity and temperature are the indicators of moisture in the air (Lawrence, 2005). In this work, the relationship between humidity and temperature post lightning is examined.

EXPERIMENT

The electric field is measured using Boltek EFM – 100 Electric Field Monitor. The electric field mill detects an electric field by repeatedly exposing and shielding a progression of sense electrodes to the air. The electric field data is displayed and graphed using the EFM – 100 display software, from the approach of lightning which gives a positive field reading, trailed by a field inversion to a negative field as the cloud moves overhead. Electric field mill utilises a mechanical chopper to shield and uncover a few sense plates to an electric field. An electric charge is attracted from ground to the plates through a sense resistor when the sense plates are presented at the electric field. The field charge streams back to ground, again through the sense resistor, when the sense plates are protected from the field. This moving charge delivered an electric current which is measured as an AC voltage over the sense resistor. The measure of the voltage corresponds with the span of the electric field connected to the plates. Charges that stream onto and off of the sense cathodes will build up a voltage over the resistor. Thus, the reading will be detected and displayed in a monitor. To measure the humidity and temperature, another equipment was used, Davis WeatherLink. This WeatherLink was mounted at the rooftop to give an accurate weather measurement. The weather data is then compared with electric field data to be analysed. Figure 1 shows the block diagram of the Boltek EFM-100 while Figure 2 shows the block diagram of WeatherLink that have been used in this work. The WeatherLink will measure the parameters of weather that can be captured around the weather station.

In this work, both equipment were used to measure the atmospheric electric field, outside temperature and outside humidity. Lightning data was validated obtained from TNB Research and meteorology department for weather validation. The monitoring process a one year from October 2014 until September 2016. The Boltek EFM-100 and the WeatherLink was mounted at the rooftop of Faculty of Engineering, Universiti Putra Malaysia, Serdang.

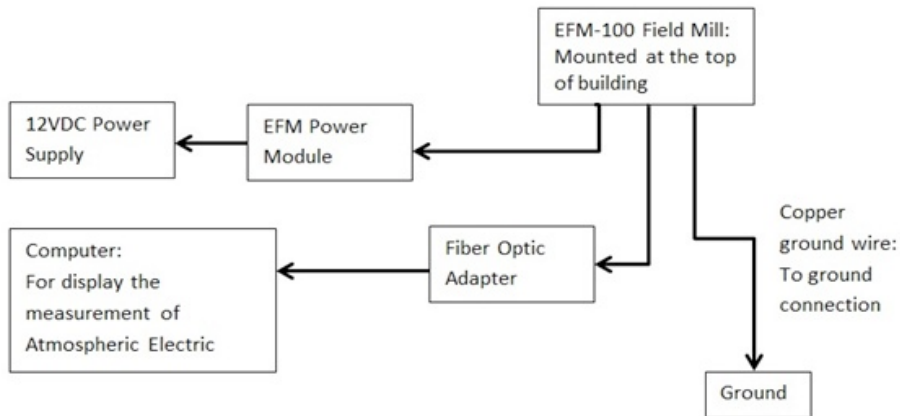


Figure 1. Block diagram of Boltek EFM-100

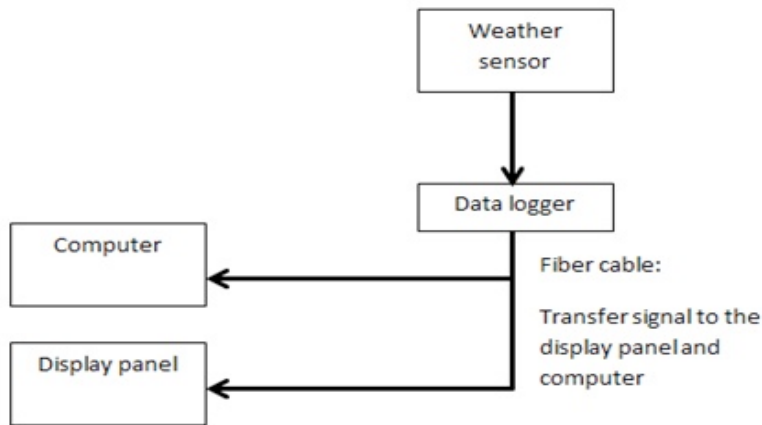


Figure 2. Block diagram of WeatherLink

RESULT AND DISCUSSION

The monitoring process of atmospheric electric field and weather has been done continuously for one year starting from October 2014. By monitoring both the atmospheric electric field using Boltek EFM-100 field mill and parameters of the weather using WeatherLink, information regarding the validity of weather prediction in a native area, lightning forecast and the reliability of lightning protection validation can be observed, measured and analysed. This study had focused on Southwest Peninsular Malaysia where a field mill was mounted at the top of the building of Faculty Engineering, Universiti Putra Malaysia, coordinated at N 3.008543 latitude and E 101.720622 longitude. Data obtained was compared with real data from TNB Research for validation. Figure 3 and Figure 4 show the monthly average of electric field through the observation process. The Meteorology Department website indicates this area experiences southwest monsoon between May and October. The graph above shows average monthly rainfall during non-monsoon and monsoon periods. Figure 3 shows the monthly average for

December and January which is the intermediate period during non-southwest monsoon. Figure 4 shows when the southwest monsoon begins (May) and when it ends (October). The electric field curve shows that it has value in both regions, positive and negative. In theory, the earth is negatively charged and the ionosphere is positively charged which causes a constant flow of electricity. There is constantly some measure of limitless positive and negative, however, remaining positive, the atmosphere electric charge nearest to the surface of the negatively charged earth on a fine day. There is free electricity in the cloud and air caused by induction on earth and electromagnetics devices. Most of the experiment dealing with atmospheric electric field shown that there will always be free electricity in atmosphere, sometimes positive, sometimes negative.

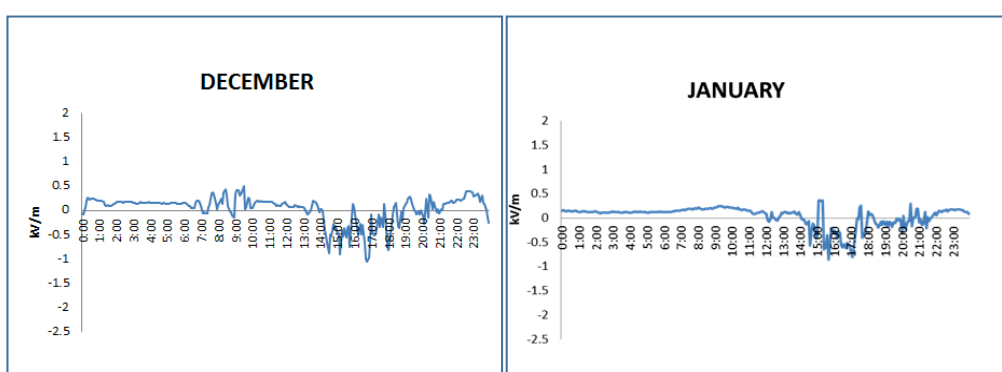


Figure 3. Monthly average electric field data curve during off the southwest monsoon

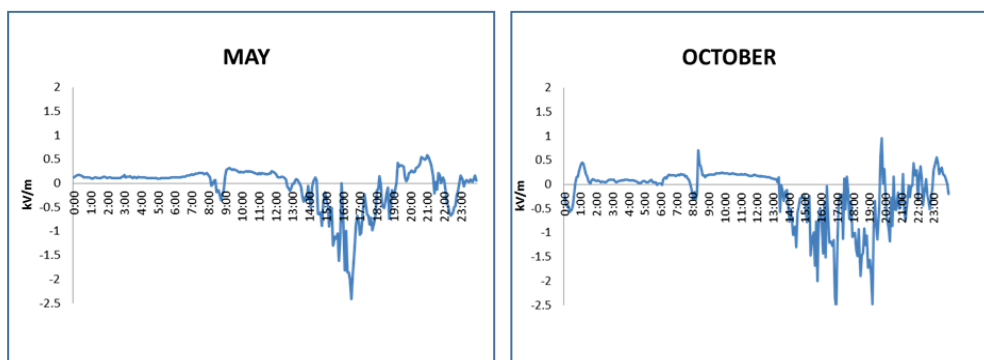


Figure 4. Monthly average electric field data curve during the southwest monsoon

From the graphs, it can be seen that rainfall and thunderstorm occur in the evenings. In the morning until noon, a flat line showed that no lightning was detected during this period. Fluctuation of the curve shows that lightning which occurs frequently and the radius of the field mill mounted point was around 50km. The trends of electric field was studied and recognised. It rains daily between 1600 until 1800. According to the Meteorology Department, it sometimes rains during the night and sometimes thunderstorm can be heard and lightning strikes can be

observed. During a thunderstorm, the electric field can reach up to 20kV/m. In this condition, the weather is disturbed, the vertical electric field can change from negative to positive value (Watt, 1960). Figure 5 shows the output of electric field, outside temperature and outside humidity during sunny days. In the mornings, humidity and temperature is stable. When the sun rises, temperature increases and humidity decreases until evening whereby temperature drops and humidity increases. The reading is stable until end of the day.

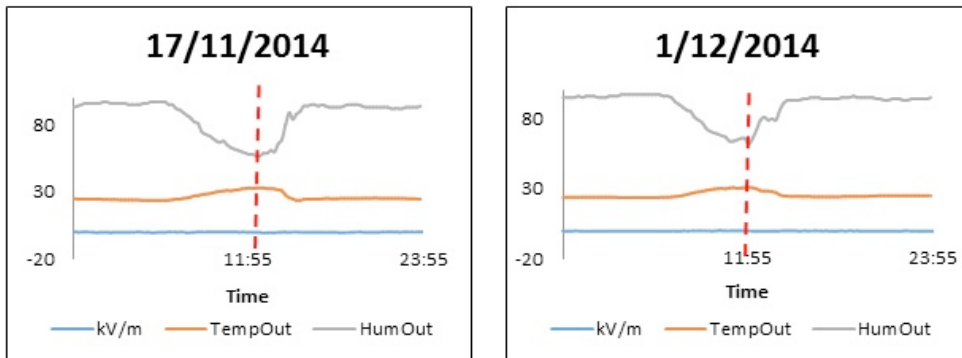


Figure 5. Data curve of electric field, outside humidity and outside temperature during sunny days

During sunny days, the electric field around the field mill is below 200V/m. The electric field is ordinarily down coordinated, and in fair weather and in unpolluted air, the strength near the ground surface is between 100-200 V/m (Xie, Zhang, Liu & Kai, 2011). It will reach a peak point between 12pm and 2pm, temperature at the maximum and humidity at the minimum reading because of the vertical position of the sun which is at the peak. The curve will be flat again. Results of the experiment show that output is almost same as theoretically principle of humidity and temperature which is the humidity will be vice versa from the temperature curve. In short, when humidity reaches the minimum reading, the temperature should record maximum reading. Figure 6 shows relative humidity and temperature as per the Comet Meteorology Education.

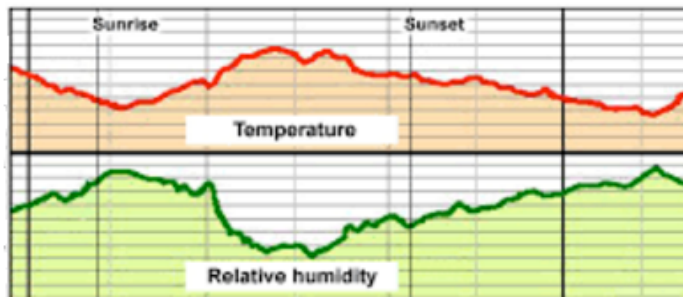


Figure 6. Illustration of relative humidity and temperature

When thunderstorm begins, the field mill will detect lightning signs. Usually, lightning strikes first, before the weather changes from sunny to cloudy. So, it can function as a lightning alarm system. Figure 6 shows the data curve of electric field, humidity and temperature in one graph when lightning was detected and thunderstorm occurred. In the morning, the curve is flat until thunderstorms are detected. During a thunderstorm, humidity and temperature fluctuate. Even when a thunderstorm clears, the reading changes because of the post rain situation.

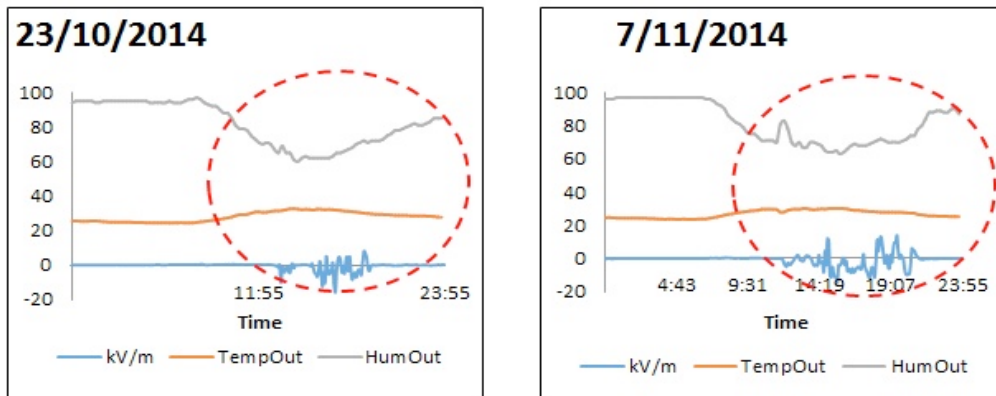


Figure 7. Data curve of electric field, outside temperature and outside humidity when lightning detected

From the field observation, at noon, humidity starts to decrease while temperature increases slightly. When a thunderstorm occurs, humidity increases slowly and temperature decreases slightly because rainfall makes the area cooler and more humid. This situation is unlike during a sunny day. As long as thunderstorms and lightning keep occurring, humidity and temperature will fluctuate until the weather normalises. When a thunderstorm dissipates, the humidity increases slowly and the temperature decreases slightly because of the reservoir of rain in this area. By studying the post lightning situation, important information can be obtained for safety alerts, and prepare for any eventualities.

CONCLUSION

The atmospheric electric field and its trend was studied. The variation of an atmospheric electric field near the ground showed the reading of the electric field to be quite high. The strength of an electric field during a thunderstorm is much higher compared with during sunny and cloudy days where humidity and temperature fluctuate.

ACKNOWLEDGEMENTS

The authors would like to thank Universiti Putra Malaysia for providing the FRGS grant that made this research possible.

REFERENCES

- Aranguren, D., Delgadillo, A., Vargas, M., Pérez, E., & Torres, H., (2006). Estimation Of Lightning Electrostatic Parameters Based On Atmospheric Electric Field Measurements And Genetic Algorithms. In *19th International Lightning Detection Conference 24-25 April*. Tucson, Arizona, USA
- Bo, Y., Bihua, Z., & Taichang, G. (2007, October). Research on distribution of electric field near ground during thunderstorm process. In *2007 International Symposium on Electromagnetic Compatibility* (pp. 267-270). IEEE.
- Gan, P. Y., & Li, Z. (2008). An econometric study on long-term energy outlook and the implications of renewable energy utilization in Malaysia. *Energy Policy*, 36(2), 890-899.
- Lawrence, M. G. (2005). The relationship between relative humidity and the dewpoint temperature in moist air: A simple conversion and applications. *Bulletin of the American Meteorological Society*, 86(2), 225-233.
- Mohamed, A. R., & Lee, K. T. (2006). Energy for sustainable development in Malaysia: Energy policy and alternative energy. *Energy Policy*, 34(15), 2388-2397.
- Oh, T. H., Pang, S. Y., & Chua, S. C. (2010). Energy Policy and Alternative Energy In Malaysia: Issues and Challenges for Sustainable Growth. *Renewable and Sustainable Energy Reviews*, 14, 1241–1252.
- Price, C., (2002). *Lightning and Atmospheric Electricity*. Encyclopaedia of Global Environmental Change, T. Nunn, Ed. Chichester, U.K, Wiley, 502-503.
- Sheftel, V. M., Chernyshev, A. K., & Chernysheva, S. P. (1994). Air conductivity and atmospheric electric field as an indicator of anthropogenic atmospheric pollution. *Journal of Geophysical Research: Atmospheres*, 99(D5), 10793-10795.
- Srinivasan, K., & Gu, J. (2006, May). Lightning as atmospheric electricity. In *2006 Canadian Conference on Electrical and Computer Engineering* (pp. 2258-2261). IEEE.
- Watt, A. D., (1960). ELF Electric Field From Thunderstorms. *Journal of Research of the National Bureau of Standards-D Radio Propagation*, 64D(5), 425-433.
- Xie, Y., Zhang, T., Liu, X., Kai, X., (2011). Electric Characteristic of Atmosphere in Yuxi Region and Its Application of the CG Lightning Warning. In *Pacific International Conference on Lightning Warning*, IEEE.



Development of Power Recovery Circuit for Bio-Implantable Stimulator

Mokhalad Khaleel Alghairi^{1*}, Nasri Bin Sulaiman¹, Roslina Bt Mohd Sidek¹ and Saad Mutashar²

¹Department of Electrical and Electronic Engineering, Faculty of Engineering, Universiti Putra Malaysia, 43400 UPM, Serdang, Selangor, Malaysia

²Department of Electrical Engineering, University of Technology-Iraq, Baghdad

ABSTRACT

This paper presents a modified design of low power recovery circuit in micro-system implanted device to stimulate the human nerve and muscle. The amplitude shift keying ASK was used to modulate data by using operating frequency 6.78MHz ISM industrial scientific medical band to be less invasive to tissue. The proposed system consists of an external part which has ASK modulator and class-E power amplifier with 94.5% efficiency. The internal part has half wave rectifier and voltage regulator to generate very stable 1.8VDC using 0.35um CMOS technology. The Orcad pspice 16.6 and MULTISIM 11 software were used to simulate the design of power recovery and class-E power amplifier respectively. The regulated voltage utilised to power the sub-electronic device implanted inside human body with very stable voltage even change implanted load resistance. The proposed system has 12.5% modulation index and low power consumption.

Keywords: ASK modulator, class-E power amplifier, inductive coupling, rectifiers, LDO low dropout regulator and power recovery

ARTICLE INFO

Article history:

Received: 24 August 2016

Accepted: 03 Jun 2017

E-mail addresses:

mokhalad_alghairi@yahoo.com (Mokhalad Khaleel Alghairi),

nasri_sulaiman@upm.edu.my (Nasri Bin Sulaiman),

roslinams@upm.edu.my (Roslina Bt Mohd Sidek),

saad_ra25@yahoo.com (Saad Mutashar)

*Corresponding Author

INTRODUCTION

Implantable biomedical systems were introduced to achieve superior data transmission and energy efficiency with minimal power consumption and optimal operating frequency according to the ISM industrial scientific medical band (Mandal & Sarpeshkar, 2008). The implanted micro-system stimulator is classified as bio-implantable device and aimed at stimulating

the nerves and muscles when disorders happen because a neural action is absent or when there is damage in the neural signal conduction pathway. An implanted micro-system made up of two main components whereby an external component is placed outside of the skin while an internal component is located under the skin.

Implant devices that are powered by RF signals through inductive coupling links help to reduce the complexity of the system, ensure the patient is not harmed in any way, avoid repeat surgeries and minimise cost (Asgarian & Sodagar, 2009; Atluri & Ghovanloo, 2007). The bio-implanted devices require very efficient RF to DC rectifier and efficient DC-to-DC converter. These devices provide the essential DC voltage to power the implanted micro-system. However, the most common technology used a signal diodes rectifier or MOSFET transistors in bridge rectifier connection (Rakers, Connell, Collins, & Russell, 2001).

The diodes are not suitable for implementation into the human body due to its size, thermal noise and they have larger threshold voltage compared with MOSFET devices (Jia, Chen, Liu, Zhang, & Wang, 2008). The voltage regulator is used to regulate the input voltage that supplies the implanted remote electronics with stable DC voltage to achieve the desired operating conditions. The linear method can be used to control the output voltage, and the reference voltage is compared with the output voltage and used for controlling the regulator feedback loop (Hoon-Kyeu & Dong-Chul, 2000). In praxis, there are different topologies based in the voltage regulator such as basic series regulator and basic shunt regulator. However, the LDO low dropout voltage regulator based on series structure is efficient and a suitable structure compared with shunt structure in power harvesting application (Heidrich et al., 2010). In this paper, low power recovery system is designed to generate a very stable 1.8VDC. This system is operated on 6.78MHz with modulation index of 12.5% and tested in air medium. The Orcad pspice 16.6 and MULTISIM 11 were used to simulate the design of power recovery and class-E power amplifier respectively.

System Architecture

The wireless power transmission (WPT) in biomedical implanted device is used to stimulate the nerves and muscle. The power recovery system design consists of two parts: the external part which touches the skin from outside and consists of ASK modulator and class-E power amplifier to drive the power and data to transmitter coil. The external part located inside the body consists of a receiver coil to receive data and power, half wave rectifier to convert AC to DC signal and LDO low dropout voltage regulator to generate 1.8VDC for powering the sub-electronic implanted as shown in Figure 1.

Development of Bio-Implanatable Stimulator

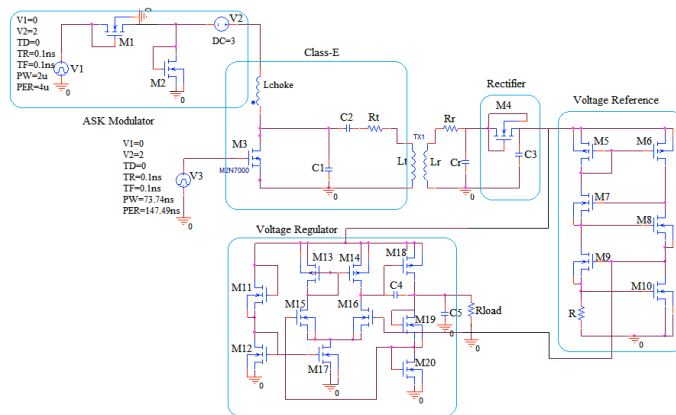


Figure 1. Power recovery system architecture

External unit

The external part consists of ASK modulator, Class-E power amplifier and RLC circuit which act as a transmitter antenna as described in Figure 1. The ASK modulator shown in Figure 2(a) is used to modulate the data and consist of two NMOS (M1&M2) act as resistor for voltage divider and one dc voltage (V2) to adjust the modulation index to be 12.5% by using equation (1).

$$\text{Modulation Index} = \frac{V_H - V_L}{V_H + V_L} \quad (1)$$

The ASK modulator offers (3-4) dc voltage, which is enough to power the class-E power amplifier. The second part is the class-E power amplifier as shown in Figure 2(b), which is widely used to drive the RLC transmitter antenna in biomedical application due to simple architecture and the need for only one active device (Kazimierczuk, 1986).

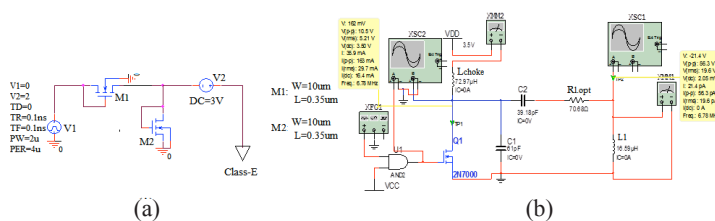


Figure 2. (a) The class-E power amplifier structure; (b) The ASK modulator structure

The class-E was powered using a 3.5 DC V to obtain an efficiency of 94.5%, and it can be observed that the model consists of two major blocks- a unit pole MOSFET transistor switch, that is the selected type (3TEN-2N7000) to reduce the transistor's switching losses (Abbas, Hannan, & Salina, 2012), along with the impedance series network which is calculated by using the equations as given in (Abbas et al., 2012; Suetsugu & Kazimierczuk, 2004). The values of class-E component are shown in Table (1).

Table 1
Class-E amplifier values

	Operate freq. F0	Choke inductor Lchoke	Trans. inductor L1	optimum resistance load Rt	Shunt capacitance C1	Series capacitance C2
Value	6.78MHz	72.79uH	16.59uh	70.68	61pf	39.18pf

Inductive coupling link

The inductive coupling link was designed to transfer data and power from the external part to the internal part. Generally, the inductive coupling link contains secondary and primary coils. The primary side has series resonance to provide a low impedance load for driving the transmitter coil, whereas the secondary side is almost invariably parallel, and uses LC circuit for better driving of a nonlinear rectifier load (Saad Mutashar, Mahammad A Hannan, Salina A Samad, & Aini Hussain, 2014). The optimum resistance $R_{L,opt}$ is still large, and it is not suitable to be used for subcutaneous applications which needs very low impedance called parasitic resistance R_t (Noor & Duffy, 2010). Therefore, the values of parasitic resistances depend on geometric of transmitter and receiver coils, which have dimensions $d_{out}=44\text{mm}$, $d_{in}=7.92\text{mm}$ and $d_{out}=10.5\text{mm}$, $d_{in}=6.61\text{mm}$ respectively (Alghairi, Sulaiman, Sidek, & Mutashar, 2016).

There are many variable effects on inductive coupling link such as transmitted coil inductance (L_t), receiver coil inductance (L_r), resonance frequency (f_0) and coupling coefficient (K). The coupling coefficient must be $0 < K < 1$ and calculated as per equation (2).

$$K = \frac{M}{\sqrt{L_t \times L_r}} \quad (2)$$

The values of the inductive coupling link are shown in Table (2).

Table 2
Inductive coupling link values

	Inductance μH	Capacitance PF	Coupling coefficient	Quality factor	Resistance Ω	Efficiency
Transmitter	16.59	39.18	0.105	70.28	10.05	84.76%
Receiver	0.654	827.17	0.105	51.56	0.54	87.77%

Internal unit

The proposed inductive coupling link technique faced weak coupling. Hence, the RF signal received at the embedded coil was seen to be lesser than the RF signal transmitted. Thus, the implantable biomedical devices required a very effective rectifier and a regulator that can provide the necessary DC voltage for powering the device. The first part from the internal power recovery is a rectifier. The rectifier refers to a voltage conversion part that converts the AC to the DC voltage in the implanted devices. It is very challenging to improve the rectifier efficiency, especially in the case of low power. For improving the efficiency of the RF-DC

MOSFET rectifier, the switching loss transistor (channel size) should be taken into account. In this paper, we developed a half wave rectifier by using a low-drop voltage along with the low-leakage CMOS diode with the help of one NMOST and one capacitor. The proposed design is presented in Figure 3(a). The structure is a very simple design comprising a small capacitor and one N-MOSFET. This design increased the gate-source transistor voltage more than the output voltage, which allowed a decrease in the V_{TH} by a similar value as the output DC voltage. The relationship between voltage drops and the transistor channel size can be rearranged to solve for (W/L) from equation (3) (Yi, Ki, & Tsui, 2007).

$$\left(\frac{W_n}{L_n}\right) = \frac{C_{load}}{\tau \mu_n C_{ox} (V_{DD} - V_{TH,n})} \times \left[\frac{2V_{TH,n}}{V_{DD} - V_{TH,n}} + L_n \left\{ \frac{4(V_{DD} - V_{TH,n})}{V_{DD}} - 1 \right\} \right] \quad (3)$$

This equation is used to size a CMOS circuit for the rectifier to achieve a desired minimum rising or falling propagation delay and also to manage constraints such as rise time/fall time or rise/fall symmetry assuming that the Cload and other parameters are known.

The second part from internal power recovery is LDO voltage regulator. An efficient voltage regulator in bio-implanted device requires voltage reference to generate a steady regulated voltage. The human body temperature has a limited variation and the implanted device with surrounding tissue has a constant temperature due to blood flow in self-surrounding tissue leading to dispense from using a band gap circuit (Saad Mutashar, M. A. Hannan, S. A. Samad, & A. Hussain, 2014). The multiple independent voltage reference circuit is a good choice in bio-implantable device (Amir M Sodagar & Najafi, 2006; A. M. Sodagar, Wise, & Najafi, 2006). The development on the circuit is produced to provide multiple independent voltage reference. The value of reference voltage (2) is 900mV which is obtained by adjusting the size of the MOSFET M9 and M10 and the value of the resistor R as shown in Figure 3(b).

The LDO voltage regulator usually incorporates an error amplifier with a negative feedback where its stability against various load conditions is of great concern. The proposed LDO voltage regulator which is modified from (Chua-Chin, Ya-Hsin, Chio, & Yu-Tzu, 2004) by replacing the passive element with NMOS transistor as a resistor, leads to decrease in size and to generate 1.8 DC output voltage. An LDO voltage regulator consists of an error amplifier as one-stage high gain differential amplifier (M11 to M17) transistor, pass power transistor PMOS (M18), a resistive voltage divider (M19 to M20) and small feedback capacitor (C4) 3 pf connected between the series-pass transistor gate and the drain to increase and ensure system stability. The goal is to design an LDO limited by the following constraints: The output voltage is to be set at 1.8 V utilising an unregulated supply voltage of 5.7 V. Figure 3(c) presents the proposed regulator's general structure. The pass transistor must have a very large width. This is to enable the transistor to source currents that have large loads with a reasonable gate-source voltage, the length is kept at minimum value towards keeping the threshold voltage low, and instead of using voltage divider resistors, (NMOS) transistors are employed at regulator output. This is to feed a fraction of the output voltage back towards the input; in doing so, the feedback path's power consumption is minimised since very little current passes through it.

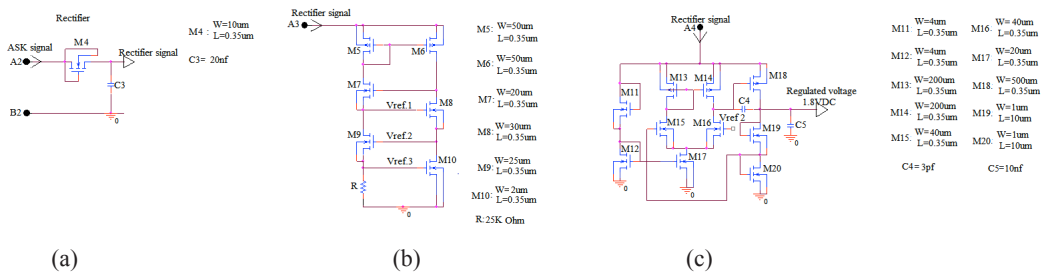


Figure 3. (a) Half wave rectifier for low power recovery; (b) Multiple supply independent voltage reference; (c) The basic LDO structure

RESULTS AND DISCUSSION

It is worth mentioning that there are many limitations in this research such as power consumption, size, feasibility and the design of the embedded biomedical device. The proposed framework includes two sections, the external section and the embedded one, as depicted in Figure 1. The first section, the external one, comprises ASK modulator and class-E power amplifier to conduct the transmitted coil for transmitting data and power. The embedded section comprises received coil, half wave rectifier, as well as voltage regulator to produce efficient and constant 1.8 DC voltage without ripple for powering other parts of the embedded device. The system utilized a low-frequency 6.78 MHz ISM band to prevent any harm to the tissue. Also, in order to power the class-E power amplifier, the ASK modulator is utilised to deliver 3 to 4 DC voltage. Moreover, the class-E power amplifier was composed with low power consumption and least amount of switching losses. The operation of class-E switch (M3) is as per the following: the Drain to Source voltage is equal (0) when the switch is in dynamic state (1) and Gate to Source voltage is (1) when the switch in the state (0), and produces a stable sinusoidal wave signal to the transmitted coil.

Table (1) displays the value for the class-E power amplifier. The transmitted coil L1 presents the exterior loop for the inductive connection and presents it as an antenna to transmit the modulated ASK signal with $V_H=27$ V and $V_L=21$ V with modulation index 12,5%. In the case of received coil in the interior section, it receives the ASK modulated signal inductively with values $V_{MAX}=6$ and $V_{MIN}=4.65$ V with modulation index 12.5% as shown in Figure 4.

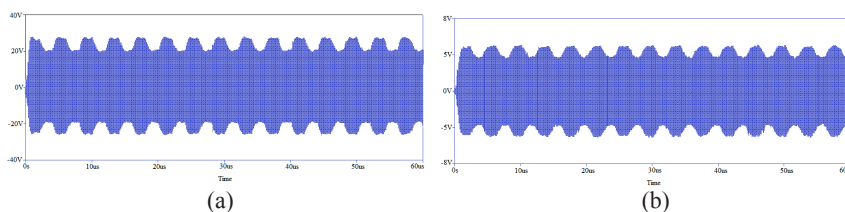


Figure 4. (a) The transmitted ASK signal; (b) the received ASK signal

The weak coupling between the exterior and interior coils is because of the constrained size of coils utilised in the embedded section. Hence, the inductive coupling connections ought to have the capacity to transfer the power at high efficiency as indicated by the values given in Table 2

The rectified signal is smoothed by stabiliser capacitor 20 nf to get a non-regulate DC signal. The non-regulated DC voltage must be constant. Therefore, the voltage reference for power recovery is intended to produce a level voltage VREF that is 900mV, half of the required value on the yield voltage regulator with an extremely stable DC voltage as shown in Figure 5(a) and 5(b). Therefore, the proposed voltage regulator is utilised to produce exceptionally stable 1.8 V VDD, notwithstanding the embedded device resistance altered from 250 Ω up to 2.5 k Ω as seen in Figure 6.

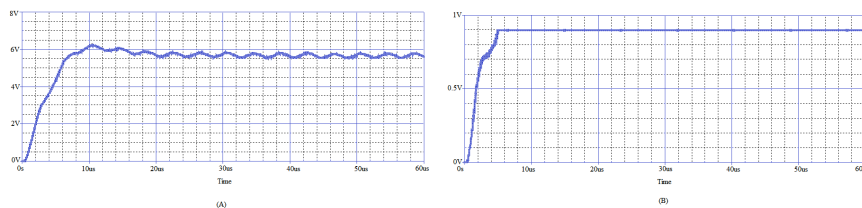


Figure 5. (a) The rectified ASK signal; (b) Reference voltage output signal

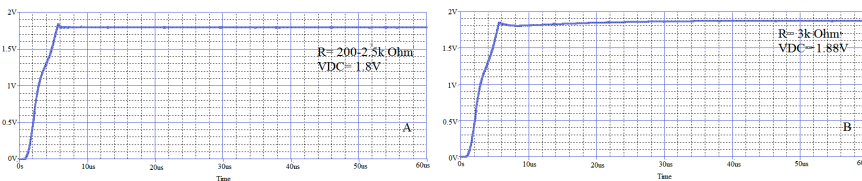


Figure 6. The constant regulated VDD = 1.8 with various load resistances

CONCLUSION

An adapted design for low-power recovery framework using an embedded micro-system was presented in this paper. The proposed system utilised operating frequency 6.78MHz ISM band. The class- E power amplifier had high efficiency of 94.5% and proficient inductive connections up to 74.4% were used to transmit power and data to the embedded device. The embedded section which is exemplified by power recovery section comprises half wave voltage rectifier utilising low-leakage CMOS diodes rectifier, multi stage voltage reference to produce independent voltage 900mV and voltage regulator was utilised to offer low-power supply 1.8 DC voltage to power the embedded sensor. This design is simulated using electronic workbench MULISIM 11 and OrCAD PSpice 16.6 software. The design is suitable for embedded micro system device to invigorate the nerves and muscles.

REFERENCES

- Abbas, S. M., Hannan, M., & Salina, A. (2012). *Efficient Class-E design for inductive powering wireless biotelemetry applications*. Paper presented at the Biomedical Engineering (ICoBE), 2012 International Conference.
- Alghairi, M. K., Sulaiman, N. B., Sidek, R. B. M., & Mutashar, S. (2016). Optimization of Spiral Circular Coils for Bio-Implantable Micro-System Stimulator at 6.78 MHz ISM Band. *ARPN Journal of Engineering and Applied Sciences*, 11(11), 7046-7054.
- Asgarian, F., & Sodagar, A. M. (2009, 3-6 Sept. 2009). *A low-power noncoherent BPSK demodulator and clock recovery circuit for high-data-rate biomedical applications*. Paper presented at the Engineering in Medicine and Biology Society, 2009. EMBC 2009. Annual International Conference of the IEEE.
- Atluri, S., & Ghovanloo, M. (2007, 27-30 May 2007). *Incorporating Back Telemetry in a Full-Wave CMOS Rectifier for RFID and Biomedical Applications*. Paper presented at the Circuits and Systems, 2007. ISCAS 2007. IEEE International Symposium on.
- Chua-Chin, W., Ya-Hsin, H., Chio, U. F., & Yu-Tzu, H. (2004, 23-26 May 2004). *A C-less ASK demodulator for implantable neural interfacing chips*. Paper presented at the Circuits and Systems, 2004. ISCAS '04. Proceedings of the 2004 International Symposium on.
- Heidrich, J., Brenk, D., Essel, J., Heinrich, M., Jung, M., Hofer, G., . . . Fischer, G. (2010, 11-15 July 2010). *Design of a low-power voltage regulator for RFID applications*. Paper presented at the Computational Technologies in Electrical and Electronics Engineering (SIBIRCON), 2010 IEEE Region 8 International Conference on.
- Hoon-Kyeu, L., & Dong-Chul, P. (2000, 2000). *Bio-medical FM-FM-FSK radiotelemetry system for multi-signal transmission*. Paper presented at the Engineering in Medicine and Biology Society, 2000. Proceedings of the 22nd Annual International Conference of the IEEE.
- Jia, C., Chen, H., Liu, M., Zhang, C., & Wang, Z. (2008). Integrated power management circuit for piezoelectronic generator in wireless monitoring system of orthopaedic implants. *IET circuits, devices and systems*, 2(6), 485-494.
- Kazimierzczuk, M. K. (1986). Class E tuned power amplifier with nonsinusoidal output voltage. *Solid-State Circuits, IEEE Journal*, 21(4), 575-581. doi: 10.1109/JSSC.1986.1052574
- Mandal, S., & Sarpeshkar, R. (2008). Power-Efficient Impedance-Modulation Wireless Data Links for Biomedical Implants. *Biomedical Circuits and Systems, IEEE Transactions*, 2(4), 301-315. doi: 10.1109/TBCAS.2008.2005295
- Mutashar, S., Hannan, M. A., Samad, S. A., & Hussain, A. (2014). Analysis and Optimization of Spiral Circular Inductive Coupling Link for Bio-Implanted Applications on Air and within Human Tissue. *Sensors*, 14(7), 11522-11541.
- Mutashar, S., Hannan, M. A., Samad, S. A., & Hussain, A. (2014). Development of Bio-Implanted Micro-System with self-Recovery ASK Demodulator for Transcutaneous Application. *Journal of Mechanics in Medicine and Biology*, 14(04), 1450062. doi: doi:10.1142/S0219519414500626
- Noor, F., & Duffy, M. (2010, 23-24 June 2010). *Amplifier design for a biomedical inductive power system*. Paper presented at the Signals and Systems Conference (ISSC 2010), IET Irish.
- Rakers, P., Connell, L., Collins, T., & Russell, D. (2001). Secure contactless smartcard ASIC with DPA protection. *Solid-State Circuits, IEEE Journal*, 36(3), 559-565. doi: 10.1109/4.910496

- Sodagar, A. M., & Najafi, K. (2006). Extremely-wide-range supply-independent CMOS voltage references for telemetry-powering applications. *Analog Integrated Circuits and Signal Processing*, 46(3), 253-261.
- Sodagar, A. M., Wise, K. D., & Najafi, K. (2006, Nov. 29 2006-Dec. 1 2006). *An interface chip for power and bidirectional data telemetry in an implantable cochlear microsystem*. Paper presented at the Biomedical Circuits and Systems Conference, 2006. BioCAS 2006. IEEE.
- Suetsugu, T., & Kazimierczuk, M. K. (2004). Analysis and design of class E amplifier with shunt capacitance composed of nonlinear and linear capacitances. *Circuits and Systems I: Regular Papers, IEEE Transactionon*, 51(7), 1261-1268.
- Yi, J., Ki, W. H., & Tsui, C. Y. (2007). Analysis and Design Strategy of UHF Micro-Power CMOS Rectifiers for Micro-Sensor and RFID Applications. *IEEE Transactions on Circuits and Systems I: Regular Papers*, 54(1), 153-166. doi: 10.1109/TCSI.2006.887974





Weakest Bus Frequency Identification of Power System via TFDI

Athraa Iessa*, Noor Izzri Abdul Wahab* and Norman Mariun

Centre for Advanced Power and Energy Research (CAPER), Department of Electrical and Electronic Engineering, Universiti Putra Malaysia, 43400 UPM, Serdang, Selangor, Malaysia

ABSTRACT

One of the concerns in power system preventive control and security assessment is to find the point where the voltage and frequency collapse and when the system forces a severe disturbance. Identifying the weakest bus in a power system is an essential aspect of planning, optimising and post-event analysing procedures. This paper proposes an approach to identify the weakest bus from the frequency security viewpoint. The transient frequency deviation index for the individual buses is used as the weakest bus identification as well as a frequency security indicator. This approach will help to determine the bus with the worst deviation, which helps to analyse the system disturbance, takes proper control action to prevent frequency failure, and most importantly, observes consumer frequency. The approach is applied to the WSCC 9 bus test system to show the feasibility of the method.

Keywords: Power frequency stability, transient frequency, deviation index

INTRODUCTION

In recent years, the integration of various renewable resources has made power system control and protection complicated. When there is any change in the operation condition due to increased load demand, it results in

generator outage or in a natural fluctuation of the generating sources. Consequently, system voltage and frequency will experience a state of instability. The detection of the weakest point of the system where the voltage or frequency collapses is a vital aspect in studies related to power system security assessment.

There are several studies on the identification of the weakest bus based on voltage security. Kuhn-Tucker's theorem has a voltage stability indicator which helps to identify the weakest voltage bus or area. This indicator is comprehensive because it covers all marginal costs (Gau, 1994). Chen (1996), describes a method to identify the weak bus using voltage collapse proximity

ARTICLE INFO

Article history:

Received: 24 August 2016

Accepted: 03 Jun 2017

E-mail addresses:

athraa_aissa_2000@yahoo.com (Athraa Iessa),

izzri@upm.edu.my (Noor Izzri Abdul Wahab)

norman@upm.edu.my (Norman Mariun)

*Corresponding Author

indicator to install the VAR source and enhance the system security margin. A study of the power system's weak bus identification using model analysis, multivariable control, and SVD (Singular Value Decomposition) was conducted by (M. K. Jalboub, H. S. Rajamani, 1998). An easy method to locate the critical voltage bus using a basic power flow equation and KVL law was carried out by (Bhonsle, Deshpande & Renge, 2004).

The above studies are focused on voltage stability indices, effects of voltage stability control on system failure and blackouts. Despite the importance of understanding frequency behaviour for different bus systems as a result of integration of renewable energy resources, there are only a few studies that deal with identifying the weakest frequency bus. Such studies are essential for post-event analysis and for minimising the individual machine deviation when the system load is suddenly increased, or when outage occurs in the online units (Adibi & Fink, 2006).

The frequency deviation differs from one bus to another. Consequently, the frequency deviation has been used in several studies either to locate each electrical area established on both coherent generators and related non-generator buses (Khalil, Member, & Irvani, 2016) or for islanding control (Bevrani & Tikdari, n.d.).

This paper recommends the use of transient frequency deviation index (TFDI) for individual system buses. The TFDI is a good indicator for frequency stability to identify the worst deviation bus in the system. This approach will contribute effectively to the analysis of system disturbances, system partitioning into control areas, as well as observe consumer frequency. The rest of this paper is structured as follows: the concept of frequency stability is discussed in Section 2 while Section 3 presents the methodology. Section 4 discusses the simulation results while Section 5 provides the conclusions.

CONCEPT OF POWER SYSTEM FREQUENCY STABILITY

Frequency stability is the ability of a power system to withstand any credible disturbances and maintain a nominal operation frequency. Frequency stability depends on the ability of a power system to restore the balance of system generation with a minimum loss of load (Sun, H. D., Tang, Y., & M. A., n.d.). Frequency stability problems are related to insufficient reverse generation, inadequate protection and control devices, and the weakness in equipment responses.

Frequency stability may be short-term such as the rapid frequency deviation of the un-generated island when it is insufficient under frequency load shedding such that the island is experiencing a blackout within seconds (Kundur et al., 2004), or it may be a long-term stability with the time frame ranging from tenths of a second to few minutes. This phenomenon can be caused by controls of over speed steam turbine or boiler protection (Hatziaargyriou & Karapidakis, 1998; Chow, Kundur, & Acchione, n.d.). Frequency deviations can damage the equipment, degrade load performance, overload transmission lines, and interfere with system protection schemes. Moreover, the significant frequency deviation events can ultimately lead

to system collapse. Therefore, frequency stability assessment is essential for power system operation and control.

TRANSIENT FREQUENCY DEVIATION INDEX OF SYSTEM BUSES

In a power system, if any generation or part of a generation unit trips, the frequency will deviate from the nominal value. Likewise, if any load disconnects from the system, the latter will experience a high-frequency deviation. In other words, the frequency deviation can reflect system generation balance.

The frequency deviation is a good indicator of system stability. Most of the frequency security assessment studies used frequency deviation indices such as maximum frequency deviation index MDFI, total frequency deviation index FDI, and frequency security index FSI (Manuel, Alvarez, Mercado, & Member, 2007). However, although these indices can measure the rigorousness of disturbances in a particular time, they are incapable of measuring the effect of frequency deviation in a period. Additionally, they are unable to indicate the different frequency decay for various buses (consumer) (Dai, Xu, Dong, Wong, & Zhuang, 2012).

Therefore, TFDI was established by Zhang, Li and Liu (2015). The TFDI can be obtained from frequency response trajectory and two elements tables (f_{cr} , t_{cr}). The general formula for the index is:

$$\eta = \frac{S_d}{(f_N - f_{cr})t_{cr}} \quad (1)$$

$$S_d = \min \int_{t_s}^{t_s+t_{cr}} (f - f_{cr}) dt \quad (2)$$

where:

S_d = the minimum area surrounded by the frequency response curve and the critical frequency (f_{cr}) in within critical time (t_{cr}). f_N = standard frequency of the system, f_{cr} = frequency deviation threshold, t_{cr} = the acceptable duration for frequency deviation for going beyond f_{cr} , t_s = starting time of statement window.

According to (Zhang et al., 2015) the determination of TFDI depends on S_d , which also depends on the relation between the frequency trajectory, the critical system frequency, critical system time, and the break time as follows:

- 1) If there is no intersection between the frequency response trajectory and the line of critical frequency $f=f_{cr}$, and the break time is zero $t_b=0$ (figure. 1a), then the TFDI will be:

$$\eta = \frac{S_1}{(f_N - f_{cr})t_{cr}} \quad (1a)$$

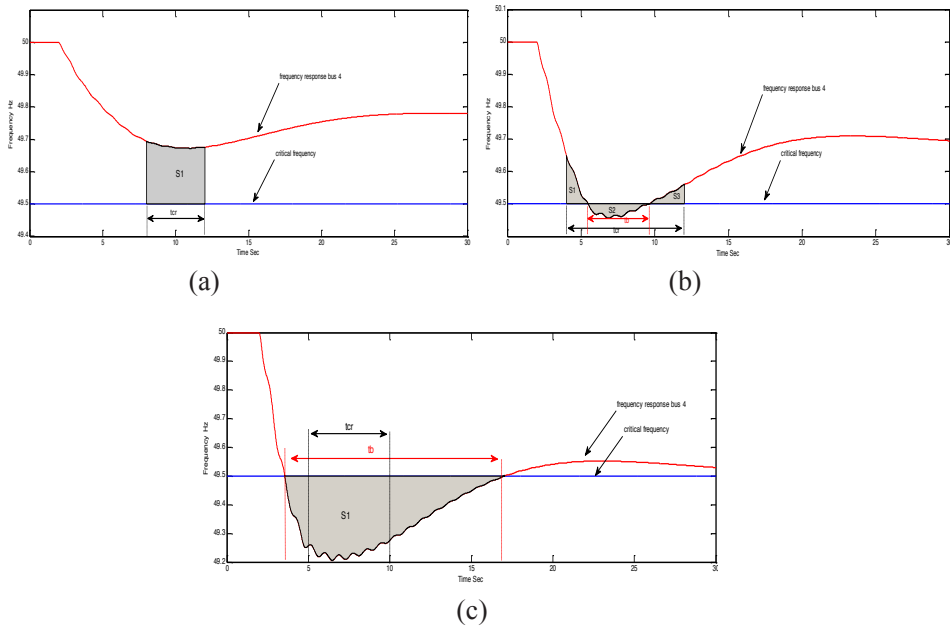


Figure 1. S_d determination (a) when $t_b=0$, (b) when $0 < t_b < t_{cr}$, (c) when $t_b > t_{cr}$

- 2) If there is an intersection between the frequency response and the critical frequency line, and, the break time t_b is less than t_{cr} (figure 1b) , the TFDI will be:

$$\eta = \frac{S_1 + S_3 - S_2}{(f_N - f_{cr})t_{cr}} \tag{1b}$$

- 3) If there is an intersection between the frequency response and the critical frequency line, and, the break time t_b is greater than t_{cr} (figure 1c), the TFDI will be:

$$\eta = \frac{-S_2}{(f_N - f_{cr})t_{cr}} \tag{1c}$$

The TFDI has the ability to evaluate the frequency security of individual buses (consumers), especially when the system withstands large disturbances such as 3-phase fault at any system buses or lines. Therefore, TFDI can be used to find the weakest or unstable bus from the frequency security viewpoint. The bus with the smallest TFDI is the worst deviation bus.

PROPOSED METHODOLOGY

The methodology to locate the TFDI for individual buses, and then to decide the wind turbine location is shown in Figure 3.

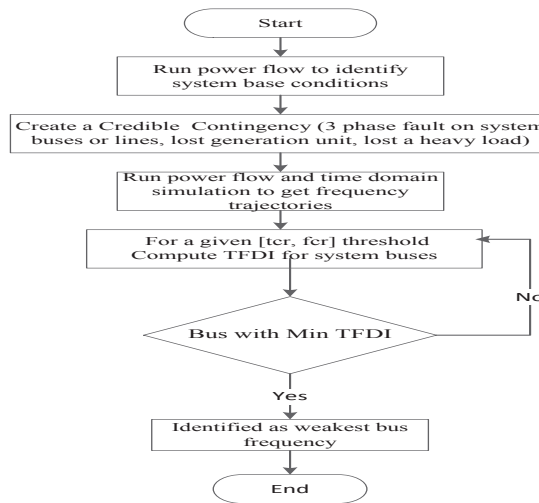


Figure 2. Flowchart of identifying weak bus frequency

SIMULATION RESULTS AND DISCUSSION:

The test system to be used for this simulation is the IEEE 9-bus, 3-machine test system shown in Figure 4. System data are given in (Ahmadi & Ghasemi, 2012). After running a power flow in order to identify the base operation conditions of the system, full-time domain simulations are applied with different contingencies. The results show that the frequencies of various buses are not the same. Therefore, the TFDI of buses is also different. Figure 5 below shows the frequency response of system buses for a 3-phase fault at bus 2. It is obvious from this plot that the responses are not similar. Consequently, the TFDI of system buses will be different.

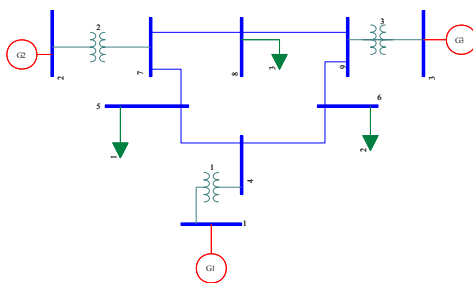


Figure 3. IEEE 9-bus test system

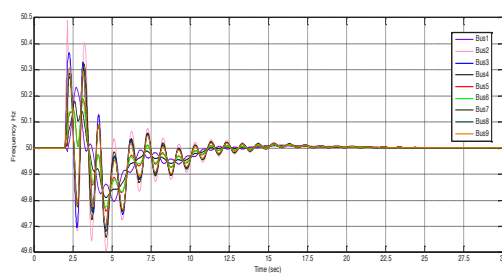


Figure 4. Frequency response of system buses for 3-phase fault at bus 2_r

The TFDI of each bus is calculated. Figures 6, 7 and 8 show the TFDI of each bus with bus numbers for different cases. It can be seen clearly from the results that we get approximately the same pattern for all cases. It can be observed that bus 2, 5 and bus 7 are the lowest TFDI buses. Thus, these buses can be mentioned as the weakest buses frequency of the system. Since

bus 5 is the lowest TFDI among all load buses it can be selected as wind power integration bus to assess perfectly the maximum wind power penetration level. These results seem to be consistent with other studies which chose bus 5 as wind farm integration bus (Ahmadi & Ghasemi, 2012).

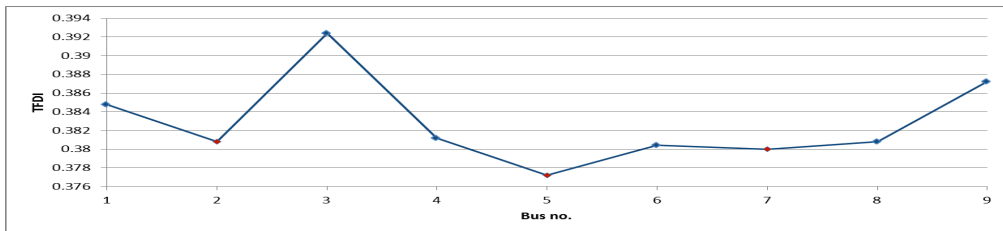


Figure 5. TFDI with bus no. for 3-phase fault at bus 7

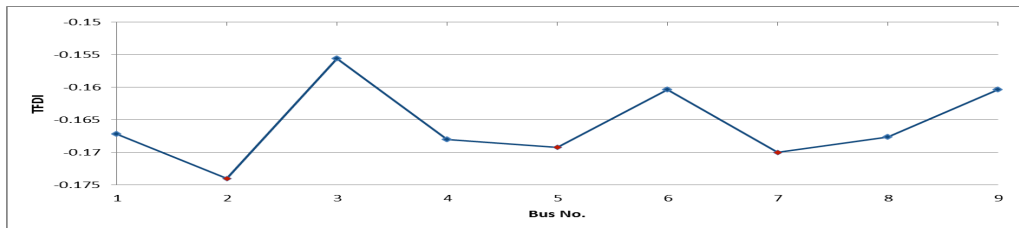


Figure 6. TFDI with bus 3-phase fault on line 4

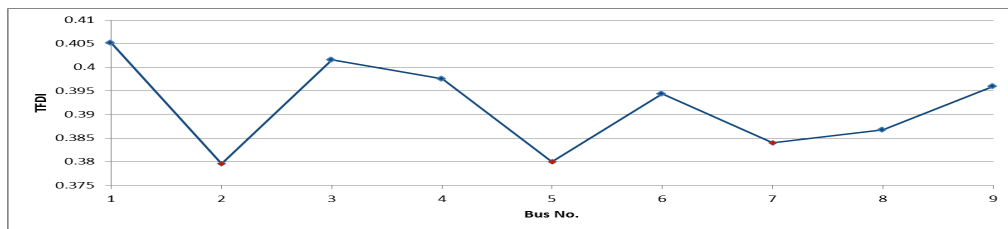


Figure 7. TFDI with bus 3phase fault at bus 2

CONCLUSION

For economic load shedding protection design, it is necessary to evaluate the frequency instability. The first step to evaluate this instability is to find the severity of frequency deviation. Another important aspect of power system frequency stability is to observe the frequency decay for different buses (consumers). There is a need to find the weak frequency points of the network to select the wind turbine integration bus to estimate the maximum allowable wind power level accurately according to the impact of this turbine on system frequency.

The main aim of this study is to show the ability of TFDI to evaluate the frequency stability for different system buses. The study also suggests an approach to find the most suitable bus

for locating the load shedding schemes and for observing the frequency of customers. The feasibility of the proposed approach has been achieved on IEEE 9- bus test system.

Determining the critical level of variable renewable resources penetration while considering the system's frequency limits can be explored in future research.

ACKNOWLEDGMENT

The authors are grateful for the support provided by the Centre for Advanced Power and Energy Research, Department of Electrical and Electronic Engineering within the Faculty of Engineering, University Putra Malaysia.

REFERENCES

- Adibi, M. M., & Fink, L. H. (2006). Restoration from cascading failures. *IEEE Power and Energy Magazine*, 4(5), 68–77. <http://doi.org/10.1109/MPAE.2006.1687819>
- Ahmadi, H., & Ghasemi, H. (2012). Maximum penetration level of wind generation considering power system security limits. *IET Generation, Transmission & Distribution*, 6(11), 1164–1170. <http://doi.org/10.1049/iet-gtd.2012.0015>
- Alvarez, J. M. G., & Mercado, P. E. (2007). Online inference of the dynamic security level of power systems using fuzzy techniques. *IEEE transactions on Power Systems*, 22(2), 717-726.
- Bevrani, H., Hiyama, T., & Tikdari, A. (2009, January). On the necessity of considering both voltage and frequency in effective load shedding schemes. In *IEEJ Technical Meeting*.
- Chen, Y. (1996). Weak Bus-Oriented Optimal Multi-objective VAR Planning. *IEEE Transactions on Power Systems*, 11(4), 1885–1890.
- Chou, Q. B., Kundur, P., Acchione, P. N., & Lautsch, B. (1989). Improving nuclear generating station response for electrical grid islanding. *IEEE Transactions on Energy Conversion*, 4(3), 406-413.
- Dai, Y., Xu, Y., Dong, Z. Y., Wong, K. P., & Zhuang, L. (2012). Real-time prediction of event-driven load shedding for frequency stability enhancement of power systems. *IET Generation, Transmission and Distribution*, 6(9), 914. <http://doi.org/10.1049/iet-gtd.2011.0810>
- Gau, H. (1994). weakest bus / area in power systems. *IEE*, 1994, 305–309.
- Hatziaargyriou, N., Karapidakis, E., & Hatzifotis, D. (1998, August). Frequency stability of power systems in large islands with high wind power penetration. In *Bulk Power Syst. Dynamics Control Symp.—IV Restructuring* (Vol. 102).
- Huadong, S., Yong, T., & Shiyang, M. (2006). A commentary on definition and classification of power system stability. *Power System Technology-Beijing-*, 30(17), 31.
- Jalboub, M. K., Rajamani, H. S., R. A. A.-A. and A. M. I. (1998). Weakest Bus Identification Based on Modal Analysis and Singular Value Decomposition Techniques. *IEEE transactions on Power Systems*, 39(6), 0–22. <http://doi.org/10.1093/bjsw/bcs140>.
- Khalil, A. M., & Irvani, R. (2016). A Dynamic Coherency Identification Method Based on Frequency Deviation Signals. *IEEE Transactions on Power Systems*, 31(3), 1779-1787.

- Kundur, P. (1981). A survey of utility experience with power plant response during partial load rejection and system disturbances. *IEEE Transactions on Power Apparatus and Systems*, 5(PAS-100), 2471-2475.
- Kundur, P., Paserba, J., Ajarapu, V., Andersson, G., Bose, A., Canizares, C., ... Vittal, V. (2004). Definition and Classification of Power System Stability. *IEEE Transactions on Power Systems*, 19(2), 1387–1401. <http://doi.org/10.1109/TPWRS.2004.825981>
- Jalboub, M. K., Rajamani H. S., Abd-Alhameed, R. A., & Ithal, A. M. Weakest Bus Identification based on Model Analysis and Singular Value Decomposition Techniques. *IEEE transaction on Power Systems*, 39(6), 0-22.
- Ms.J.S.Bhonsle, S.B.Deshpande, M.M.Renge, M. R. H. (2004). *A New Approach for Determining Weakest Bus and Voltage Stability Margine in A Power System*. National Power System Conference, NPSC.
- Zhang, H., Li, C., & Liu, Y. (2015). Quantitative frequency security assessment method considering cumulative effect and its applications in frequency control. *International Journal of Electrical Power and Energy Systems*, 65, 12–20. <http://doi.org/10.1016/j.ijepes.2014.09.027>



An FFT Computation Minimisation for an FPGA-Based MCSA while Preserving Frequency Resolution

Marut Raksa*, Thanaporn Likitjarernkul, Kiattisak Sengchuai, Nattha Jindapetch and Krerkchai Thongnoo

Department of Electrical Engineering, Faculty of Engineering, Prince of Songkla University, Hat Yai, Songkhla 90112, Thailand

ABSTRACT

This paper presents an FFT computation minimisation for Motor Current Signature Analysis (MCSA) by reducing sampling frequencies and input data samples. The frequency resolution of an FFT signal depends on the FFT length and the sampling frequency. A diagnosis of the induction motor stator winding short turn using the FFT-based MCSA has shown the performance of various FFT lengths. Preserving frequency resolution is achieved by keeping the same ratio of the sampling frequency to the FFT length. From the experimental results, the FFT length can be decreased from 64K to 8K, 1K, and 512 points respectively. All FFT processors were implemented with Xilinx Spartan-6 FPGA to compare the resource, the speed, and the power consumption. The FPGA implementation of the 512-point FFT achieved BRAM saving of 97 %, slice saving of 26%, power consumption saving of 20% and speed up to 187 times compared with the 64K-point FFT. Although the processing gain of the 512-point FFT is 24 dB and decreased from 48.1 dB in the case of the 64K-point FFT, it is enough to classify the short turn fault.

Keywords: FFT; MCSA; Sampling Frequency; Computation Reduction; FPGA

ARTICLE INFO

Article history:

Received: 24 August 2016

Accepted: 03 Jun 2017

E-mail addresses:

marut.r@rmutsv.ac.th (Marut Raksa),

l.thanapond@gmail.com (Thanaporn Likitjarernkul),

ak.kiattisak@hotmail.com (Kiattisak Sengchuai),

nattha.s@psu.ac.th (Nattha Jindapetch),

krerkchai.t@psu.ac.th (Krerckchai Thongnoo)

*Corresponding Author

INTRODUCTION

Fast Fourier Transform (FFT) is widely used in many digital signal processing and communications applications. Especially, the FFT-based MCSA is also effectively used for monitoring failure of induction motors from current signals (Cabal-Yepez, Osornio-Rios, Romero-Troncoso, Razo-Hernandez, & Lopez-Garcia, 2009). The MCSA diagnosis systems have the advantage of easy detection in induction motors. Rangel-Magdaleno, Peregrina-Barreto, Ramirez-Cortes, Gomez-

Gil, & Morales-Caporal.(2014) had proposed a broken bars fault detection of the induction motor, and the method has been implemented in an FPGA to be used in real-time. FPGA-based MCSA implementation is limited by memory for storing input data samples (Pineda-Sanchez et al., 2013). The MCSA needs high-frequency resolution for analysis of the slip frequency neighbouring harmonic frequency (Panigrahy, Konar, and Chattopadhyay, 2014). The slip frequency and the low amplitude of the current spectrum components are related to the fault (Zouzou, Sahraoui, Ghoggal, & Guedidi, 2010). In addition to this, if the induction machine runs on short turn conditions, the amplitude of slip frequencies which depend on the value of the currents, provides very low signal to noise ratio. The simplest way for solving the problem is to use a high-gain FFT processor (Iglesias, Grajal, Sánchez, & López-Vallejo, 2015).

However, a high-gain FFT processor and a high-resolution FFT need long FFT length, which suffers from long computation time and resources as well as power consumption. The FFT length is the number of samples of motor current signals that depend on the sampling frequency and the time that is used to collect the signals. Higher sampling frequency gives a large number of samples. Consequently, a large number of the sample requires a large FFT length processor.

This paper proposes a minimisation of FFT processing by reducing the sampling frequency and input data samples on motor current signature analysis. The frequency resolution is preserved by keeping the same ratio of the sampling frequency to the FFT length. The FPGA implementations of 64K, 8K, 1K, and 512 points-FFT processors for an MCSA diagnosis of the induction motor stator winding short turn have been demonstrated to show reduction in terms of area, speed, and power consumption.

This paper is organised as follows: The first section introduces FFT, while subsequent sections discuss MCSA spectrum measurement, experimental setup, FPGA implementation and results respectively. The final section is the conclusion.

Nomenclature	
N	Size of FFT
X(k)	The FFT output data
n	Integer Number (1, 2, 3...)
K	Odd Harmonic Order
f	Fundamental Frequency (50 HZ)
f_s	Sampling Frequency
f_r	FFT Frequency Resolution
f_{st}	Slip Frequency

FAST FOURIER TRANSFORM

The Fast Fourier Transform provides a divide and conquer method to estimate the Discrete Fourier Transform (DFT) algorithm. The FFT is an efficient algorithm for computing the DFT. In computing, time for a DFT depends on the number of multiplications and input data N

points. The DFT requires N^2 multiplications whereas FFT requires only $N \log_2(N)$. The FFT algorithm is the realisation that a DFT of a sequence of N points can be written in odd and even of length $N/2$. Using the symmetric property of the twiddle factor, (1) can be rewritten to (2), and we can save a lot of computation.

$$X[k] = \sum_{n=0}^{N-1} x[n] e^{-j\left(\frac{2\pi k}{N}\right)n}, k = 0, 1, \dots, N-1, \tag{1}$$

$$X[k] = \sum_{\substack{n=0 \\ \text{even } n}}^{N-1} x[n] e^{-j\left(\frac{2\pi k}{N}\right)n} + \sum_{\substack{n=0 \\ \text{odd } n}}^{N-1} x[n] e^{-j\left(\frac{2\pi k}{N}\right)n} \tag{2}$$

when N is a power of two, and $x(n)$ is an input, $k=0, 1 \dots N-1, f_s$ is a sampling frequency. The frequency resolution of the N -point FFT is determined by (3).

$$f_r = \frac{f_s}{N} \tag{3}$$

The FFT processing gain represents the signal to noise level and can be calculated by (4).

$$FFT_{gain}[dB] = 10 \log\left(\frac{N}{2}\right) \tag{4}$$

The signal to noise in an FFT is low when N is reduced. This affects the measurement of low harmonic signals, such as the frequency of the component of interest or noise.

Nyquist Frequency

The Nyquist frequency is the FFT bandwidth of a sampled signal and is equal to half the sampling frequency of that signal. The sampling frequency is the frequency of the signal at any time. Digital signals must be converted to maximum frequency of the signal frequencies. If the sampling frequency is less than the Nyquist frequency, it will result in signal loss. The FFT bandwidth is defined by (5).

$$FFT_{BW} = \left(\frac{f_s}{2}\right) \tag{5}$$

A suitable N may be selected based on the desired frequency resolution, but it may be impossible to implement on a DSP device. The frequency resolution can be explained as the lowest frequency of the signal that can be described by the FFT, and is given certain as the sampling frequency divided by N (3). Table 1 shows the frequency resolution comparison with different sampling frequencies. The sampling frequency increases from 1 kHz, 5 kHz, and 10 kHz. The FFT frequency resolution is dependent on the sampling frequency of the input signals. For Table2, the sampling frequency of the signal is 1 kHz

It is important to note that at a sampling frequency, increasing the frequency resolution decreases time resolution. That is more accurate in measuring the frequency domain, and less accurate for the time domain. We lose all time information inside the FFT length.

Table 1
Frequency resolution comparison with difference sampling frequency

Sampling Frequency (Fs)	Samples (N)	Data collect time (Sec.)	bins(Fs/N)(Hz)
1kHz	1000	1	1
5kHz	1000	0.5	5
10kHz	1000	0.1	10

Table 2
Frequency resolution comparison with difference sample (N)

Sampling Frequency (Fs)	Samples (N)	Data collect time (Sec.)	bins (Fs/N)(Hz)
6kHz	1000	0.6	6
6kHz	6000	1	1
6kHz	60,000	10	0.1

THE MCSA SPECTRUM MEASUREMENT

The following example illustrates some of the practical issues of signal spectrum frequency measurements. Figure 1 shows the amplitude spectrum of an MCSA signal that has many frequency components. The frequency of the component of interest range is $f_{st\ min}$ to $f_{st\ max}$.

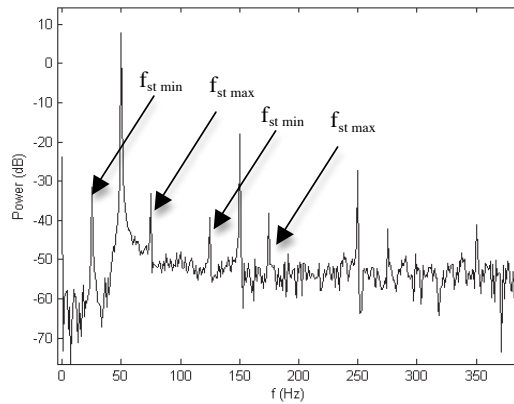


Figure 1. Motor Signature Current (shorted-turn) spectrum frequency

The MCSA is an online tool to detect the fault of stator current and it can detect many faults in the motor such as rotor faults, short turn, bearing faults, and lubrication loss. The frequency spectrum of the MCSA is used to classify the characteristics of short-turn stator faults. The frequency of the induction motor stator winding short turn fault can be calculated by (6).

$$f_{st} = f \left[\frac{n}{p}(1-s) \pm k \right] \tag{6}$$

when Nf is a fundamental frequency, k is a harmonic order, p is pole-pairs and s is a slip of the motor. The stator current signals can be selected to the FFT to extract the frequency components. Each healthy motor gives a certain signature and this signature is affected when faults exist inside the motor. Healthy motors present signature changes when the faults within the motor occur.

EXPERIMENTAL SETUP

In this section, MCSA experimental setup for an induction motor running as a short turn fault is shown in Figure 2. Amplitudes shown in this section are calculated using the frequencies determined by (6). Figure 2 shows the general block diagram of MCSA. The current in the stator of the induction motor is sensed by CTs (Current Transformer), sent to the signal converter, and saved in the data collector. Finally, the computer program identifies the condition of the motor. Its main purpose is to monitor the current of the three-phase stator. The analog signal is given to analog to a digital (A/D) converter. The current is sampled by the A/D converter at the predetermined sampling frequency. This is continued for a sampling period which is sufficient to achieve the required FFT.

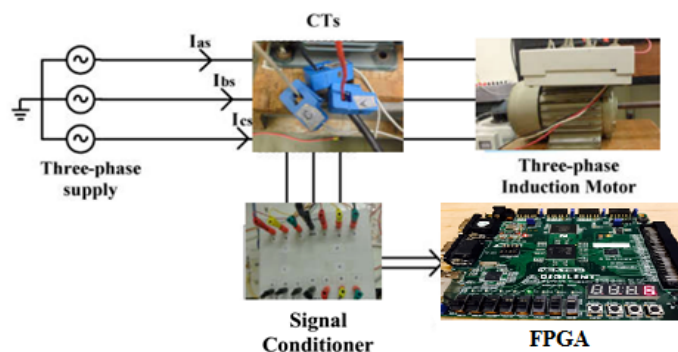


Figure 2. The FPGA based MCSA block diagram

RESULTS AND DISCUSSIONS

From the MCSA as described in the previous section, the values of motor currents are used to perform the FFT and find out the composite harmonics. The motor condition analysis was performed using MATLAB software. The FFT defines harmonic frequency components for an interesting range of magnitudes in different conditions of the motor health. Figure 3 shows the current waveform and the harmonic frequency spectrum of a healthy motor at no load condition.

The current spectrum of the induction motor at the no load condition is shown in Figure 4. In no load scenarios, a speed of the induction motor is 1,495 rpm. When synchronous speed is 1,500 rpm and $s = 0.003$, the slip frequency calculation from (6) is 25 Hz, 75 Hz, 125 Hz and 175 Hz. In full load scenarios, speed of the induction motor is 1,380 rpm and $s = 0.008$. Then the slip frequency is 27 Hz, 73 Hz, 127 Hz and 173 Hz. The current spectrums of the induction motor from no load and full load scenarios are shown in Figure 5.

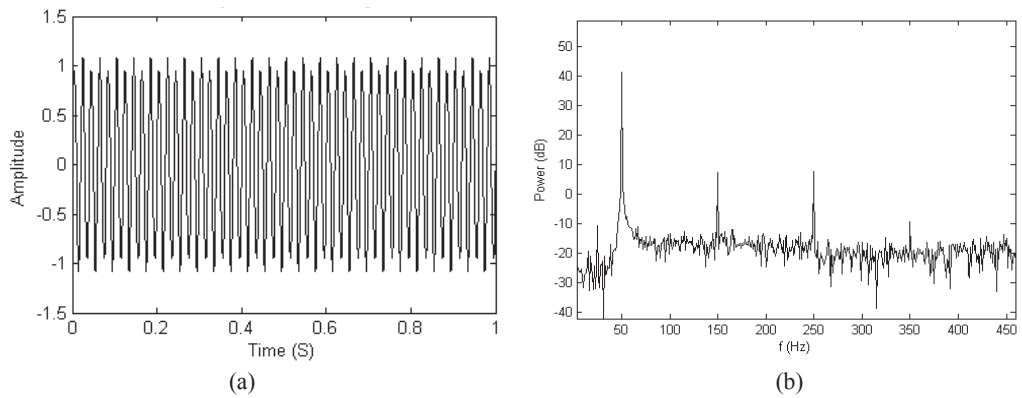


Figure 3. Healthy motor current signal (a) current signal; (b) current spectrum

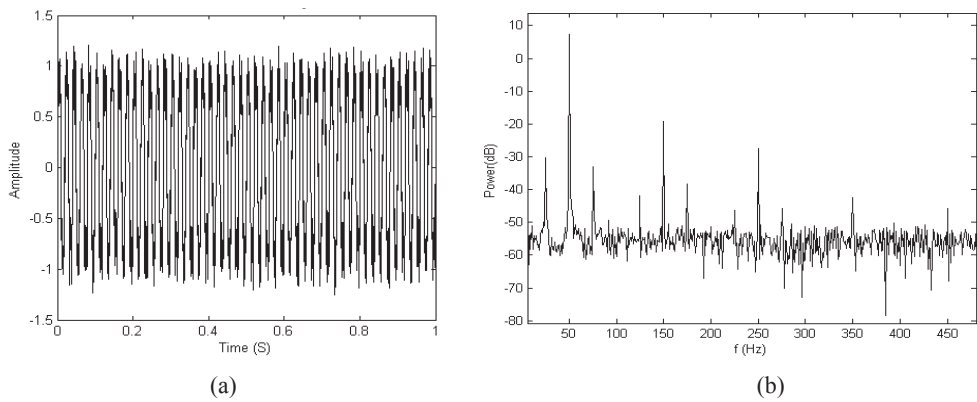


Figure 4. Short turn fault motor current signal (a) current signal ; (b) current spectrum

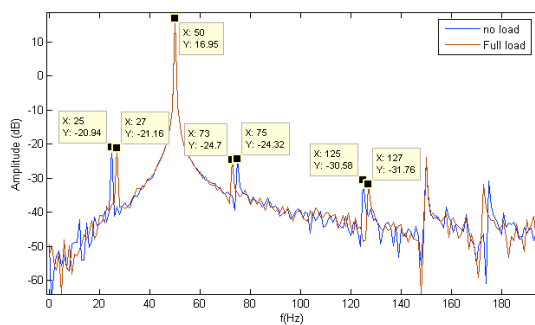


Figure 5. Full load and no load short turn fault current spectrum

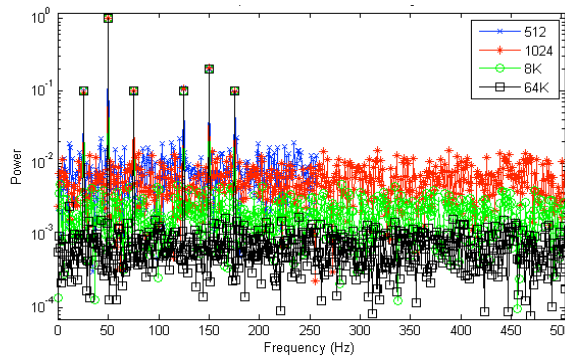


Figure 6. Difference output FFT N= 512, 1k, 8k and 64k from short turn fault motor current signal

Figure 6 shows the current waveform and frequency spectrum of the motor with stator fault (10 turns shorted) at no load condition with FFT N = 512, 1k, 8k, and 64k. The frequency spectrum of the interest range is compared in terms of its length. Observe that FFT N=512 and 64K is different in the signal to noise level. The processing gain of the 512-point FFT is 24 dB, decreased from 48.1 dB in the case of the 64K-point FFT.

FPGA IMPLEMENTATIONS OF FFT

We present four different lengths of FFT processors which apply the radix-2 architecture. The Xilinx System Generator (XSG), which is a high-level graphical programming tool, was used to design a DSP system with the MATLAB Simulink software. The FPGA-based implementations of various FFT processors are summarised in Table 3.

Table 3
A comparison of implementation results using different FFT sizes

FFT size (N)	slice	FFs	BRAMs	LUT	Latency (Clock Cycle)	Power (mW)
512	621	2,734	4	2,010	3,487	36
1,024	979	2,819	6	2,035	7,334	89
8,192	1,284	3,332	34	2,549	96,846	126
65,536	2,358	3,645	244	3,188	655,622	175

All FFT processors were implemented with a Xilinx Spartan-6 FPGA to compare the resource, speed, and power consumption. The FPGA implementation of the 512-point FFT achieved BRAM saving of 97%, slice saving of 26%, FFs saving of 25%, LUT saving of 37%, a power consumption saving of 20% and speed up to 187 times compared with the 64K-point FFT. An FPGA-based can detect short turn fault with different load conditions using MCSA.

CONCLUSION

This paper has discussed an FFT computation minimisation for an FPFA-based MCSA while preserving frequency resolution. It compared frequency spectrum amplitude of outputs with different FFT lengths. The frequency resolution of an FFT signal is dependent on FFT length and sampling frequency. Frequency resolution is preserved by keeping the same ratio of the sampling frequency to the FFT length. Finally, experimental results show the FPGA implementations of the FFT with different lengths. The area, speed and power consumption of the FFT processor depend on the FFT length. The FFT processor gains depend on the FFT length. In this case-study, the 512-point FFT is enough to classify the motor with stator short turn fault.

ACKNOWLEDGEMENT

This work received financial support from the Prince of Songkla University Graduate Studies Grant No. PSU/95000201/2554, Prince of Songkla University (ENG560014S) as well as Center of Excellence in Wireless Sensor Networks (CoE-WSN), Faculty of Engineering, Prince of Songkla University, Hat Yai, Songkhla, Thailand.

REFERENCES

- Cabal-Yepez, E., Osornio-Rios, R. A., Romero-Troncoso, R. J., Razo-Hernandez, J. R., & Lopez-Garcia, R. (2009, December). FPGA-based online induction motor multiple-fault detection with fused FFT and wavelet analysis. In *2009 International Conference on Reconfigurable Computing and FPGAs* (pp. 101-106). IEEE.
- Iglesias, V., Grajal, J., Sánchez, M. A., & López-Vallejo, M. (2015). Implementation of a Real-Time Spectrum Analyzer on FPGA Platforms. *IEEE Transactions on Instrumentation and Measurement*, *64*(2), 338–355.
- Panigrahy, P. S., Konar, P., & Chattopadhyay, P. (2014). Broken bar fault detection using fused DWT-FFT in FPGA platform. In *2014 International Conference on Power, Control and Embedded Systems (ICPCES)* (pp. 1–6).
- Pineda-Sanchez, M., Perez-Cruz, J., Roger-Folch, J., Riera-Guasp, M., Sapena-Baño, A., & Puche-Panadero, R. (2013). Diagnosis of induction motor faults using a DSP and advanced demodulation techniques. In *2013 9th IEEE International Symposium on Diagnostics for Electric Machines, Power Electronics and Drives (SDEMPED)* (pp. 69–76).
- Rangel-Magdaleno, J. de J., Peregrina-Barreto, H., Ramirez-Cortes, J. M., Gomez-Gil, P., & Morales-Caporal, R. (2014). FPGA-Based Broken Bars Detection on Induction Motors Under Different Load Using Motor Current Signature Analysis and Mathematical Morphology. *IEEE Transactions on Instrumentation and Measurement*, *63*(5), 1032–1040.
- Zouzou, S. E., Sahraoui, M., Ghoggal, A., & Guedidi, S. (2010). Detection of inter-turn short-circuit and broken rotor bars in induction motors using the Partial Relative Indexes: Application on the MCSA. In *2010 XIX International Conference on Electrical Machines (ICEM)* (pp. 1–6).



Auto-Grasping Algorithm of Robot Gripper Based on Pressure Sensor Measurement

Ahmed M. M. Almassri^{1,2*}, Chikamune Wada², W. Z. Wan Hasan¹
and S. A. Ahmad¹

¹Department of Electrical and Electronic Engineering, Faculty of Engineering, Universiti Putra Malaysia, 43400 Serdang, Selangor, Malaysia

²Graduate School of Life Science and Systems Engineering, Kyushu Institute of Technology, 2-4 Hibikino, Wakamatsu-ku, Kitakyushu 808-0196, Japan

ABSTRACT

This paper presents an auto grasping algorithm of a proposed robotic gripper. The purpose is to enhance the grasping mechanism of the gripper. Earlier studies have introduced various methods to enhance the grasping mechanism, but most of the works have not looked at the weight measurement method. Thus, with this algorithm, the weight of the object is calculated based on modified Wheatstone Bridge Circuit (WBC) which is controlled by programmable interface controller (PIC) method. Having this approach introduces and improves the grasping mechanism through an auto grasping algorithm. Experimental results show that an auto grasping algorithm based on pressure sensor measurements leads to a more precise grasping measurement and consequently enhance the sensitivity measurement as well as accurate movement calibration. Furthermore, several different grasping objects based on the proposed method are examined to demonstrate the performance and robustness of our approach.

Keywords: Auto grasping algorithm; pressure sensor; grasping mechanism; Wheatstone bridge circuit

ARTICLE INFO

Article history:

Received: 24 August 2016

Accepted: 03 Jun 2017

E-mail addresses:

eng.ahmed8989@gmail.com (Ahmed M. M. Almassri),

wada@brain.kyutech.ac.jp (Chikamune Wada),

wanzuha@upm.edu.my (W. Z. Wan Hasan),

sanom@upm.edu.my (S. A. Ahmad)

*Corresponding Author

INTRODUCTION

Human beings have long recognised the importance of robots, especially the robotic manipulators such as robotic hand or robotic gripper. Robotic grippers have become important to grasp objects, perform tasks or even emulating the human hand (Almassri et al., 2015). Robotic hands and grippers have been used for various purposes such as dexterous manipulation (Rodriguez et al., 2014), artificial limbs (Lee et al., 2008),

grasping objects (Lippiello et al., 2013), rehabilitation application (Iqbal et al., 2010) and pick and place application (Almassri et al., 2013). Some of these applications require manual labour for assembly line and material handling. Therefore, there is a need to have a dedicated machine, which is suitable for such applications taking into consideration safety issues.

However, the current issue of robotics system is to have a secure grasp during the robotic grasping operation (Pokorny et al., 2013). In addition, auto grasping algorithm remains an open and difficult problem. In order to synthesise sequences of actions to perfectly solve a complicated task, automatic calibration is important for a secure grasp and control to execute the calibration movement (Righetti et al., 2014). Examples of good grasps can be found in (Bicchi & Kumar, 2000) and (Bohg et al., 2014). In (Righetti et al., 2014), a good grasp using humans were demonstrated. The weight measurement method based on WBC was introduced by Almassri et al. (2015) that explains the optimisation of grasping object based on pressure sensor measurement for a robotic hand gripper. From that point of view, it seems natural to create an algorithm that shows the nature of grasping and manipulating objects.

A new auto grasping algorithm based on pressure sensor is hence proposed to introduce a grasping mechanism. This paper introduces a PIC control algorithm to improve a movement calibration through the grasping operation. In order to apply an auto grasping algorithm, we design and propose a robotic gripper prototype with a new configuration of pressure sensor distribution based on modified Wheatstone Bridge Circuit (WBC) as it has a high sensitivity as well as capability for grasping mechanism and weight measurement.

ROBOTIC GRIPPER SYSTEM BASED ON AUTO-GRASPING ALGORITHM

In order to fulfil an auto grasping algorithm using a robotic gripper based on pressure sensor the researcher design and propose a gripper prototype while a software PIC algorithm control based on Flexiforce pressure sensors was used for grasping and measurement purposes. These three stages are shown in the block diagram in Figure 1. The input is the object which is detected automatically using Infrared Sensor (IR). Subsequently, a modified Wheatstone Bridge Circuit (WBC) is applied to investigate the pressure distribution and measure the output. The analog readout circuit has been designed and utilised to adjust the sensor signals to be compatible with the requirements of the subsequent system and to provide a voltage supply to the whole system as shown in the figure below. The controller part (the red colour of the block diagram) is useful for grasping mechanism after detecting the object. This mechanism is based on proposed grasping algorithm that is applied based on a PIC controller for signal conditioning of multiple sensors output points simultaneously. The output part, which is grasping the object effectively and measuring its weight then, displays the measured output on LCD. A servo motor with driver circuit is selected for this purpose to be incorporated into the system. In addition, a feedback closed loop system is used during the grasping mechanism to insure the secure grasp and to control the calibration.

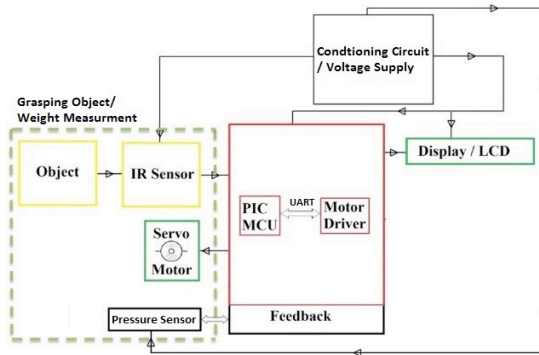


Figure 1. Block diagram of the robotic gripper based on proposed auto-grasping algorithm

Robotic gripper prototype

The function of the proposed robotic gripper prototype is to grasp the solid object effectively. Figure 2 illustrates the robotic gripper prototype from different sides. It consists of: Pressure Sensor¹, Claw², Frame³, Base⁴, Carrier⁵ and DC Servo Motor⁶ as arranged in (a) respectively. The robotic gripper prototype is equipped with two types of sensors, including IR sensor for automatic grasp purpose as well as pressure sensor for the purpose of measuring the pressure forces. A front view as shown in (b) indicates how the robotic gripper grasp a rectangular solid object automatically. The four pressure sensors are assembled and arranged on the left and right claw of the prototype robotic gripper based on modified WBC as shown in (c). The gripper's surface is covered with a thin, double-sided tape in which the distributed pressure sensors are placed under it. All these conditions are significantly important for the operation of the current robotic gripper prototype.

In this study, a new method of modified WBC is used to enhance the pressure measurement and increase sensitivity output of the pressure sensor. Based on the traditional method as presented in (Ahmed M ALmassri et al., 2014), the sensitivity output of the pressure sensor still needs to be increased. Therefore, our proposed modified WBC has investigated the sensitivity output of the pressure sensors as shown in Figure 3. It comprises four resistors and two of them are changing resistance and represented by pressure sensors (Ps1, Ps2) while the

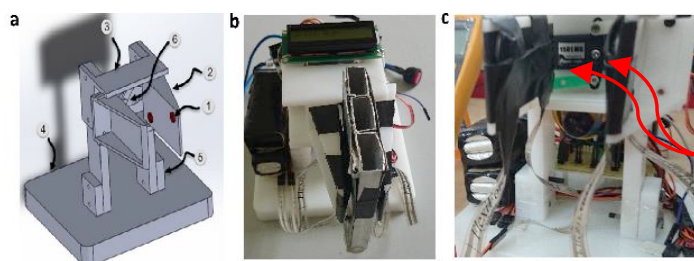


Figure 2. (a) The parts of the proposed robotic gripper; (b) front view of grasping a rectangular object; (c) pressure sensors distribution left view

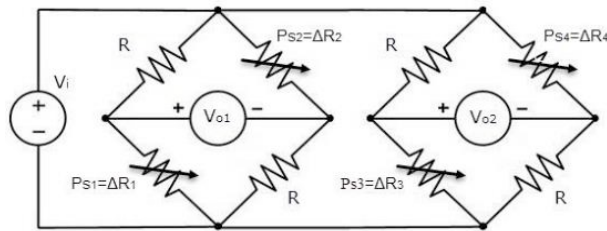


Figure 3. Schematic diagram of the proposed modified WBC

other two are constant (R). The main advantage of this proposed circuit compared with using a single and simple construction is that some of the error sources cancel each other out due to the symmetry of the circuit. Furthermore, any changes in any one of the pressure sensors will cause a change in the output voltage (V_o) as seen in equation 1. These voltages can be conditioned and transmitted for data calibration purpose. Those advantages enhance the output force measurement and increase the sensitivity output by eliminating the error. In addition, the active pressure sensors (Ps_1 , Ps_2) are assembled in front of each other in the circuit as well as in the claw of the prototype robotic gripper to insure and observe any changing of the pressure forces in both sides either in the robotic claw or detected object. Thus, sensitivity will be increased and measured output data will be enhanced.

$$V_o = V_{o1} + V_{o2} \tag{1}$$

Where V_o is the total output voltage of the modified Wheatstone bridge circuit, V_{o1} and V_{o2} is the output voltage of the modified WBC individually.

Control system

The control system of a robot gripper has been developed and investigated for different applications. The robot gripper executes a particular task of grasping the object. Nevertheless, the weight measurement method which grasps objects based on auto-grasping algorithm has not been created yet for the current robotic gripper applications. Thus, in order to fulfil the auto-grasping mechanism effectively, the control system must be executed. The feedback control is also important in this process to ensure accuracy and stability of the measurement and grasping respectively. The pressure sensor is essential to measure the interface pressure between the claw of robotic gripper and the object whereby it is useful to measure the exact weight of the object as well as the feedback of the entire system. Figure 4 shows the block diagram of the feedback system for grasping mechanism. The position of servo motor also plays a significant role in this mechanism. This position is considered as reference to execute the grasping as well as its completion.

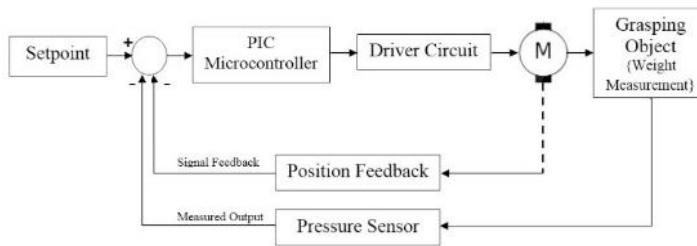


Figure 4. Block diagram of feedback system for grasping mechanism

In order to operate the auto grasping mechanism, the control of movement calibration has to be considered. For this purpose, the speed and position of the servo motor should be controlled. Basically, the claw of the robotic gripper prototype will be moved in x-axis to grasp the object after being detected automatically. To calibrate this movement, one servo motor is used. In addition, a completed system comprises the microcontroller, the motor driver and some peripheral devices that are used for sending and receiving the commands based on PIC software algorithm. The control circuit of the servo motor receives an input signal from its driver to control the speed of the motor to drive it to the desired position between 0 & 180 degrees. As a result, a series of pulses at a regular rate will move the servo motor from one position to another based on the proposed software algorithm and this will enhance the grasping mechanism.

The proposed auto grasping algorithm

Grasping an object is achieved by controlling interaction forces between the object and the claw of the robotic gripper, ensuring the stability and accuracy of the grasping mechanism. In order to execute these procedures successfully, the auto grasping algorithm is implemented based on software PIC system flowchart as shown in Figure 5. There are three stages as seen in the flowchart. The first step of the first stage after the system initialisation is to operate the claw of the robotic gripper since no object has been detected yet. The second step is to automatically check whether there is any object between the claw of the robot or not by using the digital IR sensor. The first step in the second stage is to move the claw of the robotic gripper towards the object after being detected automatically. This process is carried out with the movement calibration, as mentioned before, by controlling the speed of the servo motor. The second step is to check if the object touches all the pressure sensors which are assembled on the left and right claw of the robotic gripper. Simultaneously, the Analog to digital converter (ADC) channels of microcontroller unit (MCU) continues reading data from the analog readout circuit. Whenever the microcontroller receives data from all four pressure sensors, it converts them into digital signals to be analysed. The received data is essential for calibration process as well as the control of the servo motor movement. The third stage is to analyse and evaluate the data in order to calculate the pressure, weight, duty cycle and position of the object. Database information is required to be stored at this stage. The measured output is monitored via the LCD and using a

serial communication after analysing and calculating it. Eventually, the object will be adjusted according to the measured output and the influence of the external forces.

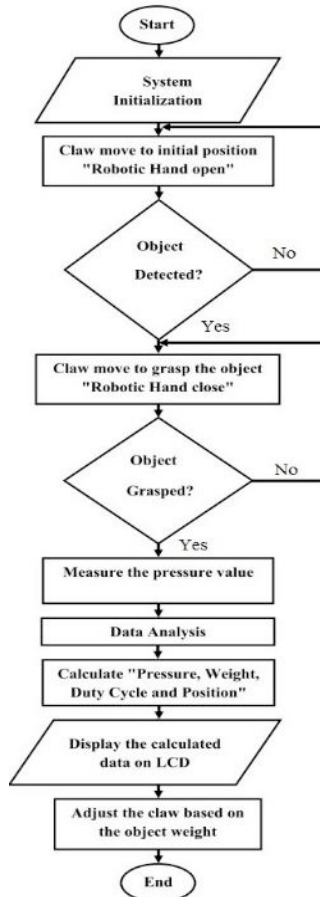


Figure 5. Flowchart of the proposed auto grasping algorithm

EXPERIMENTAL RESULTS

An experiment using with different weights of grasped object based on the proposed auto grasping algorithm are conducted in order to validate the new approach. The auto grasping algorithm is applied to a solid sample object with diverse weights. The initial object's weight is 40 grams and it is consistent with the allowed force range of the pressure sensor. Furthermore, the weight of this object can be increased by adding a weight scale . Based on the first stage of the proposed algorithm, the relationship between pressure and pulses of DC motor is depicted in Figure 6. It can be seen that the claw of the robotic gripper moves from zero to attach the object at 0.66 ms in which the object is grasped successfully with 0.09 (lbs) pressure forces. The same object with increasing different weights is grasped automatically by increasing the pressure forces as well as the pulse of motor to achieve the stability grasping based on the proposed algorithm. The weighted object with 500g requires 1.10 (lbs) with 1.09 ms . A secure

grasp was achieved by controlling the movement calibration of robot gripper based on the proposed auto grasping algorithm.

Based on the second stage of auto grasping algorithm, the sensitivity measurement of pressure sensor after detecting an object was introduced and the object was grasped effectively. The frequency and voltage output signals are very important to recognise and evaluate the signal in order to improve the performance of the grasping mechanism system. In addition, it is important to discover the relationship between two signals under different features. Figure 7 illustrates the output signal for all sensors which are set on the robotic claw based on modified WBC with 85 g weighted object. The curve of CH1 is the output signal of the front set of sensors (first Wheatstone bridge), whereas CH2 is the output signal of the set of sensors positioned in the back (second Wheatstone bridge) as illustrated in section 2.1. The CH3 represents the output voltage of the proposed WBC, which is the summation of CH1 and CH2. The Vavg (average) for both channels is different; 1.11V for CH1 and 0.191V for CH2, which implies that the total pressure is distributed between the two sensor sets and the output voltage in CH3 is 1.301 which is the total voltage of both sensors sets. Furthermore, there is a little change in the duty cycle for each set of sensor output.

After investigating the pressure distribution and sensitivity, the weight curve of the object is shown in Figure 8. It indicates a linear proportionality between the voltage and the object's weight. Comparing with the three methods of pressure distribution in (Ahmed M ALmassri et al., 2015), this proposed method has achieved a high sensitivity and offers a better grasping

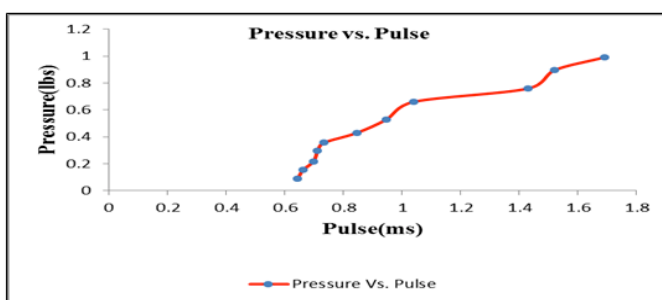


Figure 6. Output pressure value versus pulse of servo motor

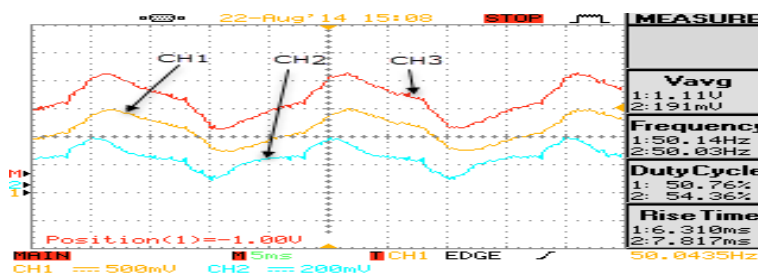


Figure 7. Output signal for 85g grasped object

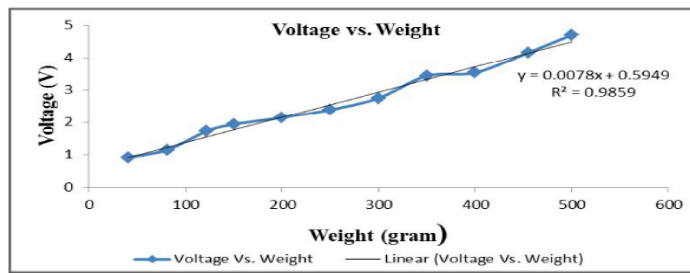


Figure 8. Output voltage versus weight based on pressure sensor measurement

mechanism and accurate data. This is due to the connection between the pressure sensors compared with previous methods that used conventional circuit and the integration with current algorithm (Ahmed M ALmassri et al., 2014). The sensitivity here refers to the small changes from pressure to the weight based on the constant (1 gram (g) equal 0.0022 lbs). The object's weight can be calculated using equation 2.

$$Voltage_{(v)} = 0.0078 \times Weight_{(g)} + 0.5949 \quad (2)$$

CONCLUSION

In this paper, we had proposed an auto grasping algorithm for robotic gripper based on pressure sensor measurement. Due to that, the enhancement of grasping mechanism is increased by controlling the interaction forces between the object to be grasped and the robotic gripper. Our system has demonstrated robust grasping in various weights of object and high sensitivity of measurement pressure using the proposed auto grasping algorithm based on the modified Wheatstone Bridge Circuit (WBC). Future research should look at the grasp quality evaluation based on accurate real time calibration algorithm for better autonomous manipulation.

ACKNOWLEDGEMENT

This research was supported by grants from the Ministry of Science, Technology and Innovation, Malaysia and Grant Putra from Universiti Putra Malaysia.

REFERENCES

- ALmassri, A. M., Abuitbel, M. B., Wan Hasan, W., Ahmad, S. A., & Sabry, A. H. (2014). *Real-time control for robotic hand application based on pressure sensor measurement*. Paper presented at the Robotics and Manufacturing Automation (ROMA), 2014 IEEE International Symposium.
- Almassri, A. M., Hasan, W., Ahmad, S. A., & Ishak, A. J. (2013). *A sensitivity study of piezoresistive pressure sensor for robotic hand*. Paper presented at the Micro and Nanoelectronics (RSM), 2013 IEEE Regional Symposium.
- Almassri, A. M., Wan Hasan, W., Ahmad, S. A., Ishak, A. J., Ghazali, A., Talib, D., & Wada, C. (2015a). Pressure sensor: state of the art, design, and application for robotic hand. *Journal of Sensors*, 2015(2015), 1-12.

- ALmassri, A. M., WanHasan, W., Ahmad, S., Ishak, A., & Wada, C. (2015b). *Optimisation of grasping object based on pressure sensor measurement for robotic hand gripper*. Paper presented at the 2015 9th International Conference on Sensing Technology (ICST).
- Bicchi, A., & Kumar, V. (2000). *Robotic grasping and contact: A review*. Paper presented at the ICRA.
- Bohg, J., Morales, A., Asfour, T., & Kragic, D. (2014). Data-driven grasp synthesis—a survey. *Robotics, IEEE Transactions, 30(2)*, 289-309.
- Iqbal, J., Tsagarakis, N. G., Fiorilla, A. E., & Caldwell, D. G. (2010). *A portable rehabilitation device for the hand*. Paper presented at the Engineering in Medicine and Biology Society (EMBC), 2010 Annual International Conference of the IEEE.
- Lee, H.-K., Chung, J., Chang, S.-I., & Yoon, E. (2008). Normal and shear force measurement using a flexible polymer tactile sensor with embedded multiple capacitors. *Journal of Microelectromechanical Systems, 17(4)*, 934-942.
- Lippiello, V., Ruggiero, F., Siciliano, B., & Villani, L. (2013). Visual grasp planning for unknown objects using a multifingered robotic hand. *IEEE/ASME Transactions on Mechatronics, 18(3)*, 1050-1059.
- Pokorny, F. T., Stork, J. A., & Kragic, D. (2013). *Grasping objects with holes: A topological approach*. Paper presented at the Robotics and Automation (ICRA), 2013 International Conference on IEEE.
- Righetti, L., Kalakrishnan, M., Pastor, P., Binney, J., Kelly, J., Voorhies, R. C., . . . Schaal, S. (2014). An autonomous manipulation system based on force control and optimization. *Autonomous Robots, 36(1-2)*, 11-30.
- Rodriguez, A., Mason, M. T., & Srinivasa, S. S. (2014). *Manipulation capabilities with simple hands*. Paper presented at the Experimental Robotics.





A Programmable CMOS Delay Line for Wide Delay Range Generation and Duty-Cycle Adjustability

Bilal I. Abdulrazzaq^{1,2*}, Izhal Abdul Halin¹, Lee Lini³, Roslina M. Sidek¹ and Nurul Amziah Md. Yunus¹

¹Department of Electrical and Electronic Engineering, Faculty of Engineering, Universiti Putra Malaysia, 43400 UPM Serdang, Selangor, Malaysia

²Department of Electronic and Communications Engineering, Al-Nahrain University, Al-Jadriya Complex, Baghdad 10070, Iraq

³Faculty of Engineering, Multimedia University, Persiaran Multimedia, 63100 Cyberjaya, Malaysia

ABSTRACT

A programmable CMOS delay line circuit with microsecond delay range and adjustable duty cycle is proposed. Through circuit simulation, approximately 2 μ s delay range can be achieved using 10-bit counter operating at a clock frequency of 500MHz. Utilising synchronous counters instead of synchronous latches has significantly reduced the large occupied active silicon area as well as the huge power consumption. The generated coarse time delay has shown excellent linearity and immunity to PVT variations. The proposed CMOS delay line is designed using a standard 0.13 μ m Silterra CMOS technology. The active layout area is (101 x 142) μ m², and the total power consumption is only 0.1 μ W.

Keywords: CMOS delay line, synchronous counter, latches, delay element, delay range, duty cycle, linearity, PVT variations

ARTICLE INFO

Article history:

Received: 24 August 2016

Accepted: 03 Jun 2017

E-mail addresses:

bilal.i.abdulrazzaq@gmail.com (Bilal I. Abdulrazzaq),

izhal@upm.edu.my (Izhal Abdul Halin),

linilee@mmu.edu.my (Lee Lini),

roslina@upm.edu.my (Roslina M. Sidek),

amziah@upm.edu.my (Nurul Amziah Md. Yunus)

*Corresponding Author

INTRODUCTION

Recently, CMOS delay lines have gained increasing interest because of the growing needs for specialised time management circuits (Murakami & Kuwabara, 1991). For example, in microprocessors, the programmable delay line which is situated between the microprocessor and its memory is used to ensure perfect synchronisation of clock signals/data packets at both the transmitting and receiving ends. In Time-of-Flight (ToF) range-finding systems, a delay

line is used to delay the light signal emitted from the sensor in order to mimic objects at different distances during ToF sensor characterisation (Halin et al., 2011; Kawahito et al., 2007). In time-dependent image sensors, the experimental setup for imaging uses an external delay line for shifting the imaging window. However, it is desirable to integrate the delay line as part of the image sensor system (Kawahito et al., 2013). Moreover, many CMOS delay line circuits play a substantial role in many sub-systems of Time-Interval Measurement (TIM) circuits such as Time-to-Digital Converters (TDCs) and Digital-to-Time Converters (DTCs) for digitization of short-time intervals (Andreani, Bigongiari, Roncella, Saletti, & Terreni, 1999; Rahkonen & Kostamovaara, 1993). In all of these applications, programmable wide delay ranges are required for proper operation in order to avoid functionality failure of the system.

On the other hand, obtaining an output digital signal with adjustable pulse-width feature is becoming a significant demand by many VLSI systems. This is attributed to two main reasons. First, different applications of these VLSI systems require different duty cycles of the input signals (Murakami & Kuwabara, 1991). Second, the heavy capacitive load of these VLSI systems needs an efficient digital driving circuitry. This driving circuitry is required to maintain the duty cycle of the output signal within acceptable boundaries (Kao, Cheng, & You, 2015).

Attaining both programmable wide delay range and adjustable duty cycle can be achieved by a delay line circuit in which these two functions are integrated. Accordingly, many designs found in the literature have been proposed. Conventional wide-range delay lines use N numbers of synchronous latches (D flip-flop) as their delay element with each latch having a delay unit of τ (s) which is equal to 1 clock cycle. Only one of these latches is tapped at a desired node to generate the delay. For example, to generate a $1\mu\text{s}$ delay, this type of delay line would require 1000 latches operating at 1GHz. The circuit topology for 1000 latches would be excessively large on silicon. Moreover, power dissipation would also be high due to the clocking of a large number of latches (Jovanovic & Stojcev, 2009). Another example is the DS1124 8-bit programmable delay line which uses tapped-delay line architecture. This architecture is implemented using an array of buffers connected to a single output line via a network of switches. For example, the buffer-based tapped delay line works on the principle that propagation delay time is added as the number of buffers in a signal line is increased. The DS1124 delay line offers a maximum delay of 64ns (Products, 2009). Although the aforementioned architecture is useful for implementing large maximum delays, they lack for the adjustable duty-cycle feature. Alternatively, the design proposed by (Murakami & Kuwabara, 1991) offers both programmable delay range and adjustable duty cycle. However, the achievable maximum delay range is only 20ns, making this architecture non-feasible for many high-performance applications.

In order to fill this research gap, this paper presents a new CMOS coarse delay line architecture which can generate both programmable microsecond delay range and adjustable microsecond duty-cycle control. The new architecture proposes the use of a synchronous counter to generate wide delay ranges, instead of a large number of latches. Thus, power consumption is significantly reduced and the occupied area is also minimised. The remainder of the paper is organised as follows. The next section presents the architecture of the proposed CMOS coarse delay line circuit before discussing the results and discussions. The last section summarises and concludes this paper.

PROPOSED ARCHITECTURE

The proposed architecture of the coarse CMOS delay line is shown in Figure 1.

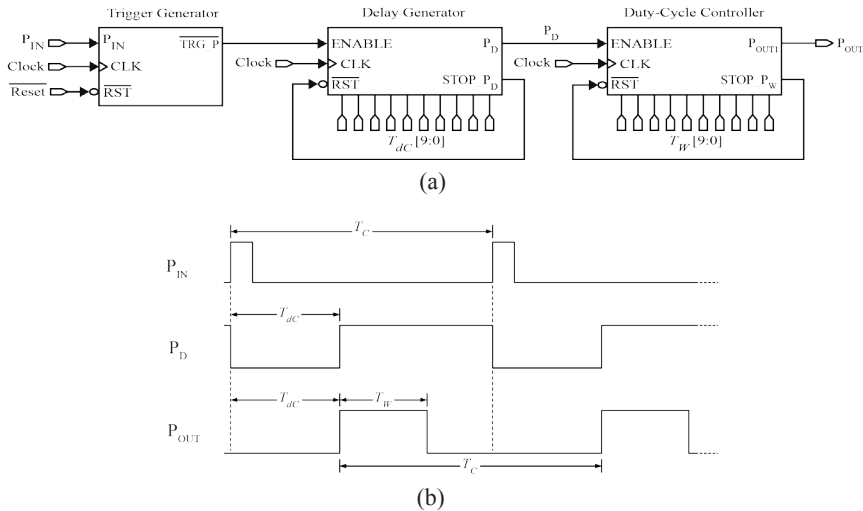


Figure 1. Simplified CMOS coarse delay line: (a) block diagram; (b) timing diagram

Figure 1 (a) shows the proposed architecture consists of three main blocks, namely Trigger Generator, Delay Generator, and Duty-Cycle Controller. Each circuit block performs one main function. To explain this, a simplified timing diagram illustrating the functionality of the three blocks is shown in Figure 1(b). The input periodic signal triggers the first circuit block which is input-pulse Trigger Generator circuit. This Trigger Generator detects the leading edge of the input signal P_{IN} which has a period T_C . Thereafter, the Delay Generator produces an output signal, P_D , which is used to enable/disable the Duty-Cycle Controller circuit. The disable period is T_{dc} which is the programmable generated coarse time delay, and the enable period is $T_C - T_{dc}$. Finally, during $T_C - T_{dc}$ period, the Duty-Cycle/pulse-width Controller circuit produces an output signal, P_{out} , whose programmable generated pulse-width is T_w and period is T_C .

The programmable duty-cycle delayed output pulses are achieved using START and STOP pulses. A detailed description of the building blocks in Figure 1 (a) are given below.

Delay Generator Circuit

The function of this circuit, which is the second block in Figure 1 (a), is the generation of a programmable wide delay range at the output pulse of the proposed CMOS coarse delay line. The Delay Generator circuit’s schematic and timing diagram are shown in Figure 2. As can be seen from Figure 2(a), the Delay Generator circuit mainly makes use of a 10-bit synchronous counter, a STOP-Pulse decoder with a network of CMOS transmission gates built inside, and an SR flip-flop. The Start Pulse, TRG_P’, is synchronised to count zero of the counter. As shown in Figure 2(b), when TRG_P’ goes LOW, the SR flip-flop’s output Q changes to HIGH. Hence, the counter’s gated clock G.CLK_1 is activated. A custom network comprising 10-bit CMOS transmission gate is designed to function as a switch connecting the synchronous

counter to a Stop-Pulse Decoder circuit. A 10-bit binary word, $T_{dc}[9:0]$, which is programmed at the switch control ports will correspond to the amount of the desired delay. When the clock count is equal to the input digital code value, the Stop-Pulse Decoder detects the count that is equal to the code and generates the first STOP Pulse, STOP_P_D. Consequently, the flip-flop's output Q changes to LOW, the counter's gated clock is deactivated, and the counter is reset. The output of the Delay Generator circuit is P_D which is the complement of Q of the SR-flip-flop. The period of LOW-logic level of P_D is approximately the desired output time delay, T_{dc} .

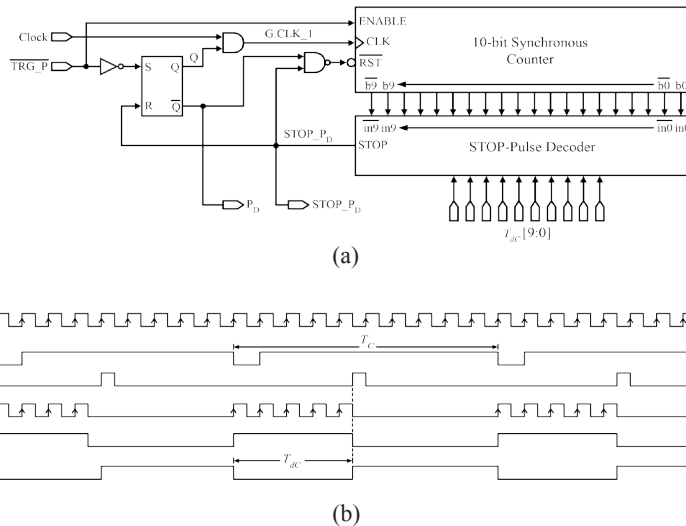


Figure 2. Delay generator circuit: (a) schematic diagram; (b) timing diagram

The minimum achievable coarse delay step, $DS_{C,min}$, at the output of the coarse delay line can be determined from the following equation:

$$DS_{C,min} = \frac{1}{f_{clock}} \tag{1}$$

where f_{clock} refers to the frequency of the counter clock. On the other hand, the maximum achievable coarse delay range, $DR_{C,max}$, at the output can be determined from the following equation:

$$DR_{C,max} = 2^{counter,bit-no.} \times DS_{C,min} \tag{2}$$

According to Equations (1) and (2) and supposing that the 10-bit counter operates with f_{clock} equals to 500MHz, $DS_{C,min}$ is 2ns and $DR_{C,max}$ is approximately 2 μ s.

The outputs P_D and STOP_P_D of the Delay Generator circuit will serve as the ENABLE and the second START Pulse respectively, for the next circuit block which is Duty-Cycle Controller circuit.

Duty-Cycle Controller Circuit

The function of this circuit, which is the third and last block in Figure 1(a), is the generation of a programmable duty-cycle/pulse-width at the output pulse of the coarse delay line. The Duty-Cycle Controller circuit's schematic and timing diagrams are shown in Figure 3. It is clear from Figure 3(a) that the digital building blocks constructing the Duty-Cycle Controller circuit are similar to that of the Delay Generator circuit. The main difference is in terms of their functionality depending on the input and output of the building blocks of each circuit. As shown in Figure 3(b), when STOP_P_D goes HIGH, the SR flip-flop's output P_{OUT} changes to HIGH.

Accordingly, the counter's gated clock G.CLK_2 is activated and the counter starts to count. A 10-bit binary word, T_W[9:0], which is programmed at the control ports of the transmission gate will correspond to the amount of the desired pulse-width. When the clock count is equal to the input digital code value, the Stop-Pulse Decoder detects the count that is equal to the code and generates the second STOP Pulse, STOP_P_W. As a result, the flip-flop's output P_{OUT} changes to LOW, the counter's gated clock is deactivated, and the counter is reset. The period of the HIGH-logic level of P_{OUT} is approximately the desired output pulse-width, T_W.

It is worth mentioning that the maximum achievable periods of the generated time delay, DR_{C,max}, and the generated pulse-width, T_{W,max}, are restricted to the following relation:

$$DR_{C,max} + T_{W,max} \leq T_C \tag{3}$$

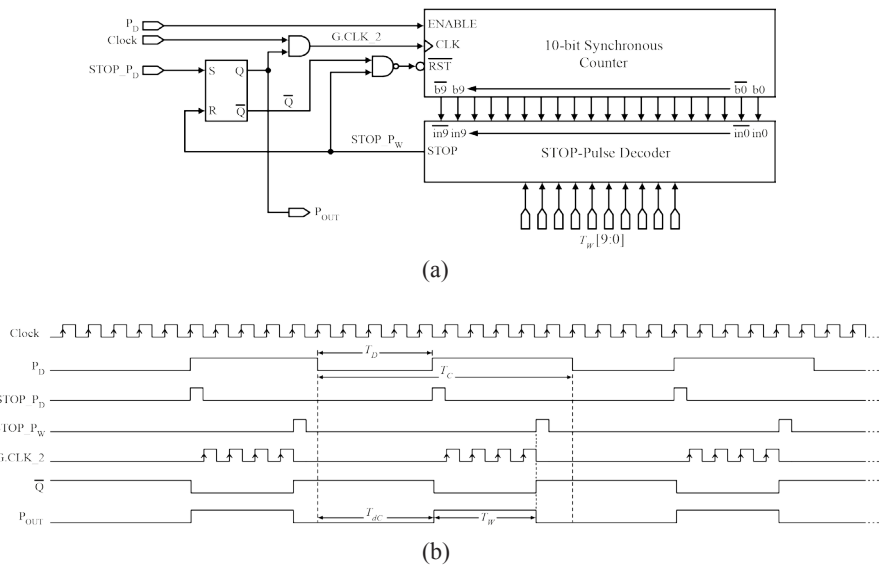


Figure 3. Duty-Cycle Controller circuit: (a) schematic diagram; (b) timing diagram

where T_C is the cycle period of the input signal. The condition illustrated in (3) is set to avoid the overlap of the programmable width delayed output pulse with the next cycle of the input pulse.

SIMULATION RESULTS AND DISCUSSION

The proposed CMOS coarse delay line is designed using a 0.13 μ m CMOS process. The power supply voltage is 1.2V. Referring to Figure 2(a), since the Delay Generator circuit makes use of a 10-bit counter operating with 500MHz clock frequency, the values of the generated $DR_{C,max}$ and $DS_{C,min}$ are approximately 2 μ s and 2ns respectively. This is illustrated in Figure 4(a).

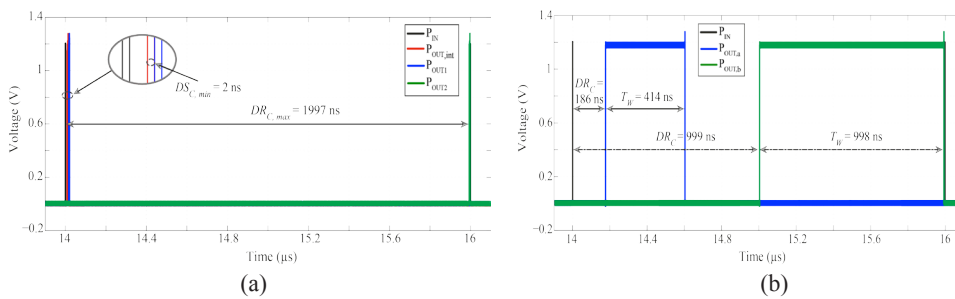


Figure 4. Different output delay and pulse-width values: (a) minimum step and maximum range of the generated coarse delays with a minimum pulse-width value fixed for both delay values; (b) two different cases of generated delay and pulse-width values

In Figure 4(a), the pulse P_{IN} (black) is the input pulse with a width of 2ns and needs to be delayed. On the other hand, pulse P_{OUT1} (blue) is delayed by 2ns which is corresponding to the minimum coarse delay step, $DS_{C,min}$. This is done by setting the digital delay code, $T_{ac}[9:0]$ of the delay generator circuit to [0000-0000-01]. The delay 1997ns of the pulse P_{OUT2} (green) represents the maximum attainable delay, $DR_{C,max}$. This is obtained by setting the digital delay code to [1111-1001-00]. It should be noted that the delay of the red-coloured pulse, $P_{OUT,int}$, in Figure 4(a) is the intrinsic delay of the CMOS coarse delay line's building circuits. This delay whose value is approximately 5ns is always added to the output delayed pulse. However, this poses no problems because the added intrinsic delay is a constant offset value that can easily be subtracted to obtain the exact desired time delay (Markovic, Tisa, Villa, Tosi, & Zappa, 2013). In Figure 4(b), P_{IN} (black) is again the input pulse to be delayed and has a pulse width of 2ns. P_{OUTa} is output pulse programmed with a delay of 186ns and a pulse width of 414ns. This is obtained by setting the delay code, $T_{ac}[9:0]$, to [0001-0111-01] and the pulse width code, $T_W[9:0]$, to [0011-0011-11]. To demonstrate the pulse width changing capabilities, pulse P_{OUTb} is shown. It is delayed by 999ns and has a pulse width of 998ns. This output is obtained by setting $T_{ac}[9:0]$ to [0111-1100-01] and $T_W[9:0]$ to [0111-1100-11]. Accordingly, the summation of the obtained values of the $DR_{C,max}$ and the $T_{W,max}$ approximately equals to 1999ns which doesn't exceed the cycle period 2000ns of the input pulse T_C . The linearity of the generated coarse time delay, T_{ac} , versus the input digital delay code is also considered and analysed as shown in Figure 5.

A Wide Range with Adjustable Duty Cycle Digital Delay Line

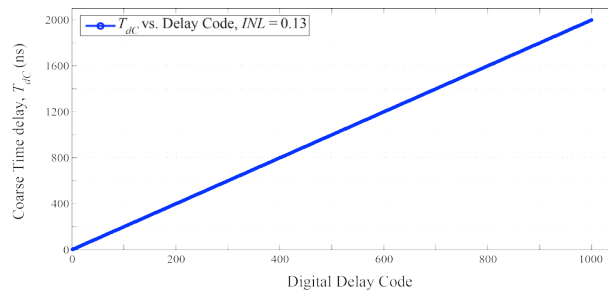


Figure 5. Output coarse time delay, T_{dc} , versus input digital delay code

The x-axis shows the Binary-Coded-Decimal (BCD) value of the programmed delay while the y-axis shows the simulated output coarse delay. Figure 5 clearly shows a linear relationship between the output delay and the input digital delay code as the INL value is only 0.13.

Regarding the effects of both process and environmental (PVT) variations on the coarse delay range, Figure 6 can be considered.

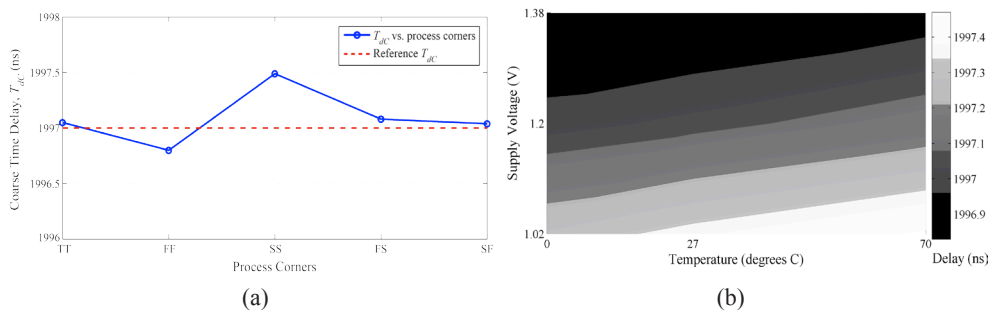


Figure 6. Maximum achievable delay range versus: (a) process corners; (b) temperature and supply voltage variations

It can be seen from Figure 6(a) and (b) that the process as well as supply voltage and temperature variations have a very limited effect on the generated maximum delay range of the coarse delay line.

Figure 7 shows that the layout area required for this circuit is approximately $(101 \times 142) \mu\text{m}^2$. Figure 7 highlights the delay generator circuit and the duty-cycle controller circuit. The circuits are enclosed by two layers of guard rings to prevent the circuits' noise from contaminating other signals if these circuits are used in a mixed signal IC.

A comparison between our coarse delay line and other CMOS implementations is seen in Table 1.

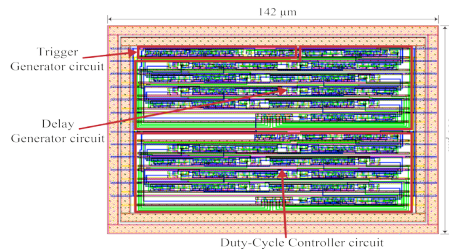


Figure 7. Layout of the proposed CMOS coarse delay line

Table 1
A comparison of this study with other reported CMOS coarse delay lines

Parameter	(Products, 2009)	(Markovic et al., 2013)	(Han, Qiao, & Hei, 2016)	This work
Technology (μm)	0.5	0.35	0.13	0.13
Maximum delay range (ns)	64	160	46	2000
Duty-cycle adjustability	No	No	No	Yes

Table 1 shows the technology used and maximum delay range. A comparison between this work and the most recently published work by (Han et al., 2016) using 0.13 μm technology shows that our technique produces the longest delay. This table also shows that only our design has the ability to adjust the delayed output's duty cycle.

CONCLUSION

It can be concluded that an input signal can be delayed for 2 μs delay range in steps of 2ns. The duty cycle can also be adjusted in the same range and step provided that the summation of the maximum delay range and the maximum pulse width doesn't exceed the cycle period of the input signal. The small layout area and the low power consumption of the proposed architecture make it suitable for many high-performance SoC circuits.

ACKNOWLEDGEMENT

The authors would like to acknowledge Universiti of Putra Malaysia (UPM) for supporting for this work through the Putra Scholar Initiative-Putra Grant (GP-IPS/2014/9438713).

REFERENCES

- Andreani, P., Bigongiari, F., Roncella, R., Saletti, R., & Terreni, P. (1999). A Digitally Controlled Shunt Capacitor CMOS Delay Line. *Analog Integrated Circuits and Signal Processing*, 18(1), 89-96. doi: 10.1023/a:1008359721539
- Halin, I. A., Din, A. u., Aris, I. b., Isa, M. b. M., Shafie, S., & Kawahito, S. (2011). Selection of amplifier for optimized charge transfer in active pixel CMOS time of flight (TOF) image sensors. *IEICE Electronics Express*, 8(22), 1913-1919. doi: 10.1587/elex.8.1913

- Han, Y., Qiao, S., & Hei, Y. (2016). A high-linearity and high-resolution delay line structure with a calibration algorithm in delay-based LINC transmitters. *Journal of Semiconductors*, 37(1), 015003.
- Jovanovic, G., & Stojcev, M. (2009). Vernier's delay line time-to-digital converter. *A: Appl Math Inform Mech, Scientific Publications of the state University of NOVI PAZAR SER*, 1(1), 11-20.
- Kao, S.-K., Cheng, H.-C., & You, Y.-D. (2015). Pulsewidth control loop with a frequency detector for wide frequency range operation. *Microelectronics Journal*, 46(4), 291-297. doi: <http://dx.doi.org/10.1016/j.mejo.2015.01.005>
- Kawahito, S., Baek, G., Li, Z., Han, S.-M., Seo, M.-W., Yasutomi, K., & Kagawa, K. (2013). *CMOS lock-in pixel image sensors with lateral electric field control for time-resolved imaging*. Paper presented at the Proc. Int. Image Sensor Workshop (IISW).
- Kawahito, S., Halin, I. A., Ushinaga, T., Sawada, T., Homma, M., & Maeda, Y. (2007). A CMOS Time-of-Flight Range Image Sensor With Gates-on-Field-Oxide Structure. *IEEE Sensors Journal*, 7(12), 1578-1586. doi: 10.1109/jksen.2007.907561
- Markovic, B., Tisa, S., Villa, F. A., Tosi, A., & Zappa, F. (2013). A High-Linearity, 17 ps Precision Time-to-Digital Converter Based on a Single-Stage Vernier Delay Loop Fine Interpolation. *Circuits and Systems I: Regular Papers, IEEE Transactions on*, 60(3), 557-569. doi: 10.1109/tcsi.2012.2215737
- Murakami, D., & Kuwabara, T. (1991, 9-10 Sep 1991). *A digitally programmable delay line and duty cycle controller with picosecond resolution*. Paper presented at the Bipolar Circuits and Technology Meeting, 1991., Proceedings of the 1991.
- Products, M. I. (2009). 5.0V 8-Bit Programmable Timing Element. In M. I. P. Inc.'s (Ed.), (DS1124 ed.). USA.
- Rahkonen, T. E., & Kostamovaara, J. T. (1993). The use of stabilized CMOS delay lines for the digitization of short time intervals. *IEEE Journal of Solid-State Circuits*, 28(8), 887-894. doi: 10.1109/4.231325



Fuzzy-Controlled Humidity Variation by Silica Gel and Nitrogen Gas in an Atmospheric Chamber

Ali Ghahraei, Nurul Amziah Md Yunus*, Izhal Abdul Halin and Nasri Sulaiman

Micro and Nano Electronic Systems Unit (MiNES), Department of Electrical and Electronic Engineering, Faculty of Engineering, Universiti Putra Malaysia, Serdang UPM, 43400 Selangor, Malaysia

ABSTRACT

Controlled humidity environment is of significance in many scientific researches and experiments. In most laboratory-scale atmospheric chambers, an electrical temperature-based control system is used to adjust humidity. Since these chambers are not affordable in every laboratory, other low cost chambers using nitrogen gas or silica gel are used to adjust humidity. In this paper, a mechanism was developed to control the relative humidity in closed lab-scale chambers. Humidification is done by spraying water through a blower fan while de-humidification is by pumping air through silica gel as well as nitrogen gas injection. A Mamdani type fuzzy controller was designed to control the components and relative humidity. The results show the proposed system and controller can adjust and maintain relative humidity from 41% to 100% with maximum overshoot of 1% and the maximum range of error of steady state of 1.2 %.

Keywords: Atmospheric chamber, humidity, silica gel, nitrogen gas, fuzzy controller

INTRODUCTION

In many laboratory processes, the effects of ambient humidity can have detrimental

effects on research quality, effectiveness, visual appearance and results. Controlled humidity environments are important in many scientific researches and experiments such as electronics and semiconductors, chemistry, food processing, corrosion tests, and solar cell researches (Hoshino et al., 2013; Kim, 2012; Mekhilef et al., 2012). Humidification is done by heating or spraying water as well as through ultrasonic vaporisation (Yasuda et al., 2011). Since these chambers are usually expensive, other physical and chemical ways are used to reduce and control humidity.

ARTICLE INFO

Article history:

Received: 24 August 2016

Accepted: 03 Jun 2017

E-mail addresses:

ali_ghahraei@yahoo.com (Ali Ghahraei),
amziah@upm.edu.my (Nurul Amziah Md Yunus),
izhal@upm.edu.my (Izhal Abdul Halin),
nasri_sulaiman@upm.edu.my (Nasri Sulaiman)

*Corresponding Author

Injecting nitrogen gas, N₂ is a method of dehumidification in closed chambers. The vapour-air mixture is pushed or eliminated out of the chamber by gradually injecting nitrogen gas into the chamber. Since N₂ is logically a dry gas and neither reacts with stored materials nor carries moisture, it has a wide usage in controlling and maintaining humidity levels in its surrounding environments such as dry boxes, archives and cleanroom (Yeager, 2008). Another solution, which is used for de-humidification in laboratories, is absorbent materials. Saturated salt solutions are a traditional way to absorb water vapour in a closed box or chamber (Young, J. F., 1967; Collins, A., 2012). Silica gel is an adsorbent when the relative humidity is in the range of 50–80% (Pramuang et al., 2007). Silica refers to a naturally occurring mineral that consists of silicon dioxide (SiO₂), which is a product of a chemical reaction between silicon and oxygen (Waksmundzka-Hajnos et al., 2010). An important characteristic of silica gel is that it can reversibly adsorb large volumes of vapour through regeneration (Zhang et al., 2011), which offers a low-cost solution for de-humidification in closed environments (Brody et al., 2008).

This work presents a new control system, which has not been done before, for controlling the relative humidity in a closed atmospheric chamber. A control system is developed using these low-cost materials for having an inexpensive humidity controlled chamber since the traditional way does not provide a precise and easy-to-use solution for controlling humidity in closed chambers. N₂ and silica materials are good for humidity setting in the chamber and therefore, a proper control and monitoring should be set up for this chamber.

METHODOLOGY

Relative humidity (RH) of an air-water mixture is described mathematically as the ratio of the partial pressure of H₂O vapor (e_w) in the air-water mixture at a certain temperature to the saturated vapour pressure of H₂O (e_w^*) at that temperature. The RH is normally represented as a percentage (RH %). Equation (1) shows how RH % is calculated:

$$RH\% = \frac{e_w}{e_w^*} \times 100\% \quad (1)$$

According to (1) and definition of RH, the saturated vapour pressure of water (e_w^*) is a constant parameter and it depends only on the temperature. Therefore, to increase and decrease the RH % at a constant temperature, a certain amount of water vapour needs to be injected or removed from the air-water mixture. The humidity control system consists of two parts: humidifier and dehumidifier.

Overall Operation

The RH control system consists of humidifier and de-humidifier parts, which can add and absorb water vapour respectively. A closed-loop control system is needed for adjusting and maintaining the amount of RH inside the chamber. A standard humidity/temperature meter (TES-1360A) was used to provide the feedback of RH% and the temperature respectively at every 300 milliseconds. The sensor was installed on the test bed and near the tested sample.

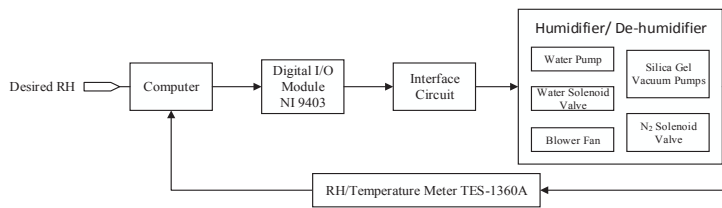


Figure 1. Block diagram of interconnection between components

Figure 1 shows the interconnection between components. The desired RH is the input of the control system, which is defined by the user. The control system algorithm is implemented using LabVIEW 2012 software and Fuzzy Toolbox. The output of the control system commands the humidifier and de-humidifier using NI cDAQ-94 and the interface circuit. The design of the controller will be discussed in the next section.

Physical Characteristics of the Chamber

The chamber which is used here is a close cube made from acrylic glass with 12mm thickness. The size of the cube is 80 cm × 40 cm × 25 cm (Height × Width × Length) as shown in Figure 2. The cube was installed with the distance of 30 cm from the wooden panel by using 4 metal shafts. The chamber was designed to be isolated from the air entering from the outside. There are two ways to access inside the chamber i.e. from the top and from the front door. The topside of the chamber is designed like a cap, which is used for installation of components. The front door has been designed to put the samples (such as a solar cell device) inside the chamber. The doors are isolated with isolation strips.

RESULTS AND DISCUSSION

The humidifier and de-humidifier components are connected to data acquisition module by using the interface circuit shown in Figure 3. The entire system is controlled by the computer (controller). The RH/Temp meter device provides the feedback. In order to design the controller, the whole of the chamber is considered as a black box. In science and engineering, a black box is a device, system or object which can be viewed in terms of its input, output and transfer characteristics without any knowledge of its internal workings (Ljung, L., 1998).

A fuzzy controller was designed to control the Relative Humidity (RH) inside the chamber. The fuzzy controller was set up in LabVIEW as a two-input, one-output structure. Figure 3 shows the two-input single-output fuzzy controller. The assembled fuzzy system is Mamdani type. The Mamdani method (most commonly used) was among the first fuzzy control systems built using the then new fuzzy set theory. It is widely accepted because it utilises expert knowledge and represents the expertise in a more intuitive, human-like manner. It provides an additional degree of freedom and expects the output membership functions to be fuzzy and use the centroid de-fuzzification method (Radakovic et al., 2002). Fuzzification helps us to evaluate the rules, but the final output of a fuzzy system has to be a crisp number. The input for defuzzification is the aggregate output fuzzy set and the outcome is a single number. There

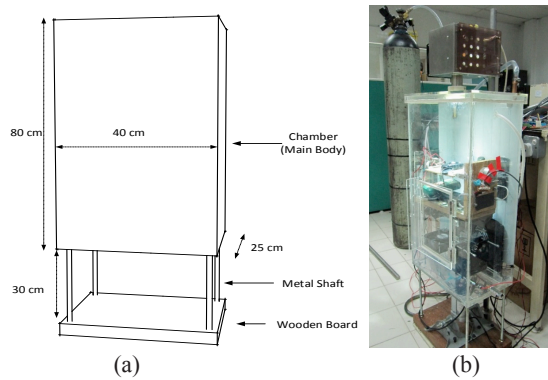


Figure 2. (a) Physical dimensions of the chamber; (b) A total view of the constructed chamber

are several defuzzification methods but the most popular is the centroid technique (or centre of gravity). Here, the first input is the Relative Humidity error (RHe), which is calculated by subtracting the current value of RH% from the desired RH%. The second input is the derivative of RH (dRH/dt), which presents the changing rate of the error. The output variable is the increment of power of the humidifier and de-humidifier.

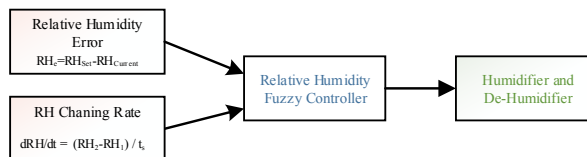


Figure 3. Inputs and output of the relative humidity Mamdani-type fuzzy controller

Membership Functions

Figure 4 shows the membership functions of the RH error. The functions information is tabulated in Table 1. The fuzzy variable RH error consists of negative, zero and positive values. For example, if the negative values show the set point of the RH is less than the current RH in the positive values mean the system needs to increase the RH to reach the set point.

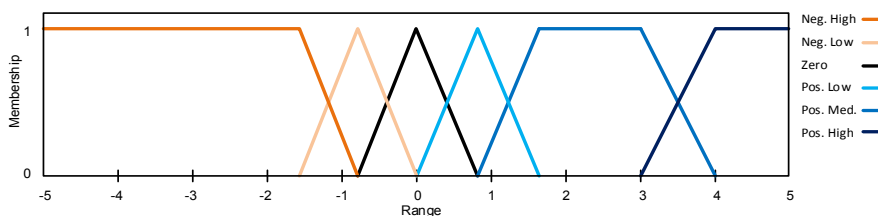


Figure 4. Membership functions of the relative humidity Error

Table 1
Membership functions of the relative humidity error

Membership function	Shape	Points
Negative High	Trapezoid	-100 ; -100 ; -1.6 ; -0.8
Negative Low	Triangle	-1.6 ; -0.8 ; 0
Zero	Triangle	-0.8 ; 0 ; 0.8
Positive Low	Triangle	0 ; 0.8 ; 1.6
Positive Medium	Trapezoid	0.8 ; 1.6 ; 3 ; 4
Positive High	Trapezoid	3 ; 4 ; 100 ; 100

The membership functions of the RH changing rate was designed by using the calculated derivative of RH increment and decrement. Figure 5 shows the membership functions of the second fuzzy input. Table 2 presents information regarding membership functions.

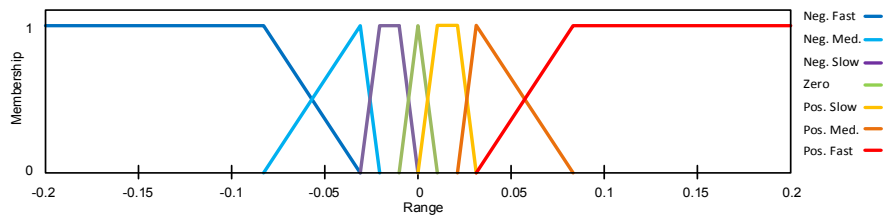


Figure 5. Membership functions of the relative humidity changing rate

Table 2
Membership functions of the relative humidity changing rate

Membership function	Shape	Points
Negative Fast	Trapezoid	-1 ; -1 ; -0.08 ; -0.03
Negative Medium	Triangle	-0.08 ; -0.03 ; -0.02
Negative Slow	Trapezoid	-0.03 ; -0.02 ; -0.01 ; 0
Zero	Triangle	-0.01 ; 0 ; 0.01
Positive Slow	Trapezoid	0 ; 0.01 ; 0.02 ; 0.03
Positive Medium	Triangle	0.02 ; 0.03 ; 0.08
Positive Fast	Trapezoid	0.03 ; 0.08 ; 1 ; 1

Figure 6 shows the membership functions of the output. The output of the controller is divided into six integer values, which is described in Table 3. Each output value enables one or two components of the humidifier or de-humidifier as well as disables other components.

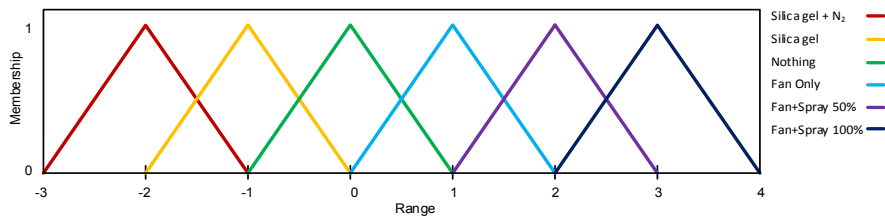


Figure 6. Membership functions of the output of the relative humidity controller

Table 3
Membership functions of the output of the relative humidity controller

Membership function	Shape	Points
Silica Gel Vacuum Pumps + N2 Injection	Triangle	-3 ; -2 ; -1
Silica Gel Vacuum Pumps	Triangle	-2 ; -1 ; 0
Nothing	Triangle	-1 ; 0 ; 1
Humidifier Fan Only	Triangle	0 ; 1 ; 2
Fan + Water Spraying at Duty Cycle 50%	Triangle	1 ; 2 ; 3
Fan + Water Spraying at Duty Cycle 100%	Triangle	2 ; 3 ; 4

Fuzzy Rules

The initial rules are defined based on the expert’s knowledge regarding how to control the system using the linguistic quantifiers. There is a finite number of possible rules since we used a finite number of linguistic variables and values (Aguilar et al., 2012). Table 4 shows the initial rules that were selected for the fuzzy controller.

Table 4
Fuzzy rules of the relative humidity fuzzy controller

Error change	Negative High	Negative Low	Zero	Positive Low	Positive Medium	Positive High
Negative Fast	Silica Gel + N2	Silica Gel	Nothing	Fan + spray 100%	Fan + spray 100%	Fan + spray 100%
Negative Medium	Silica Gel + N2	Silica Gel	Nothing	Fan + spray 100%	Fan + spray 100%	Fan + spray 100%
Negative Slow	Silica Gel + N2	Silica Gel + N2	Nothing	Fan + spray 100%	Fan + spray 100%	Fan + spray 100%
Zero	Silica Gel + N2	Silica Gel + N2	Nothing	Fan + spray 100%	Fan + spray 100%	Fan + spray 100%
Positive Slow	Silica Gel + N2	Silica Gel + N2	Nothing	Fan + spray 100%	Fan + spray 100%	Fan + spray 100%
Positive Medium	Silica Gel + N2	Silica Gel + N2	Nothing	Fan only	Fan + spray 50%	Fan + spray 100%
Positive Fast	Silica Gel + N2	Silica Gel + N2	Nothing	Nothing	Fan only	Fan + spray 100%

Control Diagram

Figure 7 shows the final block diagram of the designed RH controller. The input of the control system is the desired value of the relative humidity and the output is the actual value of RH. A function is used to round the output values since the output should be an integer value, which is between -2.49 and 3.49 to the nearest integer values.

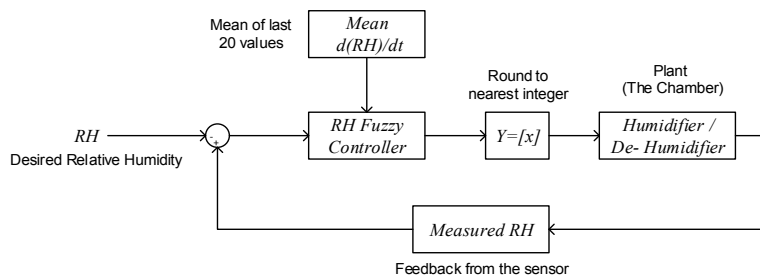


Figure 7. Control diagram of the relative humidity control system

Operation and Analysis

In this experiment three different set points of RH% were selected to be controlled; 60%, 100% and 80%. The temperature was kept at 26.5 °C (the lab temperature).

Achievable Relative Humidity Values

Another experiment was designed to find the achievable amount of relative humidity at the laboratory's temperature. First, the humidifier was conducted without the controller to reach the maximum amount of RH. Then, using the de-humidifier and without controller, the system was performed until the minimum amount of RH was reached. At the laboratory's temperature (26.5°C), the maximum and the minimum achievable amount of relative humidity were obtained as 100% and 41% respectively.

Maximum Overshoot, Steady-State Error and Settling Time

The maximum overshoot and steady state error values are of significance to find the precision of the proposed RH control system at steady-state mode. Table 5 shows the measured maximum overshoot and range of steady-state error plus settling time at 26.5°C and different RH set-points. The maximum overshoot and the maximum range of error of steady state are obtained as 1.1% and 1.4% respectively.

Table 5
Overshoot and steady-state error and settling-time of the RH control system

Temperature (°C)	RH% set-point	Maximum Overshoot	Steady-State Error (Range)	Settling-Time (Seconds) From 41%	Settling-Time (Seconds) From 100%
26.5	60	1	1.2	128	532
	80	0.9	1.1	320	186
	100	0	0.5	1140	0

CONCLUSION

This paper has presented a new mechanism to control relative humidity in atmospheric chambers without changing the temperature. A mechanism was designed to absorb water vapours and de-humidify the chamber which decrease RH by pumping air through silica gel as well as by using N₂ gas injection. In order to have precision RH adjustment, a Mamdani fuzzy controller was employed in LabVIEW platform. It is to control the components using the digital output module and designed interface circuit. The results have shown that the proposed system and controller can adjust and maintain RH from 41% to 100% (most working activities) with maximum overshoot of 1% and the maximum range of error of steady state of 1.2 %.

ACKNOWLEDGMENT

This work was supported by the Fundamental Research Grant Scheme, FRGS/1/2014/TK03/UPM/02/5 under the Ministry of Education (MOE), Malaysia. The project was conducted at Universiti Malaya (UM) and Universiti Putra Malaysia (UPM). The authors would like to acknowledge the essential and continuous assistance of Prof. Abdul Kariem Mohd Arof and Mr. Saman Akbarzadeh from Department of Physics, Faculty of Science, University of Malaya, Kuala Lumpur in the hardware implementations described in this paper.

REFERENCES

- Aguilar, R. M., Muñoz, V., & Callero, Y. (2012). *Control Application Using Fuzzy Logic: Design of A Fuzzy Temperature Controller*. INTECH Open Access Publisher.
- Brody, A. L., Bugusu, B., Han, J. H., Sand, C. K., & McHugh, T. H. (2008). Scientific Status Summary. *Journal of Food Science*, 73(8), R107-R116.
- Collins, A. (2012). *Nanotechnology Cookbook: Practical, Reliable And Jargon-Free Experimental Procedures*. Elsevier.
- Hoshino, K., Yeh, B., & Wager, J. F. (2013). Impact of Humidity on The Electrical Performance of Amorphous Oxide Semiconductor Thin Film Transistors. *Journal of the Society for Information Display*, 21(7), 310-316.
- Kim, Y. B. (2012). Study On The Effect Of Humidity And Stoichiometry on The Water Saturation of PEM Fuel Cells. *International Journal of Energy Research*, 36(4), 509-522.
- Ljung, L. (1998). *System Identification* (pp. 163-173). Birkhuser Boston.

- Mekhilef, S., Saidur, R., & Kamalisarvestani, M. (2012). Effect of Dust, Humidity and Air Velocity on Efficiency of Photovoltaic Cells. *Renewable and Sustainable Energy Reviews*, 16(5), 2920-2925.
- Pramuang, S., & Exell, R. H. B. (2007). The Regeneration of Silica Gel Desiccant by Air from a Solar Heater with A Compound Parabolic Concentrator. *Renewable Energy*, 32(1), 173-182.
- Radakovic, Z. R., Milosevic, V. M., & Radakovic, S. B. (2002). Application of Temperature Fuzzy Controller in an Indirect Resistance Furnace. *Applied Energy*, 73(2), 167-182.
- Waksmundzka-Hajnos, M., & Sherma, J. (Eds.). (2010). *High performance liquid chromatography in phytochemical analysis*. CRC Press.
- Yasuda, K., Honma, H., Xu, Z., Asakura, Y., & Koda, S. (2011). Ultrasonic Atomization Amount For Different Frequencies. *Japanese Journal of Applied Physics*, 50(7S), 07HE23.
- Yeager, D. (2008, July). Cleanroom Utilities Overview: University of Louisville. In *University/Government/Industry Micro/Nano Symposium, 2008. UGIM 2008. 17th Biennial* (pp. 191-193). IEEE.
- Young, J. F. (1967). Humidity Control In The Laboratory Using Salt Solutions. *A Review. Journal of Applied Chemistry*, 17(9), 241-245.
- Zhang, W., Yao, Y., He, B., & Wang, R. (2011). The Energy-Saving Characteristic of Regeneration with High-Intensity Ultrasound. *Applied Energy*, 88(6), 2146-2156.



Assessment of Transformer Health Index Using Different Model

J. Jasni¹, A. Azmi^{1*}, N. Azis¹, M. S. Yahaya¹ and M. A. Talib²

¹Centre for Electromagnetic and Lightning Protection Research (CELP), Department of Electrical and Electronic Engineering, Faculty of Engineering, UPM, 43400 Serdang, Selangor, Malaysia

²TNB Research Sdn. Bhd., Kawasan Institusi Penyelidikan, 43000 Kajang, Selangor, Malaysia

ABSTRACT

Transformer failures lead to interruption of power supply. Therefore, asset management is important to monitor the efficient functioning of transformers. An important approach in asset management is condition assessment whereby the health status of the transformer is assessed via a health index. There are many methods in determining the final value of a health index. This paper examines how different assessment methods can be used in order to come up with the final health index and output of final health index. The output trend shapes are almost the same for Assessment Model A, B and C except for Assessment Model D. There is no strong correlation between the health index and age of the transformer. Generally, the value of health index of the transformer is reflected by its operation and loading history. This paper hence examines the assessment steps and results that will guide the development of a new approach to determine health index value.

Keywords: Transformer, asset management, condition assessment, transformer health index

INTRODUCTION

Continuous and steady supply of electricity is crucial to support manufacturing,

production, the services industry and daily needs of residents. Power outages affect the environment, disrupt transportation system and will result in heavy losses for businesses particularly in the manufacturing and services sector in addition to bringing disrepute to the utility company leading to the latter's loss of revenue and market backlash. Continuous power supply depends on the condition of the transformer as it is the 'back-bone' of a power system. A transformer is used to step up or step down the voltage from the generator to be supplied to the end user. Thus, asset management is important to examine, analyse

ARTICLE INFO

Article history:

Received: 24 August 2016

Accepted: 03 Jun 2017

E-mail addresses:

jas@upm.edu.my (J. Jasni),

akma_lina@yahoo.com (A. Azmi),

norhafiz@upm.edu.my (N. Azis),

sharil@utem.edu.my (M. S. Yahaya),

mohdaizam@tnbr.com.my (M. A. Talib)

*Corresponding Author

and prioritise the assets and their maintenance needs of . There are a lot of methods related to asset management such as fuzzy logic, digital signal processing algorithms, principal component analysis (PCA) algorithms and back-propagation artificial neural network (BP-ANN) algorithm (Abiri-Jahromi et al., 2013; Abiri-Jahromi et al., 2013; Abu-Elanien et al., 2011; Abu-Elanien et al., 2012; Abu-Elanien et al., 2010; Arshad, et al., 2014; Brittes et al., 2014; Dominelli, 2004; Ma et al., 2015; Trappey et al., 2015).

There are a few approaches to asset management such as condition assessment of the transformer. In condition assessment, health index is used to examine the condition of the transformer and whether it needs to be maintained, repaired and upgraded, replaced, monitored or have contingency control. Health index is a combination of results from operating observations, field testing and site and laboratory testing. This results will be converted into a quantitative index to show the condition of the transformer. Health index usually consists of input, algorithm and output. Figure 1 shows the basic concept of health index. There are many assessment models available in finding the final value of health index.

In addition to the theory, this paper presents the results of transformer condition assessment using Assessment Model A, B, C and D. These are done in order to examine the steps and the output of the final health index. The input parameters for the calculation are limited to dissolved gas analysis, oil quality analysis and furan analysis. The output of the assessments is compared to each other to assess the trend of the output.

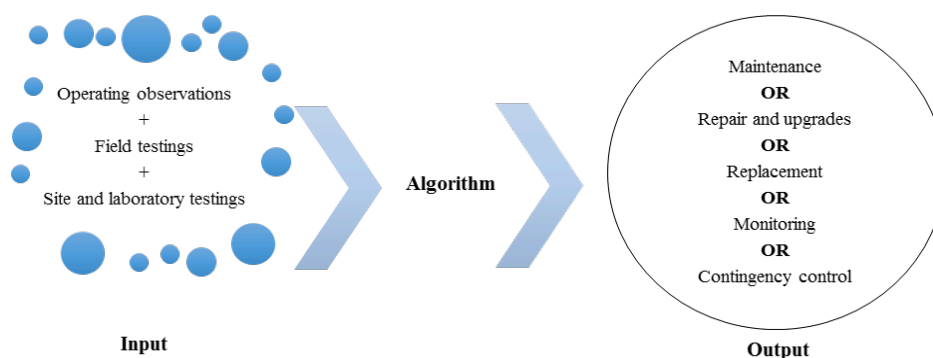


Figure 1. Concept of health index

ASSESSMENT MODEL

Assessment Model A

This model uses scoring and ranking in determining the final health index value for power transformer (Jahromi et al., 2009; Naderian et al., 2008). The input parameters for this model consist of results of operating observations, field inspections and site and laboratory testing. It will be then converted to a quantitative index which will identify the overall condition of a

transformer. Some of the inputs are dissolved gas analysis, oil quality, furfural, power factor, tap changer, load history and maintenance data.

The factor for each parameter (F_i) is determined by using scoring and weighting for all component in a parameter (if there are many components in a parameter). The needs for parameter factor determination is to combine all the components into one quantitative index. The scoring (S_i) value is determined by the recommendation limit from IEEE and IEC. Weighting (W_i) factor for the parameter is usually justified by subjective judgment from the experts. The parameter factor is then converted to health index factor (HIF) by using a certain range. The range is divided into five conditions which are good ($A=4$), acceptable ($B=3$), need caution ($C=2$), poor ($D=1$) and very poor ($E=0$). Next, the final health index is calculated by using Equation (1). The output of the health index is determined by the value of 100 which means good condition to 0 which means very poor condition. Figure 2 shows the flow for determining the final health index value for a transformer.

$$HI = 60\% \times \frac{\sum_{j=21}^{21} K_j HIF_j}{\sum_{j=1}^{21} 4K_j} + 40\% \frac{\sum_{j=22}^{24} K_j HIF_j}{\sum_{j=22}^{24} 4K_j} \quad (1)$$

K_j = weighting factor for parameter

HIF_j = health index factor

60% = weighting factor assigned to transformer

40% = weighting factor assigned to LTC



Figure 2. HI value determination

Assessment Model B

In this model, scoring and ranking is used to determine final value of health index (Haema et al., 2012; Haema et al., 2013). The input parameters are divided into three types of tests: electrical tests, insulating oil test and visual inspection. Some parameters are power factors, dissolved gas analysis for both main tank and OLTC compartment, furfural, oil quality for both main tank and OLTC compartment and visual inspection.

The scoring and weighting value is similar to the value from Naderian assessment method. The method for finding the final value of health index is similar to Naderian assessment model. The difference between this method and Naderian assessment method is the equation for factor of each parameter. In this method, the denominator for finding factor (F_i) is maximum score

(S_i) multiplied with weighting (W_i). The equation factor (F_i) is then multiplied by 100. Final health index value is calculated using Equation (2).

$$(\%)HI = \left(0.6 \frac{\sum_{j=1}^{j=17} (K_j \times HIF_j)}{\sum_{j=1}^{j=17} (HIF_{max} \times K_j)} + 0.4 \frac{\sum_{j=18}^{j=21} (K_j \times HIF_j)}{\sum_{j=18}^{j=21} (4 \times K_j)} \right) \quad (2)$$

K_j = weighting factor for parameter

HIF_j = health index factor

0.6 = weighting factor assigned to transformer

0.4 = weighting factor assigned to LTC

Assessment Model C

This model has three tiers (Ghazali et al., 2008, Ghazali et al., 2009). Tier 1 is the baseline audit for the transformer fleet to assess the presence of fault, quality of insulation oil, insulating paper degradation level, physical, thermal and operating performance. Tier 2 is applied if the result of Tier 1 is abnormal or below 55. Tier 3 is applied if the result of Tier 2 is abnormal or below 55. The input parameters involved for Tier 1 are dissolved gas analysis, oil quality analysis, furfural analysis, inspection on physical conditions and operating performance and thermography. For Tier 2, transformer turns-ratio measurement, winding resistance measurement, dielectric dissipation factor/tan delta measurement, excitation current measurement, insulation resistance and polarisation index (PI). For Tier 3, frequency response analysis (FRA) and partial discharge measurement (PD).

The scoring of the condition of a parameter is determined by referring to IEEE, IEC, and Bureau of Reclamation (*Facilities Instructions, Standards and Techniques: Transformer Diagnostics (FIST 3-31)*, 2003). The score of the parameter is ranked from 3 to 0. Next, the value of rank is converted to a fix amplified ranking number value which are 3 for 20, 2 for 12, 1 for -18 and 0 for -20. The total ranking score is calculated by multiplying amplified ranking number and weighting factor. To obtain final Tier 1 transformer condition index (TCI), percentage estimated life used above 100% is subtracted from the sum of individual total ranking score (A). The similar step of calculating final value Tier 1 is applied to obtain the final value of TCI for Tier 2 and Tier 3. Output ranked from 100 (good) to <10 (very poor).

Assessment Model D

This model also has two tiers for assessing the condition of a transformer (Malik et al., 2012). Tier 1 shows the transformer condition assessment summary and Tier 2 indicates the transformer condition summary. The input parameters for Tier 1 are insulating oil analysis (DGA & furan), power factor and excitation current tests, operation and maintenance history, mechanical parts (bushing, tank, cooling). The input parameters for Tier 2 are turn ratio and sweep frequency response analysis (SFRA).

The score and weighting factor for each parameter in Tier 1 are determined by referring to the standard set by Bureau of Reclamation. Total score for each indicator is obtained by multiplying the score and weighting factor. Sum of the individual indicator is named transformer condition index. Net transformer is defined by Tier 1 transformer condition index minus Tier 2 adjustment. Output ranked from 0 (poor) to 10 (good).

ASSESSMENT RESULT AND DISCUSSION

Four transformer condition assessment models have been performed on 73 units of transformer. The age of the transformers is between 1 and 30 years. The input parameter is limited to dissolved gas analysis, oil quality analysis and furan analysis. The output value of health index for Assessment Model A, B and C assessment model are between 0 and 100 with 0 denoting ‘very poor’ condition and 100 denoting ‘very good’ condition of a transformer. For Assessment Model D, the value range of health index is from 0 to 10; 0 indicates ‘poor’ condition and 10 indicates ‘good’ condition of a transformer. Figure 3(a), 3(b), 3(c), and 3(d) indicate the average condition of the fleet to age. Units which are above the regression line are in better

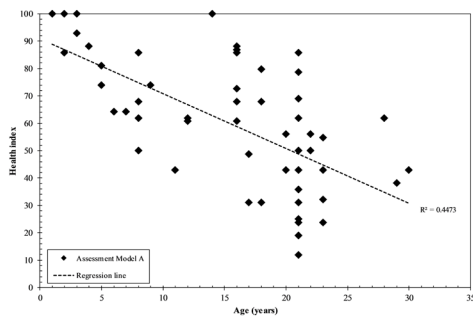


Figure 3(a). Health index as a function of age and linear relation for Assessment Model A

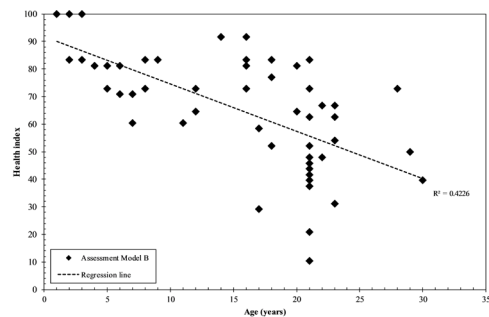


Figure 3(b). Health index as a function of age and linear relation for Assessment Model B

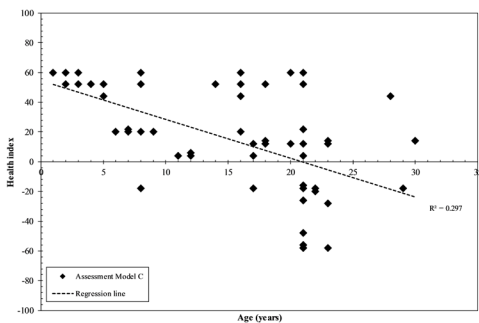


Figure 3(c). Health index as a function of age and linear relation for Assessment Model C

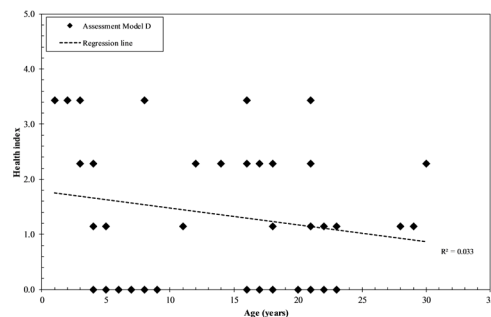


Figure 3(d). Health index as a function of age and linear relation for Assessment Model D

condition compared with the units below the regression line. This is because most of the values of health index on the upper side of regression line show ‘fair’ to ‘very good’ condition of the transformer. The same value of health index for different ages of transformers is usually because their health condition depends on the operation or loading history for a transformer. For Assessment Model D, the value of health index shows poor condition due to the limited data for calculation as the input for Tier 1 are oil analysis, power factor and excitation current test, operation and maintenance history and age.

Value of coefficient of determination, r^2 is a measure of how well the regression line represents the plotted data. Figure 4 shows the comparison of regression line obtained from four transformer assessment models. From the analysis, the range of r^2 is from 0.03299 to 0.44727. Assessment Model A shows the highest value of r^2 among all models. Assessment Model D shows the lowest value of r^2 . This value shows poor correlation between the value of health index to the age of the transformer. Figure 5 presents the trend shape comparison of all models. It can be seen that Assessment Models A, B and C show almost the same trends compared with Assessment Model D. The different value of the output is because of the different value of scoring and weighting used for calculating the final value of health index. The value of health index for Assessment Model C portrayed a negative value because of the amplified ranking number used in the calculation. This condition also shows that the units which are below 55 need to perform Tier 2 and if the condition shows an abnormal result, Tier 3 will be performed. The output shape of Assessment Model D is different because there is limited data for Tier 1 and Tier 2.

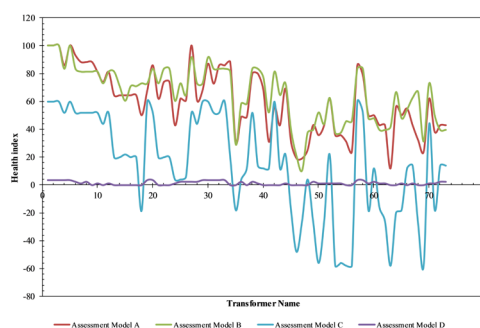
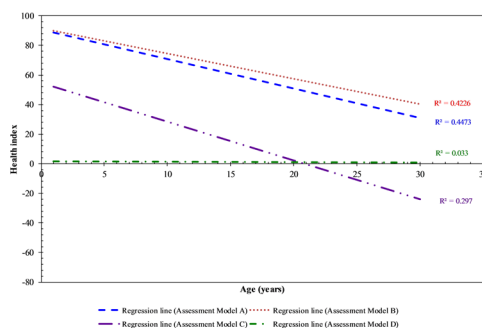


Figure 4. Regression line for all assessment models Figure 5. Waveshape for all assessment models

CONCLUSION

Evaluation of transformer health index using Assessment A, B, C and D have been presented in this paper. This study examined the methods to obtain transformer health index and trend of final output of health index for all methods. There is no strong correlation between health index and age of transformers as the value of health index of the transformer is reflected by the operation and the loading history of a transformer. Assessment Model A and B show the highest and second highest value of r^2 compared with other methods. This is due to the large weighting factor assigned to dissolved gas analysis, oil quality analysis, and furan analysis. The low value of r^2 for Assessment Model C and D is due to lack of data for the input.

Based on the transformer health index application, it helps asset managers to monitor the condition of their assets. Further action such as maintenance, repair and upgrades, replacement, monitoring and contingency control can be undertaken based on the transformer health index. It will also increase the ability of utility company to provide the best electricity supply to the end user without interruption. This is because in developing countries, the need for continuous power supply is crucial for industrial, commercial and residential areas. Hence, through a comprehensive transformer health index method, there will be no unplanned outage during in-service. Further investigation is needed to improve the accuracy of the transformer health index.

ACKNOWLEDGEMENT

The authors thank Universiti Putra Malaysia for its financial support under PUTRA IPB scheme, colleagues for their guidance and support.

REFERENCES

- Abiri-Jahromi, A., Parvania, M., Bouffard, F., & Fotuhi-Firuzabad, M. (2013). A Two-Stage Framework for Power Transformer Asset Maintenance Management - Part I: Models and Formulations. *IEEE Transactions on Power Systems*, 28(2), 1395–1403. <http://doi.org/10.1109/TPWRS.2012.2216903>
- Abiri-Jahromi, A., Parvania, M., Bouffard, F., & Fotuhi-Firuzabad, M. (2013). A Two-Stage Framework for Power Transformer Asset Maintenance Management - Part II: Validation Results. *IEEE Transactions on Power Systems*, 28(2), 1404–1414. <http://doi.org/10.1109/TPWRS.2012.2216904>
- Abu-Elanien, A. E. B., & Salama, M. M. A. (2010). Asset Management Techniques for Transformers. *Electric Power Systems Research*, 80(4), 456–464. <http://doi.org/10.1016/j.epsr.2009.10.008>
- Abu-Elanien, A. E. B., Salama, M. M. A., & Ibrahim, M. (2011). Determination of Transformer Health Condition Using Artificial Neural Networks. In *International Symposium on Innovations in Intelligent Systems and Applications* (pp. 1–5).
- Abu-Elanien, A. E. B., Salama, M. M. A., & Ibrahim, M. (2012). Calculation of a Health Index for Oil-Immersed Transformers Rated Under 69 kV Using Fuzzy Logic. *IEEE Transactions on Power Delivery*, 27(4), 2029–2036. <http://doi.org/10.1109/TPWRD.2012.2205165>
- Arshad, M., Islam, S., & Khaliq, A. (2014). Fuzzy Logic Approach in Power Transformers Management and Decision Making. *IEEE Transactions on Dielectrics and Electrical Insulation*, 21(5), 2343–2354. <http://doi.org/10.1109/TDEI.2014.003859>
- Brittes, J. L. P., Nunes, E., Jardini, J. A., Magrini, L. C., & Kayano, P. S. D. (2014). T&ERTTA, Technical & Economical Real Time Transformer Assessment: An Innovative Approach on Power Transformer Life Cycle Management. In *Transmission and Distribution Conference and Exposition - Latin America (PES T&D-LA), 2014 IEEE PES* (pp. 1–6). <http://doi.org/10.1109/TDC-LA.2014.6955186>
- Dominelli, N. (2004). Equipment Health Rating of Power Transformers. *Conference Record of the 2004 IEEE International Symposium on Electrical Insulation*, (September), 19–22. <http://doi.org/10.1109/ELINSL.2004.1380501>
- Facilities Instructions, Standards and Techniques: Transformer Diagnostics (FIST 3-31). (2003).

- Ghazali, Y. Y. Z., Talib, M. A., & Ahmad Rosli, H. (2008). Condition Assessment of Power Transformers in TNB Distribution System and Determination of Transformer Condition Index. In *Conference of the Electric Power Supply Industry (CEPSI)*.
- Ghazali, Y. Y. Z., Talib, M. A., & Ahmad Rosli, H. (2009). TNB Experience in Condition Assessment and Life Management of Distribution Power Transformers. In *Electricity Distribution - Part 1, 2009. CIRED 2009. 20th International Conference and Exhibition on* (pp. 1–4).
- Haema, J., & Phadungthin, R. (2012). Condition Assessment of the Health Index for Power Transformer. In *Power Engineering and Automation Conference (PEAM), 2012 IEEE* (pp. 1–4). <http://doi.org/10.1109/PEAM.2012.6612413>
- Haema, J., & Phadungthin, R. (2013). Development of Condition Evaluation for Power Transformer Maintenance. In *4th International Conference on Power Engineering, Energy and Electrical Drives* (pp. 620–623).
- Jahromi, A. N., Piercy, R., Cress, S., Service, J. R. R., & Fan, W. (2009). An Approach to Power Transformer Asset Management Using Health Index. *IEEE Electrical Insulation Magazine*, 25(2), 20-34. <http://doi.org/10.1109/MEI.2009.4802595>
- Ma, H., Saha, T. K., Ekanayake, C., & Martin, D. (2015). Smart Transformer for Smart Grid-Intelligent Framework and Techniques for Power Transformer Asset Management. *IEEE Transactions on Smart Grid*, 6(2), 1026–1034. <http://doi.org/Doi.10.1109/Tsg.2014.2384501>
- Malik, H., Azeem, A., & Jarial, R. K. (2012). Application Research Based on Modern-Technology for Transformer Health Index Estimation. In *International Multi-Conference on Systems, Signals and Devices, SSD 2012 - Summary Proceedings* (pp. 18–21). <http://doi.org/10.1109/SSD.2012.6198012>
- Naderian, A., Cress, S., Piercy, R., Wang, F., & Service, J. (2008). An Approach to Determine the Health Index of Power Transformers. In *International Symposium on Electrical Insulation (ISEI 2008)* (pp. 192–196). <http://doi.org/978-1-4244-2092-6/08>
- Trappey, A. J. C., Trappey, C. V., Ma, L., & Chang, J. C. M. (2015). Intelligent Engineering Asset Management System for Power Transformer Maintenance Decision Supports Under Various Operating Conditions. *Computers and Industrial Engineering*, 84, 3–11. <http://doi.org/10.1016/j.cie.2014.12.033>

Top-oil Temperature Model for Transformers based on Nonlinear Thermal Resistance, Lumped Capacitance and Thermal-electrical Analogy

M. H. Roslan^{1,2*}, N. Azis², J. Jasni² and Z. Ibrahim²

¹Faculty of Engineering, Universiti Pertahanan Nasional Malaysia, 57000 Kem Sg Besi, Malaysia

²Centre for Electromagnetic and Lightning Protection Research, Universiti Putra Malaysia, 43400 UPM, Serdang, Selangor, Malaysia

ABSTRACT

Top-Oil Temperature (TOT) is one of the basic components to estimate the Hot-Spot temperature (HST) of the transformers. This paper presents an alternative TOT model based on the heat transfer theory that utilises Nonlinear Thermal Resistance (NTR) and Lumped Capacitance (LC) approaches. It is applied in a thermal-electrical analogy and the heat transfer equivalent equation is determined. This model is tested on a measured TOT of 250 MVA ONAF and 400 MVA ONAF transformers obtained from IEC 60076-7 and previous research. A comparison of TOT is carried out with the existing models IEC 60076-7 exponential and IEEE Loading Guide clause 7 methods. It is found that the thermal model based on the NTR and LC approach could determine the measured TOT closer than the existing methods available in the standards.

Keywords: Top-oil temperature, thermal model, transformers

INTRODUCTION

Transformers are static devices which consist of windings and a core that can transmit

electrical power by electromagnetic induction between primary and secondary circuits at the same frequency but at different voltages levels (Winders, 2002). In a power system, transformers are one of the most important and expensive pieces of equipment. Due to this expense, it is important to maintain transformers in-service for as long as possible. One of the stresses that can lead to transformer failure is thermal stress which refers to the winding hottest spot temperature (HST) which can cause advance degradation of the oil and paper in transformers. It is well

ARTICLE INFO

Article history:

Received: 24 August 2016

Accepted: 03 Jun 2017

E-mail addresses:

hakirinroslan@gmail.com (M. H Roslan),

norhafiz@upm.edu.my (N. Azis),

jas@upm.edu.my (J. Jasni),

zulib78@gmail.com (Z. Ibrahim)

*Corresponding Author

known that the HST consists of Ambient Temperature (AT), top-oil temperature rise and hotspot temperature rise over the top-oil temperature (“IEEE Guide for Loading Mineral-Oil-Immersed Transformers,” 1996; Standard; Susa, Lehtonen, & Nordman, 2005). Generally, the HST can be obtained by two methods, which are direct measurement using a fibre optic sensor and a thermal model calculation. There are two standards that provide the thermal model calculation, namely the IEC 60076-7 and IEEE C57.91-1995 (“IEEE Guide for Loading Mineral-Oil-Immersed Transformers,” 1996; Standard). According to IEC 60076-7, there are two methods that can be used to determine the HST which are the exponential and differential approaches. The exponential method is suitable for a load variation according to a step function (Standard). On the other hand, the differential method is suitable for online monitoring of the HST (Standard). According to IEEE C57.91-1995, there are also two methods that can be used to determine the HST known as Clause 7 and the Annex G method (“IEEE Guide for Loading Mineral-Oil-Immersed Transformers,” 1996). The Clause 7 method is straightforward, but it is less accurate as compared to Annex G. However, the Annex G method is quite complex and requires a thermal parameter which is not usually available in the normal heat run test report.

Nomenclature

A	Area
C	Parameter with unit $W/m^2.K^{(1+n)}$
C_{oil}	Thermal capacitance
I	Load current
K	Load factor
n	A constant
P_w	Copper losses
P_E	Eddy losses
P_s	Stray losses
q_{cu}	Heat generated by load losses
q_{fe}	Heat generated by no load losses
R	Ratio of load losses at rated current to no load losses
R_{oil}	Oil thermal resistance
θ_a	Ambient temperature
θ_{oil}	Top-oil temperature
θ_{hs}	Hotspot temperature
$\Delta\theta_{oil,rated}$	Top-oil rise at rated
τ_{oil}	Oil time constant
rated	Subscript indicates rated value

A number of thermal models have been developed to estimate transformer thermal behaviour and to predict the HST and TOT with better accuracy (Pierce, 1992; Susa & Lehtonen, 2006a, 2006b; Susa et al., 2005; Swift, Molinski, Bray, & Menzies, 2001; Swift, Molinski, &

Lehn, 2001; Weigen, Chong, & Yuxin, 2009). One of the models, the Pierce model, indicates that there is a time lag between the top-oil temperature rise and the oil temperature rise inside the winding cooling ducts during overloading which leads to higher prediction of the HST (Pierce, 1992). The Swift model introduces the concept of a thermal-electrical analogy which is based on a simple equivalent RC circuit (Swift, Molinski, & Lehn, 2001). The thermal model applies a current source analogy to represent the heat input due to losses and a nonlinear resistance analogy to represent the effect of air or coil cooling convection currents (Swift, Molinski, & Lehn, 2001). The Dejan Susa model is based on a thermal-electrical analogy model which takes into account oil viscosity changes and loss variation with temperature. Other thermal models introduce the NTR and LC in the computation of TOT and HST (Susa & Lehtonen, 2006a, 2006b; Susa et al., 2005). In this paper, the researchers aim to develop an alternative TOT model which is based on the heat transfer and thermal-electrical analogy theory. The alternative TOT model also used the approximation of convection coefficient h which eliminates the input parameter such as viscosity. The input parameter of the alternative TOT model is tied with the parameter obtained from normal heat run test report which is not required input parameter such as oil temperature in cooling duct obtained from special heat run test report. This TOT model is also suitable for dynamic loading and ambient temperature, however the existing model in IEC 60076-7 exponential and IEEE C57.91-1995 Clause 7 are not suitable for this. The concept of the TOT model is presented and tested based on the measured TOT available in the standards and previous research.

HEAT TRANSFER THEORY APPLICATION TO TRANSFORMERS

Application of Nonlinear Thermal Resistance

Heat transfers occur when there is a spatial temperature difference in a medium or between media, that always flows from hot to cold (Bergman, Incropera, & Lavine, 2011). In transformers, the heat source originates from transformer losses (load and no load losses) which flow through the oil to the tank of the transformer as shown in Figure 1 (Perez, 2010). The basic components of a transformer are the windings, core, transformer oil and tank. The heat flow inside a transformer is also shown in Figure 1.

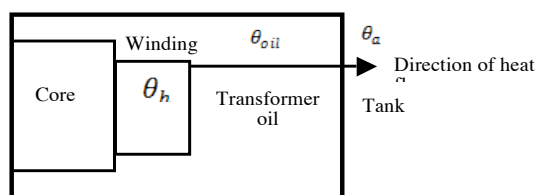


Figure 1. Heat flow inside a transformer (Swift, Molinski, & Lehn, 2001)

θ_{hs} is the HST which is the hottest temperature in a transformer and θ_a is the AT which is the coolest temperature. Heat will transfer through all the medium to the tank from θ_{hs} to θ_a . All mediums have their own thermal resistance which acts like a dissipation element. This

thermal resistance is known as a nonlinear thermal resistance (Bergman et al., 2011; Susa et al., 2005; Swift, Molinski, & Lehn, 2001). Heat sources in a transformer are generated from no load and load losses.

Load losses are copper losses q_{cu} generated from the windings and no load losses are core losses q_{fe} generated from the metal parts such as the tank, core etc. (Perez, 2010). For θ_{hs} the heat source comes from copper losses, q_{cu} and for θ_{oil} , the heat source comes from q_{cu} and q_{fe} . Based on the heat flow in Figure 1, the heat transfer thermal resistance equivalent circuit with heat sources was determined and shown in Figure 2.

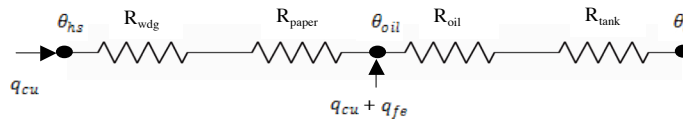


Figure 2. Thermal resistance equivalent circuit with heat source

The thermal resistance of tank R_{tank} can be neglected because it is a perfect heat conductor (Swift, Molinski, & Lehn, 2001). The heat transfer thermal resistance equivalent circuit can be re-drawn as shown in Figure 3.

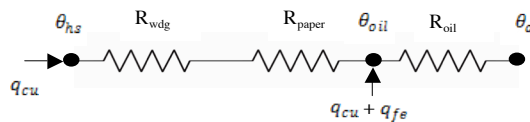


Figure 3. Thermal resistance equivalent circuit with heat sources

Application of lumped capacitance method

The thermal resistance equivalent circuit can only be used to determine the steady state condition. The LC approach is required for application in the thermal model under transient conditions (Bergman et al., 2011). In order to use this approach, the Biot number Bi must be below one (Bergman et al., 2011; Swift, Molinski, & Lehn, 2001). The Biot number is the ratio of the thermal resistance of conduction divided by the thermal resistance of convection. For transformers, it is the winding thermal resistance divided by the oil thermal resistance. This method uses capacitance as a component added to the heat transfer thermal resistance equivalent circuit which can be represented as an RC circuit as shown in Figure 4.

Thermal-electrical analogy

The thermal equivalent circuit which utilises the NTR and LC was used to derive the heat transfer equation. The thermal-electrical analogy was applied since its concept was the same as the thermal equivalent circuit. The thermal-electrical analogy variables are shown in Table 1.

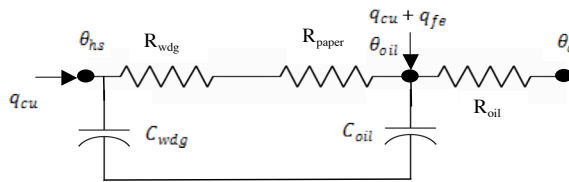


Figure 4. Thermal resistance equivalent circuit with application of lumped capacitance method

Table 1
Thermal-Electrical Analogy Variables (Susa et al., 2005; Swift, Molinski, & Lehn, 2001)

	Thermal	Electrical
Through Variable	Heat source, q units in watts	Current, i units in amperes
Across Variable	Temperature, θ unit in $^{\circ}\text{C}$	Voltage, v units in volts
Dissipation element	Thermal resistance, R_{th} unit in $^{\circ}\text{C}/\text{watt}$	Electrical resistance, R_{el} units in ohms
Storage element	Thermal capacitance, C_{th} unit in Joules/ $^{\circ}\text{C}$	Electrical capacitance units in Farads

Based on the thermal-electrical analogy variable and thermal equivalent circuit, a simple equivalent RC circuit Figure 5(a) was developed to represent the thermal heat transfer equivalent circuit. This can be divided into two models, namely the HST model and TOT model as shown in Figure 5(b). In this paper, only the TOT model is discussed.

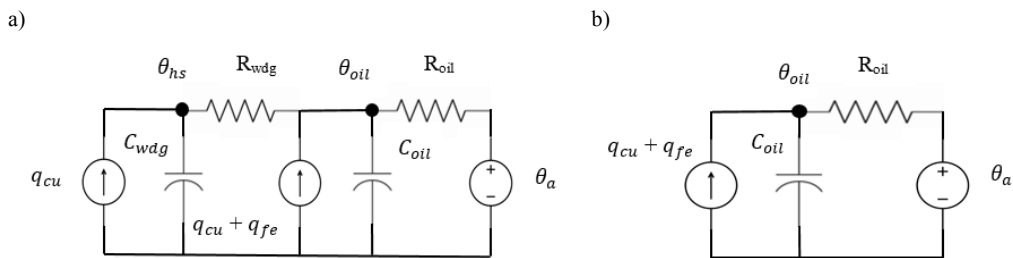


Figure 5. (a) Thermal heat transfer equivalent circuit; (b) Top-oil temperature thermal-electrical equivalent circuit

TOP-OIL TEMPERATURE MODEL

Based on the TOT thermal-electrical equivalent circuit in Figure 5(b), the differential equation can be derived by Equation (1).

$$q_{fe} + q_{cu} = C_{oil} \frac{d\theta_{oil}}{dt} + \frac{(\theta_{oil} - \theta_a)}{R_{oil}} \tag{1}$$

According to the heat transfer theory and based on previous studies (Bergman et al., 2011; Susa et al., 2005), the oil thermal resistance, R_{oil} is given by Equation (2).

$$R_{oil} = \frac{1}{h \cdot A} \tag{2}$$

Where A is the area and h is the convection coefficient. h is a complex coefficient because it can be affected by multiple factors. According to the heat transfer theory, h varies with the temperature difference between the object and the fluid. In this case, h is approximated by the expression in Equation (3) (Bergman et al., 2011).

$$h = C(\theta_s - \theta_\infty)^n \tag{3}$$

Where n is constant and the unit of C is $W/m^2 \cdot K^{(1+n)}$. θ_s refers to TOT θ_{oil} and θ_∞ refers to AT θ_a . The equation can be simplified as shown in Equation (4).

$$h = C(\Delta\theta_{oil})^n \tag{4}$$

Substitution of Equation (4) into the oil thermal resistance R_{oil} leads to Equation (5).

$$R_{oil} = \frac{1}{C \cdot A (\Delta\theta_{oil})^n} \tag{5}$$

Equation (5) is substituted in Equation (1) which leads to Equation (6).

$$q_{fs} + q_{cu} = C_{oil} \frac{d\theta_{oil}}{dt} + \frac{(\theta_{oil} - \theta_a)}{\frac{1}{C \cdot A (\Delta\theta_{oil})^n}} \tag{6}$$

The rated value for NTR, $R_{oil,rated}$ is determined based on Equation (7).

$$R_{oil,rated} = \frac{1}{C \cdot A (\Delta\theta_{oil,rated})^n} \tag{7}$$

The rated top-oil temperature rise over the ambient temperature $\Delta\theta_{oil,rated}$ is given by Equation (8).

$$\Delta\theta_{oil,rated} = (q_{fs} + q_{cu})_{rated} \cdot R_{oil,rated} \tag{8}$$

The definition of top-oil time constant τ_{oil} is obtained according to Equation (9).

$$\tau_{oil} = R_{oil,rated} C_{oil,rated} \tag{9}$$

The R constant is known as the ratio of load losses at the rated current to the no load losses which is determined according to Equation (9).

$$R = \frac{q_{cu}}{q_{fe}} \tag{10}$$

The K constant is known as the ratio of the load current to the load current and is calculated according to Equation (11).

$$K = \frac{I}{I_{rated}} \tag{11}$$

Finally, Equation (6) is reduced to Equation (12) which is the final form of the TOT model.

$$\frac{1+R.K^2}{1+R} \cdot \Delta\theta_{oil,rated} = \tau_{oil} \cdot \frac{d\theta_{oil}}{dt} + \frac{(\theta_{oil} - \theta_a)^{1+n}}{\Delta\theta_{oil,rated}^n} \tag{12}$$

For testing the alternative thermal model constant, *n* is obtained from (Susa et al., 2005) which mainly depends on the cooling method. For the oil time, constant τ_{oil} is obtained from the thermal parameter model in IEC 60076-7. If the mass of fluid is known, τ_{oil} can be calculated using the equations in (Susa et al., 2005).

RESULTS AND DISCUSSION

Table 2 and Table 3 show the load test and input data used for running the alternative thermal model. The thermal model results are also compared with the exponential model in IEC 60076-7 and the Clause 7 model in IEEE C57.91-1995. Figure 6 shows the computed TOT obtained by the alternative thermal model agrees well with the measured values as compared to the other thermal models. It is because of the alternative TOT model have only one constant *n* which controls the sensitivity of TOT value. In order to obtain the ideal value of *n*, case studies related to estimating the value of *n* that satisfied all results need to be done. The TOT obtained from the IEC 60076-7 exponential model overshoots for an increased load factor, especially for a transformer unit at 250 MVA ONAF. Since the exponential model in IEC 60076-7 consists of the constant *k*₁₁ and an exponent *x* which controls the sensitivity of the TOT model, due to this condition, the shape of the rise and fall of the exponential function is difficult to control. The TOT obtained by the IEEE C57.91-1995 Clause 7 model was closer to the alternative thermal model.

Table 2
 Performed load test (Standard) (Susa et al., 2005)

Transformer Units	Varying load Current
250 MVA ONAF	1.00pu/3h+0.60pu/3h+1.50pu/2h+0.30pu/3h+2.10pu/0.33h
400 MVA ONAF	1.00pu/5h+0.65pu/5h+1.60pu/3h

Table 3
 Input data for Thermal Model (Standard) (Susa et al., 2005)

Quantity	Transformer / Winding	
	250/118	400/120
KVA base	250 000	400 000
P_w/W	411 780	637 100
P_E/W	29 469	59 778
P_S/W	43 391	65 772
$\Delta\theta_{oil, rated}/K$	38.3	38.0
Mfluid/kg	73 887	91 397
$\theta_{oil, i}/^{\circ}C$	38.3	30.9

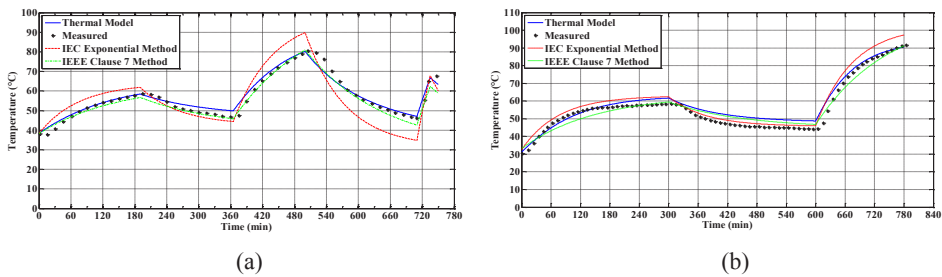


Figure 6. Top-oil temperature of (a) 250MVA ONAF; (b) 400MVA ONAF transformers

CONCLUSION

Based on the heat transfer theory which is the application of the NTR and LC method, the thermal-electrical analogy equivalent circuit was formed. The main factor of the alternative TOT model is the approximation of the convection coefficient h which eliminates the needs of information such as viscosity. Then, all the input parameters for running the alternative TOT model are tied with the parameters of normal heat run test report. The alternative TOT model was developed and tested on two different transformer units. The TOT obtained by the alternative TOT model agrees with the measured values compared with the IEC 60076-7 exponential model. The alternative TOT model results are also closer to IEEE C57.91-1995 Clause 7 model. Thus, the TOT model is fit for online monitoring system, for instance, dynamic loading and ambient temperature.

ACKNOWLEDGEMENT

The authors would like to thank Ministry of Education, Universiti Pertahanan Nasional Malaysia and Universiti Putra Malaysia for their funding under FRGS scheme (03-02-13-1280FR), (03-02-13-1279FR) and Putra IPB schemes (GP-IPB/2014/9440801) respectively. Special thanks to Malaysia Transformer Manufacturing Sdn. Bhd. for its technical support.

REFERENCES

- Bergman, T. L., Incropera, F. P., & Lavine, A. S. (2011). *Fundamentals of heat and mass transfer*. John Wiley & Sons.
- IEEE Guide for Loading Mineral-Oil-Immersed Transformers. (1996). *IEEE Std C57.91-1995*, i. doi: 10.1109/IEEESTD.1996.79665
- Perez, J. (2010). *Fundamental principles of transformer thermal loading and protection*. Paper presented at the Protective Relay Engineers, 2010 63rd Annual Conference for.
- Pierce, L. W. (1992). *Predicting liquid filled transformer loading capability*. Paper presented at the Petroleum and Chemical Industry Conference, 1992, Record of Conference Papers., Industry Applications Society 39th Annual.
- Standard, I. 60076-7 Power Transformer-Part 7: 'Loading Guide for Oil-Immersed Power Transformers': IEC.
- Susa, D., & Lehtonen, M. (2006a). Dynamic thermal modeling of power transformers: further Development-part I. *IEEE Transactions on Power Delivery*, 21(4), 1961-1970.
- Susa, D., & Lehtonen, M. (2006b). Dynamic thermal modeling of power transformers: Further development-Part II. *IEEE Transactions on Power Delivery*, 21(4), 1971-1980.
- Susa, D., Lehtonen, M., & Nordman, H. (2005). Dynamic thermal modelling of power transformers. *IEEE Transactions on Power Delivery*, 20(1), 197-204.
- Swift, G., Molinski, T. S., & Lehn, W. (2001). A fundamental approach to transformer thermal modeling. I. Theory and equivalent circuit. *IEEE Transactions on Power Delivery*, 16(2), 171-175.
- Swift, G., Molinski, T. S., Bray, R., & Menzies, R. (2001). A fundamental approach to transformer thermal modeling. II. Field verification. *IEEE Transactions on Power Delivery*, 16(2), 176-180.
- Weigen, C., Chong, P., & Yuxin, Y. (2009). Power transformer top-oil temperature model based on thermal–electric analogy theory. *European Transactions on Electrical Power*, 19(3), 341-354.
- Winders, J. (2002). *Power transformers: principles and applications*: CrC Press.



Effect of Moisture on Electrical Response of Sand and Clay under High Impulse Voltage Applications

Chun Lim, Siow^{1*}, Mohd Syariffuddin, Johari¹ and Chandima, Gomes²

¹Department of Electrical and Electronic Engineering, Faculty of Engineering, Multimedia University, Cyberjaya, Universiti Putra Malaysia, 43400 UPM, Serdang, Selangor, Malaysia

²Center for Electromagnetic and Lightning Protection, Universiti Putra Malaysia, 43400 UPM, Serdang, Selangor, Malaysia

ABSTRACT

Soil plays an important role in ground designing. Engineers normally consider only soil resistivity under normal or steady state condition when designing the grounding system. Under certain circumstances such as lightning, electrical response of the soil will change accordingly and thus, the performance of the grounding system will be affected. The purpose of this study is to investigate the effect of moisture content on the electrical behaviour of sand and clay under high impulse voltage condition. Both soil samples are dried in the oven at $110 \pm 5^\circ\text{C}$ to remove the water content until became 0%. The samples are subjected to 30 shots of standard (1.2/50 μs) lightning impulse voltage for both positive and negative impulse polarities. This is followed by moistening the samples with 5% amount of water over the volume of the samples. The corresponding V50% for both sand and clay was calculated and the value obtained was converted to standard atmospheric condition. The voltage at breakdown and time to breakdown for each soil sample was analysed a statistical analysis conducted for these two parameters to determine if type of soil and moisture content have an effect on the breakdown voltage. In general, it was found that clay is more efficient in neutralising high impulse voltage than sand likely due to the former's low resistivity and porosity.

Keywords: Breakdown voltage, soil, electrical grounding, sand, clay

ARTICLE INFO

Article history:

Received: 24 August 2016

Accepted: 03 Jun 2017

E-mail addresses:

chunlim87@gmail.com (Chun Lim, Siow),

syariffudin_91@yahoo.com (Mohd Syariffuddin, Johari),

chandima.gomes@gmail.com (Chandima, Gomes)

*Corresponding Author

INTRODUCTION

The study of electrical properties of soil yields invaluable information for research fields which include agriculture, geophysics and electrical grounding system (Lim et al., 2012, 2013a). In any electrical installation systems, it is pivotal to have an efficient grounding system. The performance of grounding system

is highly dependent on soil characteristic which is predominantly determined by the soil resistivity (Lim et al., 2013b, 2014). Yet, under transient and high voltage condition which is typically produced by lightning, the soil characteristic is significantly different from its static or steady state behaviour (Nor & Griffith, 2006). One way to characterise soil behaviour under high impulse voltage condition is by analysing its 50% breakdown voltage or $V_{50\%}$. This parameter can be used to gauge the ability of soil in discharging high impulse voltage. Soil with lower $V_{50\%}$ is expected to be more conductive within that transient period and vice versa. In addition, two more interesting parameters which can be analysed is the time to breakdown (*TBD*) and voltage at breakdown (*VABD*) of the soil sample (Lim et al., 2015).

Studies of similar nature have examined the response of soil under high impulse voltage condition (Nor & Griffith, 2006; Asimakopoulou et al., 2009). However, there is limited dearth of studies employing the statistical approach especially based on the two said parameters with the most recent one in (Lim et al., 2015). Moisture affects soil resistivity. Yet, the effect of moisture content (MC) in clay and sand on its response to high impulse voltage shot is not discussed extensively in the literature. Most of the past studies have focused on sand (Nor & Ramli, 2003; Cabera et al., 1993). Recent studies have looked at sand and clay. Clay is studied due to the fact that its physical properties are opposite to sand especially in terms of resistivity and porosity (Joffe & Lock, 2010). In addition, clay alongside with sand is also highly researched in terms of its steady state, low frequency resistivity behaviour but rarely in high frequency high voltage condition. Therefore, the primary objective of this research is to analyse and compare the electrical behaviour of both sand and clay in terms of $V_{50\%}$, *TBD* and *VABD* under high impulse voltage condition since sand and clay have contrasting values in terms of soil resistivity (Markiewicz & Klain, 2003). Results provide better understanding on the electrical behaviour of sand and clay under high impulse voltage condition in which the findings are useful for future researchers interested in electrical properties of soil. Protection engineers may also find these findings useful as protective relays may be affected by electrical responses of soil under both static and high voltage transient conditions.

METHODOLOGY

This research project is outlined in Figure 1. Two types of soil samples were used, namely sand and clay. The sand was filtered and sieved to remove the pebbles in order to get pure coarse sand. As for the clay, it was crushed into powder form and then compacted. Both samples were dried in the oven for approximately 16 hours at the temperature of 110 ± 5 °C using a metal container in order to have practically 0% MC (Department of Transportation, 2003). This is to produce soil without MC. Then, 5% water by mass was introduced to these completely dried soil samples before being uniformly mixed in the cylindrical acrylic container. This step is to produce soil with 5% MC. The temperature and relative humidity are measured and recorded at the beginning of the experiment as these parameters are required to convert the experimental values to its equivalent values at standard reference atmospheric condition. This is discussed in the next section.

Each of the soil sample prepared was then subjected to up and down analysis to determine the breakdown voltage for both positive and negative impulse polarities (Lim et al., 2015). The experiment was done for samples with 0% MC followed by samples with 5% of MC. The design setup as shown in Figure 2 consists of a cylindrical acrylic container with inner diameter of 242mm and height of 105mm with the copper rod having an approximate dimension of 15mm diameter and 300mm height. The acrylic container is filled with the samples up to a fixed 65mm for both types of soil. A cylindrical metal plate with diameter of 240mm and thickness of 5mm is placed inside and at the bottom of the acrylic container to guide the impulse current through the soil sample as well as to channel the impulse current directly to the ground through a ground wire whenever there is a breakdown detected through the waveform displayed at the oscilloscope.

The impulse voltage was generated using a 3-stage Marx Generator having the capability of producing standard high impulse voltage ($1.2/50\mu s$) as per IEC standards. For the purpose of this experiment, the generator was configured to operate in two stages with a range of 0V to 130kV per stage of configuration. Each sample is subjected to 30 shots of impulse voltage with fixed 90-second interval between each shot for both polarities to ensure that the soil has regained its initial properties before the next shot is applied. The impulse voltage signal was captured on a DSO09104A Agilent Infinium 9000 Series Oscilloscope which has the specifications of 1GHz, 4 channels and the analog sampling rate of 5GSa/s.

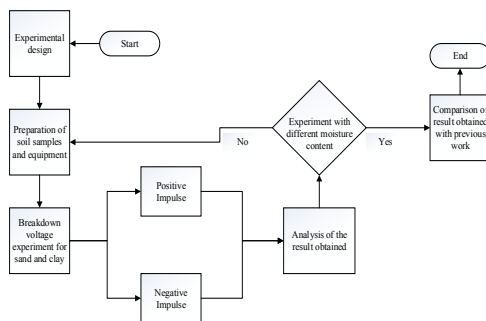


Figure 1. Research flow

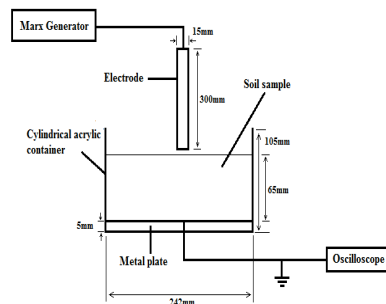


Figure 2. Setup of the experiment

Initially, the soil sample was subjected to random impulse voltage in order to determine the minimum breakdown voltage of the sample, V_0 . Up and down analysis was used in this experiment for both positive and negative impulse polarities in which after V_0 was obtained, it was then followed by stepping up whenever there was breakdown and stepping down whenever there was no breakdown with a step voltage of 2kV. The result from Up and Down analysis was used to calculate the $V_{50\%}$ and standard deviation (SD) of each soil sample using the formula (Campos, 1995). The results of the $VABD$ and TBD were analysed statistically using the independent samples T-test method in the SPSS software. Independent samples T-test compares the means of two unrelated groups and evaluates them. This test will indicate

whether the sand and clay is significantly different from each other by comparing the means between sand and clay soil sample in terms of $VABD$ and TBD .

RESULTS AND DISCUSSIONS

Table 1 depicts the breakdown voltage ($V_{50\%}$) for both positive and negative impulse polarities with 0% and 5% MC. The values shown are the values which have been converted to their corresponding breakdown voltage values under standard atmospheric condition by following the procedures recommended by Hauschild and Lemke (2004) where temperature, $T_0 = 20^\circ\text{C}$ (293 K), absolute air pressure, $P_0 = 1,013$ hPa (1,013 mbar) and absolute humidity, $h_0 = 11$ g/m³. It is clear that the $V_{50\%}$ for positive impulse is higher than the negative impulse and sand has higher breakdown voltage for both polarities compared with clay given the same amount of MC. This implies that clay is more efficient in discharging high impulse voltage compared with sand.

Table 1
Breakdown voltage of sand and clay at standard condition

Applied Voltage	MC (%)	Sample A (Sand)		Sample B (Clay)	
		$V_{50\%}$ (kV)	SD (kV)	$V_{50\%}$ (kV)	SD(kV)
Positive impulse	0	61.2	4.9	46.2	4.2
	5	35.6	2.9	34.4	4.8
Negative impulse	0	50.7	4.7	41.2	2.6
	5	34.2	2.9	32.3	2.5

The comparisons between the voltage traces for both no breakdown and breakdown voltage are shown in Figures. 3, 5, 7 and 9 for positive impulse and Figures 4, 6, 8 and 10 for negative impulse. Whenever breakdown occurs, a sudden collapse of voltage appears which indicates that the soil sample becoming conductive at that particular instant of time where the impulse current can pass through the soil and directly discharge through the grounding wire. It is also observed that the $V_{50\%}$ for positive polarity is higher than negative polarity for all the voltage traces (Figure 3 – Figure 10). Meanwhile, the voltage traces show reduction in $V_{50\%}$ between sand 0% and sand 5% (Figure 3 – Figure 6) for both polarities. The same result can be observed for clay 0% and clay 5% (Figure 7 – Figure 10). The reduction in the $V_{50\%}$ is due to the effect of moisture added to the soil sample which has caused the soil resistivity to decrease, thus increasing the tendency for the soil sample to be more conductive. When a comparison is done between sand and clay for both 0% (Figures 3, 4, 7, 8) and 5% (Figures 5, 6, 9, 10) MC for both polarities, it is found that sand has higher $V_{50\%}$ than clay. This is referring to the fact that the soil resistivity in sand is higher than clay (Markiewicz & Klain, 2003). Note that the above mentioned are based on physical observation. The following provides a statistical analysis.

When 5% amount of moisture is added to the sample, the sand and clay experience lower $V_{50\%}$ in which the efficiency of discharging the impulse voltage is higher than 0% MC. This is possibly due to some of the energy from the impulse voltage are being absorbed by the

water. It is found that there is a gap between no-breakdown and breakdown voltage as shown in Figures. 5, 6, 9 and 10. The reason why the gap for sand is bigger than clay is probably due to the porosity level of clay which is higher than sand. This means that clay particles absorb more water than sand particles, thus, the amount of water left to fill the void (outside the clay particle) between the clay particle is lesser than sand (Joff & Locke, 2010). Energy absorption by water in clay is less than the energy absorption by water in sand. In addition, the presence of moisture has caused a higher amount of reduction of $V_{50\%}$ in sand than clay under both polarities. A possible explanation is again due to the porosity of sand which retains more moisture. Therefore, a significant portion of the impulse current will flow through the moisture in sand.

Positive Impulse

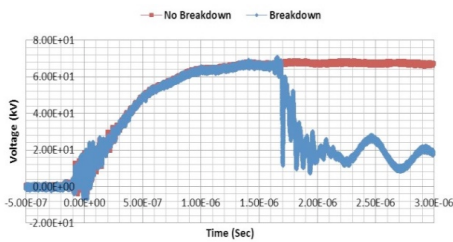


Figure 3. Sand 0% moisture

Negative Impulse

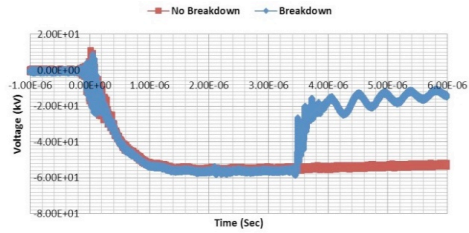


Figure 4. Sand 0% moisture

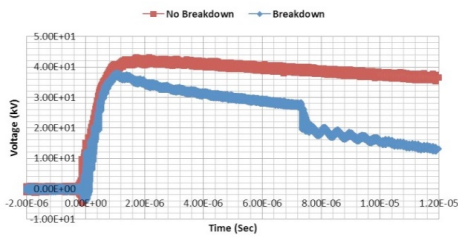


Figure 5. Sand 5% moisture

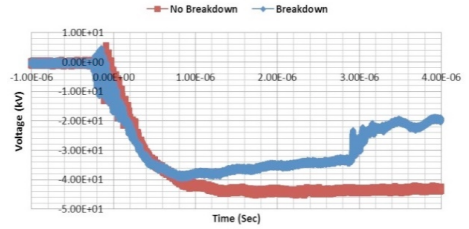


Figure 6. Sand 5% moisture

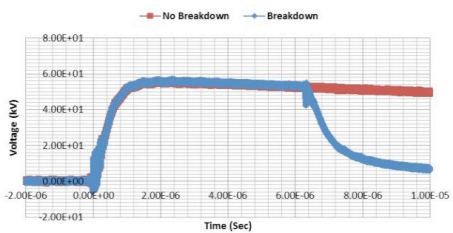


Figure 7. Clay 0% moisture

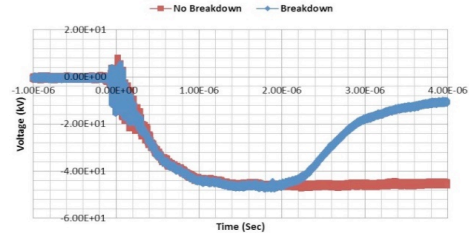


Figure 8. Clay 0% moisture

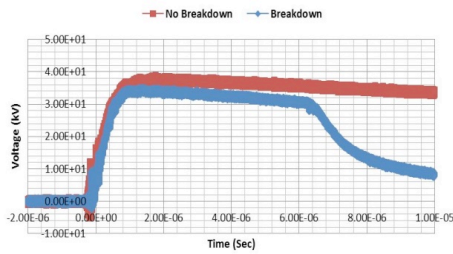


Figure 9. Clay 5% moisture

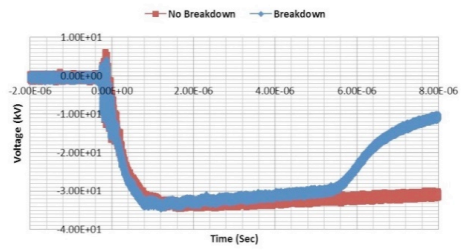


Figure 10. Clay 5% moisture

In sand 0% for both impulse polarities, the voltage profile experiences fluctuation before it reaches stable state upon completion of dampening of the oscillations. The density of oscillation decreases as the sand is moistened. This oscillation is probably due to the breakdown of the small air particles present between the sand particles before it reaches the metal plate connected to the ground wire. When 5% of moisture is added to the sand, the water particles replace the air to fill in the void. Based on Jin et al. (2001), the breakdown voltage of water is five times smaller compared with air in which it can be seen clearly in the graph that oscillation for sand 5% is much smaller than sand 0%. In clay 0% and 5%, there are no traces of oscillation in the breakdown graph. This is due to the particle size of clay (<0.002mm) which is 25 times smaller compared with sand (0.05 mm to 2mm) that caused clay having less air gap to be filled by air (Whitlow, 2004). This could explain why clay does not have any oscillation after the breakdown.

Another two parameters which can be analysed other than $V_{50\%}$ are $VABD$ and TBD . The difference between $VABD$ and $V_{50\%}$ breakdown voltage is that $VABD$ is the potential arise across the soil sample at breakdown event and $V_{50\%}$ is the voltage at which there is 50% probability of the sample experiencing electrical breakdown. The average values for $VABD$ and TBD from the up and down analysis method are depicted in Table 2 for positive impulse and Table 3 for negative impulse respectively. One interesting observation that can be found is that, the average TBD is always lower with higher amount of MC. In other word, the average TBD for sand 0% is lower compared with sand 5% for both impulse polarities. Similar results can be seen with clay 0% and clay 5% for both impulse polarities. This is probably due to the average TBD for air being lower than water. Further research needs to be done to support this hypothesis.

Table 2
Positive impulse voltage at breakdown and time to breakdown

Samples	Average $VABD$ (kV)	SD (kV)	Average TBD (μ s)	SD (μ s)	Lag / Lead
Sand 0%	61.13	2.53	1.48	0.22	Lag
Sand 5%	36.75	1.91	3.67	1.26	Lag
Clay 0%	46.27	1.98	3.65	2.09	Lag
Clay 5%	35.38	2.5	3.95	2.06	Lag

Table 3
Negative impulse voltage at breakdown and time to breakdown

Samples	Average <i>VABD</i> (kV)	SD (kV)	Average <i>TBD</i> (μ s)	SD(μ s)	Lag / Lead
Sand 0%	51.33	2.23	1.79	0.62	Lag
Sand 5%	35.13	1.93	3.58	1.35	Lag
Clay 0%	42.27	1.67	1.49	0.3	Lag
Clay 5%	33.25	1.77	5.39	2.25	Lag

Standard deviation is used to quantify the distribution of *VABD* and *TBD*. Based on Table 2, there is no trend in the standard deviation for both average *VABD* and *TBD*. Hence, more experiments at different *MC* levels are needed for any solid conclusion to be drawn with regards to the effects of the types of soil on the standard deviation values. It is also found that, the average *TBD* for all the soil samples are under the ‘lag’ behaviour which is defined as the *TBD* of soil sample being exceeded the standard 1.2μ s rise time of impulse voltage. On the other hand, when the *TBD* is less than 1.2μ s, it is considered as lead behaviour. The result of *TBD* for sand 0% positive impulse with its respective standard deviation is approximately the same with the result obtained in (Lim et al., 2015).

These two parameters were further analysed statistically using the Independent T-test to verify whether there are any significant differences between the two types of soil samples. Interestingly, a statistical analysis on *TBD* and *VABD* was rarely captured in earlier studies on this high voltage experimental research field. An exception is Lim et al. (2015) where a statistical analysis was conducted on different types of grounding backfill materials under high impulse voltage condition. The independent T-test was performed for two categories, namely positive impulse and negative impulse. The two test sample combinations are the same for both positive and negative impulse polarities and for the following; Sand 0% - Sand 5%, Sand 0% - Clay 0%, Clay 0% - Clay 5%, and Clay 5% - Sand 5%. The confidence level was set at 95% which means that if the computed P value is less than 0.05, then there is statistical significant difference between the compared test samples. Table 4 and Table 5 show the Independent T-test results for both impulse polarities.

Table 4
Positive impulse voltage independent sample t-test

Sample for Independent T-test	P-value of <i>VABD</i>	Significant Difference	P-value of <i>TBD</i>	Significant Difference
Sand 0% - Sand 5%	0.000	Yes	0.000	Yes
Sand 0% - Clay 0%	0.000	Yes	0.000	Yes
Clay 0% - Clay 5%	0.000	Yes	0.690	No
Clay 5% - Sand 5%	0.091	No	0.638	No

Table 5
Negative impulse voltage independent sample t-test

Sample for Independent T-test	P-value of <i>VABD</i>	Significant Difference	P-value of <i>TBD</i>	Significant Difference
Sand 0% - Sand 5%	0.000	Yes	0.000	Yes
Sand 0% - Clay 0%	0.000	Yes	0.107	No
Clay 0% - Clay 5%	0.000	Yes	0.000	Yes
Clay 5% - Sand 5%	0.008	Yes	0.012	Yes

It can be inferred from Table 4 and Table 5 that there are statistically significant differences for sand 0% and sand 5% for both polarities. This suggests that the moisture added to the soil sample does have an effect on both *VABD* and *TBD* for these two samples. As for clay 0% and clay 5%, it is found that the moisture only has an effect for both *VABD* and *TBD* for negative polarity. Meanwhile, for comparison between sand and clay soil samples, it is found that, the moisture does have an effect for *VABD* for both 0% and 5% MC at both polarities. As for the *TBD*, the moisture only has an effect for the combination of sand 0% - clay 0% for positive impulse and clay 5% - sand 5% for negative impulse.

CONCLUSION

In conclusion, sand has a higher breakdown voltage compared with clay for both impulse polarities and the breakdown voltage for positive impulse polarities is higher than the voltage for negative impulse polarities for both type of soil with 0% and 5% MC. When 5% of moisture was added to both soil samples, the graph of the breakdown voltage is lowered from the no-breakdown graph. Upon analysing the traces of the breakdown voltage, it can be seen clearly that right after the breakdown event, the voltage waveform for sand 0% is oscillatory and as 5% moisture is added, the oscillation is reduced. As for the clay, there is no oscillation after the breakdown. This suggests that the particle size of soil has an effect on the trend of the breakdown voltage traces. The aforementioned experiments can be replicated by considering variation of grain size and compaction level of soil. It is also worth to further investigate the oscillatory response in the breakdown phenomena of soil. Findings from this experiment may provide useful insights for other research fields as well as agriculture and geophysics especially in countries which have lightning prone areas. It would also be interesting to extend this study to find out whether there is any effect of such electrical response of soil to the tripping operation of protective relays.

ACKNOWLEDGEMENT

The authors acknowledge UPM Grant GP-IBT/2013/9411000 which supported the laboratory testing procedures and Taylor's University for funding the study materials .

REFERENCES

- Asimakopoulou, F. E., Gonos, I. F., & Stathopoulos, I. A. (2009). Experimental investigation on soil ionization. In *Proceedings of the 16th International Symposium on High Voltage Engineering*.
- Cabrera, M., Lundquist, S., & Cooray, V. (1993). On the physical properties of discharges in sand under lightning impulses. *Journal of Electrostatics*, 30, 17-28.
- Campos, R. (1995). *Guide to the laboratory on insulation coordination*. Uppsala.
- Department of Transportation. (2003). *Test procedure for determining moisture content in soil materials*. Retrieved October 08, 2014 from http://ftp.dot.state.tx.us/pub/txdot-info/cst/TMS/100-E_series/pdfs/soi103.pdf
- Hauschild, W., & Lemke, E. (2004). *High-Voltage test and measuring technique*. Springer-Verlag Berlin Heidelberg, New York.
- Jin, Y. S., Cho, C. H., Ryoo, H. J., Kim, J. S., & Rim, G-H. (2001). Long gap discharge in water. *Journal of the Korean Physical Society*, 59, 3640-3643.
- Joffe, E. B., & Lock, K-S. (2010). *Grounds for grounding*, WILEY, New Jersey.
- Lim, S. C., Gomes, C., Kadir, M. Z. A. A., & Jasni, J. (2012). Ambiguity of grounding specifications: IEC 62305 revisited. In *International Conference on Lightning Protection (ICLP)*, (pp.1-6).
- Lim, S. C., Gomes, C., & Kadir, M. Z. A. A. (2013a). Electrical earthing in troubled environment. *International Journal of Electrical Power and Energy Systems*, 47, 117-128.
- Lim, S. C., Choun, L. W., Gomes, C., & Kadir, M. Z. A. A. (2013b). Environmental effects on the performance of electrical grounding systems. In *Proceedings of the 2013 IEEE 7th International Power Engineering and Optimisation Conference, PEOCO*.
- Lim, S. C., Gomes, C., Nourirad, G. & Kadir, M. Z. A. A. (2014). Significance of localised soil resistivity in designing a grounding system. In *Proceedings of the 2014 IEEE 8th International Power Engineering and Optimisation Conference, PEOCO*.
- Lim, S. C., Gomes, C., Nourirad, G. Kadir, M. Z. A. A., & Malek, Z. A. (2015). Behaviour of backfill materials for electrical grounding systems under high voltage conditions. *Journal of Engineering Science and Technology*, 10(6), 881-826.
- Markiewicz, H., & Klajn, A. (2003). *Earthing system - fundamentals of calculation and design*. Copper Development Association (CDA), United Kingdom.
- Nor, N. M., Hadad, A., & Griffiths, H. (2006). Characterization of ionization phenomena in soils under fast impulses. *IEEE Transactions on Power Delivery*, 21, 353-361.
- Nor, N. M., & Ramli, A. (2003). Electrical properties of dry soil under high impulse current. *Journal of Electrostatics*, 65(8), 500-505.
- Whitlow, R. (2004). *Basic soil mechanics* (4th Ed.). Pearson Prentice Hall, England.



Generation of Space Vector PWM by Using Arduino Uno

Nur Ashida Salim^{1*}, Muhammad Azizi Kaprowi² and Ahmad Asri Abd Samat³

¹Faculty of Electrical Engineering, Universiti Teknologi Mara, 40450 Shah Alam, Selangor, Malaysia

²Universiti Teknologi Mara Pulau Pinang (UiTM), 13500 Pulau Pinang, Malaysia

ABSTRACT

Space Vector Pulse Width Modulation (SVPWM) method is widely used as a modulation technique to drive a three-phase inverter. It is an advanced computational intensive method used in pulse width modulation (PWM) algorithm for the three-phase voltage source inverter. Compared with the other PWM techniques, SVPWM is easier to implement, thus, it is the most preferred technique among others. Mathematical model for SVPWM was developed using MATLAB/ Simulink software. In this paper, the interface between MATLAB Simulink with the three-phase inverter by using Arduino Uno microcontroller is proposed. Arduino Uno generates the SVPWM signals for Permanent Magnet Synchronous Motor (PMSM) and is described in this paper. This work consists of software and hardware implementations. Simulation was done via Matlab/Simulink software to verify the effectiveness of the system and to measure the percentage of Total Harmonic Distortion (THD). The results show that SVPWM technique is able to drive the three-phase inverter with the Arduino UNO.

Keywords: SVPWM, Arduino UNO, PMSM, Matlab/Simulink

INTRODUCTION

Space Vector Pulse Width Modulation (SVPWM) technique is an advanced computational intensive PWM algorithm for

voltage source converter. This paper describes the digital implementation of SVPWM method using Arduino Uno microcontroller. The main focus of the study was to design and develop the mathematical model of SVPWM to drive the three-phase inverter. The parameters that are discussed in this paper are SVPWM switching signal, dead band and Total Harmonic Distortion (THD).

In the last couple of decades, Pulse Width Modulation (PWM) technique has been used to achieve variable voltage and frequency in power converters. Originally, Space Vector Modulation (SVM) was developed as a vector

ARTICLE INFO

Article history:

Received: 24 August 2016

Accepted: 03 Jun 2017

E-mail addresses:

nurashida606@salam.uitm.edu.my (Nur Ashida Salim),

muhdazizi19@yahoo.com (Muhammad Azizi Kaprowi)

ahmadasri759@ppinang.uitm.edu.my (Ahmad Asri Abd Samat)

*Corresponding Author

approach to PWM for three-phase inverters. This technique is more convenient to obtain higher voltage to the motor with lower THD for generating sine wave. The SVPWM technique can be implemented to generate switching signal into the three-phase inverter to drive permanent magnet synchronous motor (PMSM). The benefits of using PMSM in the system are: high efficiency, high power density, higher power factor, free maintenance operation and it can be used in various types of applications (Harahap et al., 2014). Vipin and George (2014) stated that a high response system is needed by a high-performance motor control system to act immediately when a motor experiences any disturbance.

DSP, PIC and Arduino are types of processors that can be used to interface between Simulink and hardware. However, these processors have their limitations and problems such as complex implementations, moderate processing, and higher switching losses (Naik et al., 2014). In this project, Arduino UNO microcontroller is used to interface the hardware with MATLAB Simulink to overcome these limitations. The advantages of using Arduino Uno are: the board is inexpensive, simple and has a clear programming environment (Zulkifli et al., 2015). Designing a signal generator of SVPWM and interfacing it with a microcontroller have an advantage, namely it is easy to be programmed (Slamet. 2013). This paper looks at both software and hardware implementations

The SVPWM is a digital modulating technique that is designed to generate PWM load line voltage that are in average equals to a given reference load line voltage. Compared with the SPWM technique, SVPWM is easier to be implemented because it has higher DC voltage utilisation ratio (Kumar et al., 2010). In SVPWM technique, the voltage reference is presented by using a revolving reference vector. The SVPWM uses only one reference space vector to generate three-phase sine wave (Badran et al., 2013).

In addition, microcontroller technologies and the power electronics device have been studied and developed to efficiently support power drive systems in designing the inverter (Quach et al., 2012). The SVPWM algorithm could improve the quality of AC motor by reducing the harmonic and adjusting the amplitude and frequency of output voltage.

The SVPWM refers to a switching scheme of the six power switches of a three-phase inverter. Six of the voltage vectors ($V_1 - V_6$) are working states that form stationary vectors in the $\alpha\beta$ frame and divide the plane into six sectors with each having an angle of 60 degree as shown in Figure 1 (Iqbal et al. 2006). The SVPWM generate a voltage vector which is close

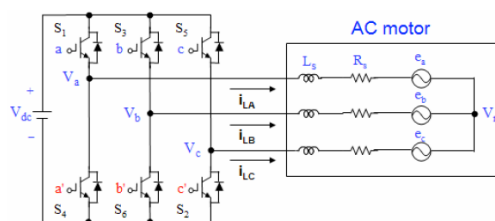
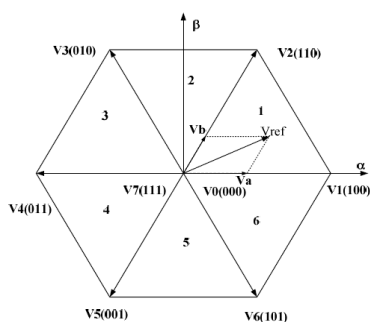


Figure 1. Voltage vectors and sectors in $\alpha\beta$ frame

Figure 2. Circuit model for three phase-inverter

to the reference circle through the various switching modes of inverter (Wang et al., 2008). The switches of the inverter are controlled according to the voltage vector at the given time with respect to the switching period (Nazlee et al., 2010).

METHODOLOGY

The switching technique in this project is used to drive the three-phase inverter by using SVPWM technique. The switching technique is designed and simulated by using the MATLAB/Simulink software. The Arduino Uno microcontroller is used to interface the switching signal designed in Matlab/Simulink to three-phase inverter. The switching signal that has been generated from Simulink software is uploaded into the Arduino Uno microcontroller. Matlab/Simulink software was used to design the mathematical model of SVPWM and the results were measured through the scope. The Arduino UNO was used to interface between the Simulink model and the three-phase inverter. The output waveforms were measured by using oscilloscope. This project was able to generate SVPWM signal by using simple interfacing platform, which is, Arduino UNO. The interfacing becomes simple without using any code of programming to generate SVPWM into three-phase inverter.

Principle of SVPWM

The SVPWM works based on the principle that when the upper leg of inverter is switched ON, the equivalent of the lower leg is switched OFF. Figure 2 shows the circuit model of the three-phase inverter which consists of six power switches that form the output. The switching signal are controlled by the switching variable of a , a' , b , b' , c and c' . From the circuit model, when a , b or c is 1, the equivalent a' , b' or c' is 0. Thus, the ON and OFF states of the upper leg of an inverter S_1 , S_3 and S_5 can be used to determine the output voltages. The generation of SVPWM signal consists of the sector calculation model, XYZ calculation model, T_1T_2 calculation model, T_{abcon} calculation model and V_{abc} calculation model.

Sector calculation model is used to determine which sector of the voltage vector is within its limit. The XYZ calculation model and T_1T_2 calculation model are sectors that determine the operation time of the fundamental vectors. T_1 is the main vector operating time in the current work sector and T_2 is the vice-vector of operating time. Another sector is T_{abcon} calculation model which is used to generate SVPWM waveform by using value T , T_1 , and T_2 . The last part for SVPWM model is V_{abc} calculation model which is the switch operation time. The generation of symmetrical SVPWM can be performed by comparing the calculated value of T_{cm1} , T_{cm2} , and T_{cm3} with the equilateral triangle diagram.

Switching time duration of sector 1 can be calculated as follows:

$$\int_0^T V_{REF} = \int_0^{T_1} V_1 + \int_{T_1}^{T_1+T_2} V_2 + \int_{T_1+T_2}^T V_o \quad (1)$$

$$TV_{REF} = (T_1V_1) + (T_2V_2) \quad (2)$$

$$TV_{REF} \begin{bmatrix} \cos \alpha \\ \sin \alpha \end{bmatrix} = T_1 \frac{2}{3} V_{DC} \begin{bmatrix} 1 \\ 0 \end{bmatrix} + T_2 \frac{2}{3} V_{DC} \begin{bmatrix} \cos \frac{\pi}{3} \\ \sin \frac{\pi}{3} \end{bmatrix} \quad (3)$$

where T_1 , T_2 , and T are times during at which V_1 , V_2 , and zero-vector are applied, V_{REF} is reference voltage of voltage vector and α is phase angle of output vector, $0 \leq \alpha \leq 60$.

From equation (3)

$$T|V_{REF}| \cos \alpha = T_1 \frac{2}{3} V_{DC} + T_2 \frac{2}{3} V_{DC} \cos \frac{\pi}{3} \quad (4)$$

$$T|V_{REF}| \sin \alpha = T_2 \frac{2}{3} V_{DC} \sin \frac{\pi}{3} \quad (5)$$

From equation (4) and (5), switching time duration for sector 1 is:

$$T_1 = T \frac{|V_{REF}|}{\frac{2}{3} V_{DC}} \sin \left[\left(\frac{\pi}{2} - \alpha \right) \right] \quad (6)$$

$$T_2 = T \frac{|V_{REF}|}{\frac{2}{3} V_{DC}} \sin \left[\frac{\alpha}{\frac{\pi}{3}} \right] \quad (7)$$

$$T_0 = T - T_1 - T_2 \quad (8)$$

where T_0 is time of the zero vector is applied. Thus, switching time duration for other sector can be gained from equation (6), (7) and (8).

Equation (9) and (10) represent the T_1 and T_2 respectively.

$$T_1 = \frac{\sqrt{3}T|V_{REF}|}{V_{DC}} \left(\sin \frac{n}{3} \pi \cos \alpha - \cos \frac{n}{3} \pi \sin \alpha \right) \quad (9)$$

$$T_2 = \frac{\sqrt{3}T|V_{REF}|}{V_{DC}} \left(-\cos \alpha \sin \frac{n-1}{3} \pi - \sin \alpha \cos \frac{n-1}{3} \pi \right) \quad (10)$$

where n is number of sector (1 to 6).

After all the mathematical equations have been derived, then all the equations are modelled in Matlab/Simulink to generate the switching signal. Figure 3 shows the block diagram that contains all the mathematical equation developed in Matlab/Simulink.

Hardware Implementation

The Arduino UNO microcontroller functions as interfacing component between the software and hardware parts. Figure 4 shows the simulation setup for interfacing Simulink with Arduino

UNO. The selected pins from Arduino UNO to generate the output are pin 3, 5, 6, 9, 10 and 11. These pins are selected because it can produce the PWM output signal.

The Arduino UNO needs a supply of 5V to turn ON. The signal from Arduino UNO is an output of SVPWM which is an ON or OFF signal that functioned as a switch for the inverter. The unit delay block is used to give the delay time between ON time and OFF time for each signal. Each of the selected pin of Arduino UNO is connected to the three-phase inverter with the gate driver. Then, the output of three-phase inverter is connected to the PMSM.

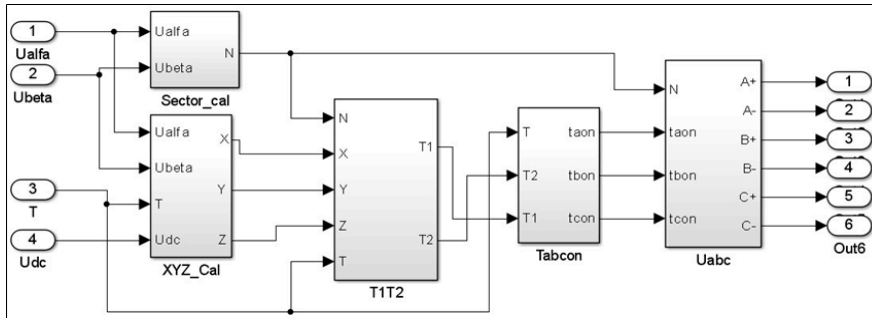


Figure 3. Simulation model of SVPWM

RESULT AND DISCUSSION

This project was simulated in Matlab/ Simulink software to test the effectiveness of the system. The mathematical model for SVPWM was developed first and then the Arduino software was designed to interface between the Matlab/Simulink and the three-phase inverter. The responses of the speed, voltage and current were observed by changing the value of the modulation index.

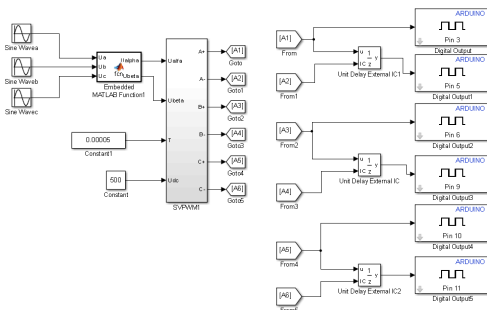


Figure 4. Interfacing model between Simulink and Arduino UNO



Figure 5. Hardware setup for Arduino UNO

Total Harmonic Distortion (THD)

Total Harmonic Distortion (THD) is the existing amount of harmonic distortion in the waveform. In this analysis, the following parameters were selected to observe the percentage of THD in the system:

$$V_{dc} = 250V$$

Fundamental frequency = 50 Hz

Modulation index = 0.5, 0.7 and 0.9

Table 1 shows the reading of THD based on the value of modulation index. Equation (11) is used to calculate the U_{dc} . Table 1 shows that by increasing the value of modulation index, it will give the less value of THD.

$$U_{dc} = m_i \cdot \sqrt{3} \cdot \frac{V_{dc}}{2} \tag{11}$$

Table 1
Modulation index and corresponding total harmonic distortion

Modulation Index	Udc (V)	THD for current (%)
0.5	108	20.74
0.7	152	20.71
0.9	195	18.72

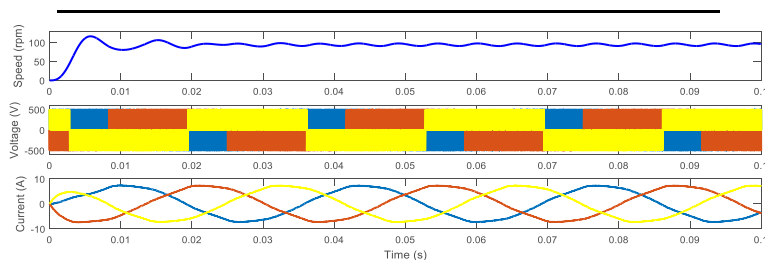


Figure 6. Simulation results with modulation index of 0.5

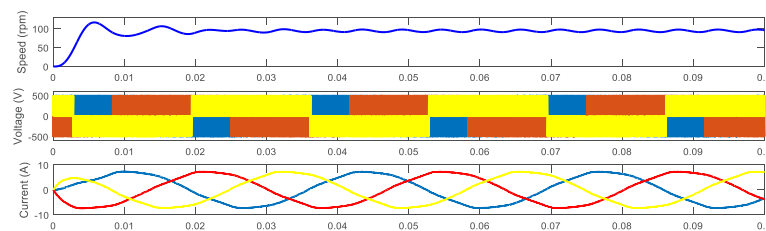


Figure 7. Simulation results with modulation index of 0.7

Generation of Space Vector PWM by Using Arduino Uno

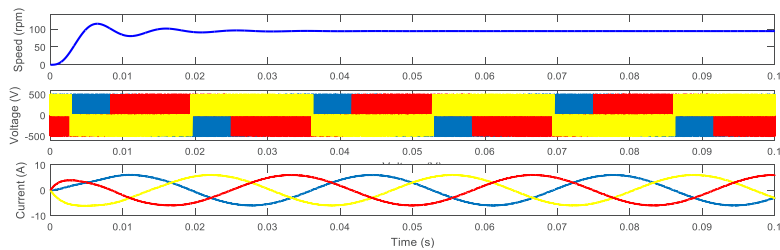


Figure 8. Simulation results with modulation index of 0.9

Figures 6,7 and 8 show the response of speed, voltage and current of the PMSM with modulation index of 0.5, 0.7 and 0.9 respectively. Results show that the higher number of THD will give more harmonics in current and cause more ripples in speed as depicted in Figure 6 and Figure 7.

In addition, as depicted in Figure 8, the speed ripple is near to zero because the harmonics contents in current are less. As tabulated in Table 1, the value of the THD in this case is 18.72%.

Switching signal

The switching signal from SVPWM that was designed in Matlab/Simulink was injected to the three-phase inverter via Arduino UNO. The interfacing between Matlab/Simulink and Arduino UNO is as shown in Figure 4 and Figure 5. Table 2 shows the pin connection at Arduino UNO board that represents the switching signal of the inverter.

Table 2
Switching signal and Arduino UNO pin setup

Switching Signal	Arduino UNO Pin
A+	3
A-	5
B+	6
B-	9
C+	10
C-	11

Table 3
Amplitude and period of switching signal before and after entering gate driver

Switching Signal	Before Gate Driver		After Gate Driver	
	Pk-Pk (V)	Period (ms)	Pk-Pk (V)	Period (ms)
A+	7.6	6.638	15.1	6.615
A-	6.4	6.613	14.5	6.357
B+	7.6	6.493	14.7	6.424
B-	7.4	6.607	14.7	6.607
C+	7.6	6.641	14.9	6.616
C-	6.4	6.677	14.6	6.617

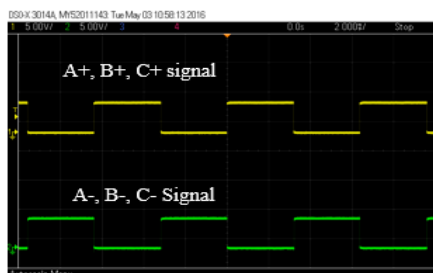


Figure 9. Switching signal from Arduino UNO pin

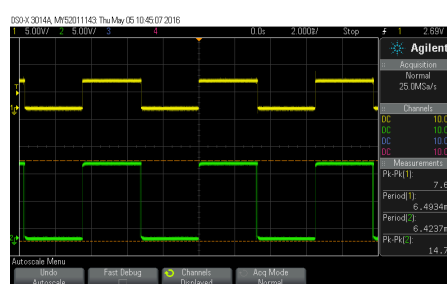


Figure 10. Output waveform after entering gate driver for signal B+

The SVPWM has 6 outputs (A+, A-, B+, B-, C+ and C-) which represent the six sector. The value of output is either 0 or 1. Figure 9 shows the switching signal for A+, A-, B+, B-, C+ and C- from the Arduino UNO. The switching signal will inject the gate driver before it triggers the switch of the three-phase inverter. The gate driver is a power amplifier that receives a low power input and produces a high voltage and current gate drive to switch ON and OFF the MOSFET. Table 3 shows the result of the amplitudes of switching signal from Arduino UNO before and after entering the gate driver and the period is for one cycle. The results show that the amplitude has been amplified by the gate driver. Figure 10 shows the output waveform after entering the gate driver for signal B+.

CONCLUSION

The basic principle and the mathematical model of SVPWM were developed using Matlab/Simulink. The Arduino UNO microcontroller was used to interface between the SVPWM modelled in Matlab/Simulink and the three-phase inverter. The results show that SVPWM switching signal is able to generate the three-phase inverter with the Arduino UNO microcontroller. The value of THD was also measured in simulation and the results shows that the modulation index of 0.9 gives the lowest percentage of THD. It validated that higher value of the modulation index will deliver lower harmonics contains in the system.

ACKNOWLEDGEMENT

The authors would like to thank the Research Management Institute (RMI), Universiti Teknologi Mara, Malaysia and the Ministry of Higher Education (MOHE), Malaysia for research grant 600-RMI/DANA 5/3/LESTARI (77/2015).

REFERENCES

- Asma, N. R., & Jangamshetti Suresh, H. (2014). Implementation of Space Vector Pulse Width Modulation using Arduino. *International Journal of Science and Research*, 3(7), 1706-1710.
- Badran, M. A., Tahir, A. M., & Faris, W. F. (2013). Digital Implementation of Space Vector Pulse Width Modulation Technique Using 8-bit Microcontroller. *World Applied Sciences Journal*, 21, 21-28.

- Harahap, C. R., Saito, R., Yamada, H., & Hanamoto, T. (2014). Speed control of permanent magnet synchronous motor using FPGA for high frequency SiC MOSFET Inverter. *Journal Engineering Science and Technology, October*(2014), 11-20.
- Iqbal, A., Lamine, A., & Ashraf, I. (2006, September). MATLAB/SIMULINK model of space vector pwm for three-phase voltage source inverter. In *Proceedings of the 41st International Universities Power Engineering Conference* (Vol. 3, pp. 1096-1100). IEEE.
- Kumar, K. V., Michael, P. A., John, J. P., & Kumar, D. S. S. (2010). Simulation and comparison of SPWM and SVPWM control for three phase inverter. *ARPJ Journal of Engineering and Applied Sciences*, 5(7), 61-74.
- Nazlee, A. M., Hamid, N. H., Hussin, F. A., & Ali, N. B. Z. (2010, December). Space Vector PWM for PMSM simulation using Matlab Simulink. In *Circuits and Systems (APCCAS), 2010 IEEE Asia Pacific Conference on* (pp. 1127-1130). IEEE.
- Quach, D. C., Yin, Q., Shi, Y. F., & Zhou, C. J. (2012, December). Design and Implementation of Three-phase SVPWM Inverter with 16-bit dsPIC. In *2012 12th International Conference on Control Automation Robotics and Vision (ICARCV)*.
- Slamet. (2013). Generation of Space Vector PWM Using Microcontroller Atmega 16. *International Journal of Scientific & Engineering Research*, 4(3), 1-5.
- Vipin, A. M., & George, S. (2014, July). Hardware implementation of space vector PWM control of Permanent Magnet Synchronous Motor. In *Annual International Conference on Emerging Research Areas: Magnetism, Machines and Drives (AICERA/iCMMD), 2014* (pp. 1-5). IEEE.
- Wang, Z. G., Jin, J. X., Guo, Y. G., & Zhu, J. G. (2008). SVPWM techniques and applications in HTS PMSM machines control. *Journal of Electronic Science and Technology of China*, 6(2), 191-197.
- Zulkifli, S. A., Hussin, M. N., & Saad, A. S. (2014, December). MATLAB-Arduino as a low cost microcontroller for 3 phase inverter. In *IEEE Student Conference on Research and Development (SCOReD), 2014* (pp. 1-5). IEEE.



Analysis of Ground Potential Distribution under Lightning Current Condition

Chandima Gomes¹ and Riyadh Z. Sabry^{1,2*}

¹*Department of Chemical and Environmental Engineering, Faculty of Engineering, Universiti Putra Malaysia, 43400 UPM, Serdang, Selangor, Malaysia*

²*Department of Electrical Engineering, Faculty of Engineering, University of Mosul, Iraq*

ABSTRACT

The grounding system of a lightning protection scheme is designed basically to avoid arcing and dangerous step potentials. The grounding impedance of the system varies depending on soil structure and frequency. This paper describes the effect of harmonic impedance (also called frequency dependence of soil) on potential distribution under lightning strike to a metal tower with single grounding path, for different soil types. The results show that the peak value of ground potential rise (GPR) and step voltage (SP) may reach extremely hazardous values even at distances in the order of 90 m from the tower footing, especially when soil resistivity is high. Hence, we emphasise that, in contrast to power grounding, when designing of grounding systems that are meant to handle transient or high frequency currents as well, the frequency dependent soil parameters should be considered to avoid hazardous situations, especially at locations with a high probability of lightning strikes such as metal towers.

Keywords: Lightning, frequency dependence of soil, grounding, transient impedance, GPR, SP

INTRODUCTION

Many empirical and experimental studies have shown that electrical behaviour of soil under transient conditions such as lightning,

is quite different from the behaviour of the same at d.c. or low frequencies (Pedrosa et al., 2010). In power systems, measurements of grounding impedance are usually performed at low frequencies as the systems are designed to handle currents at nominal power frequency (50/60 Hz). Under power frequency conditions, grounding impedance is represented by only resistance of the electrode system and the masses of soil. At low frequencies, electrical conductivity and permittivity of soil could reasonably be

ARTICLE INFO

Article history:

Received: 24 August 2016

Accepted: 03 Jun 2017

E-mail addresses:

chandima.gomes@hotmail.com (Chandima Gomes)

riyadhzaki72@gmail.com (Riyadh Z. Sabry)

*Corresponding Author

assumed to have constant or frequency independent values where the in situ is measured by Wenner method (IEEE, 2012).

On the other hand, in order to conduct accurate analysis of the behaviour of grounding systems under high frequency or impulse conditions, there are several additional parameters needed to be considered such as system geometry and the frequency dependent variation of resistivity and permittivity of the soil. Hence, a grounding system designed without considering such variables may produce dangerous potential gradients and large potential rises even at quite long distances which may be hazardous to both living beings (humans and livestock) and conducting systems (electronics, oil & gas pipelines etc.). Therefore, high accuracy in the prediction of potential distribution for a given grounding system plays a vital role in designing an appropriate grounding scheme for a given environment.

Several equations have been developed to analyse the frequency dependence of soil. In this paper we consider six different models/expressions which have been proposed by (Cavka, Mora, & Rachidi, 2014) for the representation of soil electrical parameters, namely the model by Scott (S), Messier (M), Visacro and Portela (VP), Portela (P), Visacro and Alipio (VA) and constant impedance (C). This study had investigated the dependence of soil parameters with the frequency and its effects on the response of the grounding system of a metallic tower when the structure or a conducting line connected to the structure (e.g. Power line or communication line) is struck by lightning. Negative lightning, most prevalent in tropical countries, has been considered for the analysis (both first and subsequent strokes). Heidler current model has been employed to calculate ground potential rise (GPR) and (SP) by using MATLAB code.

METHODOLOGY

Current waveforms of lightning

The lightning stroke waveform is described by the IEC-62305-1 standards (IEC62305, 2010) as shown in Equations 2-3 (Rameli, Abkadir, Izadi, Gomes, & Azis, 2014; V. A. Rakov and M. A. Uman, 2003).

$$i(t) = \left[\frac{i_0}{\eta} \frac{\left(\frac{t}{\tau_1}\right)^\eta}{1 + \left(\frac{t}{\tau_1}\right)^\eta} \exp\left(\frac{-t}{\tau_2}\right) \right] \quad (2)$$

$$i(t) = \left[\frac{i_{01}}{\eta_1} \frac{\left(\frac{t}{\tau_{11}}\right)^{\eta_1}}{1 + \left(\frac{t}{\tau_{11}}\right)^{\eta_1}} \exp\left(\frac{-t}{\tau_{12}}\right) + \frac{i_{02}}{\eta_2} \frac{\left(\frac{t}{\tau_{21}}\right)^{\eta_2}}{1 + \left(\frac{t}{\tau_{21}}\right)^{\eta_2}} \exp\left(\frac{-t}{\tau_{22}}\right) \right] \quad (3)$$

Where:

t is the time step,

i_{01}/i_{02} is the amplitudes of the channel base current,

τ_{11}/τ_{12} is the first/second front time constant,

τ_{21}/τ_{24} is the first/second decay- time constant,

η_1/η_2 is the first/second exponent (2~10),

$$\dots \eta_1 = \exp\left[-\left(\frac{\tau_{11}}{\tau_{12}}\right) \left(n \left(\frac{\tau_{12}}{\tau_{11}}\right)\right)^{1/n_1}\right],$$

$$\dots \eta_2 = \exp\left[-\left(\frac{\tau_{21}}{\tau_{22}}\right) \left(n \left(\frac{\tau_{22}}{\tau_{21}}\right)\right)^{1/n_2}\right].$$

Parameters for the first stroke and the subsequent stroke Heidler waveforms are given in Table 1. The first return stroke current is characterised by a peak value of 30 kA, zero-to-peak time of about 8μs and a maximum steepness of 12 kA/μs, whereas the subsequent return stroke current has a peak value of 12 kA, zero to-peak time of about 0.8 and a maximum steepness of 40 kA/s (Rachidi & Janischewskyj, 2001). Figure-1 shows the first and subsequent waveforms simulated with the above parameters.

Table 1
Parameters (Rachidi & Janischewskyj, 2001)

	i_{o1} (kA)	τ_{11} (μs)	τ_{21} (μs)	η_1	i_{o2} (kA)	τ_{12} (μs)	τ_{22} (μs)	η_2
First stroke	28	1.8	95	2				
Subsequent stroke	10.7	0.25	2.5	2	6.5	2	230	2

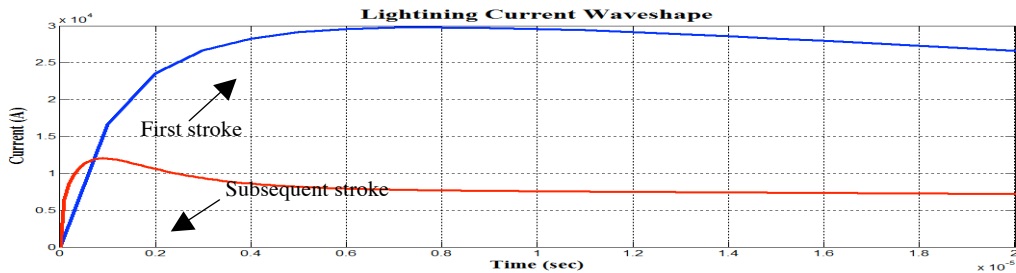


Figure 1. First and Subsequent return stroke current wave shapes

Tower grounding system

Figure 2 shows the model of the tower grounding system. The buried grounding electrode, made of steel with the radius of 6 mm, resistivity of $1.66 \times 10^{-7} \Omega\text{m}$, relatively magnetic permeability of 636 and a depth of 3m have been considered (Lu, Liu, Qi, & Yuan, 2012). We considered three values of soil conductivity ($\sigma=0.01$, $\sigma=0.001$ and $\sigma=0.0001$ S/m) that represent most of the soil types that are found in Malaysia. The computations have been repeated for several distances.

Grounding system analysis

Practically-equivalent approaches to excitation-independent ground impedance have been widely used for computation of ground protection distribution. The first is the time-domain ground surge impedance $Z(t)$, which is the ratio of the voltage response to a unit step current excitation. The second is the frequency-domain alternative to the surge impedance: ground

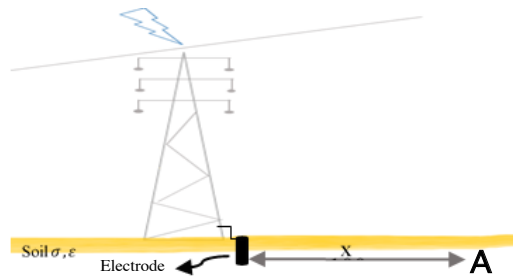


Figure 2. The geometry of problem

harmonic impedance $Z(\omega)$ (Cooray, 2010). The harmonic impedance in the frequency domain is defined as:

$$Z(\omega) = \frac{V(\omega)}{I(\omega)} \tag{4}$$

Where $V(\omega)$ and $I(\omega)$ are phasors of the steady state harmonic electric potential at the feed point with reference to the remote neutral ground and the injected current respectively, in a frequency range from 0 Hz up to the highest frequency of interest in transient studies. The harmonic impedance depends only on the geometry and electromagnetic properties of the electrodes and the medium. As it is well known, $Z(\omega)$ enables evaluation of the time functions of the transient potential $v(t)$ as a response to an arbitrary current pulse $i(t)$ by:

$$V(t) = F^{-1} \{ F[i(t)] * Z(\omega) \} \tag{5}$$

In equation (6) F and F^{-1} denote Fourier and inverse Fourier transforms respectively (Pedrosa et al., 2010). The admittance is given by

$$Y(\omega) = \left(\frac{1}{Z(\omega)} \right) = \frac{1}{R + j\omega C} = G + j\omega C \tag{6}$$

Where σ is electric conductivity, ω is angular frequency and ϵ is the electric permittivity. To calculate $Y(\omega)$ we used six empirical equations (Alipio & Visacro, 2013; Messier, 1985; C. Portela, Eng, & Grillo, 1999; S. V. and C. Portela, 1987; Scott, 1966). To determine the value of $\rho_{(f)}$ and $\epsilon_{(f)}$ we used Liew-Darveize equation (Liew & Darveniza, 1974) model:

$$R = 1/G = \frac{\rho}{2\pi h} \ln \left(\frac{x}{r_o} \right) \tag{7}$$

$$x\omega C = \frac{\omega \epsilon_o \epsilon_r}{2\pi h} \ln \left(\frac{r_o}{x} \right) \tag{8}$$

Step potential (SP) at the distance for a 0.5 m gap was calculated by the following equation:

$$SP = (v_x - v_{x+0.5m}) \tag{9}$$

Where $x = 10m, 50m, 90m$.

RESULT AND DISCUSSION

Figure 3 shows the variation of voltage distribution for the first and subsequent strokes at several distances for $\sigma = 0.01 \text{ S/m}$. At this rather low soil resistivity value $100 \Omega\text{m}$, at 10 m distance from the grounding electrode, for first stroke the peak voltage is 3.6 kV and for subsequent stroke is 1.5kV at 10 m.

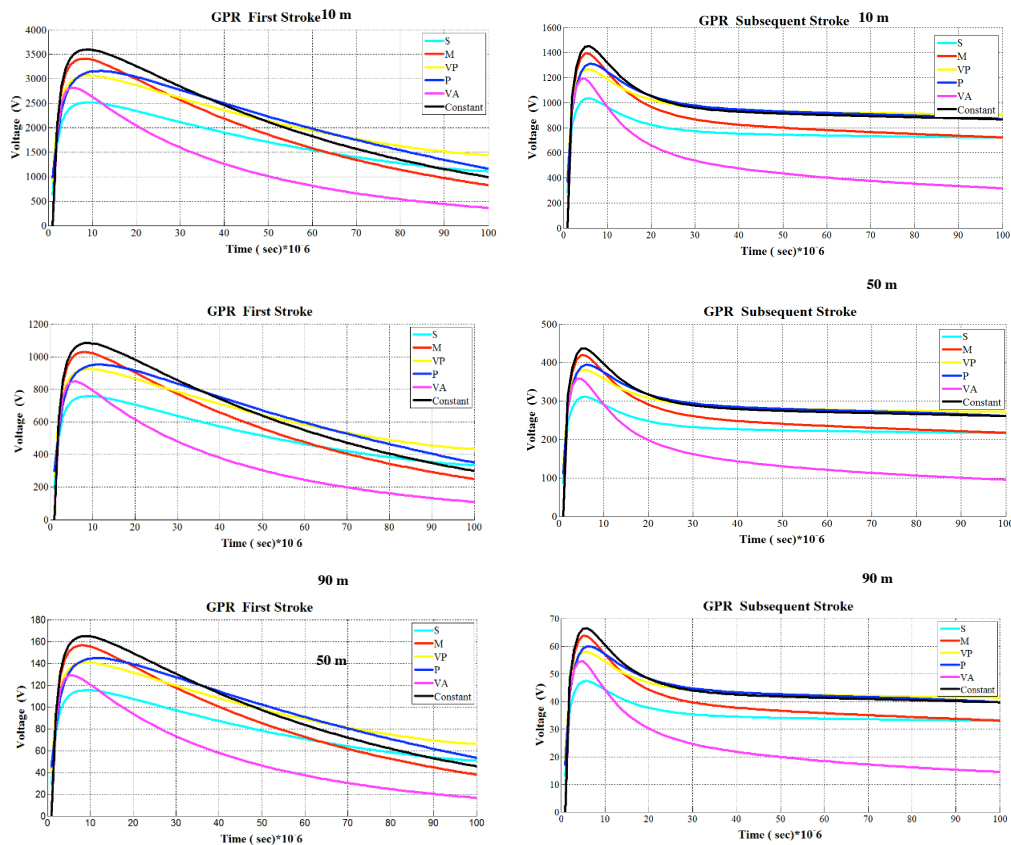


Figure 3. GPR for first and subsequent stroke at different empirical equations and $\sigma = 0.01 \text{ S/m}$

Table 2-3 shows the correlation between the distance and peak voltage GPR for the different empirical equations and different soil conductivity. As it is depicted in these tables, as the soil resistivity increases the peak potential increases rapidly and at 10 m for $\sigma = 0.0001 \text{ S/m}$ (resistivity of $10,000 \Omega\text{m}$) the value may exceed 100 kV. Such values, may heavily damage

equipment in a TT wiring system that have been grounded near the tower and connected with power neutral that has been grounded at a distant point (at the substation). Even at 50 m, the potentials may be harmful to most of the equipment that have impulse withstanding voltage of few kilo Volts. Hence equipotential sizing power and communication systems in the vicinity of towers with properly coordinated system of SPDs is essential for the safety of such equipment. In addition, such potential rises may also drive considerable transient currents in the skin of underground oil and gas pipelines in the vicinity enhancing metal corrosion. Therefore, isolation of pipelines that run close to the transmission and communication towers with suitable high resistive material is a need for their corrosion avoidance. Further studies should be done in this regard to find the most appropriate solution for a given pipeline arrangement, soil resistivity and electrode system. It should also be noted that the potential rise in the case of subsequent strokes is also significant. As a majority of negative flashes in most parts of the world may reach multiplicities above 5, the equipment in the nearby systems and metal pipelines may be

Table 2
Peak voltage GPR first stroke for six empirical equations

Conductivity	Distance (m)	Models					
		S (V)	M (V)	VP (V)	P (V)	VA (V)	Constant (V)
$\alpha = 0.01$ S/m	10 m	2518	3416	3071	3162	2816	3603
	50 m	758.3	1028.5	924.5	952	848	1085
	90 m	115.2	156.3	140.5	144.7	128.88	164.87
$\alpha = 0.001$ S/m	10 m	15566	30930	30710	27535	16440	36000
	50 m	4686	9310	9245	8288	4949	10850
	90 m	712	1415	1405	1260	750	1650
$\alpha = 0.0001$ S/m	10 m	83000	243780	307110	215850	57400	360000
	50 m	25000	73400	92450	65000	17280	108400
	90 m	3800	11155	14050	9875	2626	16500

Table 3
Peak voltage GPR subsequent stroke for six empirical equations

Conductivity	Distance (m)	Models					
		S (V)	M (V)	VP (V)	P (V)	VA (V)	Constant (V)
$\alpha = 0.01$ S/m	10 m	1034.5	1393	1265.8	1310	1191.5	1451.2
	50 m	311.4	419.3	381	394.5	358.7	436.8
	90 m	47.3	63.75	57.9	60	54.5	66.4
$\alpha = 0.001$ S/m	10 m	6477.5	12857	12685	11386	7366.7	14512
	50 m	1950	3870	3810	3425	2218	4368.5
	90 m	297	589	579.5	520	337	664
$\alpha = 0.0001$ S/m	10 m	35000	104000	126600	92000	29500	145000
	50 m	10500	31300	38100	27700	8885	43685
	90 m	1600	4760	5792	4210	1350	6640

subject to repeated high potential rises during a single flash. The protective systems should be developed by considering this factor as well.

Figure 4 shows the relation between the distance and step voltage for 0.5 m in the cases of first and subsequent strokes for different empirical equations at soil conductivity of 0.001 S/m (resistivity of 1000 Ω m). The step voltage for constant impedance is higher than that calculated by other models. At 10 m, for first stroke, the value of step voltage for different model vary between 3.8 kV to 1.0 kV and for subsequent stroke the same parameter ranges between 1.5 kV and 0.7 kV. At 50 m and 90 m the step potentials are 0.8 kV-0.15 kV and 0.3 kV-0.15 kV for first stroke. For subsequent strokes, the values are 0.4 kV-0.7 kV and 0.17 kV-0.03 kV. The results show that at a moderate soil resistivity, dangerous step potentials may be reached at close vicinity to the grounding system which may knock-off workers or visitors that walk/stand around. The SP may take much higher figures as the soil resistivity is increased to large values. These factors should be taken into account by the grounding system designers to ensure safety of the people at a tower site.

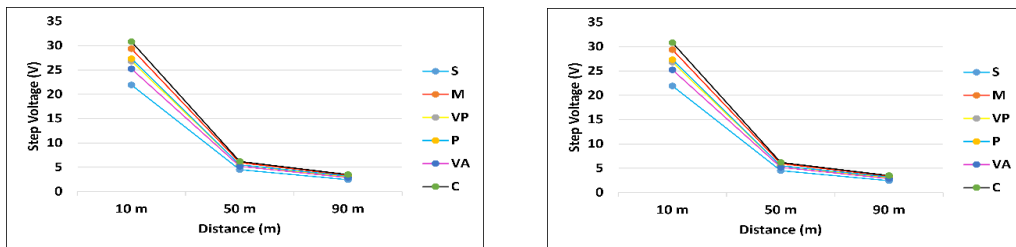


Figure 4. SP for first and subsequent stroke at different distance

CONCLUSION

This experiment has shown that lightning strikes to a metal tower or service line connected to that may drive impulse current into the soil may cause dangerous GPR and SP in the vicinity. The peak values and time variation of the GPR and SP depend on soil resistivity and the type of lightning current. They should also be a function of the grounding system arrangement as well but in this study, we have considered only a single grounding electrode connected to one footing of the tower. The engineering designers should take these parameters into account in developing the grounding system for a tower to ensure the safety of workers and visitors and the protection of equipment connected to the nearby grounded power and communication systems. The corrosion enhancement of nearby oil and gas pipelines is also a concern with respect to GPR. Further studies should be conducted in this regard with respect to various electrode arrangements, non-uniform soil resistivity profiles and positive lightning as well, to understand the frequency dependent electrical behaviour of soil in the vicinity of the grounding system.

ACKNOWLEDGEMENT

The authors wish to thank the Centre for Electromagnetic and Lightning Protection Research (CELP), Electrical and Electronic Engineering Department, Universiti Putra Malaysia,

Malaysia, for their invaluable support that has made this research possible. We also thank The Ministry of Higher Education and Scientific Researches and Mosul University, College of Engineering, electric department for providing the research grant.

REFERENCES:

- Alipio, R., & Visacro, S. (2013). Frequency dependence of soil parameters: Effect on the lightning response of grounding electrodes. *IEEE Transactions on Electromagnetic Compatibility*, 55(1), 132–139. <http://doi.org/10.1109/TEMC.2012.2210227>
- Cavka, D., Mora, N., & Rachidi, F. (2014). A Comparison of Frequency-Dependent Soil Models : *Application to the Analysis of Grounding Systems*. *IEEE*, 56(1), 177–187.
- Cooray, V. (2010). *Lightning protection*. (V. Cooray, Ed.). London UK: The Institution of Engineering and Technology.
- IEC62305. (2010). *IEC62305: 2010, Protection against lightning Part 1: General principles*.
- IEEE. (2012). *IEEE Guide for Measuring Earth Resistivity, Ground Impedance, and Earth Surface Potentials of a Grounding System IEEE Power and Energy Society* (Vol. IEEE Std 8).
- Liew, A. C., & Darveniza, M. (1974). Dynamic model of impulse characteristics of concentrated earths. *Proceedings of the Institution of Electrical Engineers*, 121(2), 123–135. <http://doi.org/10.1049/piee.1974.0022>
- Lu, D., Liu, C., Qi, L., & Yuan, H. (2012). Mitigation of electromagnetic influence on the buried metal pipeline near overhead AC transmission line. In *2012 6th International Conference on Electromagnetic Field Problems and Applications, ICEF'2012*, 1–4. <http://doi.org/10.1109/ICEF.2012.6310384>
- Messier, M. (1985). “Another soil conductivity model ” internal rep. *JAYCOR*, (Santa Barbara CA).
- Pedrosa, A. G., Shroeder, M. A. O., Afonso, M. M., Alipio, R. S., De, S., Assis, C., ... Braga, A. R. (2010). Transient Response of Grounding Electrodes for the Frequency-Dependence of Soil Parameters. *IEEE/PES Transmission and Distribution Conference and Exposition: Latin America*, (pp.839–845).
- Portela, C., Eng, R., & Grillo, C. (1999). Measurement and Modeling of Soil Electromagnetic Behavior. *IEEE*, 2, 1004–1009.
- Portela, S. V. and C. (1987). Soil permittivity and conductivity behavior on frequency range of transient phenomena in electric power systems. *Presented at the Symp. High Voltage Engineering*. Braunschweig, Germany.
- Rachidi, F., & Janischewskyj. (2001). Current and Electromagnetic Field Associated With Lightning – Return Strokes to Tall Towers. *IEEE*, 43(3), 356–367.
- Rameli, N., Abkadir, M. Z. A., Izadi, M., Gomes, C., & Azis, N. (2014). Effect of the grounding system arrangement on the lightning current along tall structures. In *2014 International Conference on Lightning Protection, ICLP 2014*, 456–460. <http://doi.org/10.1109/ICLP.2014.6973167>
- Scott, J. H. (1983). *Electrical and magnetic properties of rock and soil* (No. 83-915). US Geological Survey.
- V. A. Rakov and M. A. Uman. (2003). *Lightning: Physics and Effects. Igarss 2014*. <http://doi.org/10.1007/s13398-014-0173-7.2>



EFVD along Porcelain Insulator using the FEM

Kian Tsong Ho*, Mahdi Izadi and Mohd Zainal Abidin Ab Kadir

Centre for Electromagnetic and Lightning Protection Research (CELP), Faculty of Engineering, Universiti Putra Malaysia, Serdang, Malaysia

ABSTRACT

In this paper, cap and pin porcelain insulator was studied under an environment with different levels of humidity. The electric field strength and voltage distribution profile along the insulator string was simulated using a computational software package. In this study, ANSYS Maxwell based on the Finite Element Method (FEM) was used to simulate the short standard insulator string. The short standard insulator string was modelled as a five-unit cap and pin porcelain insulator that was stacked according to the IEC 60383 standard. Different humidity levels measured using relative humidity is applied to the insulator. From this simulation, the locations within the insulator under high electric field stress are identified when different humidity is applied.

Keywords: Porcelain Insulator, electric field strength distribution, humidity

INTRODUCTION

High quality outdoor insulators are needed to ensure the quality of the power transmitted over a transmission line, so research to improve the insulator is important. All insulators have to perform a dual task which is to mechanically hold up the transmission

line and to electrically isolate the transmission line from the metal transmission tower. The history of insulators can be traced back to 1835, the first insulator was of a ceramic type. Since then, the ceramic type design has changed over the years with the increase in transmission system voltage. In 1960, a new type of insulator made of a polymer became available and this has since become popular (Looms, 1998). A polymer insulator is lighter and has better performance under conditions of pollution compared with the conventional ceramic insulator (Izadi, Rahman, Kadir, 2014). However, the ceramic insulator is still widely used due to its well-known field performance while the polymer insulator suffers from a lot uncertainty (Costea &

ARTICLE INFO

Article history:

Received: 24 August 2016

Accepted: 03 Jun 2017

E-mail addresses:

kiantson@hotmail.com (Kian Tsong Ho),
aryphase@yahoo.com; mzk@upm.edu.my (Mahdi Izadi),
(Mohd Zainal Abidin Ab Kadir)

*Corresponding Author

Baran, 2012). In that case, a study of the porcelain insulator is important as there are many existing porcelain insulators still in service.

Previous research into the calculation of the electric field and potential distribution along a porcelain insulator includes the work of Reddy (Reddy et al., 2012) who applied the surface charge simulation method to study the surface field and potential distribution of normal and faulty insulator strings. Taklaja simulated a porcelain insulator in a distribution grid using COMSOL Multiphysics (Taklaja et al., 2015). Fouladi calculated the AC and transient potential distribution along a porcelain insulator under polluted conditions (Fouladi et al., 2014). Meanwhile, Gouda performed a laboratory test on a polluted overhead transmission line insulator under desert conditions (Gouda & Dein, 2013) while Kontargyri studied the electric field and voltage distribution along a porcelain insulator string by experimental work and simulation through the OPERA software (Kontargyri, Gonos & Stathopoulos, 2009). Thus, it can be observed that many studies have investigated the effects of pollution on the electric field strength and voltage distribution, but not many on the effect of humidity alone on the electric field strength and voltage distribution around the insulator.

In this paper, the electric field distribution along a cap and pin porcelain insulator unit is simulated in an environment with different levels of humidity. Humidity is one of the factors that affect the flashover voltage of an insulator. However, the relation between different levels of humidity with the electric field and voltage distribution around the insulator remains unclear. Hence, this study was carried out by modelling the insulator string using ANSYS Maxwell. In the simulation, the insulator model is excited by AC power frequency of 50Hz under 27 %, 70 % and 90 % relative humidity; later, the electric field and the voltage distribution at different sections of the insulator are considered.

THE MODELLING AND SIMULATION METHOD

In this work, the insulator is simulated by ANSYS Maxwell software, the 2D model of the insulator is as shown in Figure 1.

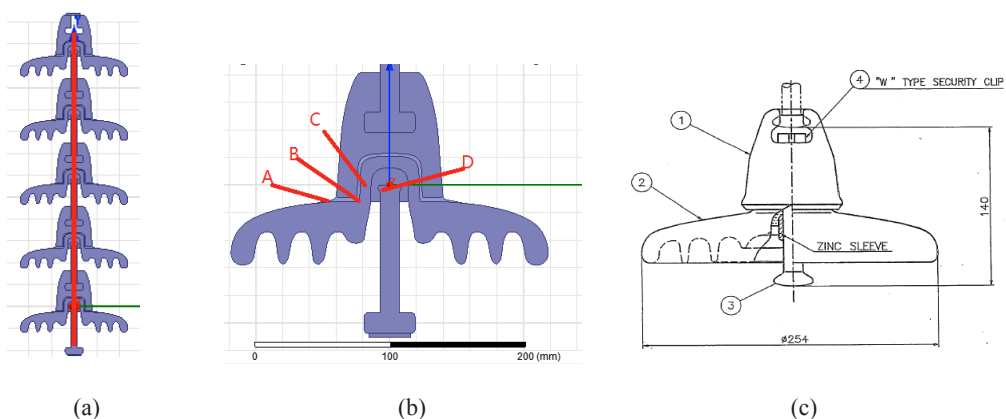


Figure 1. a) Cap and pin porcelain insulator unit; b) Point of interest in porcelain insulator model near energised end; c) Dimension of insulator model

Figure 1 shows one unit of a cap and pin porcelain insulator. The insulator string is stacked according to the line voltage. Hence, the higher the line voltage, the more insulator units are needed to be stacked up to withstand the applied voltage. In this study, the main focus is to investigate the effect of humidity on the electric field and voltage distribution on the cap and pin insulator. One cap and pin porcelain insulator is simulated to understand the relationship between humidity and electric field strength. However, it is advisable to test the high voltage insulator with a short standard string instead of a single unit insulator according to MS IEC 60383; thus, the insulator string to be modelled is a five- unit cap and pin porcelain insulator as shown in Figure 1(a) (MS IEC, 2013).

The computer used in this simulation is equipped with 16 GB ram and 2 processor core. The materials of the different parts of the insulator are defined first before the simulation begins. The relative permittivity of the cement and porcelain is 14 and 6 respectively (Asadpoor & Mirzaie, 2012). Before the simulation is started in the FEM modelling, the model undergoes a process known as meshing which discretises the insulator into small building blocks known as finite elements in a mesh which consists of triangles in 2D and tetrahedral in 3D. In this simulation, two thin electrodes are added to the top and bottom of the model to simulate the energised electrode and the ground electrode. In the energised electrode, the excitation voltage is applied according to the short standard string withstand voltage from data sheet of the porcelain insulator, so the AC power frequency voltage is set to 170 kV while the other electrode that simulates the ground is set to 0 V.

The points of interest to investigate the electric field on the porcelain insulator are shown in Figure 1(b) as A, B, C and D. These few points are chosen for investigation because on a sharp edge, the electric field strength will be intensified with a higher electric field strength compared with a flat surface. Thus, by observing these few points, the effect of humidity on the electric field distribution is more easily clarified. In order to investigate the effect of humidity on the electric field strength around the porcelain insulator, the simulation of the insulator model under different levels of humidity is undertaken using 27% RH, 70% RH and 90% RH. The first step is to determine the indoor environment humidity which acts as a reference. The average outdoor humidity on normal day in Malaysia is 70% RH, 90% RH representing a fog or dew day (Bowler & Abram, 2006; Rahman, Izadi & Kadir, 2014). As the relative humidity of air change, the permittivity of the air also changes. Thus, the relative humidity of the air can be simulated by assigning different relative permittivity to the air in the simulation. *In this work, the relative permittivity is obtained based on the following approach (Zarnik & Belavi, 2012):

$$\text{Relative permittivity} = \left[1 + \frac{211}{T} \cdot \left(P + \frac{48 \cdot P_s}{T} \cdot \text{RH} \right) \cdot 10^{-6} \right] \quad (1)$$

Where T is absolute temperature (k), p is (mm Hg) pressure of air, p_s (mm Hg) is pressure of saturated water vapour and RH is relative humidity (%)

RESULTS AND DISCUSSION

Electric field strength distribution around insulator model

Based on the simulation model shown in Figure 1, the 2D electric field strength contour plot around the porcelain insulator model near the energised end is shown in Figure 2.

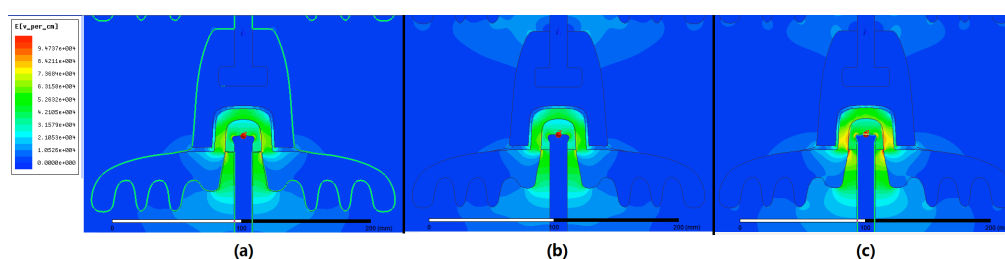


Figure 2. Electric field around the porcelain insulator model for a) 27% RH. b) 70% RH c) 90% RH

Figure 2 shows the electric field plot around the porcelain insulator for 27 % RH, 70 % RH and 90 % RH that is nearest to the energised electrode. It can be seen that the electric field strength is highest in the porcelain head portion cover inside the cap and is similar for three different humidity levels. This region suffers from high electric field strength and is at risk of corona discharge. Such discharge occurs in a location where the electric field strength exceeds the corona inception voltage of air which is roughly 30 kVcm^{-1} . From Figure 2, it can be observed that the area of blue is the region with a low electric field while the area in yellow green is the region with a high electric field. The points A and B are on the curve surface which is within the lower electric field (3 kVcm^{-1} to 30 kVcm^{-1}) region compared with other parts of the insulator with an edge surface. Another part of the insulator that is of interest is the porcelain insulator head portion inside the cap which is point C in Figure 1(b). Based on Figure 2, point C has a high electric field of up to 80 kVcm^{-1} when the applied relative humidity is 90 % RH. However, no obvious sharp edges are observed at that point in the model. The possible reason for the high electric field in this region is because of electric field intensification due to the sharp edge in the head of the pin or point D in Figure 1(b). The electric field strength of the various points in Figure 1(b) for different levels of relative humidity is tabulated in Table 1.

Table 1

Electric field distribution at specific locations in the insulator near the energised end

Location	27 % RH (kVcm^{-1})	70 % RH (kVcm^{-1})	90 % RH (kVcm^{-1})
A	3	2	3
B	22	21	27
C	62	57	74
D	68	63	82

Based on Table 1, it is clear that the electric field strength decreases when the relative humidity increases from 27% to 70% RH. However, it increases when the relative humidity is further increased to 90% RH. Point A shows almost constant electric field strength for different relative humidity. Among the four points, point D shows the highest electric field strength which is at 68 kVcm^{-1} , 63 kVcm^{-1} and 82 kVcm^{-1} for relative humidity of 27%, 70% and 90% respectively. The possible reason for this is that point D is nearest to the energised end and has a pointy edge. Furthermore, in terms of relative humidity comparison, relative humidity of 90% shows the overall highest electric field strength. For instance, the electric field strength at point C with relative humidity of 90 % shows the highest value (74 kVcm^{-1}) followed by relative humidity of 70% (57 kVcm^{-1}) and relative humidity of 27% (62 kVcm^{-1}).

All locations show a big difference in electric field strength when simulated at the same relative humidity even though these locations are near to each other. For example, when the relative humidity is 90%, the electric field strength at point A is 3 kVcm^{-1} , and the electric field strength at point D is 82 kVcm^{-1} at the same humidity level. This shows that the electric field strength around the porcelain insulator is highly uneven. Overall, there is no obvious trend for electric field when the relative humidity increases from 27% RH to 70% RH and 90% RH. However, when 90 % RH is applied, the electric field strength at all point inside the insulator head section is the highest for all four points A, B, C and D.

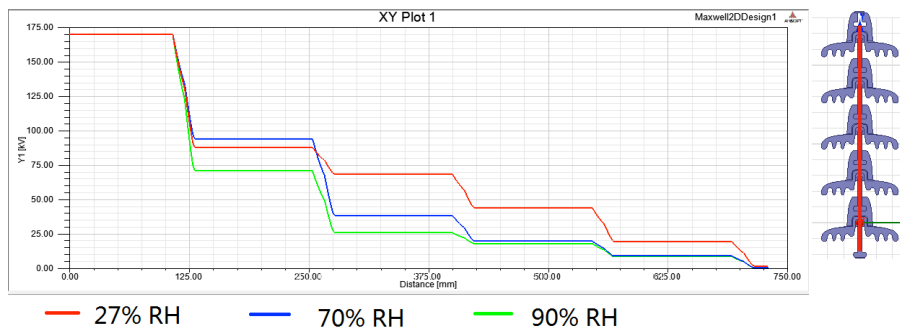


Figure 3. Voltage distribution along the porcelain insulator string model

Table 2
Voltage distribution along the porcelain insulator string

Relative Humidity (%RH)	0 mm (kV)	140 mm (kV)	280 mm (kV)	420 mm (kV)	600 mm (kV)
27	170	87	68	44	28
70	170	94	38	20	9
90	170	71	26	18	9

Voltage Distribution along the insulator string

Figure 3 provides a comparison of the voltage distribution along the cap and pin porcelain insulator string under different levels of humidity as shown by the mini model at the top right. The plot is drawn upwards, which means 0 mm is located at the bottom and 600 mm is located at the top. From Figure 3, it can be observed that in all relative humidity environments, the voltage along the insulator string shows the same shape which is a stair shape. Referring to Table 2 and taking the 27% RH plot as an example, the voltage at 0 mm shows 170 kV until it reaches the first cement and porcelain body part which is at the location of 125 mm. At that location, due to the resistance from the cement and porcelain part, the voltage drops from 170 kV to 87 kV, or a decrease of 48%. Point 140 mm is the cap of the first insulator near the energised end and the pin of the next insulator. The voltage in this region does not show an obvious change because the cap and pin of the porcelain insulator is made of stainless steel that has a low resistance so the voltage remains at 87 kV. At a point of 250 mm which is the cement and porcelain part of the second insulator from the energised end, the voltage drops from 87 kV to 68 kV, or a decrease of 21%. The voltage continues to drop at the 390 mm point from 68 kV to 44 kV, or a decrease of 35%. At the point 690 mm, the cement and porcelain part of the last insulator causes the voltage distribution to drop from 12 kV to 0 kV. From the plot, it can be seen that in the cement and porcelain part of every insulator, the voltage distribution also drops, which can be observed at the points 130 mm, 260 mm, 390 mm and 550 mm and 690mm.

When the level of the relative humidity applied to the environment around insulator string is increased, the voltage distribution in the insulator string shows decreasing trend for all location except from point 125 mm to 250 mm when relative humidity (70%) is applied. At the 130 mm location, the 90% RH indicated the highest decrease from 170 kV to 71 kV or a 58% decrease. From the plot, it can be observed that the voltage distribution along the insulator is similar when the applied humidity is 27% RH and 70% RH from point 420 mm to 750 mm; the voltage distribution along the insulator has the same shape and almost similar value. The voltage distribution along the insulator string for 90% RH humidity is the lowest among the humidity applied along the whole insulator string; for example, at point 280mm, the voltage

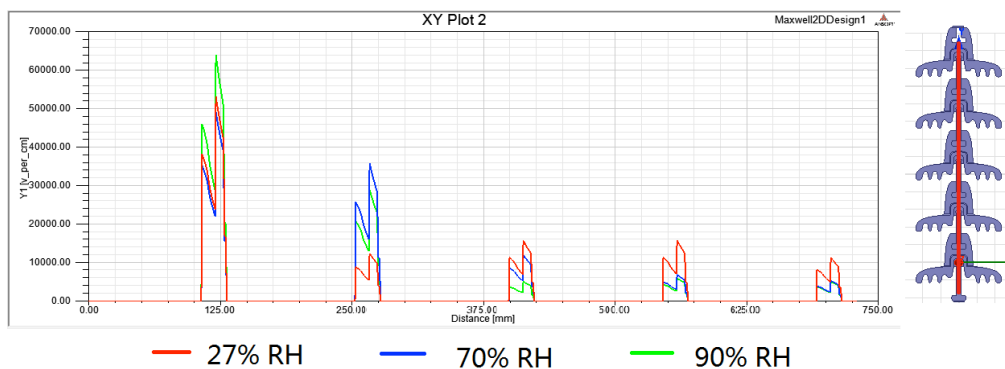


Figure 4. Electric field along the porcelain insulator model

Table 3
Electric field strength distribution along the insulator string

Relative humidity (%RH)	120 mm (kVcm ⁻¹)	260 mm (kVcm ⁻¹)	410 mm (kVcm ⁻¹)	550 mm (kVcm ⁻¹)	700 mm (kVcm ⁻¹)
27	52	12	15	15	11
70	48	35	12	7	5
90	63	28	5	6	5

of the insulator for 27% is 68 kV, but the voltage distribution for the 90% RH environment is 26 kV only, which shows a decrease of 61% when humidity of environment changes from 27% RH to 90% RH. In the same location, the voltage distribution of 70% RH is 38 kV, which show a decrease of 31% when compared with 26 kV voltage distribution when the humidity applied is 90% RH.

Figure 4 shows the electric field distribution along the cap and pin porcelain insulator string under different levels of relative humidity. It can be observed that the electric field strength only exists at point where the cement and porcelain body part meet inside the cap of the insulator for each insulator in the insulator string. There are two peaks of electric field strength inside the cement and porcelain part of every insulator unit at the intersection between two different materials. The lower electric field peak is the intersection of stainless steel and cement while the higher electric field peak is due to the intersection of cement and porcelain. From the plot, it can be seen that the electric field strength distribution follows the same shape when the applied humidity differs. However, there is no obvious trend observed in the electric field strength when the humidity increases. Moreover, it can be seen from the plot that the electric field strength for all plots at every location is different although the same shape can be observed in every location. Referring to Table 2 it can be seen that the electric field strength is the highest at the 120 mm location when compared with the other locations of the insulator string. At a location of 120 mm, the electric field strength is 63 kVcm⁻¹ when the applied humidity is 90% RH, dropping to 48 kVcm⁻¹ when the applied humidity is 70% RH, but increased to 52 kVcm⁻¹ when the applied humidity is 27% RH. Along the insulator string, the electric field strength for 27% RH, 70% RH and 90% RH did not show any trend.

CONCLUSION

A systematic simulation work was conducted to study the electric field strength along the porcelain insulator using the finite element method. The developed model was used to predict the locations within the insulator under high stress due to the electric field. The locations surrounding the intersection and sharp edge points within the insulator were found to exhibit high electric field stress. In addition, the electric field strength near the sharp edge showed electric field strength intensification due to the effects of sharp edge. Hence, in order to reduce the electric field stress, the sharp edge should be replaced with a curved surface. This work shows the effect of relative humidity on the electric field and voltage distribution. even though the simulation only shows the very basic effect of different relative humidity level to electric field and voltage distribution around insulator. Future research can look at the effect

of relative humidity to porcelain insulator by investigating the effect of relative humidity to porcelain insulator in different perspective in order to have better understanding of the relative humidity effect.

REFERENCES

- Asadpoor, M. B., & Mirzaie, M. (2012). Simulation and measurement of the voltage distribution on high voltage suspension Porcelain insulator string under pollution condition. *International Journal of Applied Sciences and Engineering Research*, 1(2), 165-175.
- Bowler, N., & Abram, E. R. (2005). Monitoring the Effect of Relative Humidity During Curing on Dielectric Properties of Composites at Microwave Frequencies. In *AIP Conference Proceedings* (Vol. 820, No. A, p. 469). IOP Institute of Physics Publishing Ltd.
- Costea, M., & Baran, I. (2012). a Comparative Analysis of Classical and Composite Insulators Behavior. *University" Politehnica" of Bucharest Scientific Bulletin, Series C: Electrical Engineering*, 74(1), 147-154.
- Fouladi, R., Mirzaie, M., & Moradi, M. (2014). Calculation of AC and Transient Potential Distribution along HV Insulator String under Polluted Condition based on FEM. *International Journal of Engineering Innovation and Research*, 3(1), 74-78.
- Gouda, O. E., & Dein, A. Z. E. (2013). Simulation of overhead transmission line insulators under desert environments. *IET Generation, Transmission & Distribution*, 7(1), 9-13.
- Izadi, M., Rahman, M. A., & Ab Kadir, M. Z. A. (2014, March). On the voltage and electric field distribution along polymer insulator. In *2014 IEEE 8th International Power Engineering and Optimization Conference (PEOCO2014)*.
- Kontargyri, V. T., Gonos, I. F., & Stathopoulos, I. A. (2009). Measurement and simulation of the electric field of high voltage suspension insulator. *European Transactions on Electrical Power*, 19(3), 509-517.
- Looms, J. (1998). *Insulators for High Voltages*. London, United Kingdom: Peter Peregrinus Ltd.
- MS IEC (2013). *Insulator for overhead lines with a nominal voltage above 1000 V*. MS IEC 60383.
- R Rahman, M. A., Izadi, M., & Ab Kadir, M. Z. A. (2014, December). Influence of air humidity and contamination on electrical field of polymer insulator. In *IEEE International Conference on Power and Energy (PECon), 2014* (pp. 113-118). IEEE.
- Reddy, B. S., Naik, B. S., Kumar, U., & Satish, L. (2012). Potential and electric field distribution in a ceramic disc insulator string with faulty insulators. *Properties and Applications of Dielectric Materials (ICPADM), 2012 IEEE 10th International Conference*. Bangalore.
- Taklaja, P., Kiitam, I., Niitsoo, J., Kluss, J., & Hyvonen, P. (2015). Electric field distribution in glass and porcelain pin insulators. *Environment and Electrical Engineering (EEEIC), 2015 IEEE 15th International Conference*. IEEE.
- Zarnik, M. S., & Belavi, D. (2012). An Experimental and Numerical Study of the Humidity Effect on the Stability of a Capacitive Ceramic Pressure Sensor. *Radioengineering*, 21, 201-206.

Metal Shape Detection and Evaluation using Giant Magneto Resistance System

Norhisam M.^{1,2*}, M. K. Roslan², Ishak A.¹ and M. N. Hamidon¹

¹Department Of Electric and Electronic Engineering, Faculty of Engineering, Universiti Putra Malaysia, 43400 UPM, Serdang, Selangor

²Institute of Advanced Technology UPM, Universiti Putra Malaysia, 43400 UPM, Serdang, Selangor, Malaysia

³Electrical and Electronic Engineering, Faculty of Engineering, Shinshu University, Wakasato, Nagano, 380-8553, Japan

ABSTRACT

Visual inspection to locate metals embedded in walls or floors is impractical. Detection of these metals can only be done with a proper metal detection. Accordingly, the development of a magnetic imaging system based on giant magneto-resistance (GMR) sensors is presented for metal shape detection. This system is based on magnetic flux leakage testing (MFLT) principle for detecting the shape of ferromagnetic material specimens. The imaging system is constructed using 21 linear GMR sensors array as signals sensing unit (SSU). In this study, a few ferromagnetic SS400 mild steels specimens in various shapes are used as specimens. Image produced confirm system functionality in detecting and evaluating metal shapes.

Keywords: Magnetic flux leakage testing (MFLT), giant magneto-resistance (GMR) sensors, shape evaluation

INTRODUCTION

Metal embedded in walls or floors cannot simply be determined by visual inspection. This research focuses on detecting and

evaluating metal shapes using giant magneto resistance sensor magnetic imaging (GMR-i) system. The GMR-r system is proposed as a method carry out inspections to determine shapes of metal specimens. Magnetic flux leakage (MFL) is introduced to discover any cavity or defect in embedded metal specimens.

Examination and inspection of tested objects without alteration is a kind of non-destructive evaluation (NDE) in order to find out the discontinuities that may affect the function of a specific system as discussed by Lee et al. (2008). Many studies have examined the effectiveness of NDE for system

ARTICLE INFO

Article history:

Received: 24 August 2016

Accepted: 03 Jun 2017

E-mail addresses:

norhisam@upm.edu.my (Norhisam M.),

modemelo900@gmail.com (M. K. Roslan),

ihak_ar@upm.edu.my (Ishak A.),

mnh@upm.edu.my (M. N. Hamidon.)

*Corresponding Author

maintenance. The key feature in NDT industries is the measurement time. Therefore, it is not practicable to use a single small sized magnetic sensor element to scan an object in a fine grid. Instead, a sensor array housing a number of simultaneously operating elements is more effective.

Magnetic sensors for various NDE applications are developed for solenoid coil, hall sensor and GMR sensor (Lehnz & Edelstein; 2006). The effectiveness of these sensors varies according to their specific systems. These magnetic sensors function under high magnetic field condition except the GMR sensor which also functions at low magnetic field condition. According to Wakiwaka (2004) in order to determine the right magnetic sensor, three criteria must be met: low field operating range, wide operating frequency and small dimensions in order to obtain high spatial resolution. Hence, based on previous studies, GMR sensor is suitable for NDE application.

New application of GMR sensor for NDE application is presented in this paper. The GMR sensor for magnetic flux leakage testing (MFLT) probe was fabricated as a metal inspection probe for shape detection of ferromagnetic metal specimens.

MAGNETIC FLUX LEAKAGE TESTING (MFLT)

Basic Principles

In recent years, non-destructive testing industries have set up magnetic flux leakage testing (MFLT) as a magnetic method to identify pitting and corrosion in steel structures. It is most frequently used during inspection of metal storage tanks and steel pipelines using a powerful magnet to magnetise the steel; where there is rust, corrosion or missing metal, the magnetic field “leaks” from the steel. The MFLT could distinguish the condition of metal steel according to the distribution of magnetic field produced. In a MFL tool, a magnetic detector is to be found between the poles of the magnet to detect the leakage field. Magnetic sensors may be used in most conditions using MFLT.

This paper examines the metal and shape detection in a metallic steel using flux leakage testing method. This method allows magnetic flux to be induced into the specimen plate from a magnetic field which is formed by an excitation coil placed near the specimen metal. A temporary magnetic field environment is created near the specimen material. The flow of magnetic flux is disturbed when a metal edge is present resulting in magnetic field which contains the information relating to the perturbation. In this work, magnetic flux is induced by moving a steady magnetic field in the area of the sample plate plane. An even magnetic field is produced by the excitation coil creating a constant magnetic field variant in the metallic surface as it moves.

Under normal condition, Figure 1(i) illustrates permanent magnet with magnetic flux flow through it. As shown in Figure 1 (ii), magnetic flux leakages (MFL) are developed and some of the magnetic flux flows through the specimen as the ferromagnetic specimen moves along the y-axis. When the specimen is at the GMR sensor, the MFL is detected by the array. A higher MFL density value is sensed as the specimen gets closer to the GMR sensor as in Figure 1 (iii).

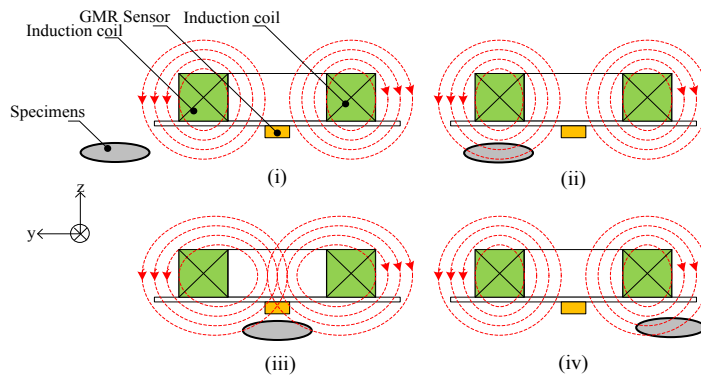


Figure 1. The application of MFLT method where (i) condition before evaluation, (ii) specimen navigates into the system, (iii) the magnetic flux distribution changes according to the disturbance and (iv) system fully evaluates the specimen

As the specimen moves further away from the GMR sensor array as in Figure 1 (iv), there is no MFL flow detected, indeed, no induced signals are developed by the sensor array. A complete evaluation of metal specimen is deemed done when the evaluation is comprehensive .

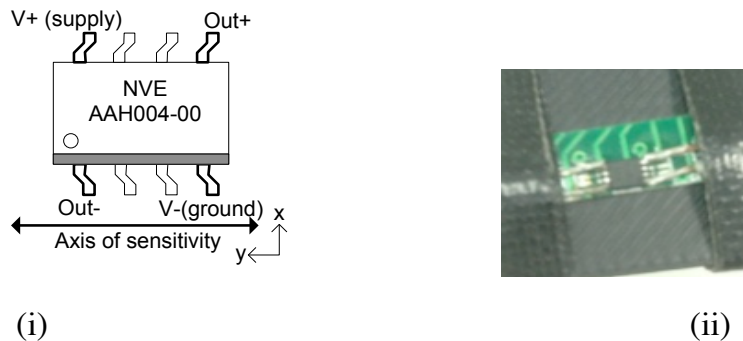


Figure 2. GMR sensor pin-out where (i) shows the axis of sensitivity of sensors in y-axes. (ii) GMR sensors is simply miniaturised and could be easily mounted simultaneously as it is small in size

Giant Magnetoresistance (GMR Sensor)

In this study, GMR sensor is selected from an AA-Series analog of NVE’s company as in Figure 2. These GMR sensors are versatile as they are characterised by high sensitivity to applied magnetic fields, low power utilisation, outstanding temperature stability, and small in size. The sensor has distinctive and unparalleled magnetic sensing capabilities.

These GMR sensors have broad applications, from rough industrial and automotive position, speed and current sensors to low-voltage battery-powered sensors for hand-held instruments and implantable medical procedures(see Table 1). These GMR sensors are unique and flexible which makes them an excellent choice for a range of analog sensing applications.

Table 1
GMR specifications

Parameter	GMR AAH004-00
Applied fields sensitivity	Very high
Operation field range	Low
Hysteresis	High
Range of temperature	Very high

These sensors employ patented GMR materials and on-chip flux concentrators to supply a directionally sensitive output signal. Table 2 displays the overall performance of GMR sensors. These sensors are sensitive with a cosine-scaled falloff in sensitivity as the sensor is rotated away from the sensitive direction and it is also sensitive in one direction in the plane of the IC. The GMR sensors are designed in a Wheatstone bridge configuration to provide temperature compensation. Besides, these devices offer the same output for magnetic fields in the positive or negative direction along the axis of sensitivity which is the omni-polar output.

Table 2
GMR performances

Sensor	Saturation field (Oe ¹)	Linear range (Oe ¹)	Sensitivity (mV/V- Oe ⁻¹)	Resistance (Ohms)	Package ²	Die size ³ (µm)
GMR AAH004-00	15	Min 1.5 Max 7.5	Min 3.2 Max 4.8	2K ± 20 %	MSOP	411 x 1458

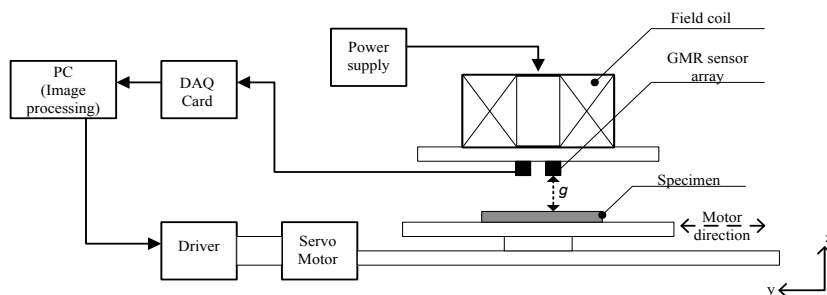


Figure 3. The experimental setup block scheme

System

A sensing application system consists of an induction coil as the flux source and GMR sensor for the sensing application. As shown in Figure 3, there are induction coils winded up between a holder and an array of GMR sensors located beneath it. The induction coil is made up of two sides, left and right, which producing flux to the centre direction between them. An array of GMR sensors is located at the centre in between the coils for better sensing purposes. The

magnetic imaging system is displayed in Figure 4. As depicted in Figure 3, an array of GMR sensors is installed in a plate which moves above the specimen. The sensors are made up of 21 high sensitivity GMR sensors. The Induction coil above the sensors has an array of functions to produce the magnetic flux in the conductive material and GMR sensors measure the magnetic field in the vicinity of the specimens.

A San-MotionR motor (Sanyo Denki) with 200mm long sliding glide system was placed below the sensor that seizes the specimen during inspection. The motor is powered by an AC servo motor which can accelerate the specimen holder at a rate 8000pulse/mm. A R-setup motion driver/controller which controls the motor is used based on the input. The GMR sensors array is connected to the National Instrument USB-6229 DAQ which is used to measure the output voltage of the sensor with 16-bit resolution. This is illustrated in Figure 3 where there are R-setup motion device, the driver/controller, an array of GMR sensors, DAQ, computer and ferromagnetic plate specimen.

The signal flow

This section explains the operations of the magnetic imaging system which is based on the magnetic flux leakage testing principle. Magnetic flux leakage is sampled on the surface of ferrous objects which is then detected by the signal sensing unit (SSU) of the system. The SSU detects the changes of induced magnetic field, B, on the ferrous object’s surface. The signals are then forwarded to the Signal Acquisition Unit (SAU) and finally, to the Signal Processing Unit (SPU) for signals processing as shown in Figure 4.

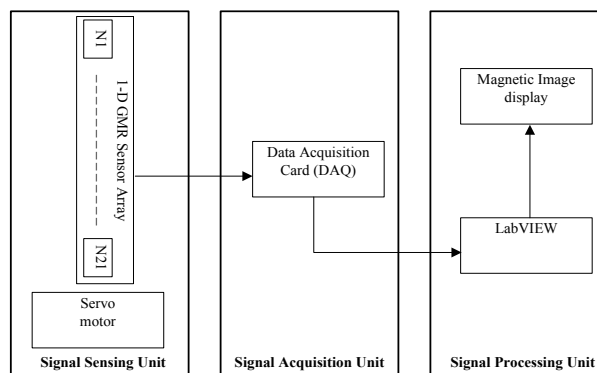


Figure 4. Signals flow of system

SYSTEM EVALUATION

This section discusses results of the magnetic imaging system experiment for ferromagnetic material shape evaluation. One could observe magnetic images of ferromagnetic shapes being plotted. Three ferromagnetic metal specimens of a square shape, round shape and triangular shape were used as specimens for magnetic imaging inspection verification. These specimens are standardised with 3.0mm thickness. They are made up of a soft iron ferromagnetic (SS400)

as shown I Figure 5. Specimens are referred to as sp i, sp ii, sp iii sp iv. They are classified according to their shapes and structures.

The experiment was conducted to evaluate the shape of the ferromagnetic metal specimens as shown in Figure 5 and performed based on the steps described in Figure 4. The system is moving with a constant displacement of 1.0mm. It is placed within the imaging area underneath the GMR sensors system. The magnetic gap which is the distance between sensors and specimens is kept constant at 7.0mm.

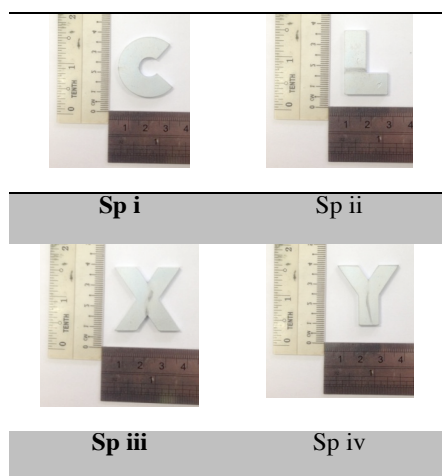


Figure 5. Dimensions of specimens

In the magnetic flux leakage testing (MFLT) application, the absolute induced voltage signals are obtained in order to employ the image interpolation technique in the OriginPro8 application used for magnetic image display. Figure 6 illustrates the magnetic image of ferrous specimens which are round, triangular and square shaped. Since the induced current signals are directly proportional to the magnetic field, B , it can be said that the magnetic field strength is increasing with induced current signals. The induced current signal is fixed at 3.0A. This is due to too low magnetic field when less current is used as the system malfunctions when high magnetic field is used. In Figure 6, images are produced at the parameter of 3.0A with the magnetic gap of 7.0mm. The shapes of the specimens are visible.

Table 3
Experiment condition

Item	Values
Coil number of turn, n	200
Coil size (mm)	0.5
Current, I (A)	3.0
Magnetic gap, g (mm)	7.0

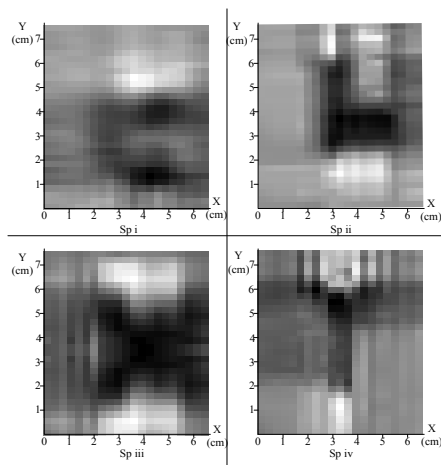


Figure 6. Magnetic image produced using Origin-Pro 8.0

CONCLUSION

The development of a magnetic imaging system using Giant Magneto-resistance (GMR) sensors has been discussed in this paper. It focuses on the development of magnetic imaging system for shape evaluation of ferrous metal specimens. The magnetic flux leakage testing (MFLT) principle is used in developing the system. All measurements taken out are taking care regarding the shapes evaluation of metal. The prototype of this system is successfully developed by integrating SSU, SAU and SPU. The SSU launches the system with sensing capabilities which captures the flux changes between the sensors and specimen and data is later analysed analysis. Finally, images are formed by the SPU using Origin-Pro 8 software. An induction coil is fixed with 200n of 0.5mm copper wire and current supply of 3.0A to produce a suitable magnetic flux for the system to function well. The sensor is able to detect the shape of ferromagnetic metal specimen with a perpendicular gap of 7mm between the sensors and specimen. The GMR sensor is able to produce the measurement by crossing the edge of the specimens. Future research is needed to improve the usage model of the magnetic imaging system of GMR sensor.

ACKNOWLEDGEMENT

The authors would like to thank Department of Electric and Electronic Faculty of Engineering, UPM, and Electric and Electronic Department, Faculty of Engineering Shinshu University for funding this research.

REFERENCES

- Baibich, M. N., Broto, J. M., Fert, A., Van Dau, F. N., Petroff, F., Etienne, P., ... & Chazelas, J. (1988). Giant magnetoresistance of (001) Fe/ (001) Cr magnetic superlattices. *Physical Review Letters*, 61(21), 2472-2475.

- Dehmel, G. (1989). Magnetic field sensors: induction coil (search coil) sensors. *Sensors Set: A Comprehensive Survey*, 5, 205-253.
- Gasparics, A., Vártesy, G., Farkas, T., & Szollosy, J. (2010). Magnetic Imaging in non-destructive testing. In *2nd International Conference on Mechanical and Electrical Technology (ICMET) 2010* (pp. 47-49).
- Lee, J., Hwang, J., Jun, J., & Choi, S. (2008). Nondestructive testing and crack evaluation of ferromagnetic material by using the linearly integrated hall sensor array. *Journal of Mechanical Science and Technology*, 22(12), 2310-2317.
- Lenz, J., & Edelstein, S. (2006). Magnetic sensors and their applications. *IEEE Sensors Journal*, 6(3), 631-649.
- Lijian, Y., Gang, L., Guoguang, Z., & Songwei, G. (2009, August). Sensor development and application on the oil-gas pipeline magnetic flux leakage detection. In *2009 9th International Conference on Electronic Measurement & Instruments* (pp. 2876-2878).
- Tumanski, S. (2007). Induction coil sensors—A review. *Measurement Science and Technology*, 18(3), 31-46
- Wakiwaka, H. (2004). Characteristics of Giant Magnetoresistance Sensors and Their Applications. *Journal-Magnetics Society of Japan*, 28(7), 825-833.
- Yamada, S., Chomsuwan, K., & Iwahara, M. (2006, October). Application of giant magnetoresistive sensor for nondestructive evaluation. In *2006 5th IEEE Conference on Sensors* (pp. 927-930). IEEE.

Zero-Padding in DWT Satellite Image Compression

Suhaidi Shafie^{1,2*}, Halah Saadoon Shihab¹, Fauzan Ahmad³ and A. R. Ramli²

¹*Institute of Advanced Technology, Universiti Putra Malaysia, 43400 UPM, Serdang, Selangor, Malaysia*

²*Faculty of Engineering, Universiti Putra Malaysia, 43400 UPM, Serdang, Selangor, Malaysia*

³*Malaysia-Japan International Institute of Technology (MJIT), Universiti Teknologi Malaysia, 54100 Kuala Lumpur, Malaysia*

ABSTRACT

Discrete Wavelet Transform (DWT)-based image compression techniques have been utilized in most of the earth observation (EO) satellites launched during the last few decades, since they have proved to be more efficient than other methods used previously with remote sensing multispectral imaging payloads. The efficiency of these techniques is mainly due to their high compression ratio that can be achieved while maintaining the quality of the compressed image. Also, they are considered multi-resolution compression techniques. However, these techniques are considered computationally demanding, due to their complex and sophisticated hardware. Due to the limited computational resources available on-board small satellites, they are considered one of the important criteria when choosing the satellite image compression method, along with the compression ratio and quality of the reconstructed image. Hence, an alternative DWT-based method was proposed, developed and implemented in this work with the aim of reducing the computational resources on-board a small satellite, replacing the regular DWT thresholding and quantization processes that are usually used to achieve lossy compression, with the zero-padding technique. This method will also help to control the change in the compression ratio and quality of the reconstructed image according to the end-user's scientific needs of the satellite image. The results of this work indicated, objectively and subjectively, that a decrease in the computational resources required on-board satellites was achieved by decreasing the processing time needed to complete the compression, without a significant difference in quality of the image reconstructed at the ground station.

Keywords: Satellite images, Remote sensing, Image compression, Discrete Wavelet Transform

ARTICLE INFO

Article history:

Received: 24 August 2016

Accepted: 03 Jun 2017

E-mail addresses:

suhaidi@upm.edu.my (Suhaidi Shafie),

hala_alubaidi@yahoo.com (Halah Saadoon Shihab),

fauzan.kl@utm.my (Fauzan Ahmad),

art@upm.edu.my (A. R. Ramli)

*Corresponding Author

INTRODUCTION

Optical remote sensing imagers mounted on-board satellites employ multispectral sensors, such as visible, near infrared and shortwave infrared sensors, to form images of the earth's surface by detecting solar radiation reflected from objects on the ground (Dumitru et al.,

2015), converting the reflected surface information into an image format (Mulla et al. 2015). Hence, multispectral images are used in remote sensing to a large degree, and they are beginning to be used in several other applications as well, such as medical imagery and quality control (Delcourt et al., 2010).

Since on-board computational resources are limited (Thiebaut & Camarero, 2011), image compression is used in many space missions to reduce on-board data storage and transmission bandwidth requirements from the satellite to the ground station (Yu et al., 2009).

Image compression schemes are divided into two main categories: Lossless and Lossy (CCSDS Secretariat Space Communications and Navigation Office 2011). Lossless image compression allows an image to be compressed and decompressed without any information loss. In lossy compression schemes, a certain amount of loss of data is accepted. Although it is impossible to reconstruct the exact original image using lossy image compression, it provides a much higher compression ratio than lossless compression (Faria et al., 2012), hence, it is used in this work.

Raw multispectral images captured by remote sensing satellites have very high *resolutions* (Raju et al., 2016). Hence, satellite images cannot be dealt with in the same manner as low resolution images, especially when taking into consideration the limited resources on-board satellites (Yu et al., 2009). Hence, choosing the suitable compression technique for such images should be carefully considered in order to achieve high compression ratios (CR) to decrease the bandwidth required to transmit data from satellite to earth while maintaining as much as possible the important scientific information in the image when reconstructed on earth.

Discrete Wavelet Transform (DWT)-based compression methods, such as JPEG2000 (Taubman 2002), have been widely used more than other transform-based methods, such as the DCT (Yu et al. 2009) since DWT is considered a multi resolution transform (Singh & Tripathi, 2014), and also due to the high compression ratio that can be achieved using these techniques (Thiebaut & Camarero, 2011) while maintaining a good level of quality of the reconstructed images. However, this method will cause an increase in the computational resources when used on-board satellites, due to its complexity. The zero-padding of DWT detail coefficients was used instead of thresholding and quantization process in this work since:

1. This method can decrease the computational resources on-board satellites.
2. It was not discussed in detail in previous works, especially with respect to satellite images.

DWT-BASED LOSSY IMAGE COMPRESSION

Basic Architecture of a DWT-based Lossy Image Compression System

The DWT-based lossy image compression systems are usually accomplished using three forward main steps and three inverse steps as shown in Figure 1.

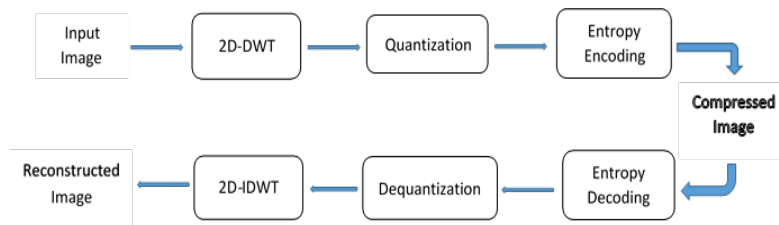


Figure 1. A basic DWT-based lossy image compression system

The first stage is the forward transform (transformation from spatial domain to frequency domain), represented in the current work by 2 Dimensional-DWT, acquiring separated high and low frequency coefficients in order to concentrate the most important information into as few low frequency components as possible.

The second stage is represented by thresholding and quantization. *Thresholding* can be identified by setting all 2D-DWT coefficients that are less than a specific value to zero, in order to eliminate the less important information from the DWT coefficients to increase the compression ratio, thus, the higher the threshold value, the more CR but lower quality will be obtained. *Quantization* is an irreversible process, represented by rounding the resulting coefficients after thresholding.

The third forward stage is usually represented by the entropy encoding lossless process, adjusting the coded information to get further bit rate reduction in order to increase the compression ratio.

The DWT-based image compression can be classified into several methods according to the entropy coding technique used, such as JPEG2000 (Rabbani & Joshi 2002), Embedded Zero tree Wavelet algorithm (EZW) (Shapiro, 1993), Set Partitioning In Hierarchical Trees (SPIHT) (Said et al., 1996), and the CCSDS-IDC (Image Data Compression) (Faria et al., 2012). The coding for all these DWT-based methods depends on separating the significant from the insignificant values.

The entropy coding will not be considered in this paper since it will have an impact on the compression ratio (CR) results according to the type of the encoder used.

The forward compression stages take place on-board the satellite whereby the compressed satellite image is transmitted through a radio frequency (RF) link to a ground station, where the inverse stages take place to reconstruct the image.

Each level of the 2D- DWT transform produces two types of coefficients according to the filters used, based on the fact that the human visual system can recognize low frequency information much more efficiently than the high frequency information. These coefficients are:

- The *approximation coefficients* (cA): they indicate the most important information of the image, resulting only from low pass filters.
- The *detail coefficients*: they indicate the high frequency, less important information of the image, identified by the horizontal (cH), vertical (cV) and diagonal (cD) coefficients.

These coefficients are represented for 2-levels of 2D-DWT as shown in Figure 2 (Anon n.d.), where the symbols L and H indicate the Low and High pass filters used in this process respectively. Hence, the LL in each level represents the Approximation coefficients, while the other HL, LH and HH indicate the Horizontal, Vertical and Diagonal detail coefficients respectively.

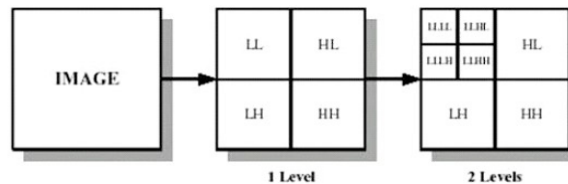


Figure 2. DWT- image compression levels

Image Compression Metrics

The image compression performance can be evaluated based on several factors. These factors will be presented in the current work:

- Objectively (using CR and PSNR, as defined below)
- Subjectively (visually)

Compression Ratio (CR): indicates the compression achieved for an image. It can be computed using equation (1).

$$CR = \frac{\text{Size of Original Image}}{\text{Size of Compressed image}} \tag{1}$$

Peak Signal to Noise Ratio (PSNR): gives the numerical value for the quality of an image after being compressed and decompressed. It can be computed using equation (2). Units are in (dB).

$$PSNR = 10 \log_{10} \frac{I^2}{MSE} \tag{2}$$

Where I : The allowable image pixel intensity level

Ex: for (8bpp) image, $I = (2^8 - 1) = 255$

Mean Square Error (MSE): Indicates level of distortion by comparing original data with the reconstructed data. It can be computed using equation (3).

$$MSE = \frac{1}{MN} \sum_{i=1}^M \sum_{j=1}^N (A_{ij} - B_{ij})^2 \tag{3}$$

Where: A : Original image of size $M \times N$

B : Reconstructed image of size $M \times N$

THE PROPOSED DWT SATELLITE IMAGE COMPRESSION:

The thresholding and quantization processes in the DWT-based compression technique were replaced in this work by a process which can be identified by padding one, two or all the three of the 2D-DWT detail coefficients with zeros, resulting in 8 zero-padding cases. This technique will help to decrease the computational resources on-board satellites and also change the CR and PSNR values of the satellite image as required by changing the zero-padding cases.

The proposed technique should decrease the computational resources on-board satellites for several reasons:

1. Rounding is not used, as no thresholding or quantisation is needed.
2. The task of the DWT encoder that should be used after this process to accomplish the separation of the significant from the insignificant coefficients will be much simpler, since the coefficients were already separated using this technique.

This will result in a decrease in image compression time and cost due to the decrease of compression hardware requirements used on-board the satellite.

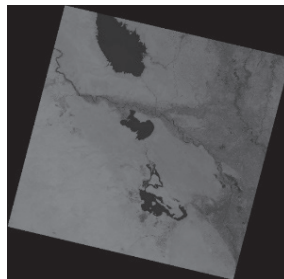


Figure 3. Baghdad (B6)



Figure 4. 2nd level of 2D-DWT image compression using Zero-Padding technique cases (compressed images)

Figure 4 illustrates the 8 zero padding cases of the 2nd level of 2D-DWTcompression applied to the Baghdad B6 satellite image shown in Figure 3,captured by the LANDSAT 8 earth observation satellite, having a resolution of (7924×7924) pixels and a bit depth of 16 bpp, to simulate an on-board satellite image compression process.

RESULTS AND DISCUSSION

Results of the Proposed DWT Technique

Figure 5 shows the results of the second level of 2D-DWT (represented by CR and PSNR), according to the change in the zero-padding cases, after being applied to the Baghdad (B6) satellite image (Figure 3), employing the bior 3.7 wavelet. The results were generated using MATLAB software.



Figure 5. Objective results for 2nd level of 2D-DWT image compression

It can be noticed from the results that when the zero-padding technique is used, the CR and PSNR values change according to the *type* and *number* of the 2D-DWT detail coefficients to be reconstructed.

Types of detail coefficients. Different types of detail matrices in each image contain different amounts of data according to the image type and the filter used. In the Baghdad satellite image, for example, the Horizontal coefficient matrix (cH) is the highest in information followed by the vertical (cV) while the diagonal (cD) includes the least information. However, that is not the case for all types of images, which may differ in that order.

Number of Detail Coefficient Matrices. The more matrices of 2D-DWT detail coefficients are zero padded in each level, the higher compression ratios and less but satisfactory PSNR values can be achieved, since less detail coefficients will be reconstructed.

The Time Gain Resulting From using the Proposed DWT Method

Figure 6 demonstrates the processing time during two-levels of 2D-DWT satellite image compression when using the DWT-standard quantization or the zero-padding technique for different values of PSNR.

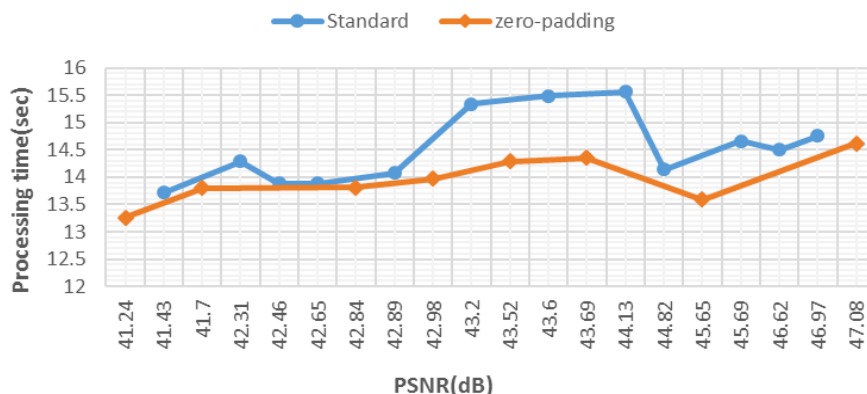


Figure 6. Processing time for image compression when using the DWT-standard quantization & the zero-padding technique

It can be noticed from Figure 6 that a time gain was achieved using the Zero-Padding technique. This was accomplished without a significant difference in the reconstructed image quality (PSNR), as shown objectively in Figure 7, for different values of compression ratio, and subjectively in Figure 8.

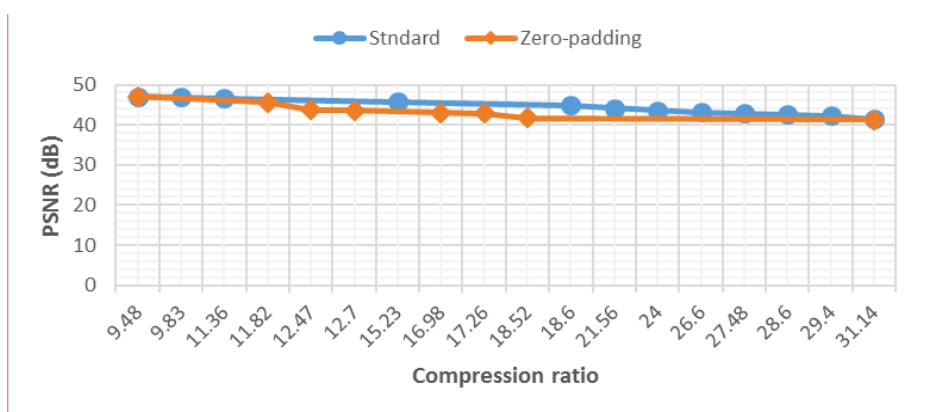


Figure 7. Quality of the reconstructed image when using the DWT-standard quantization & the zero-padding method

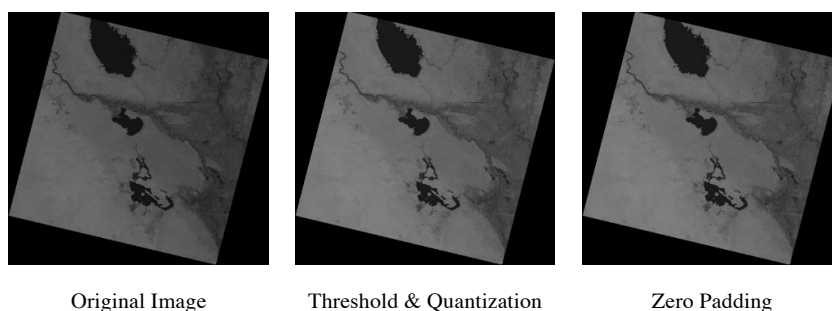


Figure 8. The visual representation of the reconstructed image quality difference between the DWT-standard quantization & the zero-padding method when CR=26

CONCLUSION

In conclusion, it is feasible to employ the zero- padding technique in the DWT- based image compression on-board satellites instead of the regular thresholding and quantization processes, since 1) it will help decrease the computational resources required for image compression on-board satellites, without losing the good quality of the satellite image after being reconstructed at the ground station, and 2) a good level of control to change the CR and PSNR values for each DWT-level can be achieved while guaranteeing that all the important information in the approximation coefficients will not be involved in the zero-padding process. This is easier than choosing a threshold value for all coefficients, which can be tricky, since some of the important information might be lost.

REFERENCES

- Anon, Silicon Mentor. Available at: <http://www.siliconmentor.com/image-compression-using-dwt/>.
- CCSDS Secretariat Space Communications and Navigation Office, 7L70 Space Operations Mission Directorate NASA Headquarters, 2011. *IMAGE DATA COMPRESSION (Recommendation for Space Data System Standards)*, Washington, DC 20546-0001, USA.
- Delcourt, J., Mansouri, A., Sliwa, T., & Voisin, Y. (2010, June). An adaptive multiresolution-based multispectral image compression method. In *International Conference on Image and Signal Processing* (pp. 54-62). Springer Berlin Heidelberg.
- Dumitru, C. O., Cui, S., & Datcu, M. (2015, March). A study of multi-sensor satellite image indexing. In *2015 Joint Urban Remote Sensing Event (JURSE)* (pp. 1-4). IEEE.
- Faria, L. N., Fonseca, L. M., & Costa, M. H. (2012). Performance evaluation of data compression systems applied to satellite imagery. *Journal of Electrical and Computer Engineering*, 2012(18), 1-5.
- Mulla, A., Baviskar, J., Naik, R., & Baviskar, A. (2015, March). Enhanced quality LANDSAT image processing based on 4-level Sub-Band Replacement DWT. In *2015 IEEE Aerospace Conference* (pp. 1-7). IEEE.
- Rabbani, M., & Joshi, R. (2002). An overview of the JPEG 2000 still image compression standard. *Signal processing: Image communication*, 17(1), 3-48.

- Raju, V. B., Sankar, K. J., Naidu, C. D., & Bachu, S. (2016). Multispectral Image Compression for various band images with High Resolution Improved DWT SPIHT. *International Journal of Signal Processing, Image Processing and Pattern Recognition*, 9(2), 271-286.
- Said, A., & Pearlman, W. A. (1996). A new, fast, and efficient image codec based on set partitioning in hierarchical trees. *IEEE Transactions on Circuits and Systems for Video Technology*, 6(3), 243-250.
- Shapiro, J. M. (1993). Embedded image coding using zerotrees of wavelet coefficients. *IEEE Transactions on signal processing*, 41(12), 3445-3462.
- Singh, A. K., & Tripathi, G. S. (2014). A comparative study of dct, dwt & hybrid (dct-dwt) transform. *Global Journal of Engineering Science and Researches(GJESR)*, 1(4), 16–21.
- Taubman, D. S., Marcellin, M. W., & Rabbani, M. (2002). JPEG2000: Image compression fundamentals, standards and practice. *Journal of Electronic Imaging*, 11(2), 286-287.
- Thiebaut, C., & Camarero, R. (2011). CNES Studies for On-Board Compression of High-Resolution Satellite Images. In B. Huang (Ed.), *Satellite Data Compression*. New York, NY: Springer New York.
- Yu, G., Vladimirova, T., & Sweeting, M. N. (2009). Image compression systems on board satellites. *Acta Astronautica*, 64(9), 988-1005.



Design of Readout Circuit for Piezoresistive Pressure Sensor Using Nodal Array Approach Reading Technique

W. Z. Wan Hasan¹, F. R. M. Rashidi^{1,2*}, M. N. Hamidon and Y. Wahab³

¹Department of Electrical and Electronic Engineering, Faculty of Engineering, Universiti Putra Malaysia, 43400 UPM, Serdang, Selangor, Malaysia

²Faculty of Electrical & Electronics Engineering, University Malaysia Pahang, 26600 Pekan, Pahang, Malaysia

³Centre for Industrial Collaboration, School of Microelectronic Engineering, Universiti Malaysia Perlis, Arau 02600, Malaysia

ABSTRACT

In this paper, we proposed a new readout circuit in order to improve measurement output while reading the grouped resistive value in matrix array form. The purpose of having this circuit is to overcome the main problem in applying piezoresistive pressure sensor array for foot plantar application. This new approach is called Nodal Array Approach (NAA), a modified version of Wheatstone Bridge Circuit based on nodal analysis technique using Kirchhoff Current Law. The NAA calculates the sensors' resistance values by solving simultaneous equations from reading voltages of the proposed readout circuit. Therefore, it is found that the readout circuit connection is of low complexity as it only uses resistive element as the major component of reading technique with only four iterations involved for each voltage nodes. Through simulation results, it shows that NAA is able to achieve high accuracy in obtaining a sensor's resistance value by adhering to several limitations in order to avoid miscalculation (< 5% average calculation error).

Keywords: Resistive readout circuit, resistive sensor array, foot plantar application

ARTICLE INFO

Article history:

Received: 24 August 2016

Accepted: 03 Jun 2017

E-mail addresses:

wanzuha@upm.edu.my (W. Z. Wan Hasan),

fairuz@ump.edu.my (F. R. M. Rashidi),

mnh@upm.edu.my (M. N. Hamidona),

yufridin@unimap.edu.my (Y. Wahab)

*Corresponding Author

INTRODUCTION

It has been a trend in medical fields to search for an alternative approach to diagnose a patient without having to probe him/her with needles for blood samples. This alternative method should be pain-free while still maintaining the same quality as the traditional technique. For an example, by examining foot pressure patterns doctors can tell whether the person has diabetes or not (Aziz et al., 2012; Boulton, 1983). Abnormal

standing or walking postures may lead to ulcer in the soles, which is a side effect of diabetes (Bacarin, Sacco, & Hennig, 2009; Stess, Jensen, & Mirmiran, 1997; Young, Breddy, Veves, & Boulton, 1994; Veves, Murray, Young, & Boulton, 1992; Duckworth, Boulton, Betts, Franks, & Ward, 1985). Hence, foot plantar measurement system has been developed to help doctors, especially endocrinologist and podiatrist, in analysing a patient’s foot pressure distribution pattern (Rashidi, Hussein, & Hasan, 2015; Almassri et al., 2015; Hussein, Hasan, & Jafaar; Shu et al., 2010; Orlin, & McPoil, 2000; Urry, 1999).

However, the measurement system of this product needs to be improved especially its circuit complexity and reading technique (Shu, Tao, & Feng, 2015). We suggest an alternative method of reading technique called Nodal Array Approach (NAA) which uses iterations rather than the normal scanning approach which is very time consuming for a large network of sensors (Zhang, Zhou, Balasundaram, & Mason, 2003; Liu, Zhang, Liu, & Jin, 2010; D’Alessio, 1999). The proposed readout circuit also has the advantage of low complexity in its circuitry and connections which is achieved by developing it to only have resistive elements as its main components. Due to linearity characteristic of resistive elements, its connections, current flows and electrical analysis will be kept simple and ensure easy calculation. Nevertheless, there are some limitations which need be considered in order for NAA to work flawlessly giving the best accurate results.

This paper will focus on the NAA technique and the efforts made by the authors to make it a reality. A 7-node NAA network was constructed in Proteus ISIS software in order to simulate and analyse its results. The simulation results will be discussed by pointing NAA’s major advantages and limitations. This paper will also discuss the advantages of this new approach as a resistive sensor array’s readout circuit with suggestions for future improvements and recommendations.

NODAL ARRAY APPROACH (NAA)

The NAA consists of a sensory network and a controlling mechanism within the readout circuit. and a reading algorithm to calculate sensor’s resistance value as shown in Figure 1. An applied foot pressure will change the resistivity of the arrayed piezoresistive sensors to produce voltage on each of its node. This analog voltage will be converted into a digital form by using

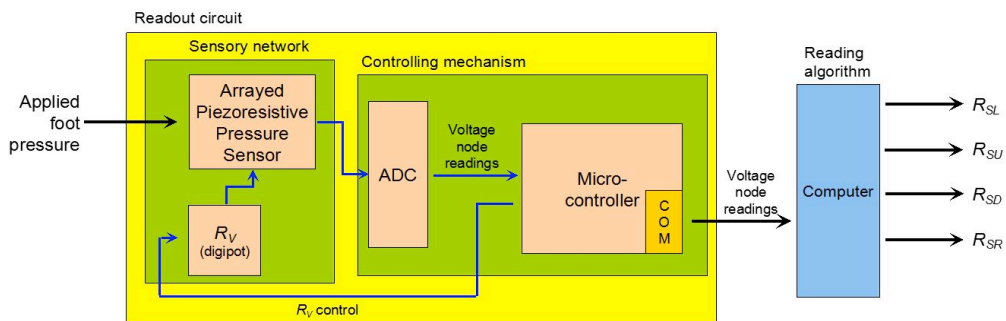


Figure 1. NAA block diagram

Analog-to-Digital Converter (ADC) and stored in a microcontroller. The microcontroller will give command to change the variable resistors value for next iteration. Once all the iteration has been completed, the stored value of each voltage node will be sent to a computer that has been installed with NAA's reading algorithm. The sensors' resistance values will be the end results of this research where they are arranged according to their location in a sensory network.

Sensory network

The sensory network consists of sensors and variable sensors arranged in an array form which looks like a cascade Wheatstone Bridge Circuit. It has a node on each junction that is label as U (up), D (down), L (left) and R (right). The first and last node is special as they only have three junctions of U, D, R and U, D, L respectively. The variable resistors (RV) will be infused in the arrayed piezoresistive pressure sensor as shown in Figure 2. The size of the sensory network depends on Equation (1) and (2), used to calculate the nodes, sensors and variable resistors needed for the whole circuit construction. We have developed a 7-node NAA sensory network which can obtain 20 sensor's resistance values and assisted by 8 variable resistors such as in Figure 2.

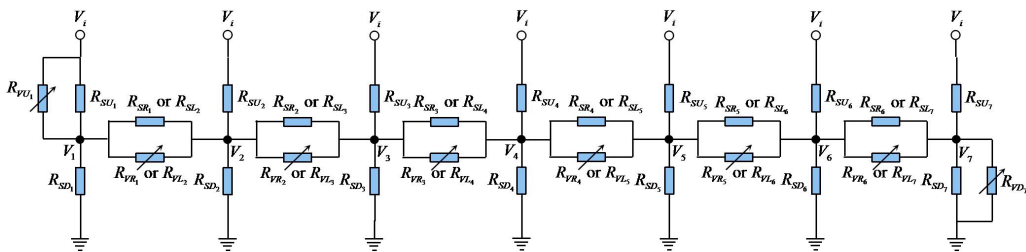


Figure 2. 7-node NAA sensory network

$$s = 3n - 1 \tag{1}$$

$$v = n + 1 \tag{2}$$

- s - number of sensors
- v - number of variable resistors
- n - number of voltage nodes

Controlling mechanism

By observing Figure 1, the voltage nodes readings obtained from sensory network need to be converted into a digital form in order to store them in microcontroller's register. This task is performed by an ADC and seven of them are needed for our experiment of 7-node sensory network. We have selected a 22-bit delta-sigma ADC which has become one of the major factor

affecting NAA's calculation accuracy. In microcontroller, three major tasks are performed during the reading process:

- Storing all the digital values of voltage nodes
- Command the variable resistors to change their resistance values
- Sending all the digital voltage node values to computer through serial communications port

The microcontroller should have at least three I/O ports containing 8 pins where each port represents the task it needs to perform. It also needs to have a large amount of available register for storing all the 22-bit digital representation of voltage node values which is at least 7 (nodes) X 4 (iterations) X 3 (8 bit per register block) = 84 in total. Last but not least, it should have a fast clock frequency in order to perform all the tasks within a second or less to give way for the next foot pressure measurement.

Reading algorithm

As mentioned earlier, NAA implements iteration reading instead of a scanning technique that has been used by many other approaches of resistive readout circuit (Hussein, Hasan, & Jafaar; Shu et al., 2010; Orlin, & McPoil, 2000; Urry, 1999; Shu, Tao, & Feng, 2015; Zhang, Zhou, Balasundaram, & Mason, 2003; Liu, Zhang, Liu, & Jin, 2010; D'Alessio, 1999). Each node will have a specific nodal equation according to the resistive value of sensors and variable resistors attached to it. When the sensory network is given a power supply, voltage can be read at each node while all the variable resistors value will be initially set up. Now, the nodal equation will only have an unknown sensor's value in each of them. As each node only has four sensors (R_{SU} , R_{SD} , R_{SL} and R_{SR}) that is attached to it, it only needs a maximum of four different readings in order to calculate those unknown sensor's value. These four readings will be made through four iterations by varying the variable resistors' resistive values in between. Finally, all these four simultaneous equations are to be solved by using matrix manipulation and the end results will be each sensor's resistance value. This iteration reading procedures can be visualised as a flowchart in Figure 3.

In order to use matrix manipulation for solving four simultaneous equations from each node, Mathworks Matlab was chosen as it is the most convenient and user-friendly software that provides a quick solution. The NAA reading algorithm is kept in a computer's platform rather than burdening the microcontroller with matrix manipulation codes that can decrease its output timing results. These results needed to be processed further to produce useable data using the same platform .

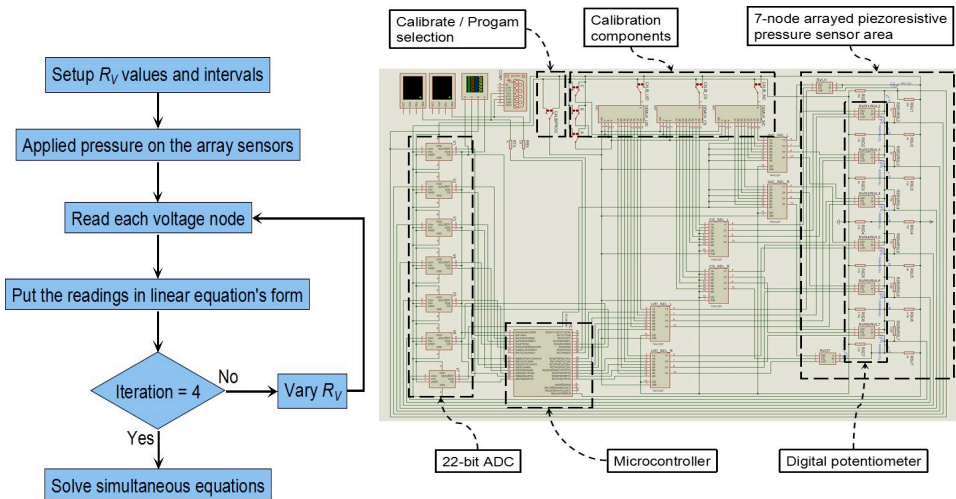


Figure 3. NAA's reading procedures

Figure 4. Schematic diagram of the readout circuit

NAA's limitation

In NAA, each nodal equation from any voltage node needs to have a unique set of variables and values. Several limitations need to be observed in order for NAA to produce the best accurate results and to avoid miscalculation. Three major limitations in NAA are:

- Reading resolution of 5 decimal point
- The uniqueness of each middle variable resistor's value
- The permutation of variable resistors values

The NAA needs to have at least 5 decimal points of resolution because the changes between voltage node value is very small between each iteration. Any attempt on rounding that value less than 5 decimal point might produce the same result with other voltage node which will disregard the unique requirement of NAA. As for the middle variable resistor's value a unique resistance value among each other for the same reason of uniqueness is needed. While iterating, all the variable resistor's value must only be swapped among themselves where there will be no other new value added to the network. This is called permutation.

RESULTS AND DISCUSSION

The readout circuit was successfully developed in Proteus ISIS software while the reading algorithm is implemented in Mathwork Matlab under Windows 10 platform. The overall circuit is also simulated using Proteus ISIS, where the virtual serial communication between readout circuit and computer is established by Virtual Serial Port Driver 6.9 from Eltima Software, while MicroCode Studio from Mecanique served as the PicBasic Pro language compiler tool. As this is only a simulation, all sensors are modelled as standard resistors with fixed resistance value according to the real sensor resistance value. These values are randomly

selected within the minimum and maximum range of piezoresistive pressure sensor resistance values. Voltage supply is 5V in order to supply all the electronic components in the readout circuit. Figure 4 shows the overall schematic of the readout circuit including the calibration circuit. Calibration is needed to set the initial value of each digital trimmer potentiometer as the variable resistors. This calibration process is only done one time as those potentiometers are non-volatile which means that they can lock their resistance at a certain value even after the circuit has been turned off or reset.

Table 1 shows the values obtained from seven voltage nodes where a comparison can be made between the analog values (taken before entering ADC) probed by Proteus ISIS and the final value (taken before entering NAA reading algorithm) retrieved from Mathwork Matlab output results. Through observation, it has shown that the voltage nodes have been successfully digitised by 22-bit ADC with an accuracy of at least 0.00001 from the analog readings. This means that NAA's 5 decimal point resolution requirement has been satisfied, resulting in a very closed sensor's resistive value when compared with the actual one shown in Table 2. Furthermore, the potentiometer's resistive value has been carefully configured in order to follow the uniqueness limitation. However, these potentiometers seem to fluctuate in values during each iteration which does not obey the permutation limitation, just like the example of RVU1 fluctuation values shown in Figure 5. Fortunately, these instabilities very small and only involve values which are beyond the decimal point. As for that, only the integer part of the resistance value is taken (for example $R_{VU1} = 3897 \Omega$) which has only a minor effect on NAA's calculation.

Table 1
Voltage node readings value's in analog and its decimal representations after the conversion

Voltage node	Numbers representation	Iteration 1	Iteration 2	Iteration 3	Iteration 4
V_1	Analog	2.53762	2.52901	2.51912	2.50405
	Decimal	2.537620067596436	2.529008388519287	2.519123554229736	2.504053115844727
V_2	Analog	2.26896	2.26735	2.26534	2.23859
	Decimal	2.268962860107422	2.267348766326904	2.265341281890869	2.238593101501465
V_3	Analog	2.65734	2.66549	2.66955	2.64832
	Decimal	2.657344341278076	2.665491104125977	2.669544219970703	2.648322582244873
V_4	Analog	3.30628	3.30426	3.29652	3.29729
	Decimal	3.306281566619873	3.304262161254883	3.296518325805664	3.297293186187744
V_5	Analog	2.77611	2.76664	2.75754	2.74667
	Decimal	2.776110172271729	2.766637802124023	2.757534980773926	2.746672630310059
V_6	Analog	2.25267	2.24998	2.22165	2.18574
	Decimal	2.252666950225830	2.249982357025147	2.221648693084717	2.185740470886231
V_7	Analog	2.05329	2.03709	1.99547	1.88618
	Decimal	2.053294181823731	2.037088871002197	1.995470523834229	1.886177062988281

Even though almost perfect results have been achieved using NAA, it seems to generate quite a sluggish results time. After careful observation, this low frequency execution process is detected from the 22-bit ADC. This ADC can only have the maximum sampling rate of 60

SPS (sample per second). Based on the availability of current products, all ADCs that are higher than 16-bit use delta-sigma method as their technique of conversion. Delta-sigma ADCs can generate very precise results with high resolution but their drawback is the conversion and data output time. The conversion method uses comparator to sense the voltage difference and then the integrator sums the comparator's output with the input signal (Patel, & Bhatt, 2012; Eshraghi, & Fiez, 2004; Geerts, Steyaert, & Sansen, 2000). This will decrease the sampling rate timing as the oversampling method requires several op-amps and D-type flip-flops as its main components. To fulfil this ADC's requirement, we need to put the command 'PAUSE' of 50 milliseconds for each rising and falling edge of output data clock in our microcontroller. This command is used for all 24-bits output transmission (2 bits for signed overflow indicator which is both '0' for our case) from all 7 ADCs which delays the total execution time by more than a minute as calculated in Equation (3). Unfortunately, this is the only option for

Table 2
Sensor's resistive value compared with the exact value

Sensor's name	Exact value (k Ω)	Value calculated by NAA's algorithm (k Ω)	Percentage of calculation error (%)
R_{SU1}	0.25	0.254790407361186	1.91616
R_{SU2}	3	2.994791273064735	0.17362
R_{SU3}	3.5	3.504383419775587	0.12524
R_{SU4}	0.75	0.749612615444893	0.05165
R_{SU5}	4	3.995045015993616	0.12387
R_{SU6}	3.75	3.749980595404416	0.00052
R_{SU7}	3	2.998251423540472	0.05829
R_{SD1}	0.25	0.256111857812884	2.44474
R_{SD2}	1.5	1.498102302701005	0.12651
R_{SD3}	3	2.997401225484398	0.08663
R_{SD4}	2.5	2.495719723305165	0.17121
R_{SD5}	3.5	3.492461853631187	0.21538
R_{SD6}	2.75	2.746869990611188	0.11382
R_{SD7}	2.5	2.495972627045837	0.16109
R_{SR1} or R_{SL2}	1	R_{SR1} 0.821954472256171	17.80456
		R_{SL2} 1.000864024519932	0.08640
R_{SR2} or R_{SL3}	2	R_{SR2} 2.004099649082407	0.20498
		R_{SL3} 2.000032807596361	0.00164
R_{SR3} or R_{SL4}	1.75	R_{SR3} 1.747678986385587	0.13263
		R_{SL4} 1.750175940401880	0.01005
R_{SR4} or R_{SL5}	1.5	R_{SR4} 1.498726796819304	0.08488
		R_{SL5} 1.500291017297411	0.01940
R_{SR5} or R_{SL6}	4.25	R_{SR5} 4.247567522578707	0.05723
		R_{SL6} 4.250415515986798	0.00978
R_{SR6} or R_{SL7}	2.25	R_{SR6} 2.249973356893091	0.00118
		R_{SL7} 2.252485410403882	0.11046

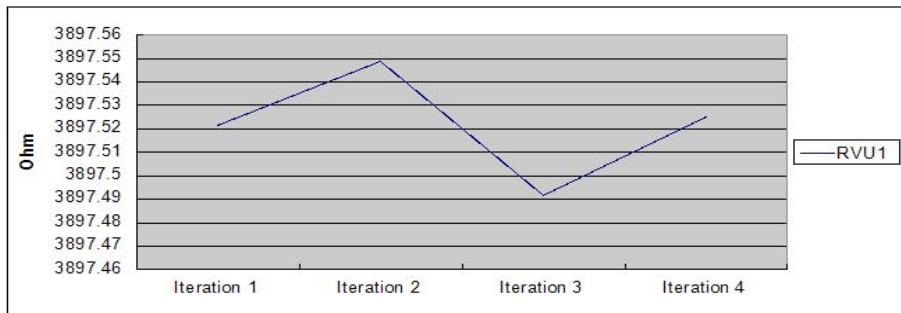


Figure 5. Fluctuation of R_{VU1} value in each iteration

22-bit ADC that is available in Proteus ISIS. Nevertheless, this issue needs to be solved in the future if NAA's is adopted as a full working prototype of a foot plantar measurement system. A recommendation for high speed delta-sigma ADC can be considered as a solution but which is currently available only as a hardware device.

$$50\text{ms} \times 24 \times 2 \times 7 \times 4 = 67.2 \text{ seconds} \quad (3)$$

(delay) (ADC (rising and (voltage (iterations) (total ADC's output falling edge nodes) delay) bit) of data output clock)

CONCLUSION

A 7-node sensory network of readout circuit to serve the NAA's reading architecture was developed by selecting suitable components in Proteus ISIS which are powerful enough for schematic drawing and simulation analysis. The NAA provides accurate results of sensor's resistive values when its requirements and limitations are satisfied. By only having resistive element as its components, NAA can improve the conventional readout circuit which has too many non-resistive elements resulting in higher circuit complexity. Furthermore, NAA's reading technique that requires only four iterations has a very high potential in higher speed output results. However, Proteus ISIS only provides low conversion and sample rate of 22-bit delta-sigma ADC which has downgraded the speed of NAA's reading technique and become unsuitable for a foot plantar measurement application that needs quicker results. Thus, a hardware readout circuit needs to be constructed in the future in order to have a variety of faster ADCs available in the market.

REFERENCES

- Almassri, A. M., Wan Hasan, W. Z., Ahmad, S. A., Ishak, A. J., Ghazali, A. M., Talib, D. N., & Wada, C. (2015). Pressure sensor: state of the art, design, and application for robotic hand. *Journal of Sensors*, 2015(2015), 1-12.

- Aziz, N. A., Fatimah, A. B., Aznida, F. A. A., Hamid, M. Z. A., Syanaz, M. H., Zuhra, H., & Mustafa, N. (2012). The Association of Various Risk Factors and Plantar Pressures in the Development of Peripheral Neuropathy amongst Diabetic Patients Attending Outpatient Clinics. *International Medical Journal*, 19(1), 1-1.
- Bacarin, T. A., Sacco, I. C., & Hennig, E. M. (2009). Plantar pressure distribution patterns during gait in diabetic neuropathy patients with a history of foot ulcers. *Clinics*, 64(2), 113-120.
- Boulton, A. J., Hardisty, C. A., Betts, R. P., Franks, C. I., Worth, R. C., Ward, J. D., & Duckworth, T. (1983). Dynamic foot pressure and other studies as diagnostic and management aids in diabetic neuropathy. *Diabetes Care*, 6(1), 26-33.
- D'Alessio, T. (1999). Measurement errors in the scanning of piezoresistive sensors arrays. *Sensors and Actuators A: Physical*, 72(1), 71-76.
- Duckworth, T., Boulton, A. J., Betts, R. P., Franks, C. I., & Ward, J. D. (1985). Plantar pressure measurements and the prevention of ulceration in the diabetic foot. *Bone and Joint Journal*, 67(1), 79-85.
- Eshraghi, A., & Fiez, T. S. (2004). A comparative analysis of parallel delta-sigma ADC architectures. *IEEE Transactions on Circuits and Systems I: Regular Papers*, 51(3), 450-458.
- Geerts, Y., Steyaert, M. S., & Sansen, W. (2000). A high-performance multibit $\Delta\Sigma$ CMOS ADC. *IEEE Journal of solid-state circuits*, 35(12), 1829-1840.
- Hussein, O., Hasan, W. W., & Jafaar, A. C. S. H. (2015, June). Investigation on Touch Area of Under Foot Pressure Based-on Weight Measurements. In *7th International Conference on Engineering and Technology ICET-2015*. Phuket, Thailand
- Liu, H., Zhang, Y. F., Liu, Y. W., & Jin, M. H. (2010). Measurement errors in the scanning of resistive sensor arrays. *Sensors and Actuators A: Physical*, 163(1), 198-204.
- Orlin, M. N., & McPoil, T. G. (2000). Plantar pressure assessment. *Physical Therapy*, 80(4), 399-409.
- Patel, J. V., & Bhatt, H. (2012, December). Performance evaluation of different types of analog to digital converter architecture. In *International Journal of Engineering Research and Technology* (Vol. 1, No. 10 (December-2012)). ESRSA Publications.
- Rashidi, F. R. M., Hussein, O., & Hasan, W. Z. W. (2015, August). Investigation on developing of a piezoresistive pressure sensor for foot plantar measurement system. In *Micro and Nanoelectronics (RSM), 2015 IEEE Regional Symposium on* (pp. 1-4). IEEE.
- Shu, L., Hua, T., Wang, Y., Li, Q., Feng, D. D., & Tao, X. (2010). In-shoe plantar pressure measurement and analysis system based on fabric pressure sensing array. *IEEE Transactions on information Technology in Biomedicine*, 14(3), 767-775.
- Shu, L., Tao, X., & Feng, D. D. (2015). A new approach for readout of resistive sensor arrays for wearable electronic applications. *IEEE Sensors Journal*, 15(1), 442-452.
- Stess, R. M., Jensen, S. R., & Mirmiran, R. (1997). The role of dynamic plantar pressures in diabetic foot ulcers. *Diabetes Care*, 20(5), 855-858.
- Urry, S. (1999). Plantar pressure-measurement sensors. *Measurement Science and Technology*, 10(1), R16.

- Veves, A., Murray, H. J., Young, M. J., & Boulton, A. J. M. (1992). The risk of foot ulceration in diabetic patients with high foot pressure: a prospective study. *Diabetologia*, *35*(7), 660-663.
- Young, M. J., Breddy, J. L., Veves, A., & Boulton, A. J. (1994). The prediction of diabetic neuropathic foot ulceration using vibration perception thresholds: a prospective study. *Diabetes Care*, *17*(6), 557-560.
- Zhang, J., Zhou, J., Balasundaram, P., & Mason, A. (2003, October). A highly programmable sensor network interface with multiple sensor readout circuits. In *Sensors, 2003. Proceedings of IEEE* (Vol. 2, pp. 748-752). IEEE.



Transparent Solar Cell Using Spin Coating and Screen Printing

A. A. F. Husain^{1*} and W. Z. Wan Hasan^{1,2}

¹Department of Electronic Engineering, Universiti Putra Malaysia, 43400 UPM, Serdang, Selangor, Malaysia

²Institute of Advance Technology, Universiti Putra Malaysia, 43400 UPM, Serdang, Selangor, Malaysia

ABSTRACT

The development of Transparent Solar Cells (TSC) has become the main focus of solar energy research in recent years. The TSC has a number of applications and make use of unexploited space such as skyscraper windows. In this paper, TSC is fabricated using commercially available titanium dioxide (TiO_2) P25 to make a paste, which is deposited on FTO glass using screen printing and spin coating methods. The effects of the thickness of the TiO_2 film on transparency are examined. The paste is synthesised in the Cleanroom and used in both methods of deposition. The final cell fabrication is a Dye sensitised solar cell (DSSC). The obtained transparency of the FTO glass is 83%, and after the deposition of TiO_2 it is reduced to less than 80%. The overall transparency of the DSSC, which was made using the spin coating method, is 70% with an I_{sc} of 9.5 mA and V_{oc} 853mV.

Keywords: Transparent, Solar cell, TiO_2 , screen printing, spin coating

INTRODUCTION

In the last decades, solar energy has gained substantial attention from researchers due to its sustainability, environmental-friendly, and a great substitute to fossil fuel (Da, 2015) (Atul Tiwari (Editor), 2013) (M. Hosenuzzaman, 2015) (Bube, 1983). Various applications and technologies employ solar

energy, such as cars, trains as well as organic and nonorganic solar cells respectively. This research is interested in photovoltaic solar cell, in particular dye sensitised solar cell (DSSC). This technology is the lowest in fabrication complexity and the solar cells. The DSSC converts photons from the sun to electricity through semiconductor materials such as Titanium Dioxide TiO_2 . Titanium Dioxide has a photo catalytic property that helps convert solar energy into chemical energy to oxidise the material (Prochazka, Kavan, Zukalova, & Vlckova Zivcova, 2013). Additionally, TiO_2 has properties such as oxidation, superhydrophilicity, chemical stability and it is also durable, non-toxic, cheap and transparent to visible light (Nakataa

ARTICLE INFO

Article history:

Received: 24 August 2016

Accepted: 03 Jun 2017

E-mail addresses:

alaa.a.f.husain@gmail.com (A. A. F. Husain),

wanzuha@upm.edu.my (W. Z. Wan Hasan)

*Corresponding Author

& Fujishimaa, 2012). The photo catalytic properties of TiO_2 are due to the photogeneration of holes and electrons which occur after the absorption of the UV light that contains the equivalent energy to the band gap (Ikeda, Sakai, Baba, Hashimoto, & Fujishima, 1997). The holes diffused from the valence band to the surface of the TiO_2 react to the photons forming hydroxyl radicals ($\bullet OH$). On the TiO_2 surface, organic molecules oxidise with the holes and the hydroxyl radicals, while electrons in the conducting band produce superoxide radical anions ($O_2 \bullet^-$) (Fujishima, N. Rao, & A. Tryk, 2000).

In order to develop the properties of TiO_2 , new structures have been created in nano and micro sizes. Many nano structured materials have been fabricated such as spheres, nanorods, fibers, tubes, sheets, and interconnected architectures. These structures have wide applications specially in DSSC. This research is focused on nano structure for achieving transparent TiO_2 without affecting the efficiency of light harvesting. The transparency is achieved through thin film technology. Thin film solar cell (TFSC) technology has semiconducting material deposited on the substrate with a thickness not more than few micrometers (Chopra, Paulson, & Dutta, 2004). Through this technology, cost can be lowered by reducing the amount of the active layer. Moreover, thin film technology is flexible, which increases its applications (Matsuno, Naomoto, & Arimoto, 1995) (Bjorkman, Kessler, & St, 2006). Through controlling the thickness of the film, the transparency will be controlled and eventually increased (Kim, Kim, & Seong, 2015). There are different methods of depositing thin film on the substrate such as chemical bath deposition (CBD) technique, physical vapour deposition (PVD) technique and sputtering (Reichelt, 1990), electro deposition (Deposition of transparent TiO_2 nanotube-films via electrophoretic technique for photovoltaic applications, 2015) (Bahramian & Vashae, 2015) (T. Yuasa, 2012), screen-printing (Ramasamy, 2007; Nam, 2010; Lee, 2007; Fan, 2010), pulsed laser deposition (PLD) (Kumar, Ntwaeaborwa, & C, 2016; Liu, et al., 2016), Spray and Atomic layer deposition (ALD).

Screen printing is one of the most popular methods in depositing thin film due to ease of controlling the thickness by managing fabric thickness. In addition to that, quality of the paste, mesh opening size and fabric thickness are other factors to be controlled for improving the performance of the thin film and its transparency (Ito, Chen, Comte, & Khaj, 2007) (Park, 2008). Spin coating is also used to apply thin film onto substrate in many applications. The advantages of spin coating are that it requires less time and effort to make a thin film. The solvent is cast on the glass in an uniformed way because of the centripetal force and the tension of the solution on the surface. In order to make a thin film using spin coating, the rotation speed must be more than 1000 rpm. In this study, the methods of screen printing and spin coating are employed.

METHODOLOGY

In this section, the experiment is discussed and illustrated in Figure 3. The experiment is divided into two stages: the first is spin coating and the second is screen printing. Before the experiment begins, the paste is prepared in the clean room. Below describes the materials used in the experiment.

Materials

For making the paste, the following materials were used: titanium dioxide TiO₂ (P25) (Aldrich, USA), Acetic acid, Water, Ethyl alcohol, α Terpineol and Ethyl cellulose. FTO glass (100mm \times 100mm \times 1.6mm), transmission \geq 83%, resistance sheet 15 Ω /sq (Kivo, China) was used as a base, and for cleaning the glass Isopropyl alcohol (IPA), Acetone AR Grade were used. Scotch tape was used for framing. Hydrogen Hexachloroplatinate (IV) Hexahydrate was used for coating the counter electrode. The materials for preparing the dye are: acetonitrile (solvent), Iodine (I₂) (QRĕC, New Zealand), Lithium iodide crystalline powder 99.9% trace metals basis (LiI) (Aldrich, USA), 4-tert-Butylpyridine 96% (Aldrich, USA), Ethyl-methyl-Imidazolium iodide (Aldrich, USA), Di-tetrabutylammoniumcis-bis (isothiocyanato)bis(2,2'-bipyridyl-4,4'-dicarboxylato) ruthenium(II) 95% (NMR) Synonym: N-719 dye (Aldrich, USA).

Experiment

TiO₂ paste was fabricated using the method reported by (Ito S. C., 2007). Three replicas of the solution were prepared. Each of the replicas was evaporated to form a paste with different concentration. The volume of each paste was 166.6ml. After evaporating to P1 (5/10), P2 (3/10), and P3 (1/10), the paste volumes in orders were 80ml, 50ml, and 16.6ml. The deposition was carried out directly to experiment the effect of temperature during deposition. The experiment is divided into two stages. The first, spin coating, and the second, screen printing.

Spin coating. The paste which was prepared in the previous section was used for spin coating using Polos spin coater. Three variables were controlled to of the film; speed, concentration, and temperature. The paste amount was fixed to less than 0.5ml per drop. The solution temperature and concentration were 42-65 C and 5/10 and 3/10 respectively, The speed in spin coating was fixed to 10000 rpm for 120 s while the acceleration was 100 rpm /s. The acceleration remained the same when the solution was 5/10 at room temperature. In addition, the speed was 10000, the time 300 s, and the acceleration 1000, when the concentration was 1/10 and the temperature 40-42 C. The same speed and acceleration remained for the rest of samples, 3/10 and 1/10, at room temperature.

Screen printing. For the screen printing experiment, a special board was designed for preparing nine samples with three controlled variables (i.e. concentration, temperature, and numbers of layers). The characteristics of the board are 90 T-mesh/cm (230T mesh/inch), 60 μ m mesh opening, 50 μ m thread diameter, 29.8% open surface, 20 μ m fabric thickness, 24.5 (cm³) (m⁻²) theoretical paste volume, (17cm³)(m⁻²) k/k volume, 48gm⁻² weight.

The amount of paste to be deposited was fixed to less than 0.3ml; the first three samples were prepared using high temperature for the three concentrations of pastes (P1, P2, and P3). The same pastes were used to prepare another three samples at 28°C. After that, 10 samples were prepared using P1 at room temperature by increasing numbers of layers in each sample. In each layer, a drop of paste with a volume of less than 0.2 ml was deposited on the FTO

glass. After preparing the samples, the counter electrode of the solar cell was prepared using spin coating by dropping 50 μ , 1500 rpm for 20s of $H_2+Pt+Cl_6$ solution on the FTO glass. All the samples were annealed in furnace at 450 $^{\circ}$ C for 30 minutes and then left in the oven overnight to cool down.

DSSC fabrication

The DSSC assembling was done following the conventional method reported in (Ito, Chen, Comte, & Khaj, 2007). After testing the effects of using screen printing and spin coating on transparency, the assembling was carried out to test the efficiency. The electrode TiO_2 was immersed in N791 dye solution at room temperature for 36 hours. After taking the TiO_2 sample glass out of the dye solution, it was cleaned with some ethanol and air-dried for 10 minutes. The electrolyte was prepared out of Acetonitrile solvent 10ml, I_2 0.05M, LiI 0.1M, 4-tert-Butylpyridine 0.5M, and Ethyl-methyl-Imidazolium iodide 0.6M. The electrode covered with dye and the counter electrode covered with Pt were assembled in a sandwich form using polymer sheets with a 25 μ m thickness on a hotplate. For depositing the electrolyte, a small space was left open as shown in Figure 1. In this experiment, no hole was made in the counter electrode. Finally, between one and two drops of the electrolyte were added from the open corner of DSSC and the cell was sealed using Epoxy resin to finish the assembling of the cell.

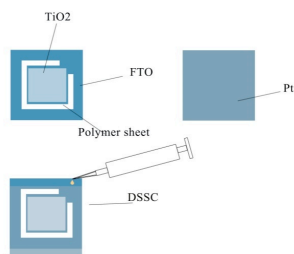


Figure 1. DSSC assembling



Figure 2. TiO_2 spilled while depositing using screen printing

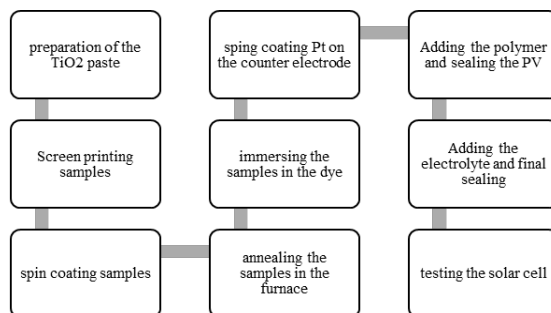


Figure 3. Methodology flow chart

RESULTS AND DISCUSSION

Paste fabrication and deposition

Three replicas of TiO₂ Paste were fabricated in the clean room based on the method explained in (Ito, Chen, Comte, & Khaj, 2007). The first variable in the experiment was the paste concentration of the titanium dioxide. The solution was evaporated alcohol to form a different percentage of pastes, P1 (0.1), P2 (0.3), and P3 (0.5).

During the spin coating deposition of the paste, it is noticed that when the paste is highly concentrated, it was harder to deposit on the FTO glass than the less concentrated paste ending up with a thicker layer. Moreover, at high temperature, the viscosity of the paste was reduced which made the deposition easier. On the other hand, when P3 is used, it is recommended to reduce the acceleration while for P3 and P1, it is better to increase the acceleration to 1000/s. when P1 was used for preparing the samples, after annealing it in the furnace dried and peeled off the FTO. As for screen printing, when P1 was used it is hard to deposit unless the temperature is high, while P2 deposited easily. As for P3, its viscosity is very high for screen printing and much of it is spilled outside the active area (Figure 2).

Transparency and efficiency measurement

The tables below show the measurements of the highest transparency, the voltage open circuit (V_{oc}) and the current short circuit (I_{sc}) achieved by each sample in spin coating (Table 1) and screen printing methods (Table 2). The transmittance was measured using UV-Vis spectrometer (Perkin Elmer Lambda 35, USA). The V_{oc} and the I_{sc} were measured using digital multimeter and light source with a power of $100mW/cm^2$.

It is clear from the results shown in the table below that number of layers have a slight effect on transparency. The transparency drops slightly from 79% to 76% when the number of layers increases (Figure 4). On the other hand, the voltage open circuit decreases by increasing the number of layers while it is the opposite for the current short circuit - it increases by increasing the number of layers until 5 layers after which it drops again (Figure 6). As for the concentration of the paste, the best one is P2, which has the highest transparency (Figure 6) and the best V_{oc} and I_{sc} when it is deposited in room temperature (Figure 7). Furthermore, when the temperature of the paste was more than 40 C, the transparency dropped for P1 & P3 but remained the same for P2 (Figure 8) and V_{oc} and I_{sc} decreased as shown in Figure 9.

Table 1
Spin coating testing measurements

Sample	Temperature C°	Paste	Transparency peak %	Voc	Isc
S15	42	P3	73.9	126	2.2
S16	28	P3	70	743	4.5
S17	63	P2	70	191	2
S18	28	P2	71	295	2.3
S19	40	P1	69	620	2.3
S20	28	P1	27	-	-

Table 2
Screen printing testing and measurements

Sample	Layers	Temperature C°	Paste	Transparency peak %	Voc(mV)	Isc(mA)
S1	1	28	P3	80	509	1.5
S2	1	28	P2	82	720	8.6
S3	1	28	P1	79	644	1.7
S4	2	28	P1	78	621	3
S5	3	28	P1	77.5	628	2.7
S6	4	28	P1	77	629	6.6
S7	5	28	P1	76	340	4.8
S8	6	28	P1	78.4	319	2.9
S9	7	28	P1	76.7	625	5
S10	8	28	P1	77.4	212	2.3
S11	9	28	P1	77	296	2.9
S12	10	28	P1	76.2	393	1.6
S12	1	46	P3	78	300	1.6
S13	1	63	P2	81	127	.9
S14	1	61	P1	78	580	1.3

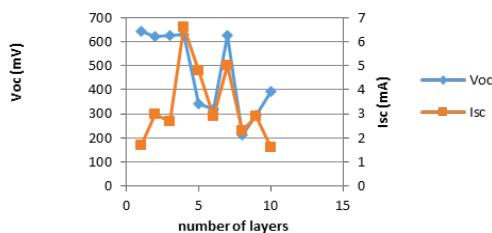
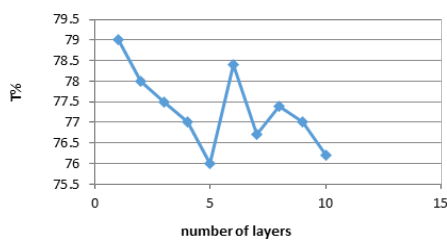


Figure 4. The transmittance spectra of TiO₂ on FTO glass using Screen printing In Room temperature

Figure 5. Voltage open circuit and current short circuit of DSSC made using screen printing

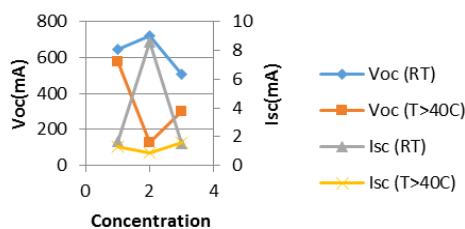
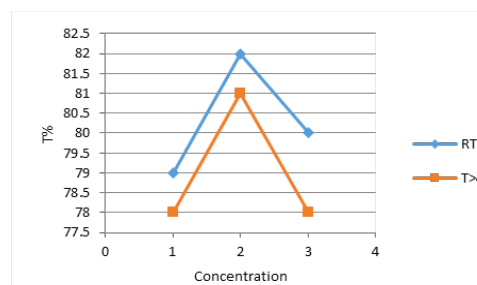


Figure 6. The transmittance spectra of TiO₂ on FTO glass using screen printing

Figure 7. Voltage open circuit and current short circuit of DSSC made using screen printing

Transparent DSSC

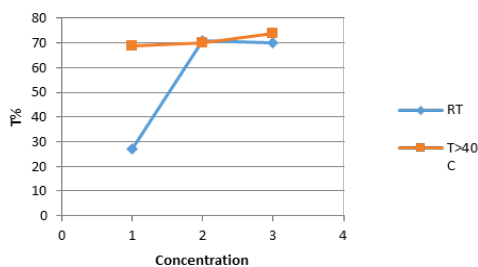


Figure 8. The transmittance spectra of TiO₂ on FTO using spin coating

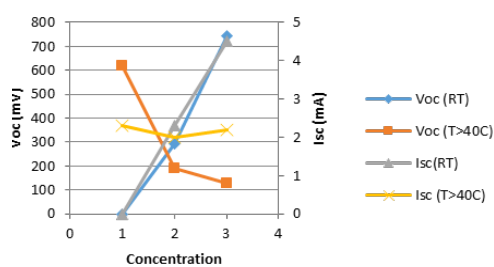


Figure 9. Voltage open circuit and current short circuit of DSSC made using spin coating

Spin coating performed better when the paste was deposited in temperature higher than 40 C. The three pastes had almost the same transparency. It dropped when the paste was deposited on RT for P1 due to its low viscosity. This means, increasing the temperature of the paste during the deposition will increase its viscosity. However, V_{oc} and I_{sc} were better with the low concentration than high concentration paste at room temperature. As for high temperature, V_{oc} was better with higher concentration and I_{sc} was almost the same for the three concentrations.

The transparency ranges from 75-80% and from 27-73% in screen printing and spin coating respectively. During deposition, screen printing was much better in terms of homogeneity and transparency than spin coating. For spin coating when the solution had low concentration it was easier to deposit and the resulted transparency was high.

Finally, a model sample was prepared with 5cm* 5cm measurement from FTO glass. The active area was 4cm*4cm. The TiO₂ was deposited on the glass using screen printing with the same characteristic as the previous samples and using the paste with a concentration of 3/10 at RT. A final DSSC was fabricated using this sample and the transmittance was measured using UV-Vis spectrometer (Perkin Elmer Lambda 35, USA) as shown in Figure 10. It can be concluded that the peak transmittance obtained in this sample was 70%. The V_{oc} of this sample was 853mV and the I_{sc} was 9.4mA.

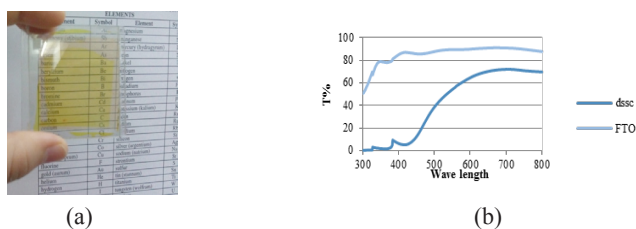


Figure 10. (a) Transparent DSSC, (b) The transmittance spectra of DSSC and FTO glass

CONCLUSION

Transparent DSSC is hard to achieve fully as transparency is the total opposite of the concept of solar cell. However, this research tested two methods and their effects on transparency: spin coating and screen printing. When the results of both methods were compared, screen printing

was better for making the thin film of titanium dioxide. Spin coating is not recommended because of the high viscosity of titanium dioxide which makes it dry faster and restricts its uniform coating on the surface of the substrate. In screen printing, three variables were considered to observe their effects on transparency, temperature, concentration, and number of layers. We inferred from our experiment that the best number of layers is 4 or 5, the best concentration is 3/10, and the best temperature is room temperature. Additionally, the variables in the spin coating were temperature and concentration. In using spin coating, the best concentration is P2, and the best temperature is above 40°C. It is noticed that P1 has a low viscosity which makes it dry and peels off after annealing. Spin coating is more suited for research purposes rather than manufacturing because it requires single sample each time which results in material wastage which is not feasible for manufacturing purposes. On the other hand, screen printing is faster, more economical in terms of the amount of materials consumed in deposition and the thickness is easily controlled using this method. The best Paste to use in screen printing is P2 due to its suitable viscosity compared with P3 which is not advisable. In this study, the transparent solar cell was successfully fabricated with more than 70% transmittance peak using screen printing method.

REFERENCES

- Bahramian, A., & Vashae, D. (2015). In-situ fabricated transparent conducting nanofiber-shape polyaniline/coral-like TiO₂ thin film: Application in bifacial dye-sensitized solar cells. *Solar Energy Materials and Solar Cells*, 143, 284-295.
- Bjorkman, C. P., Kessler, J., & St, I. (2006, August 17). *Patent No. US 20060180200 A1*. United States .
- Bube, A. F. (1983). *Fundamentals of solar cells*. . New York, United State of Amirica : Academic Press.
- Chopra, K. L., Paulson, P. D., & Dutta, V. (2004). Thin-Film Solar Cells: An Overview. *Progress In Photovoltaics: Research And Applications*, (12), 69–92.
- Da, Y. X. (2015). From light trapping to solar energy utilization: A novel photovoltaic–thermoelectric hybrid system to fully utilize solar spectrum. *Energy*, 95, 200-210.
- Fan, K. L. (2010, Feb). Effects of paste components on the properties of screen-printed porous TiO₂ film for dye-sensitized solar cells. *Renewable Energy*, 35(2), 555-561.
- Fujishima, A., Rao, T. N., & Tryk, D. A. (2000). Titanium dioxide photocatalysis. *Journal of Photochemistry and Photobiology C: Photochemistry Reviews*, 1(1), 1-21.
- Hosenuzzaman, M., Rahim, N. A., Selvaraj, J., Hasanuzzaman, M., Malek, A. B. M. A., & Nahar, A. (2015). Global prospects, progress, policies, and environmental impact of solar photovoltaic power generation. *Renewable and Sustainable Energy Reviews*, 41, 284-297.
- Ikeda, K., Sakai, H., Baba, R., Hashimoto, K., & Fujishima, A. (1997). Photocatalytic Reactions Involving Radical Chain Reactions Using Microelectrodes. *American Chemical Society*, 101, 2617-2620.
- Ito, S. C. (2007, Nov). Fabrication of screen-printing pastes from TiO₂ powders for dye-sensitised solar cells. *Progress in Photovoltaics: Research and Applications*, 15(7), 603-612.
- Ito, S., Chen, P., Comte, P., & Khaj, M. (2007, May). Fabrication of Screen-Printing Pastes From TiO₂ Powders for Dye-Sensitised Solar Cells. *Wiley InterScience* , 15, 603–612.

- Kim, J. H., Kim, D. H., & Seong, T. Y. (2015, Oct). Realization of highly transparent and low resistance TiO₂/Ag/TiO₂ conducting electrode for optoelectronic devices. *Ceramics International*, (41), 3064–3068.
- Kumar, V., Ntwaeaborwa, O. M., & Swart, H. C. (2016). Deep level defect correlated emission and Si diffusion in ZnO: Tb³⁺ thin films prepared by pulsed laser deposition. *Journal of Colloid and Interface Science*, 465, 295-303.
- Lee, W. J. (2007, Nov). Dye-sensitized solar cells: Scale up and current–voltage characterization. *Solar Energy Materials and Solar Cells*, 91(18), 1676-1680.
- Liu, B., Luo, R., Li, B., Zhang, J., Li, W., Wu, L., ... & Wu, J. (2016). Effects of deposition temperature and CdCl₂ annealing on the CdS thin films prepared by pulsed laser deposition. *Journal of Alloys and Compounds*, 654, 333-339.
- Matsuno, Y., Naomoto, H., & Arimoto, S. (1995, Mar 14). *Patent No. 5397400*. United States.
- Nakata, K., & Fujishima, A. (2012). TiO₂ photocatalysis: design and applications. *Journal of Photochemistry and Photobiology C: Photochemistry Reviews*, 13(3), 169-189.
- Nam, J. G. (2010, Feb). Enhancement of the efficiency of dye-sensitized solar cell by utilizing carbon nanotube counter electrode. *Scripta Materialia*, 62(3), 148-150.
- Park, N. G. (2008, Aug). Transparent solar cells based on dye-sensitized nanocrystalline semiconductors. *Physica Status Solidi*, 205(8), 1895-1904.
- Prochazka, J., Kavan, L., Zukalova, M., & Vlckova Zivcova, Z. (2013). Dense TiO₂ films grown by sol-gel dip coating on glass, F-doped SnO₂, and silicon substrates. *Journals Cambridge*, 28(3), 385-393.
- Ramasamy, E. L. (2007, Feb). Portable, parallel grid dye-sensitized solar cell module prepared by screen printing. *Journal of Power Sources*, 165(1), 446-449.
- Reichelt, K. &. (1990, OCT). The preparation of thin films by physical vapour deposition methods. *Thin Solid Films*, 191(1), 91-126.
- Tiwari, A., Sharon, M., & Boukherroub, R. (2013). *Solar cell nanotechnology*. New Jersey, United States of America: Wiley.
- Yuasa, T. R. (2012). Dye adsorption for dye-sensitized solar cell. *Solar Energy Materials and Solar Cells*, 102, 2-7.
- Zhang, J., Li, S., Yang, P., Que, W., & Liu, W. (2015). Deposition of transparent TiO₂ nanotubes-films via electrophoretic technique for photovoltaic applications. *Science China Materials*, 58(10), 785-790.



Transmission Lines Modelling based on RLC Passive and Active Filter Design

Ahmed Qasim Turki*, Nashiren Farzilah Mailah and Ahmed H. Sabry

Department of Electrical & Electronic Engineering, Faculty of Engineering, Universiti Putra Malaysia, 43400 UPM, Serdang, Selangor, Malaysia

ABSTRACT

This paper presents a transmission line (TL) modelling which is based upon vector fitting algorithm and RLC passive filter design. Frequency Response Analysis (FRA) is utilised for behaviour prediction and fault diagnosis. The utilities of the measured FRA data points need to be enhanced with suitable modelling category to facilitate the modelling and analysis process. This research proposes a new method for modelling the transmission line based on a rational approximation function which can be extracted through the Vector Fitting (VF) method, based on the frequency response measured data points. A set of steps needs to be implemented to achieve this by setting up an extracted partial fraction approximation, which results from a least square RMS error via VF. Active and passive filter design circuits are used to construct the model of the Transmission line. The RLC design representation was implemented for modelling the system physically while MATLAB Simulink was used to verify the results.

Keywords: Transmission lines modelling, vector fitting method

INTRODUCTION

The electrical power system mainly consists of three standard divisions: Generating Stations, Transmission system and Distribution System. The transmission line is the most vital

energy corridor in a power system. (Pourmir & Akbarkehkhajavan, 2013). The performance of a power system depends mainly on the performance of the transmission lines in the system. Generally, transmission lines have three parameters: resistance, inductance, and capacitance and each one is distributed over the length of the line.

The classification of transmission lines depends on the accuracy and simplicity of the model. While the short transmission line model is simple, the longer line model is complex and the medium line is in between the two. Fidanboylu (2003) discusses a

ARTICLE INFO

Article history:

Received: 24 August 2016

Accepted: 03 Jun 2017

E-mail addresses:

ahmed.q.t.91@gmail.com (Ahmed Qasim Turki),

nashiren@upm.edu.my (Nashiren Farzilah Mailah),

ahmed_hsabry@yahoo.com (Ahmed H. Sabry)

*Corresponding Author

transmission line method by using time domain synthesis approach. The parameters of each transmission line are determined using a constraint, nonlinear, least-squares optimisation technique performed in the time domain. The proposed modelling has several uses in microwave measurements material characterisation and microwave device modelling. (M & Semlyen, 1998) the author presents two highly accurate transmission line models. The first one is particularly suitable for overhead lines. In the second model, we use for propagation a modal decomposition of a constant transformation matrix and an optional phase domain correction term. Both models are computationally highly efficient due to their time domain realisations based on vector fitting. This research proposes a new method for modelling the transmission line based on a rational approximation function which can be extracted through the Vector Fitting (VF) method and RLC passive/active filter design.

VECTOR FITTING METHOD

Vector Fitting method is an approximation of a measured transmission line frequency response recently adopted in this application which is based on complex rational function models. Frequency dependent transmission line models have been used in the simulation of power system since the 1970s (Semlyen & Dabuleanu, 1975; Marti, 1982). The vector fitting method used in transmission line is transient. (Bjørn Gustavsen & Semlyen, 1998) According to the authors, this is a fast and robust method for the rational fitting of frequency domain responses well suited for both scalar and vector transfer functions (TF). The new method results in increased computational efficiency for transmission line models using modal decomposition with frequency dependent transformation matrices. This is due to the fact that the method allows the fitted elements of each eigenvector to share the same set of poles and that accurate fitting can be achieved with a relatively low number of poles. Gustavsen (2004) studied the time, delay identification for transmission lines modelling and found that to simply use the time delay of lossless propagation can lead to significant loss of accuracy of the rational approximation. Combining Brent's method with Vector Fitting (VF) optimises the time delay together with the poles and residues of the rational approximation. .

Past studies either addressed the modelling of transmission line in different categories or they used vector fitting algorithm with power transformer only. In this work, we propose the fundamentals of a method of TL modelling from measured data points based on RLC modelling of the rational approximation function attained from the VF method. The RLC modelling of this research uses the concept of passive and active filter representation of the partial fractions of the system transfer function.

PASSIVE FILTER DESIGN

The basic types of filter are Low-pass, high-pass, band pass, and band reject filter as shown in Figure 1(Ramsden, 2001).

The passive filter contains the resistor, inductor, and capacitor. The number of capacitor and inductor is equal to the higher power of frequency. The lumped values for each filter type for normalised frequency have been computed and tabulated (Matzner & Levy, 2008).

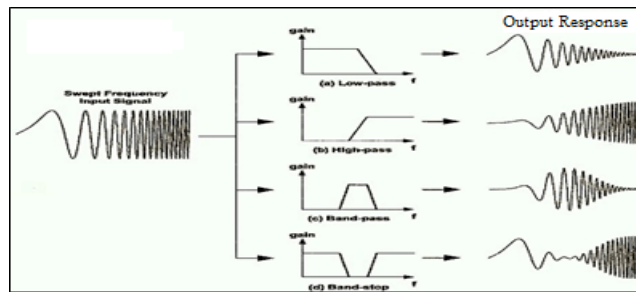


Figure 1. The effect of filter types on input signals

In this work, only passive filter circuits are utilised and described in detail.

Voltage divider circuit

The voltage divider circuits are very common. It is only two series resistors to simulate the reducing of the input signal.

$$\frac{v_o}{v_i} = \frac{R_2}{R_1 + R_2} \quad (1)$$

Low pass filter

Low Pass Filter (First order TF)

$$\frac{v_o}{v_i} = \frac{1}{S + \frac{1}{RC}} \quad (2)$$

RLC second order Low Pass Filter

Low pass filter (Second-order TF)

$$\frac{v_o}{v_i} = \frac{1}{SL + \frac{1}{Rc} + R} = \frac{1}{S^2LC + 1 + SRC} = \frac{1}{S^2 + S\frac{R}{L} + \frac{1}{LC}} \quad (3)$$

Band Pass Filter

Band Pass Filter (Second-order TF)

$$\frac{v_o}{v_i} = \frac{R}{SL + \frac{1}{SC} + R} = \frac{SRC}{S^2LC + 1 + RSC} = \frac{S\frac{R}{L}}{S^2 + S\frac{R}{L} + \frac{1}{LC}} \quad (4)$$

METHODOLOGY

The vector fitting algorithm has been used in different ways in (Adam SEMLYEN and Bjørn Gustavsen, 2000; Bjørn Gustavsen & Semlyen, 1999). MATLAB program was used in this

paper as it has suitable commands to get the parameters and the rational approximation function which are the key equations to acquire.

After the transmission line, RAF is obtained based on the FRA data points using VF method. The first step is to , set up the extracted partial fraction approximation, which results have less RMS error because of VF method, also expressed in eq. (5)

$$H(S) = \frac{r_1}{S - p_1} + \frac{r_2}{S - p_2} + \dots + \frac{r_n}{S - p_n} + K \tag{5}$$

Eq. (5) consists of three parts as follows:-

- Real numbers, first order parts $\frac{r}{S + p}$
- Second order parts result from the result of two complex conjugate poles parts $\frac{as + b}{S^2 + cs + d}$
- Constants K.

Second, passive filter design circuit is conducted in order to build up the model that represents the TF of the transmission line by:-

- Implementation the required calculations to know the values of the circuits components.
- Using MATLAB Simulink to confirm the results.

Based on Bjørn Gustavsen and Semlyen (1999), the flowchart in Figure 2 describes the algorithm of the research, where the measured data points are presented as an input to the program. These data are changed to Cartesian form to generate a row of complex matrix for n dimension, and the process is described clearly in the flowchart.

Referring to the flowchart of Figure 2, the resultant RAF needs to be processed by some numerical filters to ignore the very low or the ineffective imaginary part from each element with respect to its combined real part. As an example, if one complex number has a value like $p_n = a*106 + b*10-7j$, then $p_n = a*106$, then, rearranging eq. 1 all the rational partial parts of the system function again to sum each two pair that has complex conjugate numbers together to get second order partial function elements without imaginary part for all system RAF, so, as an example, eq. 5. could be ,changed to the following form.

$$H(S) = \frac{r_1}{S - p_1} + \frac{r_2}{S - p_2} + \frac{as + b}{S^2 + CS + d} + \dots + \frac{r_n}{S - p_n} + K \tag{6}$$

APPLICATION AND RESULTS

In order to validate the proposed method, a model mentioned in (“Power_piline,” 2016) as shown in Figure 3 has been adopted to analyse the frequency response analysis (FRA). The modelling of the transmission line represents the TL behaviour to modelled together with this proposed method as shown in Figure 4 together with the curve fitting of the modelling procedure.

RLC Circuit from Vector Fitting Transmission Line Model

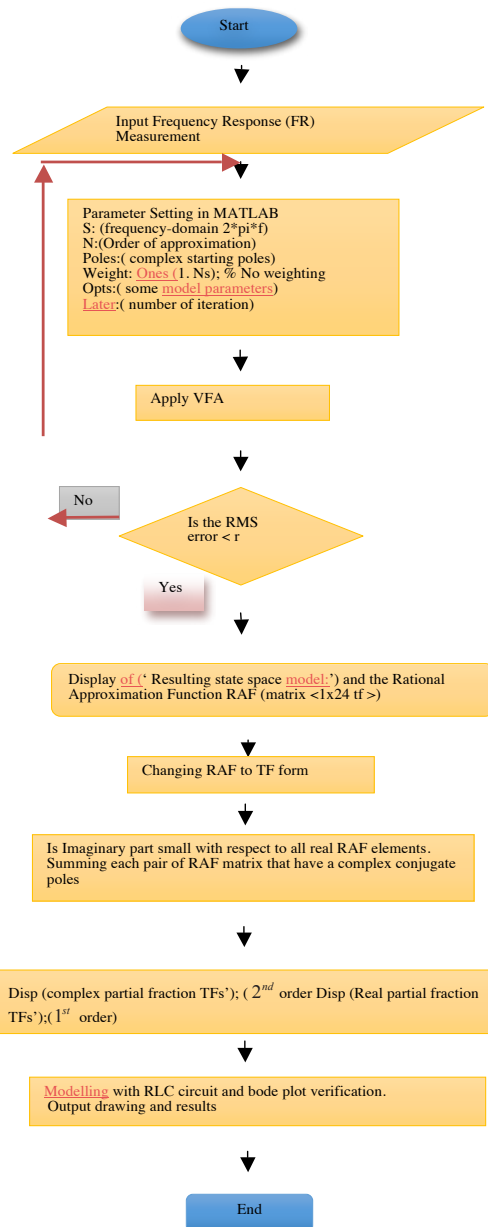


Figure 2. Flowchart of the proposed VF Algorithm

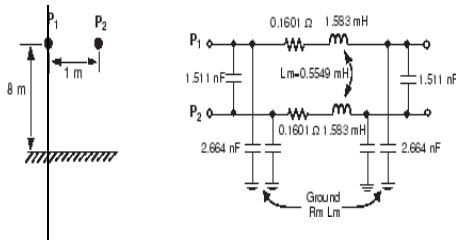


Figure 3. The adopted TL Model as a case study

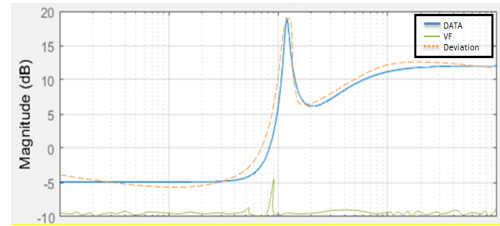


Figure 4. Plotting the measured data with proposed VFA vs frequency

Referring to eq. 5 and the proposed algorithm of (Bjørn Gustavsen & Semlyen, 1999), the resultant Rational Approximation Function parameters can be listed as follows:

$$\begin{aligned}
 r &= \begin{aligned} &-21.0633 + 0.0000i \\ &1.0510 + 0.0000i \\ &-0.4939 - 0.0546i \\ &-0.4939 + 0.0546i \end{aligned} \\
 P &= \begin{aligned} &-4.8095 + 0.0000i \\ &-1.3091 + 0.0000i \\ &0.0593 + 1.1941i \\ &0.0593 - 1.1941i \end{aligned} \\
 K &= 4
 \end{aligned}$$

So, the partial fraction expansion for the above transfer functions are as follows:-

$$\begin{aligned}
 TF1 &= \frac{-21}{S + 4.809} \\
 TF2 &= \frac{1.051}{S + 1.309} \\
 TF3 &= \frac{-(0.4939+0.0546i)}{S - (0.0593+1.194i)} \\
 TF4 &= \frac{-(0.4939-0.0546i)}{S - (0.0593-1.194i)}
 \end{aligned}$$

After all transfer functions are obtained, the equation is rearranged to eq (5):

$$H(S) = \frac{-21}{S + 4.809} + \frac{1.051}{S + 1.309} + \frac{-(0.4939 + 0.0546i)}{S - (0.0593 + 1.194i)} + \frac{-(0.4939 - 0.0546i)}{S - (0.0593 - 1.194i)} + 4$$

Based on eq. (5), each of two complex conjugate poles must be added to each other as follows to obtain equation such as in eq. (6):-

$$H(S) = \frac{-21}{S + 4.809} + \frac{1.051}{S + 1.309} + \frac{-0.9878S + 0.189}{S^2 - 0.1186S + 1.429} + 4$$

As described in the flowchart of Figure 2, a sequence of filtering and complex conjugate pair summation has been implemented to avoid the presence of the imaginary part in all partial fractions of the RAF and therefore, the elements of eq. 6 are listed in Table 1.

Table 1 has the final transfer functions of first and second order group that would be translated to their respective RLC equivalent circuit. Hence, according to Eq. 6, all these partial fraction functions have the same input and accumulated output as represented in Figure 5.

Table 1
First and second order group

Second order	First order
$\frac{-0.9878s + 0.189}{s^2 - 0.1186s + 1.429}$	$\frac{-21}{s + 4.809}$
	$\frac{1.051}{s + 1.309}$

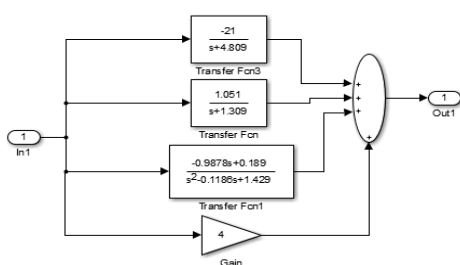


Figure 5. T.L modelling in terms of transfer function

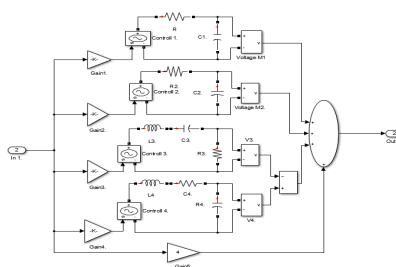


Figure 6. RLC passive circuit modelling for tested T.L

CONCLUSION

This paper discussed the results of transmission line modelling based on passive filter design and rational approximation function which can be extracted through the Vector Fitting (VF) method. The RLC circuit representation has been implemented for modelling the transmission line while MATLAB Simulink was used for verifying the results.

REFERENCES

Adam SEMLYEN AND Bjørn Gustavsen. (2000). *Vector_Fitting_By_Pole_Relocation.Pdf*.

Fidanboyly, K. M., Korkmaz, N., & Korkmaz, K. (2003, May). A transmission line modeling technique using time domain synthesis. In *2003 IEEE International Symposium on Electromagnetic Compatibility, 2003. EMC'03.* (Vol. 1, pp. 331-334). IEEE.

Gustavsen, B. (2004, May). Time delay identification for transmission line modeling. In *8th IEEE Workshop on Signal Propagation on Interconnects, 2004. Proceedings.* (pp. 103-106). IEEE. <http://doi.org/10.1109/SPI.2004.1409018>

- Gustavsen, B., & Semlyen, A. (1998). Simulation of transmission line transients using vector fitting and modal decomposition. *IEEE Transactions on Power Delivery*, 13(2), 605–611. <http://doi.org/10.1109/61.660941>
- Gustavsen, B., & Semlyen, A. (1999). Rational approximation of frequency domain responses by vector fitting. *IEEE Transactions on Power Delivery*, 14(3), 1052-1061. <http://doi.org/10.1109/61.772353>
- M, B. G., & Semlyen, A. (1998). Gustavsen” &I?), 13(2), 596–604.
- Marti, J. R. (1982). Accurate Modeling of Frequency-Dependent Transmission Lines in Electromagnetic Transient Simulations. *IEEE Power Engineering Review*, PER-2(1), 29–30. <http://doi.org/10.1109/MPER.1982.5519686>
- Matzner, S. H., Levy, H. M., & Ackerman, D. (2008). RF Laboratory Manual - Passive Filter Design. Retrieved 2016, February 25, from http://www.hit.ac.il/upload/engineering/experiment_5_-_filter_design109.pdf
- Pourmir, M. R., & Akbarkehkhajavan, A. (2013). Simulation Of Extra High Voltage Long Transmission Lines. *International Research Journal of Applied and Basic Sciences*, 7(7), 451–461.
- Power_piline. (2016). *Mathworks*. Retrieved from <http://www.mathworks.com/help/physmod/sps/powersys/ref/pisectionline.html;jsessionid=82e73e6c3de92aedeb4515f46c58>
- Ramsden, E. (2001). *An Introduction to Analog Filters | Sensors*. Retrieved 2016, February 25, from <http://www.sensorsmag.com/sensors/electric-magnetic/an-introduction-analog-filters-1023>
- Semlyen, a., & Dabuleanu, a. (1975). Fast and accurate switching transient calculations on transmission lines with ground return using recursive convolutions. *IEEE Transactions on Power Apparatus and Systems*, 94(2), 561–571. <http://doi.org/10.1109/T-PAS.1975.31884>

Modelling and Control of Standing Up and Sitting Down Manoeuver

A. J. Ishak^{1*}, M. O. Tokhi², M. S. Al-Quraishi¹, D. M. Linares² and S. K. Ali²

¹*Department of Electrical and Electronic Engineering, Faculty of Engineering, Universiti Putra Malaysia, 43400 UPM, Serdang, Selangor, Malaysia*

²*Department of Automatic Control and Systems Engineering, The University of Sheffield, United Kingdom*

ABSTRACT

Exoskeleton Robot is one of the most significant examples of human-oriented robotic devices. Nevertheless, the main challenge remains the complexity of their mechanical design and human-robot interfaces. This paper is an outcome of a research to model and to simulate the support of mobility of an elderly people using exoskeleton. Exoskeleton is developed in order to complement the corporal deficiencies of an elderly person in standing up and sitting down. When the natural joint torques is integrated with the exoskeleton's torque the result is in an overall torque that is comparable to that of a physically normal person. This work focuses on standing-up and sitting-down movements. Appropriate simulation models are formulated and their performances examined against measured data. The results with PID control show that at different speed of standing up and sitting down, the joint torques can be compromised. This is done within allowable limits.

Keywords: Exoskeleton, humanoid model, PID control, Joint Torque International Conference on Electrical & Electronic Technology 2016

ARTICLE INFO

Article history:

Received: 24 August 2016

Accepted: 03 Jun 2017

E-mail addresses:

asnorji@upm.edu.my (A. J. Ishak),
o.tokhi@sheffield.ac.uk (M. O. Tokhi),
mdg_eng@hotmail.com (M. S. Al-Quraishi),
d.miranda-linares@sheffield.ac.uk (D. M. Linares),
skalil@sheffield.ac.uk (S. K. Ali)

*Corresponding Author

INTRODUCTION

The aptitude to perform daily activities can be affected by accident or chronic diseases. This may result in the loss of human abilities. There is a dire need for rehabilitation programme and physical therapy for human recovery especially for post patients recovering from stroke. Research has focused on developing exoskeleton robots, which are used to rehabilitate the patient, in particular to support the upper or the lower limbs, for example, ankles, knees and hip joints.

Exoskeleton robots play an important role in biomedical, industrial, and aerospace applications. For instance, in biomedical applications, they are used to support patients recovering from stroke. Stroke victims often require assistance and regular physiotherapy during their recovery period. The elderly and the disabled face difficulties with mobility and researches and scientists have developed different types of exoskeletons robots to enhance their mobility, and for rehabilitation purposes. What is the Exoskeleton Robot? It is an external mechanical structure having joints similar to the body of a human. This wearable robot is able to transmit torques from the actuators to the joints of the human body through the rigid links of the exoskeleton (Kiguchi et al., 2012). The exoskeleton can be controlled using different techniques according to the interaction between the human body and the devices. Those techniques can be classified according to the human-robot interaction method: the signals measured from the exoskeleton, the interaction force signal measured between the human and the exoskeleton, and the biosignal measured from the human body.

Several studies have been conducted in the field of exoskeleton robots. The devices can be categorised according to the mechanical architecture, control approach, degree of freedom and the assistance provided. Lower limb exoskeleton with three degrees of freedom for each leg by Exso Bionics is one of the most innovative assistive robots (Strickland, 2012). Three joints are implemented whereby two are active joints, namely hip and knee, and one is passive, namely ankle joint. The active joints are actuated by brushless DC motors. More than 15 sensors (force sensors and encoders) are employed for control and balancing purposes. The EXPOS is a lightweight exoskeleton system which is attached to an intelligent cast walker and provides mobility to senior citizens (Kong et al., 2006). The Center for Intelligent Mechatronics of the Vanderbilt University successfully developed Vanderbilt Exoskeleton which has two degrees of freedom (Quintero et al., 2011). The actuation of the movements of the hip and knee are done by positioning two brushless DC motors at the thigh position. One of the advantages of this exoskeleton is the lightweight design that reflects a slender profile. Further, there is no need for footplate or large backpack components. Nevertheless, the equilibrium of the subject is managed using a set of crutches. One of the most popular exoskeletons is Cyberdyne's robot Fit HAL (Hybrid Assistive Limb) (Aach et al., 2013). It is an exoskeleton completely equipped with a lower limb. It supports the person in terms of movement such as standing up and sitting down by detecting the Electromyography signal to comply with the movements of the user (Cyberdyne, 2015). Compared with the exoskeletons mentioned above, HAL provides both a lower and upper limb exoskeleton, in order to supply and to enhance the human physical ability in different fields such as rehabilitation, physical training, large labour and safe support.

Taking into account the challenges of mechanical design and the control approaches, this paper describes the modelling and simulation phase of the sit-to-stand and stand-to-sit tasks, and analyses the system torque and force requirements under various situations.

MATERIALS AND METHODS

The mathematical model of the complete lower limb musculoskeletal system is complex. Therefore, the MSC Visual Nastran 4D (VN4D) software is used to model and to simulate the movements of standing up and sitting down. The VN4D setting makes it possible for the creation of a humanoid model which responds in a genuine way to external forces, namely

gravity and weight. There are three main goals to be achieved by utilising VN4D in this work. The first goal is to construct the humanoid model segments designed by Solid Work and to integrate them with suitable dynamic properties. Second, to measure the mechanical parameters such as torque, orientation and centroids of the links which interface with Matlab Simulink model later for further analysis and to utilise them as a control input to drive the exoskeleton. Finally, it attempts to capture the interaction of the exoskeleton with external energies and disorders in a realistic way and at the same time display the humanoid motions [6].

Humanoid Model Design

Solid Works generated different segments of a human-like model based on specifications by Winter (2009). Its weight is 80kg and its height is 1.8m. When the design is completed, each segment can be exported and constructed in VN4D. The position of the joints is anatomically taken into consideration. Generally, the human body has 32 main degrees of freedom (DoF). In the proposed human form as shown by the model in Figure 1, only 13 DoF were involved in both frontal and lateral planes. The transversal plane on the other hand, is blocked.

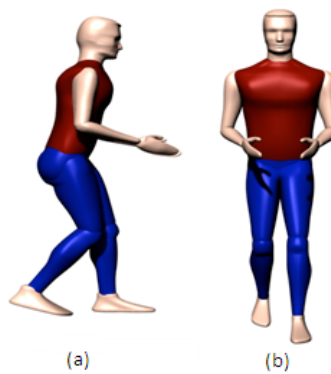


Figure 1. (a) Lateral Plane (b) FrontalPlane (Strickland, 2012)

Standing Up and Sitting Down Motion

Karlj and Bajd (1989) divided the standing-up manoeuvre into four segments: initiation, seat uploading, ascending and stabilisation, lasting around 1.5s. The required torque profiles for standing up and sitting down movement are given in Figure 2.



Figure 2. Joint's orientation during standing up and sitting down manoeuvres (Kralj et al., 1989)

EXPERIMENTS AND RESULTS

A closed loop PID control was implemented for set-point tracking of each joint. In order for the value to stay below the normal limits, a saturation block was included at the PID controller output as depicted in Figure 3.

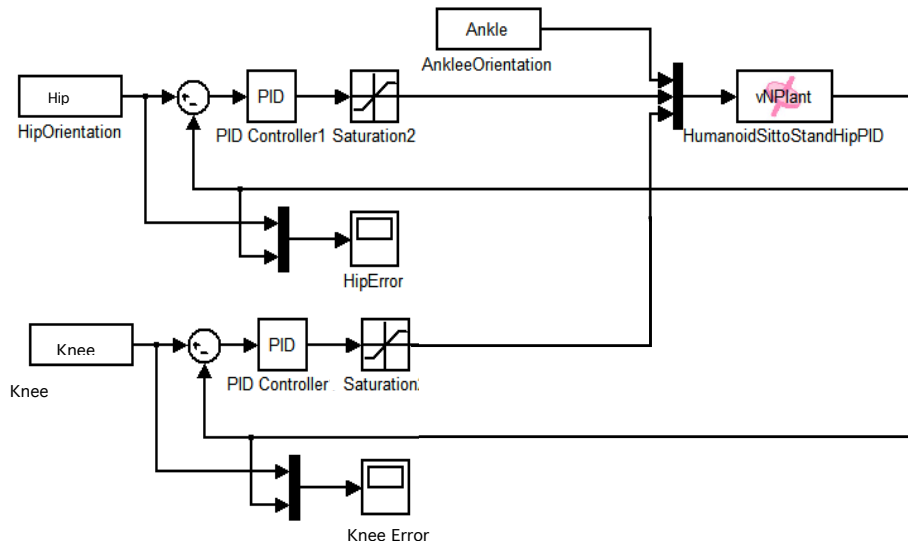


Figure 3. PID control in Simulink for ankle, hip and knee joints

P, I and D gains for each joint were obtained separately. Ankle and knee trajectories were directly connected to motors actuated by orientation at the plant. The Mean squared error (MSE) between hip orientation reference and actual value was calculated and a comparison of the resulting MSE was performed and the gains which generated the lowest error were recorded. The same process was repeated to get P, I and D gains for knee, having the reference trajectories of ankle and hip directly sent to the plant. Table 1 and Table 2 illustrate the best results of the initial and lower torque level trials by setting the saturation level 160 Nm and 210Nm for the hip and knee joints respectively.

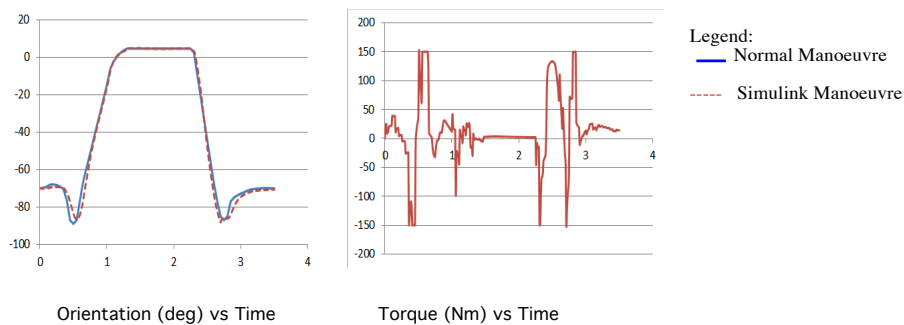
Table 1
PID gains for initial trial

PID gains	Hip	Knee
Proportional	16	16
Derivative	2	8
Integral	1.6	3.2
MSE	9.19	7.57
Saturation Limit	160 Nm	210 Nm

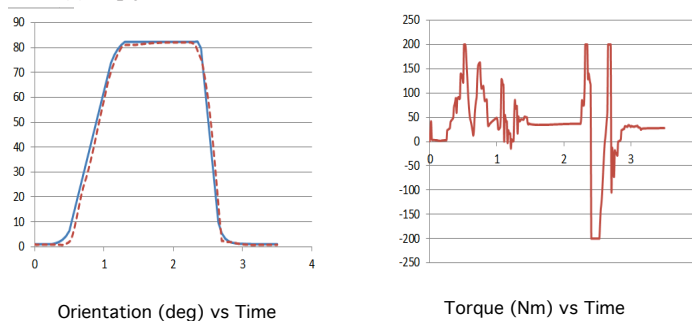
Table 2
PID gains for lower torques

PID gains	Hip	Knee
Proportional	14	14
Derivative	2	7.2
Integral	1.2	2.5
MSE	9.7	8.9
Saturation Limit	160 Nm	210 Nm

Thereafter, an assessment was carried out if an acceptable standing up and sitting down manoeuvre was achievable with lower torque with respect to different saturation levels. The results show that better performance was achieved with a saturation limit of 150 Nm for the hip joint and 210 Nm for the knee joint as described in Figure 4. Acceptable behaviour was achieved with lower saturation limits although the MSE was inversely proportional to the saturation value.



(a) Hip joint with 150 Nm saturation and 8.61 MSE



(b) Knee joint with 200 Nm saturation and 10.72 MSE

Figure 4. Hip and knee joint trajectory and torque profile

A new Simulink diagram was later created with torques from the hip and knee PID controllers as input to the plant, and ankle orientation trajectory directly sent to the plant. Following 100 trials were run and the P, I and D gains were tuned and the model was tested

with different saturation levels. Figure 5 shows sample results with saturation limits of 160 Nm for the hip joint and 210 Nm for the knee joint and 40 Nm for ankle joint. It is noted that the reference joint orientations were achieved with mean-squared errors of 7.35, 6.11 and 9.98 for the hip, knee and ankle joints respectively.

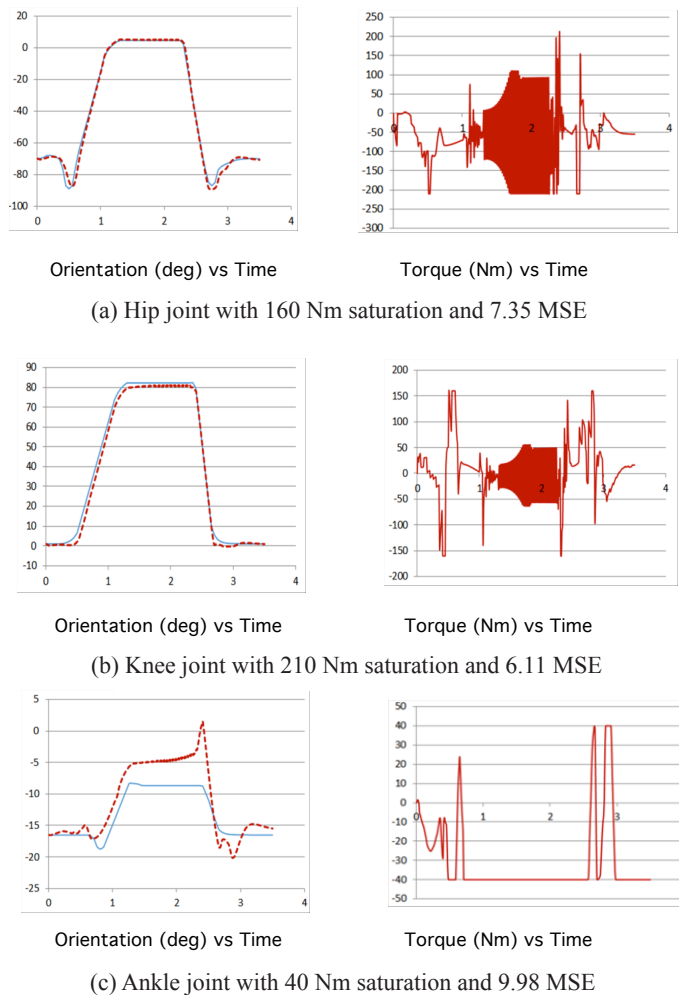


Figure 5. (a) Hip, (b) knee and (c) ankle joints trajectory and torque profiles

CONCLUSION

The modelling and simulation of the human-like model and exoskeleton model have been developed using a virtual setting for theoretical studies. This was achieved through modelling levels of movements support for senior citizens. The analysis of the required torque profiles was performed to actuate the various joint motors in order to obtain the normal joint movements. It has been shown that within appropriate control method and allowable limits, the joint torques can be developed even at different speeds of standing up and sitting down movements. Further

research is needed to understand if these investigations are adequate and within human limits with different torque saturation limits

REFERENCES

- Aach, M., Meindl, R., Hayashi, T., Lange, I., Geßmann, J., Sander, A., & Schildhauer, T. A. (2013). Exoskeletal neuro-rehabilitation in chronic paraplegic patients—initial results. In *Converging Clinical and Engineering Research on Neurorehabilitation* (pp. 233-236). Springer Berlin Heidelberg.
- Cyberdyne (2015). HAL for living support (lower limb type). (March, 2015)
- Kiguchi, K., & Hayashi, Y. (2012). An EMG-based control for an upper-limb power-assist exoskeleton robot. *IEEE Transactions on Systems, Man, and Cybernetics, Part B (Cybernetics)*, 42(4), 1064-1071.
- Kong, K., & Jeon, D. (2006). Design and control of an exoskeleton for the elderly and patients. *IEEE/ASME Transactions on Mechatronics*, 11(4), 428-432.
- Kralj, A. R., & Bajd, T. (1989). *Functional electrical stimulation: standing and walking after spinal cord injury*. CRC press.
- Miranda-Linares, D., Lopez-Coronado, J., Diaz-Hernández, C. A., Ishak, A., & Tokhi, M. (2015, August). Modelling and Simulation of Assistive Exoskeleton for Elderly Mobility. In *Assistive Robotics: Proceedings of the 18th International Conference on CLAWAR 2015* (p. 95). World Scientific.
- Quintero, H. A., Farris, R. J., & Goldfarb, M. (2011, June). Control and implementation of a powered lower limb orthosis to aid walking in paraplegic individuals. In *2011 IEEE International Conference on Rehabilitation Robotics* (pp. 1-6). IEEE.
- Strickland, E. (2012). Good-bye, wheelchair. *IEEE Spectrum*, 49(1), 30-32.
- Winter, D. A. (2009). *Biomechanics and motor control of human movement*. John Wiley & Sons.





Silicon Nanowire Interface Circuit for DNA Detection

Kamilu Iman Usman¹, Mohd Nizar Hamidon^{1,2}, Siti Fatimah Abd Rahman^{1,3} and Guan Ling Sim²

¹*Institute of Advanced Technology, Universiti Putra Malaysia, 43400 UPM, Serdang, Selangor, Malaysia*

²*Faculty of Engineering, Universiti Putra Malaysia, 43400 UPM, Serdang, Selangor, Malaysia*

³*Institute of Nano Electronics Engineering, Universiti Perlis Malaysia, 01000 Kangar, Perlis, Malaysia*

ABSTRACT

Detection and quantification of DNA is critical to many areas of life sciences and health care, from disease diagnosis to drug screening. The transduction of DNA through electrochemical methods have a fast response rate and with a conductometric device like the silicon nanowire which can be fabricated to have a similar diameter of the DNA molecule being targeted, detection is real-time. Critical to this is the interfacing of a current-source and an amplifier capable of achieving a maximum of 10 pico ampere input bias. In this project, we fabricated a silicon nanowire using the top down approach and built a circuit that can mimic the output signal as low as 12 nA and achieved a gain of 1 million to be interfaced with the nanowire for real-time DNA detection.

Keywords: Silicon nanowire, nanoelectronics, interface circuit, DNA detection

INTRODUCTION

Recently, biochemical sensors have attracted interest among research areas in different applications due to their efficiency in monitoring and regulating certain areas such as food industry, toxicology testing, medical

diagnostics, environmental monitoring and drug industries (Yuan, Duan, Yang, Luo, & Xi, 2012). Biochemical sensors are defined as analytical devices that incorporate sensing materials with molecular recognition elements (enzyme, protein, antibody, nucleic acid, hormone, chemical compounds, etc.) that gets integrated within the transducers (Usman & Hamidon, 2015).

DNA detection is one area that drives innovation of biochemical sensing and with the rapid development of advanced nanotechnology, many nanomaterials for sensing with unique properties, favoured size, and chemical compositions have been fabricated to be incorporated within the

ARTICLE INFO

Article history:

Received: 24 August 2016

Accepted: 03 Jun 2017

E-mail addresses:

icekace@gmail.com Kamilu Iman Usman),

mnh@ng.upm.edu.my (Mohd Nizar Hamidon),

siti_fatimah0410@yahoo.com (Siti Fatimah Abd Rahman),

guanling_24@hotmail.com (Guan Ling Sim)

*Corresponding Author

transducer to aid DNA detection. One of them is the application of one-dimensional (1D) nanostructures (nanotubes, nanowires, nanorods, nanobelts and heteronanowires). Silicon nanowire (SiNW) is one of the 1D nanostructures that has emerged as the promising sensing nanomaterial upon its unique optical properties, mechanical and electrical (Gao et al., 2011). The SiNWs have gained popularity in the field of sensor development due of their ultrasensitive nature and high surface-to-volume ratio, fast response, biocompatibility, good reversibility, and H-terminated surface, which allows easy attachment to various functional groups. Additionally, the reliability and reproducibility of their fabrication process make them promising candidates for highly sensitive sensors. (Talin, Hunter, Leonard, & Rokad, 2006; Vu et al., 2010).

Nano-scale bioelectric devices achieve extraordinary sensitivity when used to detect molecular interactions (Vu et al., 2010). These devices are useful in the analysis of biomedical diagnostics. Most diseases are diagnosed based on symptoms which can sometimes be misleading. Biological molecules such as lipids, proteins and nucleic acid are related to the primary cause of disease.

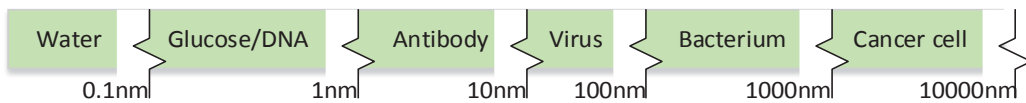


Figure 1. The molecules in the nanoscale

Figure 1 shows why the SiNW is very useful in detecting biological molecules because they can be designed to match the scale of the target molecule. Disease diagnosis can be successful by screening for disease biomarkers which has given rise to the need for ultrasensitive bioassays making bio-functionalisation of nanomaterials in high demand.

The SiNW with widths (1 μm , 80 nm, 60nm, 40nm and 20nm) were characterised using a voltage source of 1 V and it demonstrated a linear ohmic behaviour. It generated current outputs of 115 pA, 146 pA, 201 pA, 327 pA and 2.6 nA respectively. For DNA hybridisation

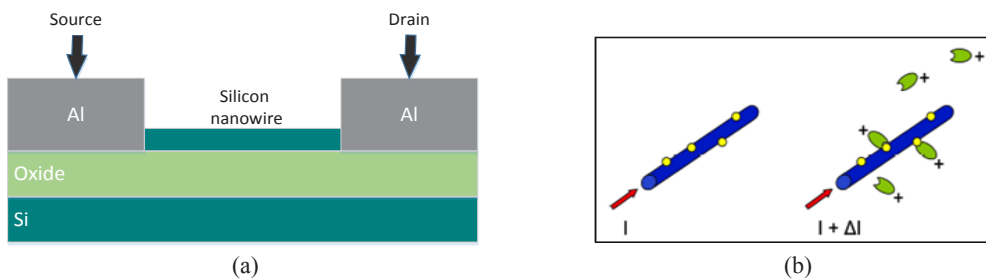


Figure 2. (a) cross-sectional diagram of top-down fabricated SiNW. (b) Schematic showing the principle of the NW sensor. The surface is coated with receptor molecules (yellow). As charged molecules (green) attaches to the receptor molecules the current is changed

of concentration 10 μM , 1 μm width showed output of 4.25 nA demonstrating the quality of transduction of SiNW (Nuzaihan et al., 2016). When utilised as an electrochemical sensor, detection is based on redox reaction as a result of chemical reaction between immobilised biomolecule or chemical species on working electrode and target analyte which finally produces measurable electrical current (Monošík, Středanský & Šturdík, 2012).

The SiNWs-FET sensor consists of three electrodes: source, drain, and gate and its functions based on conductive change of the carrier on the surface of SiNWs either accumulation or depletion charge. When negatively charged, molecules bind on the n-type SiNW surface resulting in accumulation of the negative carriers thus, increasing the resistance reading and vice versa if using p-type SiNWs (Zhang & Ning, 2012).

There are many studies on SiNWs with most examining the latter's effects of a biosensing event, for example, protein detection or pH measurement on the electrical properties of the nanowire (Kargar & Christen, 2008). They have also been used for glucose detection (Shao, Shan, Wong, & Lee, 2005). DNA hybridisation detection (Stern et al., 2007), viral detection (Patolsky et al., 2004), and even for extracellular recording from electrogenic cells (Patolsky, 2006). Despite the great potential of the SiNW, no device based on specific SiNW has been integrated with all-day-life in the last decade. This is mainly due to the need to interface these nanomaterials with nanoscale platforms (Serre, Ternon, Stambouli, Perival, & Baron, 2013). The proposed sensing schemes implemented on silicon nanowire are inherently compatible with modern CMOS process (Ramírez-Angulo, Carvajal, & Torralba, 2004). Although the signal generated is ultra-small, it can be amplified using a pico-Ampere sensitive amplifier (Steadman, Vogtmeier, Kemna, Quossai, & Hosticka, 2005). Current modules on a single chip makes it possible to realise ultralow-current-mode circuit as they suffer less fluctuations (Halloran & Sarpeshkar, 2004; Linares-barranco & Serrano-gotarredona, 2003). This helps in maintaining the integrity of the signal.

This work investigates the ohmic properties of a top-down fabricated SiNW for its optimised electrical sensitivity for biosensing applications and proposes an interface circuit that will make the device readable and portable thus, enhancing the utility of silicon nanowire to be a point-of-care device which can be integrated with all-day-life.

MATERIALS AND METHOD

For the purposes of this research, SiNW biosensor was designed with electron beam lithography (EBL) using the top-down fabrication method. The device structure was formed by implementing reactive ion etching (RIE) in order to integrate the fabrication with a CMOS process. A p-type silicon on insulator (SOI) wafer with a 160 nm silicon layer on a 200 nm buffered-oxide (BOX) insulating layer with a resistivity of 1-20 $\Omega\text{-cm}$ was used as the starting material. Standard cleaning procedure using RCA1, BOE and RCA 2 were employed to remove all contaminants on the surface of the sample before it was washed in de-ionised water and dried on a hot conduction plate at a temperature of 200°C for not less than 5 minutes to eliminate the water residue and cooled down to room temperature for not less than 10 minutes.

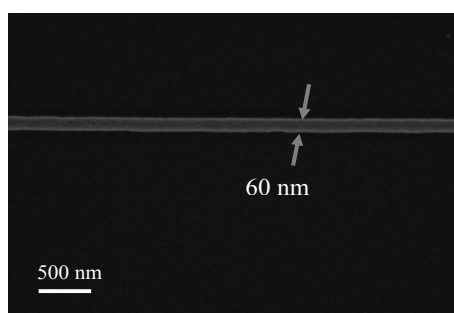


Figure 3. FESEM image showing the morphology of fabricated SiNW

Figure 3 shows the morphology of the SiNW with a width of 60 nm we have developed as a high-performance sensor that is label free and direct time for DNA detection using SiNWs-FET sensor top-down approach. We also managed to improve the sensitivity of SiNWs-FET sensor by optimising probe concentration, buffer ionic strength, and the gate voltage. The Keithley 4200 Semiconductor Parameter Analyzer (SPA) is used to demonstrate the usefulness of the fabricated sample.

The OPA129 is a monolithic operational amplifier manufactured by Texas instruments with ultra-low current using dielectrically-isolated FET (DIFET) with advanced geometry which makes the amplifier achieve a high level of performance. Dielectrically-isolated FET fabrication eliminates leakage current at isolation-junctions which is a contributing factor to input bias current with the traditional monolithic FETs. This decreases input bias current by a factor of 10-100. The OPA129 has an offset current unit of femto ampere and is fitted with a noise-free cascode which makes the device capable and efficient in handling nanoscale sensitivity.

RESULTS AND DISCUSSION

The idea behind SiNWs as conductometric devices for electrochemical sensing is to monitor the conductance across the surface by measuring its resistance which is altered by the charges along its surface. When molecules bind with the SiNWs, their ability to conduct is altered and this change serves as the mechanism for detection. Depending on the surface-to-volume ratio, the resistance of the NWs increases with the decreasing width of the NWs. The I-V characterisation of the SiNW illustrates the effectiveness of the fabrication sample as a DNA detection device and gives us a target-range of Gain for our interface circuit. Figure 4 shows the ohmic properties of the SiNW and presents the device as a useful sensor.

Using a Keithley 4200 Semiconductor Parameter Analyzer (SPA) and supplying the SiNW with a sweep voltage of 0-2 V (Figure 4b), 39 data points were generated indicating an increase in resistance from $6.05E8 \Omega$ at 0.05 V to $6.81E9 \Omega$ at 1.95 V leading to a decrease in conductance.

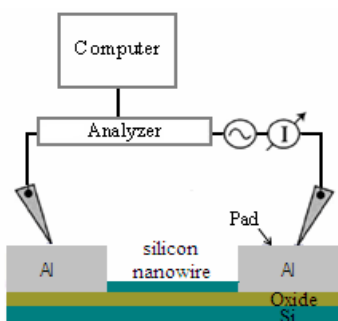


Figure 4a. Measurement setup

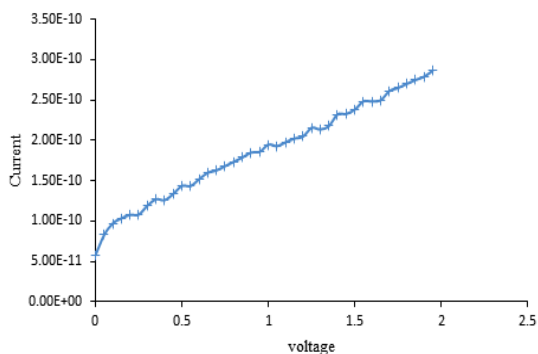


Figure 4b. I-V graph of the SiNW with 60nm width

Considering the I-V properties of the SiNW derived from I-V characterisation, the range of current to be sensed is (0.8E-11 to 2.8E-10) Ampere although a significant hike is expected after the sensing event. There are very few CMOS components designed for nanoelectronics as this field is still widely untapped but the OPA129 operational amplifier is one that has the capability to be integrated in nano range. In trying to amplify the signal, there was unwanted interaction between the feedback resistor of the op-amp and the SiNW which caused the current to be unpredictable. In order to successfully amplify this sort of signal, we designed a current source that will mimic the output signal of the SiNW. The quality of such a circuit must be such that it isolates the signal it produces to prevent unwanted interaction in the next phase. We used the diamond buffer topology which is primarily used in audio applications. Using this famous configuration as a current source model, we were able to design a constant current source that can isolate capacitive loads and boost op-amp signal.

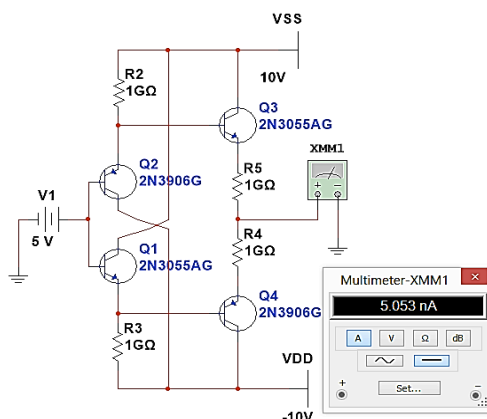


Figure 5. Simulation of the current source

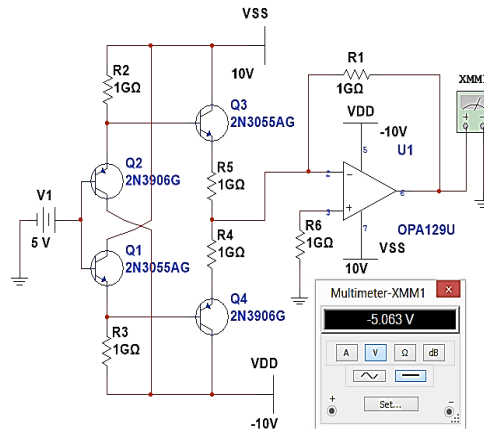


Figure 6. Simulation of the OPA129 Op-Amp

Figure 5 shows the classic diamond buffer structure renowned for isolation, transistors Q1 and Q3 are identical devices, and so are Q2 and Q4. These four transistors must operate at the same bias current. This symmetry is essential and results in exceptionally low distortion and isolation.

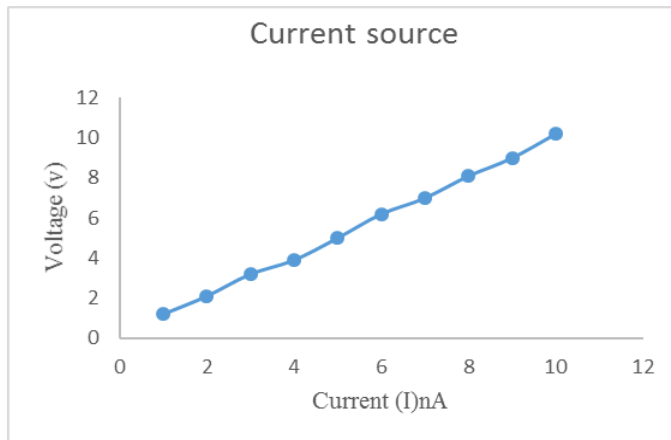


Figure 7. Current source measurement

The current voltage graph in Figure 7 shows the measurement of the output current from the prototype using a keithley 480 picoammeter with voltage ranging from 1-10 volts. Figure 8 shows the output signal from the amplifier in volts. The similarity of the curves indicates a very high integrity in the amplification of the signal.

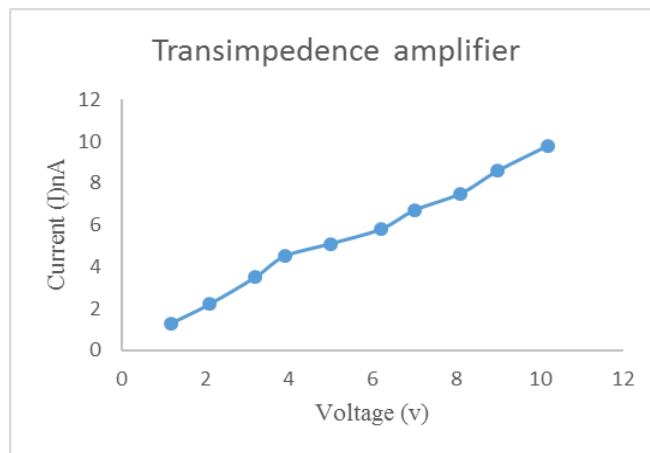


Figure 8. Current source amplifier

CONCLUSION

In order for interfacing to occur with a SiNW, it has to be fabricated with the top-down approach for good ohmic contact and easily integrated with nanoelectronic components. Our circuit has proven to be capable of signal isolation and amplification but we are not yet convinced of the method of integrating the SiNW onto the circuit due to lack of interfacing projects in nanoelectronics. In designing a nano range current source, isolation can be achieved using a diamond buffer configuration. The successful amplification of this ultra-small signal indicates that the SiNW can be interfaced for further utility, making the SiNW a portable sensing device with numerous applications in everyday life such as; point-of-care or field testing for bioassays.

ACKNOWLEDGEMENT

Authors would like to acknowledge Ministry of Education (GP-IPS/2014/9447400) Malaysia for their financial support.

REFERENCES

- Gao, A., Lu, N., Dai, P., Li, T., Pei, H., Gao, X., ... & Fan, C. (2011). Silicon nanowire-based CMOS-compatible field-effect transistor nanosensors for ultrasensitive electrical detection of nucleic acids. *Nano Letters*, 11(9), 3974–3978. <http://doi.org/10.1021/nl202303y>
- Halloran, M. O., & Sarpeshkar, R. (2004). A 10-nW 12-bit Accurate Analog Storage Cell With 10-aA Leakage. *IEEE Journal of Solid-state Circuits*, 39(11), 1985–1996.
- Kargar, A., & Christen, J. M. B. (2008). Theoretical investigation of silicon nanowire pH sensor. In *2008 2nd IEEE RAS & EMBS International Conference on Biomedical Robotics and Biomechanics*. <http://doi.org/10.1109/BIOROB.2008.4762861>
- Linares-Barranco, B., & Serrano-Gotarredona, T. (2003). On the design and characterization of femtoampere current-mode circuits. *IEEE Journal of Solid-State Circuits*, 38(8), 1353-1363.

- Monošík, R., Stred'anský, M., & Šturdík, E. (2012). Biosensors - classification, characterization and new trends. *Acta Chimica Slovaca*, 5(1), 109–120. <http://doi.org/10.2478/v10188-012-0017-z>
- Nuzaihan, M. M. N., Hashim, U., Md Arshad, M. K., Kasjoo, S. R., Rahman, S. F. A., Ruslinda, A. R., ... Shahimin, M. M. (2016). Electrical detection of dengue virus (DENV) DNA oligomer using silicon nanowire biosensor with novel molecular gate control. *Biosensors and Bioelectronics*, 83, 106–114. <http://doi.org/10.1016/j.bios.2016.04.033>
- Patolsky, F. (2006). Detection, Stimulation, and Inhibition of Neuronal Signals with High-Density Nanowire Transistor Arrays. *Science*, 313(5790), 1100–1104. <http://doi.org/10.1126/science.1128640>
- Patolsky, F., Zheng, G., Hayden, O., Lakadamyali, M., Zhuang, X., & Lieber, C. M. (2004). Electrical detection of single viruses. *Proceedings of the National Academy of Sciences of the United States of America*, 101(39), 14017–14022. <http://doi.org/10.1073/pnas.0406159101>
- Ramírez-Angulo, J., Carvajal, R. G., & Torralba, A. (2004). Low supply voltage high-performance CMOS current mirror with low input and output voltage requirements. *IEEE Transactions on Circuits and Systems II: Analog and Digital Signal Processing*, 51(3), 124–129. <http://doi.org/10.1109/TCSII.2003.822429>
- Serre, P., Ternon, C., Stambouli, V., Periwal, P., & Baron, T. (2013). Sensors and Actuators B : Chemical Fabrication of silicon nanowire networks for biological sensing. *Sensors and Actuators: B. Chemical*, 182, 390–395. <http://doi.org/10.1016/j.snb.2013.03.022>
- Shao, M. W., Shan, Y. Y., Wong, N. B., & Lee, S. T. (2005). Silicon nanowire sensors for bioanalytical applications: Glucose and hydrogen peroxide detection. *Advanced Functional Materials*, 15(9), 1478–1482. <http://doi.org/10.1002/adfm.200500080>
- Steadman, R., Vogtmeier, G., Kemna, A., Quossai, S. I., & Hosticka, B. (2005). A high dynamic range, high linearity cmos current-mode image sensor for computed tomography. In *Proceedings of the 31st European Solid-State Circuits Conference, 2005. ESSCIRC 2005*. (pp. 415–418). <http://doi.org/10.1109/ESSCIR.2005.1541648>
- Stern, E., Klemic, J. F., Routenberg, D. A., Wyrembak, P. N., Turner-Evans, D. B., Hamilton, A. D., ... Reed, M. A. (2007). Label-free immunodetection with CMOS-compatible semiconducting nanowires. *Nature*, 445(7127), 519–22. <http://doi.org/10.1038/nature05498>
- Talin, A. A., Hunter, L. L., Leonard, F., & Rokad, B. (2006). Large area, dense silicon nanowire array chemical sensors. *Applied Physics Letters*, 89(15), 153102. <http://doi.org/10.1063/1.2358214>
- Usman, K. I., Hamidon, M. N., Yusof, N. A., Azhari, S., Hasan, I. H., Nicodemus, K., & Rahman, S. F. A. (2015, August). Silicon nanowire interface circuit for biosensing applications. In *Micro and Nanoelectronics (RSM), 2015 IEEE Regional Symposium on* (pp. 1–4). IEEE.
- Vu, X. T., GhoshMoulick, R., Eschermann, J. F., Stockmann, R., Offenhäusser, a., & Ingebrandt, S. (2010). Fabrication and application of silicon nanowire transistor arrays for biomolecular detection. *Sensors and Actuators, B: Chemical*, 144(2), 354–360. <http://doi.org/10.1016/j.snb.2008.11.048>
- Yuan, J., Duan, R., Yang, H., Luo, X., & Xi, M. (2012). Detection of serum human epididymis secretory protein 4 in patients with ovarian cancer using a label-free biosensor based on localized surface plasmon resonance. *International Journal of Nanomedicine*, 7, 2921–2928. <http://doi.org/10.2147/IJN.S32641>
- Zhang, G. J., & Ning, Y. (2012). Silicon nanowire biosensor and its applications in disease diagnostics: A review. *Analytica Chimica Acta*, 749, 1–15. <http://doi.org/10.1016/j.aca.2012.08.035>



Sensitivity Study of Graphene Nanoribbon with NH₃ at Room Temperature

Mohd Nizar Hamidon^{1*}, Guan Ling Sim² and Kamilu Iman Usman¹

¹*Institute of Advanced Technology, Universiti Putra Malaysia, 43400 UPM, Serdang, Selangor, Malaysia*

²*Department of Electrical and Electronics Engineering, Faculty of Engineering, Universiti Putra Malaysia, 43400 UPM, Serdang, Selangor, Malaysia*

ABSTRACT

This study presents the sensitivity of graphene nanoribbon (GNR) when exposed to ammonia gas at room temperature. Alumina were used as a substrate and coated with GNR as sensing film for ammonia gas detection. Four different concentration of GNR in the category of maximum, high, low, and minimum were prepared. Each category of GNR will be dispersed on alumina substrate with area of 1cm² and 4cm². 30nm of gold contacts are sputtered on both ends of the sensing film. The ammonia gas can be detected by measuring the changes in resistance. The GNR as ammonia sensor shows good responses at room temperature. In repeatability test, maximum GNR shows least variation when exposed to ammonia with the value of 1.01% (4cm²) and 2.12% (1cm²). In a sensitivity test, 0.25% to 1.00% of ammonia gas was used and tested on maximum GNR. Maximum GNR on 4cm² substrate shows higher sensitivity as compared to 1cm². Reaction time of GNR on ammonia gas decreased as the concentration of ammonia increased. Larger surface area of sensing element required lesser reaction time.

Keywords: GNR, alumina substrate, ammonia, sensitivity

INTRODUCTION

Concerns over air pollution which directly affects the health of human beings and animals

have led to increased demands for low power consumption, low temperature operation, and smaller size sensors that are highly sensitive in detecting pollution (Somov et al. 2015). Recent researches on nanotechnologies gas sensors have shown good responses on the targeted chemical gas such as polymer fibres for hydrogen gas (Chen et al., 2014), polymer dispersed liquid crystal doped with carbon nanotube for acetone gas (Lai et al., 2013), and carbon nanotube for carbon dioxide detection (Wang et al., 2014). Ammonia gas, NH₃ is a toxic gas which is harmful to the

ARTICLE INFO

Article history:

Received: 24 August 2016

Accepted: 03 Jun 2017

E-mail addresses:

mnh@upm.edu.my (Mohd Nizar Hamidon),

guanling_24@hotmail.com (Guan Ling Sim),

icekace@gmail.com (Kamilu Iman Usman)

*Corresponding Author

environment and living beings. Long periods of exposure to NH₃ will cause severe irritation to the skin, harm the respiratory systems and damage the internal organs. Hence a high sensitivity and fast response ammonia gas detector is needed to curb these problems.

Graphene with excellent electronic properties had received attention in the sensor field. Its properties are suitable for sensing with high mobility at room temperature, high current densities, and high thermal conductivity (Kara et al., 2013). The two-dimensional honeycomb-like structure of graphene also helps in promoting gas sensing sensitivity exposing large areas to the targeted gas (Huang et al., 2012). Many researches on ammonia gas sensor have been reported using graphene as sensing elements which basically can be divided into: graphene with polymers (Wu et al., 2013) and graphene with oxide (Huang et al., 2012) which shows good response. There is not much research on the sensitivity of GNR coated on alumina substrate. This paper aims to study the sensitivity of GNR coated on alumina substrate with ammonia gas at room temperature.

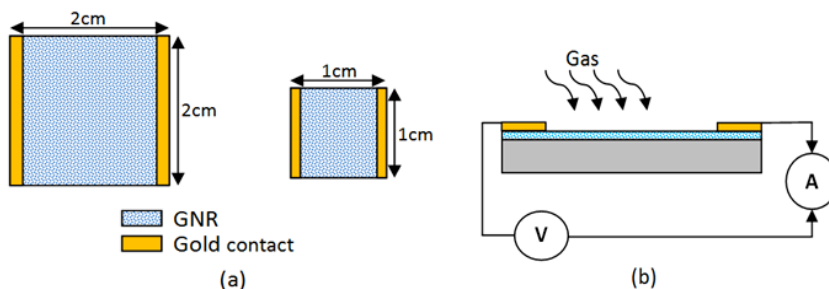


Figure 1. Schematic diagram of (a) sensor with different surface area; (b) measurement design when sensor exposed to gas

Table 1
Category of different amount of GNR on type I and type II substrate

Alumina Substrate	Label for GNR coated	GNR coated on substrate (cm/Ω)
Type I 2cm x 2cm	Maximum	4.03×10^{-4}
	High	3.16×10^{-4}
	Middle	1.02×10^{-4}
	Low	0.73×10^{-4}
Type II 1cm x 1cm	Maximum'	3.92×10^{-4}
	High'	2.39×10^{-4}
	Middle'	1.27×10^{-4}
	Low'	1.63×10^{-4}

EXPERIMENT DETAILS

Figure 1(a) shows the schematic diagram of the sensing part. Alumina is used as the substrate for the sensing part. GNR is prepared and coated in Kyutech, Kyushu Institute of Technology. Double walled carbon nanotube was used to obtain single layered GNR. The method of preparation is adopted from (Tanaka et al. 2015).

Alumina substrate can be divided into two categories: type I and type II. Type I and Type II indicate the substrate with area of 4cm² and 1cm² respectively. A thin layer of GNR is coated on the alumina substrate (Tanaka et al., 2015). Two strips of gold contact are sputter coated on top of GNR at both ends. Thickness of the gold contact is 30nm. Gold is used as contact for two reasons: its resistance to corrosion and it does not produce any chemical reaction with ammonia gas. Table 1 shows the preparation of the sensing part with different amount of GNR on type I and type II substrate. The amount of GNR is obtained from the resistivity equation (1).

$$R = \rho l/A \quad (1)$$

Figure 1(b) shows the electrical connection to the sensing part. A constant voltage supply of 1.5V is connected to the sensing part throughout the experiment. Resistance of the GNR can be obtained by measuring the current as shown in Figure 1(b). Fluke 289 True RMS Multimeter is used for current measurement. Chemical gas flowed in and out are indicated as gassing and degassing respectively.

Sensing part is placed into the airtight stainless steel gas chamber with the connection of gas inlet, gas outlet, and measuring probe to the power supply and multimeter. The gas flow is controlled by computerised Aalborg Gas Controller Module. Amount of gas flow into the chamber can be observed through the Aalborg Command Module.

Repeatability Test

The sensing element was stabilised during the pre-experiment stage whereby 15 minutes of air is flowed in to stabilise the GNR. Ammonia gas with concentration of 0.5% was used during repeatability test. Duration of ammonia gassing and degassing was 10 minutes for each session and both were repeated for two cycles.

Repeatability of the sensing element can be determined by observing the difference (variation) between the first and the second gassing response as stated in Table 2. Equation (2) and (3) show the mathematical calculation to determine the variation and consistency. Maximum concentration shows the least variation followed by high, middle and low concentration. Low variation indicates high consistency.

$$\text{Variation (\%)} = \frac{\text{Second peak} - \text{First peak}}{\text{First peak}} \times 100\% \quad (2)$$

$$\text{Consistency} = \frac{1}{\text{Variation}} \quad (3)$$

Table 2
GNR with different concentrations towards 0.5% ammonia gas for type I and type II

	Type I	Type II
Concentration of GNR	Variation (%)	Variation (%)
Maximum	1.01	2.12
High	2.81	2.18
Middle	4.61	2.23
Low	4.77	3.44

Sensitivity Test

GNR with maximum concentrations for type I and type II were used to further the experiment on sensitivity test. The sensing part was stabilised before gassing. Ammonia gas with 0.25%, 0.5%, 0.75% and 1% concentrations respectively were gassed into the chamber alternately with air in between. The sensing element sensitivity in this experiment is measured and expressed:

$$Sensitivity (\%) = \frac{R_g - R_o}{R_o} \cdot 100 \tag{4}$$

where R_g and R_o are the resistance of GNR exposed to ammonia gas and air respectively.

RESULT AND DISCUSSION

Repeatability Test

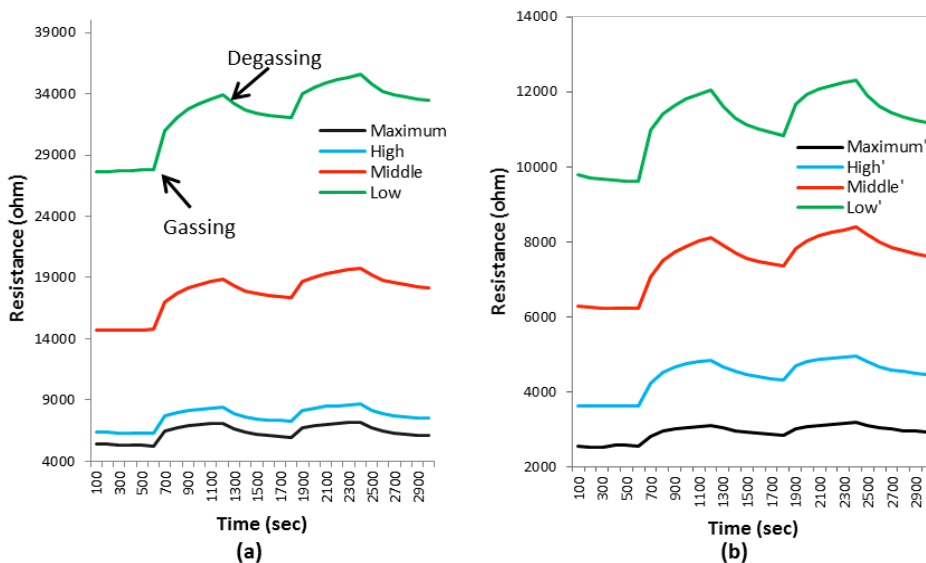


Figure 2. Response of ammonia gas on sensing part (a) Type I (b) Type II

Responses for the repeatability test were shown in Figure 2. Adsorption of ammonia gas on the GNR surface will alter the conductivity of the GNR. Significant changes can be observed from the response of the sensor. Resistance of the GNR increased when ammonia gas is introduced to the sensing element.

The resistance of the GNR was obtained by measuring the current change with constant voltage supply of 1.5V throughout the experiment. The response of GNR towards ammonia can be explained based on the chemical adsorption between sensing element and the targeted gas. Ammonia gas tends to be a donor of electron (Yunusa et al. 2015). Resistance of the GNR increased due to the space charge region on the surface. This region appears due to the donating electrons which eventually depletes the holes and increases the distance between the conduction band and valence band.

Repeatability test on GNR could be observed through the injection of 0.5% of ammonia gas. Variation of each concentration of GNR is shown in Table 2. Variation of the response increased for the Low concentration of GNR. Maximum concentration of GNR shows lowest variation (type I: 1.01% and type II: 2.12%) which means the response for the second gassing session has little changes compared with the first gassing session (higher consistency).

Sensitivity Test

The same sample of GNR with maximum concentration from repeatability test was used for sensitivity test. Responses from type I and type II with maximum concentration of GNR exposed to different concentration of ammonia gas are shown in Figure 3. Ammonia with concentration of 0.25%, 0.50%, 0.75%, and 1.00% respectively were injected and the response is recorded. The experiment is carried out at room temperature and with the supply of 1.5V throughout the experiment. These have satisfied the aim of target for sensors: response at room temperature and low power consumption (Giselle et al., 2007).

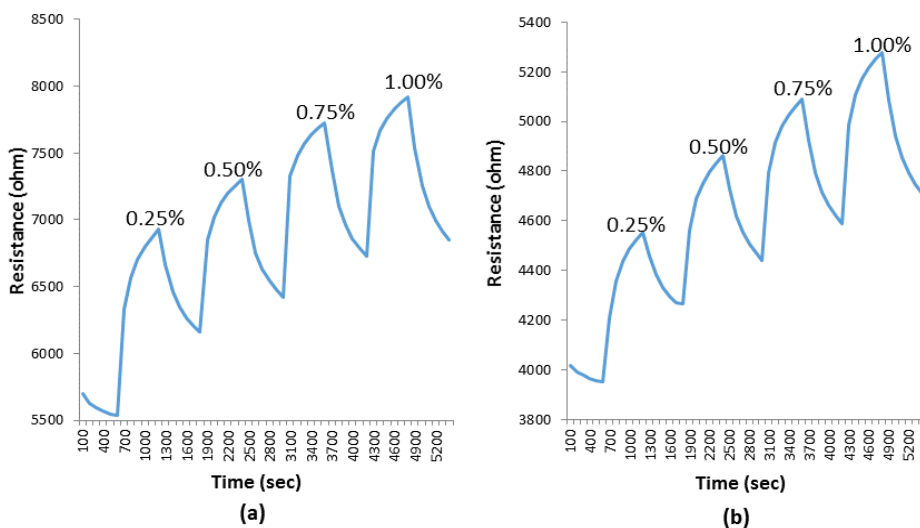


Figure 3. Response of GNR maximum (a) Type I (b) Type II on variation of ammonia concentration

Table 3 shows the reaction time and sensitivity for type I and type II in sensitivity test. Sensitivity of type I is higher than type II. Larger surface area caused larger surface of GNR exposed to ammonia gas; hence, higher sensitivity and lower reaction time for type I compared with type II. Reaction time refers to the time taken for the GNR response during injection of ammonia gas.

Table 3
Reaction time and sensitivity of sensing part with different ammonia concentration

Concentration of NH ₃ (%)	Reaction Time (sec)		Sensitivity (%)	
	Type I	Type II	Type I	Type II
0.25	22	28	25.21	15.27
0.50	20	23	32.03	23.15
0.75	15	20	39.61	28.87
1.00	13	16	43.12	33.64

CONCLUSION

Ammonia gas sensor with GNR as sensing element shows good responses at room temperature. Sensing elements with surface area of 4cm² and 1cm² were studied. Repeatability test using 0.5% ammonia gas were tested on all type I and type II GNR. Maximum concentration of GNR shows least variation when exposed to ammonia at room temperature with the value of 1.01% and 2.12% for type I and type II respectively. Maximum concentration of GNR shows highest consistency compared with lower concentration of GNR. Sensitivity tests were performed on GNR with maximum concentration. An experiment was carried out by injecting variation of ammonia gas with concentration of 0.25% to 1.00%. The sensitivity of GNR towards ammonia increased as concentration of ammonia increased. Type I which has a bigger area, 4cm², shows higher sensitivity compared with type II with an area of 1cm². Time for GNR to react with ammonia gas decreased as the concentration of ammonia increased. Larger surface area of sensing element required lesser reaction time. Graphene with excellent electrical properties have shown responses with 1.5V of supply throughout the experiment.

ACKNOWLEDGEMENT

The author acknowledges the financial support of Look East Policy Programme (Project No. UPM/ITMA/TP/6300172-13501) and Kyushu Institute of Technology, Graduate School of Life Science and Systems Engineering, Department of Human Intelligence Systems for the GNR.

REFERENCES

- Chen, R., Ruan, X., Liu, W., & Stefanini, C. (2014). A reliable and fast hydrogen gas leakage detector based on irreversible cracking of decorated palladium nanolayer upon aligned polymer fibers. *International Journal of Hydrogen Energy*, 40, 746-751.

- Giselle, J. C., Riu, J., & Rius, F. X. (2007). Gas sensors based on nanostructured materials. *The Royal Society of Chemistry Analyst*, 132, 1083-1099.
- Huang, X., Hu, N., Gao, R., Yu, Y., Wang, Y., Yang, Z., ... & Zhang, Y. (2012). Reduced graphene oxide-polyaniline hybrid: Preparation, characterization and its applications for ammonia gas sensing. *Journal of Materials Chemistry*, 22, 22488-22495.
- Sharma, S., & Madou, M. (2016). A new approach to gas sensing with nanotechnology. *Philosophical Transactions of the Royal Society A*, 370, 2448-2473.
- Somov, A., Karpov, E. F., Karpova, E., Suchkov, A., Mironov, S., Karelin, A., Baranov, A., & Spirjakin, D. (2015). Compact low power wireless gas sensor node with thermo compensation for ubiquitous deployment. *IEEE Transactions on Industrial Informatics*, 11(6), 1660-1670.
- Lai, Y. T., Kuo, J. C., & Yang, Y. J. (2013). A novel gas sensor using polymer- dispersed liquid crystal doped with carbon nanotubes. *Sensors and Actuators A*, 215, 83-88.
- Tanaka, H., Arima, R., Fukumori, M., Tanaka, D., Negishi, R., Kobayashi, Y., ... & Ogawa, T. (2015). Method for controlling electrical properties of single-layer graphene nanoribbons via adsorbed planar molecular nanoparticles. *Scientific Reports*, 5(12341), 1-10.
- Wang, Y., Chyu, M. K., & Wang, Q. M. (2014). Passive wireless surface acoustic wave CO₂ sensor with carbon nanotube nanocomposite as an interface layer. *Sensors and Actuators A*, 220, 34-44.
- Wu, Z., Chen, X., Zhu, S., Zhou, Z., Yao, Y., Quan, W., & Liu, B. (2013). Enhanced sensitivity of ammonia sensor using graphene/ polyaniline nanocomposite. *Sensors and Actuators B*, 178, 485-493.
- Yunusa, Z., Hamidon, M. N., & Ismail, A. (2015). Development of a hydrogen gas sensor using a double SAW resonator system at room temperature. *Sensors*, 15, 4749-4765.





Transformer Incipient Fault Identification Using Depolarisation Current Ratio Index Analysis Technique

Mohd Aizam Talib^{1*}, Nor Asiah Muhamad² and Zulkurnain Abdul Malek³

¹TNB Research, No 1 Jalan Air Itam 43000 Bangi, Kajang, Selangor

²School of Electrical and Electronic Engineering, Universiti Sains Malaysia, 14300, Nibong Tebal, Pulau Pinang

³Institute of High Voltage and High Current, Faculty of Electrical Engineering, Universiti Teknologi Malaysia, Jalan Skudai, 81310 Johor

ABSTRACT

Preventive tests and diagnosis of in-service power transformer are important for early fault prediction and increased reliability of electricity supply. However, some existing diagnostic techniques require transformer outage before the measurement can be performed and need expert knowledge and experiences to interpret the measurement results. Other measurement techniques such as chemical analyses of insulating oil may cause significant variance to measurement results due to different practices in oil sampling, storage, handling and transportation of oil. A cost-effective measuring technique, which is simple, providing fast and an accurate measurement results, is therefore highly required. The extended application of Polarisation and Depolarisation (PDC) measurement for characterisation of different faults conditions in-service power transformer has been presented in this paper. Earlier studies on polarisation and depolarisation current of oil samples from in-service power transformer shows that depolarisation has provided significant information about the change of material properties due to faults in power transformer. In this paper, a new approach based on Depolarisation Current Ratio Index (DRI) was developed for identifying and classifying different transformer fault conditions. The DRI at time interval of 4s to 100s was analysed and the results show that DRI of depolarisation current between 5/100s and 10/100s provides higher correlation on the incipient faults in power transformer.

Keywords: Transformer, fault analysis, depolarisation current, ratio index analysis

ARTICLE INFO

Article history:

Received: 24 August 2016

Accepted: 03 Jun 2017

E-mail addresses:

mohdaizam@tnbr.com.my (Mohd Aizam Talib),

norasiah.m@usm.my (Nor Asiah Muhamad),

zulkurnain@utm.my (Zulkurnain Abdul Malek)

*Corresponding Author

INTRODUCTION

Demands for non-invasive or non-destructive testing techniques for diagnosing and assessing the condition of transformer insulation system have increased in recent years. The need for better and improved diagnostic methods is required due to the

rapidly ageing transformer population in the electrical network and the pressure of power utility to reduce operation and maintenance cost and prolong the assets' life (Lapworth et al., 1995; Schwarz & Muhr, 2008).

The well-established electrical and chemical diagnostic testing methods have been used to assess the condition of transformers due to different fault and ageing mechanisms. The presence of moisture in insulation system can be determined by dielectric dissipation factor (DDF) and insulation resistance (IR) measurement; the mechanical integrity of winding and core clamping structure due to short circuit forces can be confirmed by Frequency Response Analysis (FRA) and the problems with bad joints or connections are identified through winding resistance measurement (Wang et al., 2002; Borsi & Gockenbach; 2007). The changes in properties of insulating oil and its degree of deterioration, on the other hand can be discovered through chemical diagnostic analysis (Gradnik, 2002). In addition, decomposition of the hydrocarbon chain caused by thermal and electrical faults will liberate small quantities of gases which can be classified and quantified by means of Dissolved Gases Analysis (DGA) (Duval & DePablo, 2001; Sherif et al., 2012).

An advanced dielectric response in frequency and time domain have gained immense popularity as supplements to the existing insulation assessment techniques, and more recently, polarisation and depolarisation current (PDC) measurement has been used to estimate the moisture content and ageing of insulation system (Küchler et al., 2003) as a result of decomposition of insulation structure.

In addition, this will change the material properties which likely will change the material conductivity level as well as its charging and discharging current response behaviour. Initial research has been done by Muhamad et al. (2013) and Talib et al. (2013, 2014) on the effect of faults to dielectric response in time domain. PDC measurement on oil insulation that had experienced overheating and arcing faults showed higher polarisation and depolarisation current. Bhumiwat (2004, 2013) and Jun-Hao et al. (2008) found overheating in transformer is identified by the curved shape of depolarisation current.

The authors of this paper have investigated and analysed the effect of different faults in power transformer on polarisation current and depolarisation current spectrum of the insulating oil (Talib et al., 2015). In this paper, a new method of analysing the depolarisation current using ratio index was introduced for detecting incipient fault in power transformers.

EXPERIMENTAL MEASUREMENTS

This section describes the experimental set-up and measurement of polarisation and depolarisation current (PDC) of oil samples.

Measurement Set-Up

The polarisation and depolarisation currents are measured using the commercial PDC Analyser-IMOD Alff Engineering Switzerland, which can supply the excitation voltage up to 2kV DC and measure the dielectric response in time domain up to 10000s. The analyser is then connected

to the test cell with electrode gap of 1.5mm and capacitance of 60pF. Two electrodes circuit are used, one for application of the test voltage and the other is for current measurement. The amount of insulating liquid required for the measurement is about 210ml. Figure 1 shows the measurement set-up used in the laboratory experimental works. All the measurements are carried out at 1000V and 10,000s both for polarisation and depolarisation time.

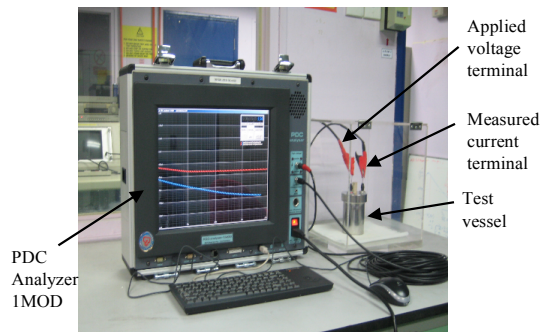


Figure 1. Experimental measurement set-up [16]

Measurement Procedure

An oil sample was taken from in-service transformers and tested for its condition using Dissolved Gases Analysis (DGA). The test samples were classified into four conditions: normal, partial discharge, overheating and arcing. The charging and discharging current of the oil samples were determined by polarisation and depolarisation current measurement. For every condition, at least 10 transformers with rated voltage of 33/11kV were selected which cover the capacity of 15MVA to 30MVA. In addition, three oil samples were taken on every transformer and the testing was repeated five times for each oil samples to ensure consistency of the results.

Before the excitation voltage is applied to the test sample, the oil will be discharged initially for 500s to minimise the effect of residual charges on measurement results. In addition, to reduce the effect of noise on polarisation and depolarisation current, all the measurements were conducted in the shielded case. Figure 2 shows the flow chart of experimental works.

TRANSFORMER INCIPIENT FAULT ANALYSIS USING DEPOLARISATION RATIO INDEX (DRI)

The analysis of both polarisation and depolarisation current has shown that different fault conditions have changed the property of oil insulation and affect the initial duration of measured current. Figure 3 (a) and (b) shows the average measured polarisation and depolarisation current.

It can be seen that polarisation and depolarisation current starts to stabilise and saturate almost after 100s of being charged and discharged. The oil with normal condition has the lowest

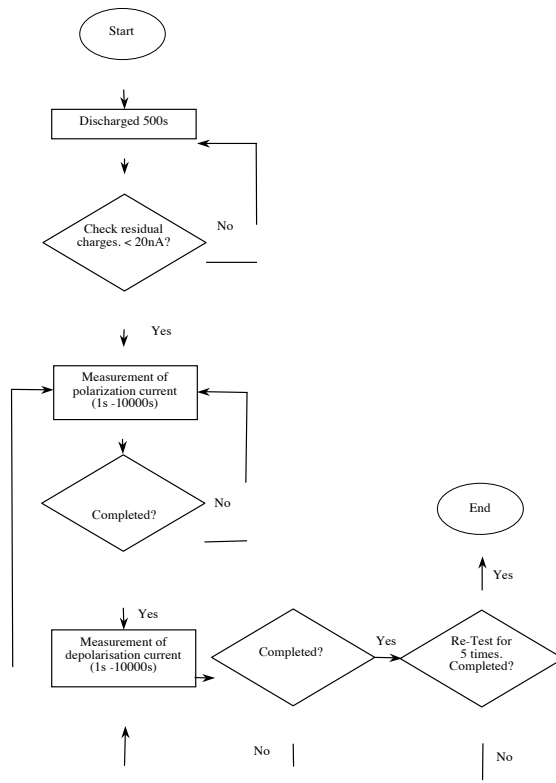
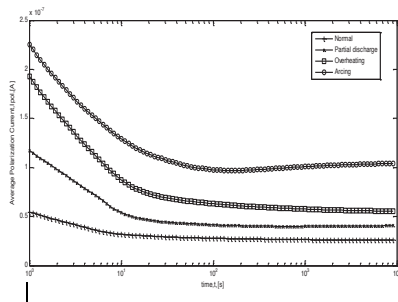
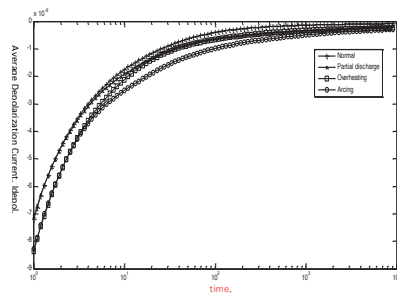


Figure 2. Flow chart of experimental works



(a) polarisation current



(b) depolarisation current

Figure 3. Polarisation and depolarisation current of transformer with different conditions

magnitude current and the values were progressively higher on oil sample with partial discharge, overheating and arcing fault conditions. The high measured current of oil samples with fault conditions can be attributed to the fact that faulty power transformers cause breakdown of

hydrocarbon structures of oil, thus, leading to higher charge carrier mobility and high current magnitude when any external electric field is applied (Houhanessian & Zaengl, 1996).

Talib et al. (2015) using Artificial Neural Network (ANN) demonstrated that depolarisation current has better accuracy in identifying incipient fault in power transformers and the current pattern at duration of 4s to 100s was found to have deviated differently between normal, partial discharge, overheating and arcing fault of oil samples as illustrated in Figure 4.

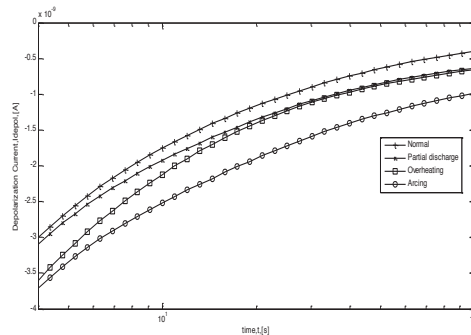


Figure 4. Depolarisation current pattern of oil samples at duration of 4s to 100s

On the other hand, the incipient fault in the transformer can be further analysed by determining the steepness of each of the current pattern to denote the changes in depolarisation current. In this research, a single unique numerical dimensionless quantity known as Depolarisation Ratio Index (DRI) was proposed to characterise different faults in power transformers.

Depolarisation current is continuously decreased and after 100s, the currents reach its steady condition and almost zero current is finally recorded. Thus, depolarisation current at 100s can be used as denominator of the dimensionless variable.

Meanwhile, the numerator of the dimensionless variable of depolarisation current is initially selected from the period of 5s to 40s and was analysed for every 5s interval. The Depolarisation Ratio Index (DRI) on every sample is then calculated using (1) and a detailed analysis is made on the respective DRI interval that gives the highest correlation.

$$DRI = \frac{\text{Depolarisation Current at } n^{\text{th}}}{\text{Depolarisation Current at } 100} \quad (1)$$

RESULTS AND DISCUSSION

The DRI of dimensionless variables between 5s to 40s intervals and its correlation with different transformer conditions are shown in Table 1. The correlation is determined based on number of transformers that the calculated DRI is within the range and consistent with the condition identified from Dissolved Gases Analysis.

Table 1
Results of DRI between 5s to 40s interval for transformer with normal, partial discharge, overheating and arcing condition

Transformer Condition	Dimensionless Variable	DRI	% Correlation
Normal	5s/100s	>6.305	91.62%
	10s/100s	>4.463	66.67%
	15s/100s	>3.657	25.00%
	20s/100s	>2.958	25.00%
	25s/100s	>2.637	16.67%
	30s/100s	>2.345	25.00%
	35s/100s	>2.066	16.67%
	40s/100s	>1.935	16.67%
Partial Discharge	5s/100s	6.052<x<6.305	25.00%
	10s/100s	4.015<x<4.463	25.00%
	15s/100s	2.239<x<3.657	37.50%
	20s/100s	1.845<x<2.958	37.50%
	25s/100s	1.682<x<2.637	37.50%
	30s/100s	1.541<x<2.345	37.50%
	35s/100s	1.419<x<2.066	37.50%
	40s/100s	1.365<x<1.935	37.50%
Overheating	5s/100s	5.644<x<6.052	72.72%
	10s/100s	3.784<x<4.015	72.72%
	15s/100s	2.136<x<2.239	63.63%
	20s/100s	1.757<x<1.845	81.81%
	25s/100s	1.607<x<1.682	63.63%
	30s/100s	1.481<x<1.541	63.63%
	35s/100s	1.373<x<1.419	27.27%
	40s/100s	1.327<x<1.365	45.45%
Arcing	5s/100s	2.846<x<3.564	66.67%
	10s/100s	2.223<x<2.612	58.33%
	15s/100s	1.945<x<2.136	25.00%
	20s/100s	1.688<x<1.757	16.67%
	25s/100s	1.571<x<1.607	25.00%
	30s/100s	1.466<x<1.481	16.67%
	35s/100s	1.371<x<1.373	33.33%
	40s/100s	1.327<x<1.365	16.67%

The longer time interval selected as the dimensionless variable, the higher the DRI calculation compared with the shorter time interval as depolarisation current at lower time response is higher and slowly diminishes at the end of completion of discharging process.

The DRI of 5/100s and 10/100s has higher correlation and percentage correlation calculated for normal condition is 91.62% and 66.67%. The overheating fault has correlation of 72.72% for both variables and arcing fault was 66.67% and 58.33% respectively. However, it can be seen that the DRI of 20/100s for overheating fault has higher correlation with calculated value

of 81.81%. On the other hand, it is observed that partial discharge fault has low correlation with only 25% accuracy calculated for both variables. Multiple faults in the test samples is one of the possible reasons that contributed to the difficulty in differentiating the partial discharge fault using the DRI.

Meanwhile, DRI for the dimensionless variable of 15/100s, 20/100s, 25/100s, 30/100s, 35/100s and 40/100s was found to have lower correlation with less than 50% accuracy. This can be explained by the fact that the changes in depolarisation current are relatively small at higher time response as the current has been fully discharged.

The result demonstrated that the time interval of depolarisation current between 5/100s and 10/100s provide significant information on the incipient faults in power transformer as the percentage of correlation calculated is more than 50% accurate.

CONCLUSIONS

In this paper, changes of depolarisation current pattern of different transformer conditions was further analysed by Depolarisation Ratio Index (DRI) technique. The dimensionless quantity at time interval of 4s to 100s was analysed and it is found that DRI of depolarisation current between 5/100s and 10/100s provide higher correlation on the incipient faults in power transformer especially the units with normal, overheating and arcing condition.

The result demonstrated that DRI analysis technique of depolarisation current is feasible as diagnostic indicator for incipient fault analysis and immediate action can be taken at an early stage to prevent outage of power transformers.

ACKNOWLEDGEMENTS

The authors would like to acknowledge the support of TNB and Malaysia Ministry of Higher Education, Universiti Teknologi Malaysia (Vot 10H16 and 4F515) for technical and financial support.

REFERENCES

- Bhumiwat, S. A. (2004). The latest on-site non-destructive technique for insulation analysis of electrical power apparatus. In *Proceedings of Weidman ACTI Annual Technical Conference* (pp. 1-8).
- Bhumiwat, S. A. (2013, June). Identification of overheating in transformer solid insulation by Polarization Depolarization Current analysis. In *2013 IEEE Electrical Insulation Conference (EIC)* (pp. 449-453). IEEE.
- Duval, M. (2001). Interpretation of gas-in-oil analysis using new IEC publication 60599 and IEC TC 10 databases. *IEEE Electrical Insulation Magazine*, 17(2), 31-41.
- Ghoneim, S. S., & Ward, S. A. (2012). Dissolved Gas Analysis as a Diagnostic Tools for Early Detection of Transformer Faults. *Advances in Electrical Engineering Systems (AEES)*, 1(3), 152-156.
- Gradnik, M. K. (2002). Physical-chemical oil tests, monitoring and diagnostics of oil-filled transformers. In *Dielectric Liquids, 2002. ICDL 2002. In Proceedings of 2002 IEEE 14th International Conference* (pp. 242-247). IEEE.

- H. Borsi, E. Gockenbach (2007). Monitoring, Diagnosis and Life Management of Power Transformer. *TechCon Asia-Pacific Conference*.
- Houhanessian, V. D., & Zaengl, W. S. (1996, June). Time domain measurements of dielectric response in oil-paper insulation systems. In *Conference Record of the 1996 IEEE International Symposium on Electrical Insulation* (Vol. 1, pp. 47-52). IEEE.
- Jun-Hao, L., Wen-Rong, S., Hai-Tao, B. I., Peng, Y., & Yan-Ming, L. (2008, June). PDC and PD pulse burst characteristics in differently aged transformer oils. In *International Symposium on Electrical Insulation, 2008. ISEI 2008. Conference Record of the 2008 IEEE* (pp. 343-346). IEEE.
- Küchler, A., Leibfried, T., Breitenbach, B., Alff, J. J., Houhanessian, V. D., & Zaengl, W. S. (2003, September). Transformer Insulation Diagnosis by Polarization and Depolarization Current Analysis. In *48 International Wissenschaftliches Colloquium Techniscahe Universitat Ilmenau* (pp. 161-167).
- Lapworth, J. A., Jarman, P. N., & Funnell, I. R. (1995, March). Condition assessment techniques for large power transformers. In *Second International Conference on the Reliability of Transmission and Distribution Equipment, 1995*. (pp. 85-90). IET.
- Muhamad, N. A., Suleiman, A. A., Phung, B. T., & Blackburn, T. R. (2013). Faults identification of biodegradable oil-filled transformers based on polarization and depolarization current measurement (PDC) method. *IEEE Transactions on Dielectrics and Electrical Insulation*, 20(6), 2299-2306.
- Schwarz, R., & Muhr, M. (2008, April). Diagnostic methods for transformers. In *International Conference on Condition Monitoring and Diagnosis, 2008. CMD 2008*. (pp. 974-977). IEEE.
- Talib, M. A., Muhamad, N. A., & Malek, Z. A. (2015, July). Fault classification in power transformer using polarization depolarization current analysis. In *2015 IEEE 11th International Conference on the Properties and Applications of Dielectric Materials (ICPADM)* (pp. 983-986). IEEE.
- Talib, M. A., Muhamad, N. A., Malek, Z. A., & Ghazali, A. (2014, March). Changes of PDC measurement pattern on services mineral oil filled power transformer after experienced faults. In *Power Engineering and Optimization Conference (PEOCO), 2014 IEEE 8th International* (pp. 291-296). IEEE.
- Talib, M. A., Muhamad, N. A., Malek, Z. A., & Jamail, N. A. M. (2013, October). Application of PDC analysis to identify effect of overheating on dielectric response and conductivity of mineral insulating oil of in-services transformers. In *2013 Annual Report Conference on Electrical Insulation and Dielectric Phenomena* (pp. 583-586). IEEE.
- Wang, M., Vandermaar, A. J., & Srivastava, K. D. (2002). Review of condition assessment of power transformers in service. *IEEE Electrical Insulation Magazine*, 18(6), 12-25.

Tuberculosis Bacteria Counting Using Watershed Segmentation Technique

M. K. Hassan^{1,2*}, N. F. H. Eko¹ and S. Shafie^{1,2}

¹*Department of Electrical and Electronics, Faculty of Engineering, Universiti Putra Malaysia, 43400 UPM, Serdang, Selangor, Malaysia*

²*Institute of Advanced Technology, Universiti Putra Malaysia, 43400 UPM, Serdang, Selangor, Malaysia*

ABSTRACT

Tuberculosis (TB) is the second biggest killer disease after HIV. Therefore, early detection is vital to prevent its outbreak. This paper looked at an automated TB bacteria counting using Image Processing technique and Matlab Graphical User Interface (GUI) for analysing the results. The image processing algorithms used in this project involved Image Acquisition, Image Pre-processing and Image Segmentation. In order to separate any overlap between the TB bacteria, Watershed Segmentation techniques was proposed and implemented. There are two techniques in Watershed Segmentation which is Watershed Distance Transform Segmentation and Marker Based Watershed Segmentation. Marker Based Watershed Segmentation had 81.08 % accuracy compared with Distance Transform with an accuracy of 59.06%. These accuracies were benchmarked with manual inspection. It was observed that Distance Transform Watershed Segmentation has disadvantages over segmentation and produce inaccurate results. Automatic counting of TB bacteria algorithms have also been proven to be less time consuming, contains less human error and consumes less man-power.

Keywords: Automated bacteria counting, Image Processing, Watershed Segmentation, Graphical User Interface

ARTICLE INFO

Article history:

Received: 24 August 2016

Accepted: 03 Jun 2017

E-mail addresses:

khair@upm.edu.my (M. K. Hassan),

farahhidayah3272@gmail.com (N. F. H. Eko),

suhaidi@upm.edu.my (S. Shafie)

*Corresponding Author

INTRODUCTION

Tuberculosis (TB) is a disease caused by bacteria. There is evidence of its existence in the Americas since Pre-Columbian times. Signs of this disease was discovered in the preserved spines of Egyptian mummies as described by Allaoui (2012). The TB is now the second biggest killer disease after HIV/AIDS with an estimation of 9.4 million new cases and 1.68 million deaths recorded by the World Health Organization in 2010 (Sandy,

2015). The TB disease is caused by the mycobacterium tuberculosis bacteria, which is a member of mycobacteriaceae family and actinomycetales ordo (Rachna & Mallikarjuna, 2013). The bacteria can infect and attack any part of the organs such as kidney, heart, liver, bones, brain and other but it predominantly affects the lungs especially those who have a weak body. Fortunately, with the development of modern technologies and proper treatments, TB disease is curable. The number of TB patients who have been successfully treated especially in United States has been increasing since 1993 (Ibnu et al., 2012; Daniel, 2006).

Researchers have come up with various techniques to examine TB bacteria. The latest technology uses microscope imaging to count TB bacteria. Acid-fast bacillus stain (AFB) or sputum stain test is performed on the sputum sample taken from the patients' lung (Daniel, 2006; Kauleshwar et al., 2013). This test determines whether the patients have positive or negative TB infection. These staining dye process provides good contrast between the bacilli bacteria and the background, thus, improving detection. The image of the bacteria will be captured using camera to be viewed through computer screen (Rachna & Mallikarjuna, 2013). With the help of computer-aided system such as MATLAB software, the image of TB disease can be further processed and diagnosed. In order to perform an automated counting of TB bacilli in the image, some processing algorithms have been introduced such as Image Acquisition techniques, Image Pre-processing techniques, Image Segmentation techniques and others. In Image Processing, segmentation technique is the most important stage. There are two approaches that can be applied in segmentation, which are the frontier approaches and region approaches. Watershed segmentation combines both the approaches (Uppal & Raman, 2012). Thus, it results in rapid detection of both edges and regions. Matrix Laboratory, also known as MATLAB, is a high-level language, which is widely used by engineers and scientist all over the world (Allaoui, 2012). Generally, it has been used extensively in mathematics, engineering and science. In addition, it covers all varieties of fields such as signal and image processing, control system, communication and many more. Another component in MATLAB is Graphical User Interface (GUI) in which the user is allowed to interact with the system using graphical icon and visual indicators (Raof et al. 2011). It is also user-friendly.

In this research, images of the stained sputum were processed and diagnosed. The sample images of TB bacteria were obtained from the Pathology Department of Hospital Serdang, Selangor where they were detected using microscope and captured using digital camera. The counting was done using the proposed algorithm of Watershed Segmentation techniques via Image Processing Toolbox MATLAB in software. The image is displayed through GUI for the ease of the user. The advantages of using watershed segmentation are: it reduces human error, consumes less man-power and saves time compared with manual TB diagnosis (Ibnu et al., 2012).

METHODOLOGY

General Algorithm of Image Counting Using MATLAB

Figure 1 shows block diagram of algorithm used for Image Counting in this research. These algorithms consist of Image Acquisition, Image Pre-Processing and Image Segmentation.

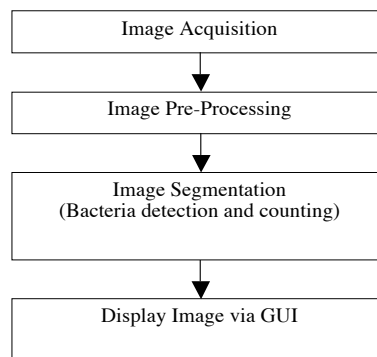


Figure 1. Block Diagram of the Algorithm used for Bacteria Counting using MATLAB

Image Acquisition. In the Image Acquisition, the stained-sputum sample image that consists of TB bacteria was obtained from Pathology Department of Hospital Serdang, Selangor. The stained-sputum images were captured through the microscope and read as input to the MATLAB software for analysis. The image must be in specific format such as JPG, JPEG, PNG, BMT (Steve, 2010).

Image Pre-Processing. There are several steps in the image pre-processing stage. In order to eliminate any unwanted objects, Image Pre-Processing is performed on the input image before the segmentation stage. The technique consists of reading an image, applying the colour thresholding segmentation before converting it into greyscale colour, enhancing the contrast of the greyscale image, and binarisation. The processed image is now ready for Image Segmentation. (Rachna & Mallikarjuna, 2013).

Image Segmentation. Image Segmentation is aimed at identifying and differentiating between the bacteria with the background image so that the former can be detected and counted (Allaoui, 2012). The segmentation process is the process of decomposing an image into sub-images of individual character. The segmentation will only stop when unwanted objects have been eliminated. In this project, two techniques of Watershed Segmentation had been applied and compared in order to separate and count overall amount of bacteria including any overlap between the bacteria that existed in the sample of images. To avoid any over segmentation, morphology segmentation was implemented before Watershed Segmentation.

Watershed Segmentation. In the acquired image, overlapping always happen. These overlapping bacteria need to be separated in order to ensure a high degree of accuracy in counting. Therefore, Watershed Segmentation was implemented to solve the problem. It can define the border between two regions which has been set up by the morphology segmentation (Kauleshwar et al., 2013). In this research, two methods involving Watershed Segmentation was used and the results verified. The first technique directly uses Watershed Segmentation on the image, also known as Watershed Distance Transform Segmentation method. Distance transform of a binary image is the distance from every pixel to the nearest non-zero valued

pixel (Pedro & Daniel, 2012). The second method, Marker Based Watershed Segmentation, limits the number of regions by using the internal markers to specify the object of interest. On the other hand, the external marker is those pixels, which belongs to the background. Each region that is being segmented consists of external markers and single internal marker. All of these markers result in the separation between the overlapped bacteria and avoid over segmentation from happening (Parvati et al., 2008).

Process in detecting and counting of bacteria. The shape of the TB bacteria is almost similar to the ellipse. By applying the parametric form of the ellipse equation, the outline of the ellipse is plotted over each of the segmented edge of TB bacteria object in the sample of images. In addition, by using 'region props' function in Image Processing Toolbox, the regions such as major axis length, minor axis length and centroids for each of the detected bacteria can be measured and finally detected and counted.

RESULTS AND DISCUSSION

Figure 2(a) shows TB bacteria sample images obtained from the Pathology Department of Hospital Serdang, which are processed using the Image Processing algorithm using Watershed Segmentation, the Distance Transform and Marker Based method. This image was read as an input and displayed via the GUI on computer screen. The TB bacteria are shown in red colour pixels while the non-TB bacteria are shown other colour pixels such as blue, green and so on. Meanwhile, Figure 2(b) shows the implementation of colour thresholding segmentation on the sample image in Figure 2(a). The red colour pixel which represents the TB bacteria had increased rapidly overtaking the other colour pixels. Hence, this is a good method to detect TB bacteria. Next, the red colour was extracted from the background while the other colours were rejected to background.

Figure 2(c) shows the conversion of the Figure 2(b) into the greyscale colour so that the hue and saturation information of the RGB image can be eliminated while retaining the luminance of the image. The greyscale colour shown in Figure 2(c) is the extracted red pixels which is the TB bacteria together with some noises (unwanted objects). All of the noises will be further eliminated in the segmentation process. Figure 2(d) shows the binary image of TB bacteria sample image. The previous image need to be converted into the binary pixel image first before proceeding into segmentation. This is because some segmentation techniques only processed the image in binary pixel format. As illustrated in Figure 2(d), the white colour or also known as pixel 1 is the TB bacteria while the black colour which is pixel 0 is the unwanted object that had been rejected into the background. Figure 2(d) needs more filtration process in order to eliminate the existing noises. Figure 2(e) illustrates the edges of all the TB bacteria that had been detected by using Sobel Edge Detection. All complete connecting of pixel 1 is counted as 1 bacteria. Figure 2(f) displays the image after applying Gaussian filter and morphological segmentation.

From Figure 2(a) - (e), it can be noticed that the image consists of the TB bacteria and non-TB bacteria (noises). Gaussian filter was used to remove some of the unwanted noises. In order to totally remove the unwanted noises, morphology segmentation techniques had been

added together with the Gaussian filter. Morphology Segmentation techniques that has been used in this research is the erosion followed by dilation techniques. As a result, the image consists only TB bacteria and free from all noises. Furthermore, Watershed Segmentation is needed in order to recognise and separate any overlap that occurs between the TB bacteria. Figure 2(g) shows the image after applying the Watershed Distance Transform Segmentation Method. Figure 2 (h) is the image after it has undergone Marker Based Watershed Segmentation Method. It can be observed that the total amount of TB bacteria in the images is based on the total colour present in the images. Any overlap between the bacteria had been separated and filled by colour. Figure 2(i) and (j) view the same sample images that had been processed by using two different methods. Figure 2(i) shows the detected TB bacteria by using Watershed Distance Transform Segmentation Method. On the other hand, Figure 2(j) shows the TB bacteria detection by using Marker Based Watershed Segmentation Method. The red colour ellipse line in Figure 2(i) and (j) show the eclipse shape of detected TB bacteria that had been separated (if any overlap existed). By comparing both of the images, Figure 2(i) and (j), different amount of TB had been detected. Figure 2(i) shows 46 TB bacteria had been detected and for Figure 2(j), only 45 TB bacteria had been detected in the sample of images. The blue inside the red eclipse line is the centroid of detected TB bacteria. The manual inspection for this sample of images show that total amount of 42 bacteria. Moreover, the exact length of minor axis and major axis of the eclipse shape of TB bacteria can be known and calculated. Additionally, the exact location of X-centroid and Y centroid for each of the bacteria in the image can be located.

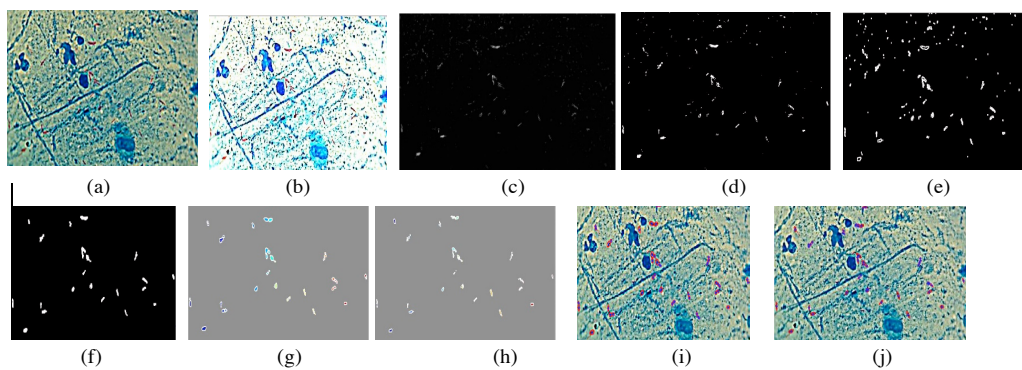


Figure 2. TB bacteria sample images

Many sample images were obtained from Pathology Department of the Hospital Serdang. However,, most of the sample images have different light intensity and result in different pixel values. Hence, the value of RGB adjustment must be different for each of the sample images. To gain images with similar light intensity, the camera distance and light intensity must be controlled. In addition, auto gain control function must be disabled. Table 1 shows seven different sample images of TB bacteria with almost similar light intensity and were used in this research. By analysing Table 1, total amount of TB bacteria that is counted by the Marker Based Segmentation method is more accurate with the average percentage of 81.08

%. Meanwhile, the accuracy of Distance Transform Watershed Segmentation only achieved an average percentage of 59.06 %. All of the percentage accuracies were benchmarked with manual inspection that had been done in Hospital Serdang.

Table 1
Comparison between automated counting and manual counting

Image	Manual Count	Automated Count			
		Distance Transform Segmentation Method	Percentage Accuracy (%)	Marker Based Segmentation Method	Percentage Accuracy (%)
A	1	4	25.0	1	100.0
B	2	4	50.0	2	100.0
C	42	46	91.3	45	93.3
D	1	2	50.0	1	100.0
E	9	10	90.0	10	90.0
F	4	8	50.0	1	25.0
G	14	8	57.1	9	64.3
Average Percentage (%)		59.06		81.80	

Figure 3 shows a comparison between manual counting (blue lines) and automatic counting using Distance Transform Watershed Segmentation (red line) and Marker Based Segmentation method (green line). The graph shows that the counting value that used Marker Based Segmentation method is closer to the manual counting than the counting value that applied Distance Transform Watershed Segmentation method.

The reason behind the lack of accuracy in Distance Transform Watershed Segmentation method is because of over segmentation . This method is very sensitive to any local minimum in the image. It tends to detect the lines of the watershed transform where each local minimum gives rise to a region. Hence, false objects can be detected. The worst can happen when it separates the connected pixel and leads to the wrong counting process. To overcome this

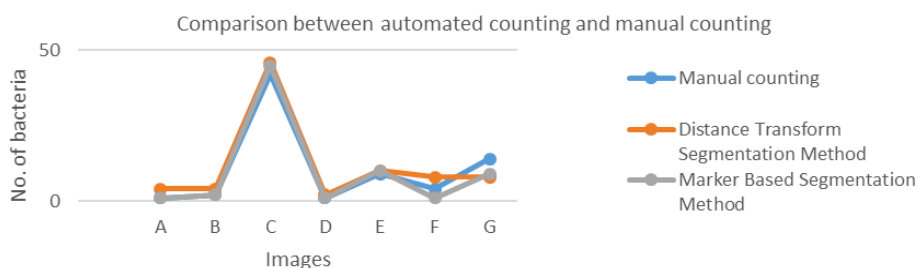


Figure 3. Graph in comparing both, manual counting and automatic counting using Watershed Segmentation

problem, the number of minima should be reduced and calculation of too many regions should be avoided. Marker Based Watershed Segmentation can be applied in order to reduce the number of regional minima together in solving the over segmentation problem. To increase the accuracy of the segmentation, the contrast of greyscale image needs to be enhanced before proceeding to the Image Segmentation technique. There are some advantages of automatic counting compared with the manual counting as the latter has several weaknesses which can be tackled through automatic counting. The list of weaknesses can be described as follow:

a. Counting Time per slide of TB Bacteria

The manual counting time is around 10-15 minutes per slide. On the other hand, automatic counting is done between one and three 1-3 minutes.

b. Human error

Human error is common in manual counting. It has to be counted three times in order to validate the count. The first count usually always suffers from over count or under count. On the contrary, automatic counting of bacteria that had been validated can reduce any errors.

c. Man power

In manual counting, more manpower is needed to count the bacteria. However, with the existence of automatic counting, less man power is needed because the counting is done within the algorithm in the software.

d. GUI

The front panel of GUI to ease the counting process had also been developed as shown in Figure 4. It offers the user two different methods for bacteria counting. It was developed using MATLAB environment.

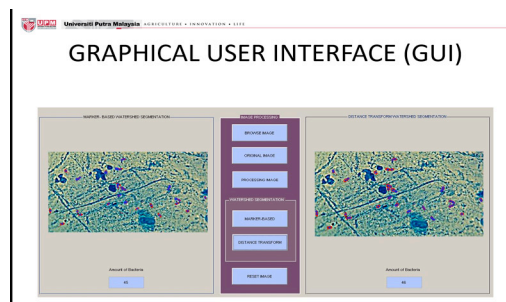


Figure 4. GUI front panel

CONCLUSION

In conclusion, the most suitable algorithm techniques in Image Processing, such as Image Acquisition, Image Pre-Processing and Image Segmentation, for counting the total amount of TB bacteria in the stained-sputum image was successfully implemented, applied and validated. Marker Based Segmentation method had been proven to be the best method in counting the TB

bacteria with an average percentage accuracy of 81.08%. On the contrary, Distance Transform Watershed Segmentation only achieved an average percentage of 59.06%. The GUI had also been successfully developed for displaying the image and user interaction. Automatic and manual counting of TB bacteria had been discussed and it was proven from this research that the former is the best technique in order to reduce human error and man power, with minimum time consumed.

ACKNOWLEDGEMENTS

A big Thank You to Pathology Department of Hospital Serdang in providing all of the stained-sputum sample images that contain Tuberculosis (TB) bacteria. This project would not have been completed without the Hospital's cooperation. We also record our gratitude to Universiti Putra Malaysia under Putra Grant GP-IPB/2013/9412702 which funded this research.

REFERENCES

- Allaoui, A. E. (2012). Medical Image Segmentation by Marker Controlled Watershed and Mathematical Morphology. *The International Journal of Multimedia and Its Applications*, 4(3), 1-9.
- Daniel, T. (2006) The history of tuberculosis. *Respiratory Medicine*, 100(11),1862-1870.
- Ibnu, S. A. Kusworo, G. R., & Nelly, M. (2012). Development of Algorithm Tuberculosis Bacteria Identification Using Color Segmentation and Neural Network. *International Journal of Video and Image Processing and Network Security*, 12(1), 9-13.
- Kauleshwar, P. N., Devvrat, L. A., & Dheeran, U. (2013). Character Recognition Using Matlab's Neural Network Toolbox. *International Journal of u- and e- Service, Science and Technology*, 6(1), 13-20.
- Parvati, K., Prakasa, B. R., & Mariya, D. M. (2008). Image Segmentation Using Gray-Scale Morphology and Marker-Controlled Watershed Transformation. *Discrete Dynamics in Nature and Society*, 2008, 1-8.
- Pedro, F. F., & Daniel, P. H. (2012). Distance Transforms of Sampled Functions. *Theory of Computing*, 8, 415-428.
- Rachna, H., & Mallikarjuna, M. S. (2013). Detection of Tuberculosis Bacilli using Image Processing Techniques. *International Journal of Soft Computing and Engineering*, 3(1), 2231-2307.
- Raof, R. M., Mashor, R. A., & Noor, S. (2011). Image Segmentation of Ziehl-Neelsen Sputum Slide Image for Tubercle Bacilli Detection. *Journal of Engineering and Medical Science, USM*, 1(1), 365-378.
- Sandy, C. R. (2015). *Sputum Stain for Mycobacteria*. Retrieved May 16, 2015, from: <http://www.healthline.com/healthline.com>
- Steve, E. (2010). Visualizing region props ellipse measurements. Retrieved May 20, 2015, from <http://blogs.mathworks.com/>
- Uppal, N., & Raman, G. (2012). Computational Approach to Count Bacteria Colonies. *International Journal of Advances in Engineering and Technology*, 4(1), 364-372.

Analysis of AC - to - DC Uncontrolled Converters Harmonics for Electric Vehicles Applications

Shaker M. Khudher^{1,3*}, Ishak Bin Aris¹, Nashiren F. Mailah¹
and R. K. Z. Sahbudin²

¹Department of Electrical and Electronic Engineering, Faculty of Engineering, Universiti Putra Malaysia, 43400 UPM, Serdang, Selangor, Malaysia

²Department of Computer and Communication Engineering, Faculty of Engineering, Universiti Putra Malaysia, 43400 UPM, Serdang, Selangor, Malaysia

³Department of Electrical Engineering, Faculty of Engineering, University of Mosul, Iraq

ABSTRACT

This paper discusses the harmonic analysis of the AC-to-DC uncontrolled converters commonly used in electric vehicles charging station. The aim of this paper is to model and simulate different rectifier models in addition to explaining the differences in input current harmonics, the total Harmonic Distortion (THD) as well as the power factor (pf). The converter configurations include single-phase bridge, 6-pulse and 12-pulse rectifier circuits. The single phase is normally used for electric scooter charging, while three-phase converters can be used for both electric bus and car charging. The circuit configurations of the rectifiers were modelled and simulated using Matlab R2014a to achieve the objective of the study. The results revealed that the THD levels were extremely high which is unacceptable if the system is connected to the utility grid.

Keywords: Harmonic analysis, AC to DC converters, electric vehicles

INTRODUCTION

Electric vehicles have become part of our lives revolutionising the transport sector.

They are environmental friendly as they are not powered by fossil fuel. The main source of energy in an electric vehicle is a battery which is a DC power supply. Thus, to provide sustainability and continuity for the battery, stations are needed to charge the battery. The only fix energy source available is the grid which provides AC, which means the AC will be converted to DC by using a charger. The charger is basically a rectifier which converts AC to DC). However, the problem is when rectifiers are considered a source of

ARTICLE INFO

Article history:

Received: 24 August 2016

Accepted: 03 Jun 2017

E-mail addresses:

shakeralhyane@yahoo.com (Shaker M. Khudher),

ishak_ar@upm.edu.my (Ishak Bin Aris),

nashiren@upm.edu.my (Nashiren F. Mailah),

ratna@upm.edu.my (R. K. Z. Sahbudin)

*Corresponding Author

harmonics. Thus, the first issue appears the harmonics mitigation to the grid.(Liu, Dow, & Liu, 2011; Wanik et al., 2013).

Most of the effects of harmonics are caused by the nature of nonlinear loads which are connected to the system. The total harmonic distortion (THD) shows why there are a lot of standards for acceptable percentages and limitation at the point of connection to the grid (Duffey & Stratford, 1989; Kazem, Albaloshi, Al-jabri, & Al-Saidi, 2005; Mahar & Uqaill, 2011)

Diode rectifiers are commonly utilised for the process of conversion, bridge configuration is one of them but it produces high harmonics and THD. The 6-pulse is widely used because it is cheap and has the simplest structure. A 12-pulse rectifier consists of two sets of 6-pulse rectifier and it is very commonly used for high power grid application.(Venkatesh & Dinesh, 2014)

Bridge, 6 Pulse and 12 Pulse Uncontrolled Circuits

The bridge is a 1-phase model which utilises 4-diodes combined in a particular way to provide the output voltage (Rashid, 2001; Singh et al., 2004). All the 4-diodes are D1,4 and they connected in two arms; two diodes are ON at each 1/2 period. At first 1/2 cycle of the source, D1 and D2 are ON, while diodes D3 and D4 are OFF as shown in Figure.1.

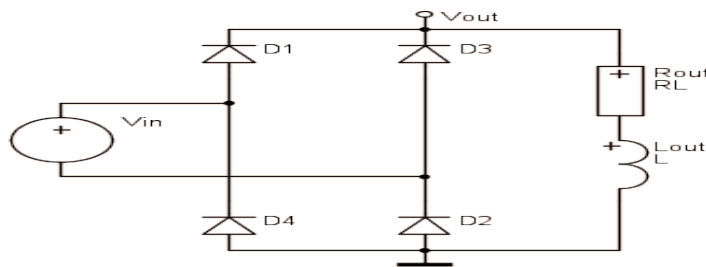


Figure 1. Uncontrolled single-phase converter

The three phase 6-pulse converters have 6-diodes and any pair is connected to one arm of 3-phase power supply (see Figure.2a). As a matter of fact, 2- diodes in the model are simultaneously ON, first one is represented by the three diodes (D1, D3 and D5) and the second one (D2, D4 and D6). The two conducting diodes are connected to two arms of 3-phase source in the series to output DC points. The output DC voltage is known as the combination of two arms of 3-phase voltages. However, 12- pulse model is mostly two 6-pulse configurations combined in a series at the output points and organised with a phase shifting in the input source as shown in Figure.2b.

Harmonics

A harmonic is a periodic element of a complex signal with a frequency that is an integral multiple of the main frequency (Mahar & Uqaill, 2011; Venkatesh & Dinesh, 2014; Rashid, 2001). Any non-pure signal which is neither pure sine nor levelled DC is considered a source

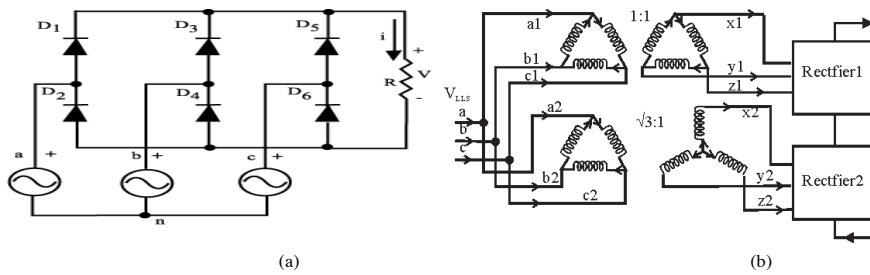


Figure 2. (a) Uncontrolled Six-Pulse Converter; (b) Uncontrolled 12-pulse converter

of harmonics. The term complex signal consists of all the repeating waveforms which are not sinusoidal. The 2nd harmonic has a double frequency of the main frequency; therefore, nth harmonics have frequency equals to (n*f). where (f) is the main source frequency, n=1,2,3,.....,∞

Harmonics are defined as an individual and even components; when a signal has difference between the positive half and the negative half, even components will appear (2nd,4th,...) and perhaps some odd components may appear as well. On the other hand, when the signal has identity between the positive and the negative half, odd components appear (3rd,5th,...).and this signal is free of DC component. Therefore, a distorted signal consists of multi harmonics, dissimilar amplitudes and frequencies with a phase shifting between them. Harmonics can be obtained by using Fourier analysis. Common code for Fourier analysis, periodic function f (t) of any signal alter with cycle of 2π is expressed as

$$f(t) = a_o + \sum_{n=1,2,\dots}^{\infty} (a_n \cos n\omega t + b_n \sin n\omega t) \tag{1}$$

Where a_o is the DC level of the main signal, (a_n Cos nωt + b_n Sin nωt) is the nth component for the signal. a_o, a_n and b_n calculated using the formulas (2-4).

$$a_o = \frac{1}{2\pi} \int_0^{2\pi} v_l d \omega t \tag{2}$$

$$a_n = \frac{1}{\pi} \int_0^{2\pi} v_l \cos n\omega t d \omega t \tag{3}$$

$$b_n = \frac{1}{\pi} \int_0^{2\pi} v_l \sin n\omega t d \omega t \tag{4}$$

formula (1) could given in 5 :

$$f(t) = a_o + \sum_{n=1,2,\dots}^{\infty} c_n \sin(n\omega t + \phi_n) \tag{5}$$

Where $c_n = \sqrt{a_n^2 + b_n^2}$, $\phi_n = \tan^{-1} \frac{a_n}{b_n}$ c_n & ϕ_n is amplitude and angle of nth element of the signal.

THD Calculation

The percentage of distortion in any signal (THD) is defined as Root-Sum-Square (RSS)(Wanik et al., 2013; Rashid, 2001). In order to determine the THD, take the root square of summations of the squares of the first few components of the fundamental. The THD may be calculated as below which can be used for both current and voltage.

$$THD_i = \frac{\sqrt{i_2^2 + i_3^2 + \dots + i_{\infty}^2}}{i_1} = \frac{\sqrt{\sum_{i=2}^{\infty} i_i^2}}{i_1} \tag{6}$$

Where I_n is the RMS current

Converters Simulation

Matlab software is one of the powerful tools to design and model different types of systems, starting from generation, transmission among others. Matlab 2014a release 8.3.0.532 with SimPowerSystems block set was used in this paper. All the models were simulated without using any type of filters.

Load. The load in our model was different electric vehicles battery which has the specific details:

V Battery =600 V, I battery =100 A (bus)

V Battery =300 V, I battery =50 A (car)

V Battery =48 V, I battery =25 A (scooter)

Single Phase rectifier. The Matlab library contains most of the electrical elements which can be used for all the purposes. One of them is the power electronics library used in our models.

Figure.3 shows the single phase converter with the scooter as a load and capacitor as a smoothing tool.

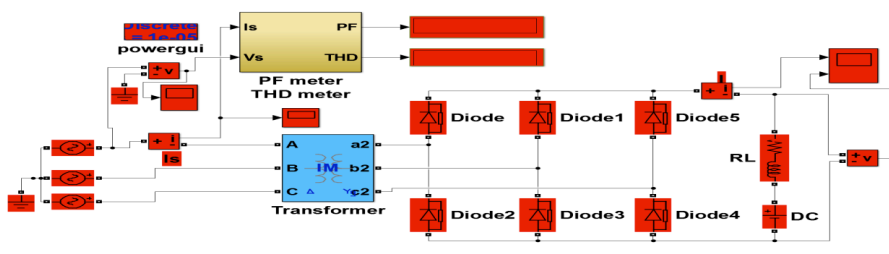


Figure 3. Single-phase rectifier

3-Phase 6-diodes rectifier. It utilises the same elements as in the single phase full wave rectifier this time to model the three phase converter which can be used for the electric bus or car. This configuration has 6-diodes combine with 3 single phase AC sources shifted by 120 degrees. Figure.4 shows 6-pulse diode rectifier.

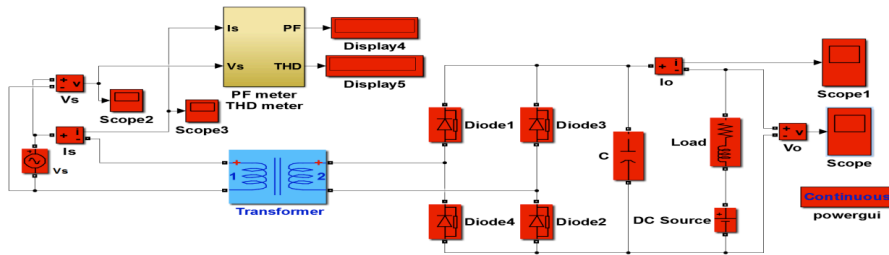


Figure 4. Three-phase 6-diodes rectifier

3-Phase 12-diodes rectifier. This type of converter is also used for charging cars or buses; it has 12-diode which is normally 2 sets of 6-diode connected either in series or parallel. In this paper, we connected the sets in series. Figure 5 shows the 12-pulse diode rectifier.

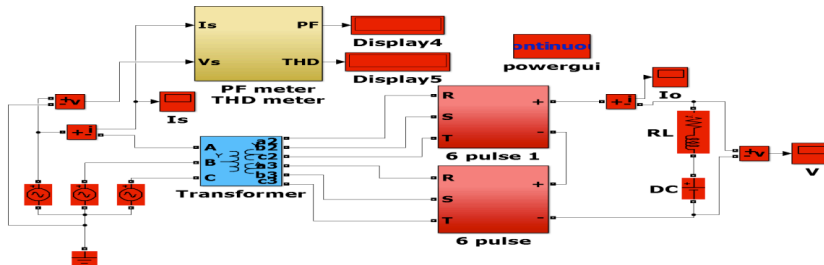


Figure 5. Three-phase 12-diodes rectifier

Simulated Results

All the three types of converters were simulated for the three loads without using any filters. The results showed that increasing the number of pulses leads to improved performance of the system and reduce the THD for the current supply. For the scooter as a load, the results are shown below. single phase full wave rectifier Figure.6 shows the input current and voltage.

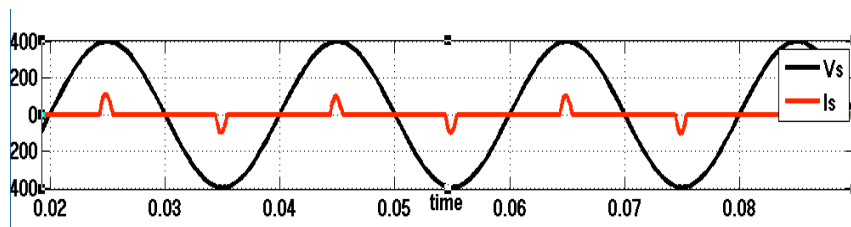


Figure 6. Input current and voltage for single phase rectifier with scooter as a load Fourier analysis is available in Matlab library to analysis the input current, the harmonics order and the THD percentage are displayed in Figure7. which shows that THD=217.21%

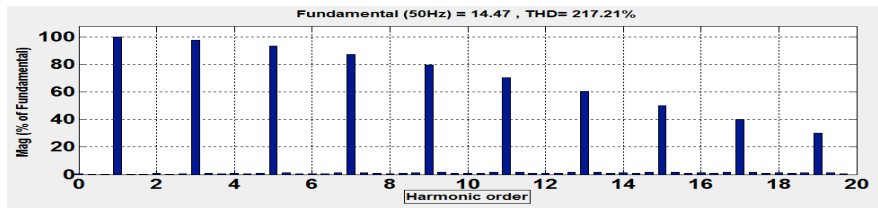


Figure 7. FFT for input current with scooter as a load

For three phase 6-diode converter, Figure 8 shows the input current and voltage. The load is electric car.

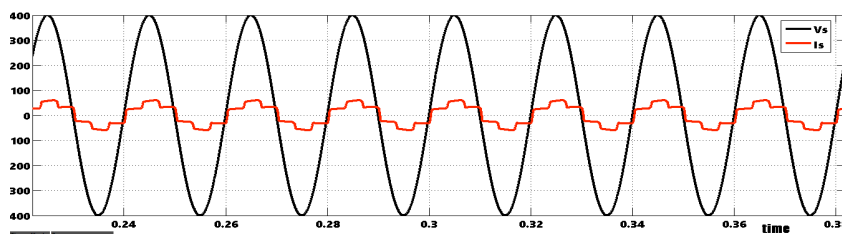


Figure 8. Input current and voltage for 3-phase 6-diode rectifier with car as a load

Applying FFT for the input current show that some of the harmonics are cancelled and the THD was reduced to THD=25.97% as shown in Figure.9.

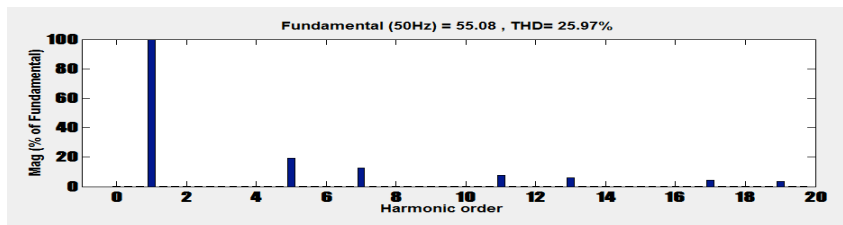


Figure 9. FFT for input current with car as a load

For three phase 12-diode converter the input current and voltage are shown in Figure.10 (the load is bus).

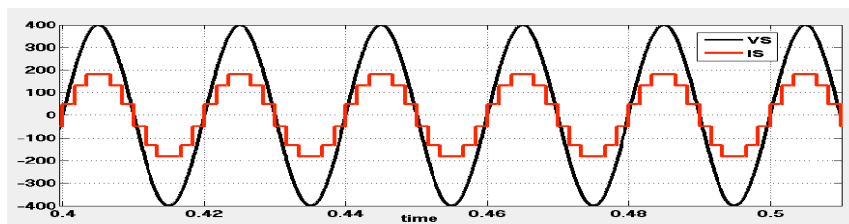


Figure 10. Input current and voltage for 3-phase 12-diode rectifier with bus as a load

Using FFT to analyse the input current shows that the THD level is less than in other configurations as seen in Figure 11, THD=15.20%.

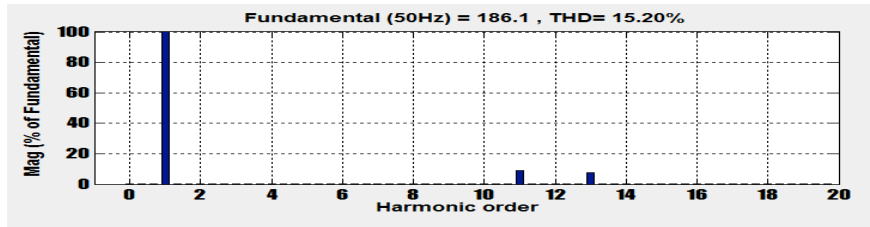


Figure 11. FFT for input current with bus as a load

The results can be summarised in Table 1 which shows a comparison between the three models. Table 1

Table 1
Simulation results of the converters

Type of converter	load	Harmonics order	Fundamental	THD %	Pf
Single phase	scooter	1,3,5,7,9,11,13,15,17,19	12.88	217.21	0.39
3-phase 6-diode	car	1,5,7,11,13,17,19	55.28	25.97	0.68
3-phase 6-diode	bus	1,5,7,11,13,17,19	181.5	24.07	0.68
3-phase 12-diode	car	1,11,13	56.31	14.32	0.704
3-phase 12-diode	bus	1,11,13	187.4	15.20	0.7046

Table 1 shows that if the number of pulses increases, the THD of the input current decreases, and the efficiency of the system as well as the power factor improves.

CONCLUSION

A 12-diode converter shows that the THD level and input current harmonics were lower than other types of converters. As the number of pulses increased, the DC output quality was better and the input harmonics were reduced. Thus, increasing the number of pulses can be considered harmonics filtering. However, it was still not enough to reduce the THD levels to the standard levels which is less than 5%; thus, requiring some types of filters (passive filters, active filters, adaptive filters). On the other hand, using converters with pulses higher than 12 such as 18, 24, 26, 48 pulse would give better results, yet, this requires more elements and leads to high complexity circuits which makes the analysis difficult and complicated.

ACKNOWLEDGEMENTS

This work was supported by Universiti Putra Malaysia under grant ref: (GP-IPB)/ (2013-9412103). The author would like to thank The Ministry of Higher Education and Scientific

Researches and Mosul University, College of Engineering, electric department for providing the research grant.

REFERENCES

- Duffey, C. K., & Stratford, R. P. (1989). Update of harmonic standard IEEE-519:IEEE Recommended Practices and Requirements for Harmonic Control in Electric Power Systems. *Conference Record of the IEEE Industry Applications Society Annual Meeting*, 25(6), 249–255. <http://doi.org/10.1109/IAS.1989.96858>
- Kazem, H. A., Albaloshi, A. A., Al-jabri, A. S. A., & Al-Saidi, K. H. (2005). Simple and Advanced Models for Calculating Single-Phase Diode Rectifier Line-Side Harmonics. *World Academy of Science, Engineering and Technology*, 9, 179–183. <http://doi.org/10.1109/IAS.2003.1257849>
- Liu, R., Dow, L., & Liu, E. (2011, January). A survey of PEV impacts on electric utilities. In *Innovative Smart Grid Technologies (ISGT), 2011 IEEE PES* (pp. 1-8). IEEE. <http://doi.org/10.1109/ISGT.2011.5759171>
- Mahar, M. A., Uqaili, M. A., & Larik, A. S. (2011). Harmonic analysis of ac-dc topologies and their impacts on power systems. *Mehran University Research Journal of Engineering and Technology*, 30(1), 273-278. Retrieved from http://publications.muett.edu.pk/research_papers/pdf/pdf73.pdf
- Rashid, M. H. (2001). *Power Electronics*. Academic Press Series in Engineering.
- Singh, B., Singh, B. N., Chandra, A., Al-Haddad, K., Pandey, A., & Kothari, D. P. (2004). A review of three-phase improved power quality ac-dc converters. *IEEE Transactions on Industrial Electronics*, 51(3), 641–660. <http://doi.org/10.1109/TIE.2004.825341>
- Venkatesh, P., & Dinesh, M. N. (2014). Harmonic Analysis of 6-Pulse and 12-Pulse Converter Models. *International Journal of Modern Engineering Research (IJMER)*, 4(9), 31–36.
- Wanik, M., Siam, M. F., Ayob, A., Mohamed, A., HanifahAzit, A., Sulaiman, S., ... & MatHussin, A. K. (2013). Harmonic Measurement and Analysis during Electric Vehicle Charging. *Engineering*, 05(01), 215–220. <http://doi.org/10.4236/eng.2013.51B039>



Investigating Insulator UV Signal Frequency Components as Potential Tools for Condition Monitoring of Ceramic Insulators

Saiful Mohammad Iezham Suhaimi¹, Nouruddeen Bashir^{1,3*},
Nor Asiah Muhamad^{1,2} and Mohd Aizam Talib⁴

¹*Institute of High Voltage & High Current, Faculty of Electrical Engineering,
Universiti Teknologi Malaysia, 81310, UTM Johor Bahru, Malaysia*

²*School of Electrical & Electronic Engineering, Engineering Campus,
Universiti Sains Malaysia, 14300 Nibong Tebal, Penang*

³*Power Equipment & Electrical Machinery Development Institute (PEEMADI),
National Agency for Science and Engineering Infrastructure (NASENI),*

PEEMADI Complex, KM 6, Okene-Auchi Expressway, P.M.B. 1029, Okene, Kogi State Nigeria

⁴*No. 1, Kawasan Institusi Penyelidikan, Jalan Ayer Itam, 43000 Kajang, Selangor, Malaysia*

ABSTRACT

Contaminated and ageing transmission line insulators often suffer from temporary or permanent loss of their insulating properties due to flashover resulting in power system failure. Surface discharges are precursors to flashover. To pre-empt any occurrence of flashovers, utility companies monitor the conditions of their insulators. There are numerous insulator surface monitoring techniques such as Leakage Current, Acoustics, and Infrared. However, these techniques may not be suitable for in-situ condition monitoring of the insulators as they are prone to noise, affected by environmental conditions or contact methods. Monitoring of the UV signals emitted by the surface discharges of these insulators has been reported to be a promising technique. However, comprehensive studies on this technique is lacking, especially on aged insulators. This paper investigated the UV signals of contaminated and aged insulators detected during surface discharge activities using UV pulse method. The time and frequency domain of the UV signals were analysed for a group of insulator samples having varying levels of contamination and phases of ageing. Results show that there is a strong correlation between the contamination level and ageing of the insulators with the amplitude and harmonic components of the UV signals. This correlation can be useful to monitor in-service insulator surface conditions.

Keywords: UV pulse method, UV pulse sensor, surface discharge, THD, discharge intensity

ARTICLE INFO

Article history:

Received: 24 August 2016

Accepted: 03 Jun 2017

E-mail addresses:

saifuliezham91@gmail.com (Saiful Mohammad Iezham Suhaimi),

nouruddeen@gmail.com (Nouruddeen Bashir),

norasiah@utm.my (Nor Asiah Muhamad),

mohdaizam@tnbr.com.my (Mohd Aizam Talib)

*Corresponding Author

INTRODUCTION

Transmission lines are one of the most important parts of a power system. This is due to the fact that they electrically insulate the

line from the towers (which are grounded) as well as mechanically support (hold) the lines. During service, these insulators experience operational hazards which affect their functionality. These hazards are mainly environmental in nature. Surface contamination due to pollution from various sources such as industrial and coastal as well as wetting of their surfaces reduce surface resistance of the insulators (Looms, 1988). This leads to discharges on the surface of the insulators which are precursors to flashover or surface degradation (ageing). It has been reported that 70% of line outages are as a result of insulator failures with the cause of such failures due to contamination flashover or ageing. Ironically, although these insulators account for a very small fraction of transmission line capital costs, almost half of the line maintenance costs are incurred by transmission line insulators (Gorur et al., 2005).

When insulators are contaminated or experience degradation, leakage current (LC) flows on the surface of the insulators. The presence of surface discharges distorts the LC waveform thereby leading to harmonics. The frequency components of LC waveforms have been reported to be a good indicator of insulator surface discharges and ageing (Du & Liu, 2008; El-Hag et al., 2003; Suda 1999; Bashir & Ahmad 2010).

Many types of surface discharge detection methods have been studied in the past to monitor corona discharges with new methods introduced from time to time. The most common methods that have been reported are LC method, infrared method, and acoustics method. These methods have their own advantages and drawbacks. Leakage current method, has ceased to be the preferred detection method for surface discharges due to its detection inaccuracy as it is prone to noise and electromagnetic interference, thus, affecting the reliability of leakage current data. In addition, the method involves direct contact measurement which is undesirable to utility companies. The Acoustics detection method is mostly used for partial discharge detection but is immune to electromagnetic interference (Markalous et al., 2008; Tsuji et al., 2005; Lundgaard, 1992). Ultrasonic detection method is sensitive to the background noise. Although it can easily locate discharges, it has poor sensitivity and sound attenuation. Infrared method is mostly related to temperature detection and most commonly used to detect the temperature of the corona discharge current. The reliability of infrared detection method is affected by weather especially during hot and sunny conditions. Additionally, as the temperature of the discharges is very small it makes the detection using the infrared method difficult, thus affecting detection accuracy (Kim & Shong 2011).

Studies have shown that electrical discharges on the surface of insulators emit UV radiation (Wang et al., 2014) which can be detected in many sources such as sunlight, electric discharge and special lights (mercury-vapor lamp, back light) (Zhao et al., 2003). These UV radiations have different wavelengths. The UV radiations from electrical discharges such as surface discharge are usually in the waveband of 240 nm to 280 nm (Lu et al., 2010) which is also known as the solar blind region. This means that in this wavelength, the UV radiations detected from the discharges are not affected by UV from sunlight. These ultraviolet signals have been shown to be a good method to detect corona discharge from insulator transmission line. Studies have shown that this method could locate the discharge area with relatively high accuracy. The method also has high sensitivity, thus, making the detection more accurate and reliable compared with the other methods mentioned earlier. In addition, it is a non-contact method. Ultraviolet pulse method and ultraviolet imaging method are two methods involved

in the detection of the ultraviolet signals emitted by the surface discharges. With regards to the UV pulse method, most of the studies have been limited to detection and measurement of the UV pulse signals of the insulator surface discharges. Studies on characterisation and pattern recognition of the UV pulse signal in relation to surface condition of the insulators are lacking.

The objective of this paper is to study the correlation between the time and frequency components of UV signals due to emitted UV radiations during surface discharge activities and the surface condition of commercial field-aged insulator samples.

METHODOLOGY

Insulator Samples and Artificial Contamination

In this study, insulator samples of varying degrees of ageing were used. The samples were full scale commercial ceramic glass insulators that were naturally aged while in service. The insulators were obtained from the 132 kV transmission lines of the Malaysian national power company, Tenaga Nasional Berhad (TNB); they have standard profile having leakage distance of 290 mm. Table 1 shows the description of the insulators.

Table 1
Insulator Samples

Insulators	Service History	Number of samples	Ageing
A	Less than 10 years	2	Good condition
B	Between 10 to 20 years	2	Mild corrosion at cap
C	Greater than 20 years	2	Discoloration of glass dielectric, severely corroded cap and pin

To investigate the relationship between the UV signals emitted during surface discharge activities and surface condition of the insulators, the insulator samples were artificially contaminated with salt as the contaminant according to IEC 60507 (IEC 1991). Three contamination levels were produced, and the ESDD level of each contamination level measured. Using the ESDD level, the contamination levels were classified using IEC 60815 (IEC 1986). Table 2 shows the contamination levels used in this study. During service, contaminated insulators could possess dry contamination or wet contamination depending on the environmental conditions. In this study, only the former was considered.

Table 2
Insulator samples' artificial contamination

Salt (g/L)	ESDD (mg/cm ²)	Contamination Level
0	N/A	N/A
5	0.06	Light
30	0.21	Medium
120	0.47	High

Experimental set-up and procedure

Figure 1 shows the experimental set-up of this study. A 100 kV step-up transformer was used to inject high voltage to the insulator. The high voltage supply from the transformer was controlled using a voltage regulator. The insulator sample was housed in a chamber made up of acrylic glass measuring 80 cm X 80 cm X 80 cm. The UV radiation emitted during discharge activities was detected using a UV pulse sensor which was placed outside the chamber. The UV sensor used in this study had a waveband between 185nm and 260nm (Zang et al., 2009), which defines the waveband of the UV signals produced on the surface discharge which can be detected by the sensor. The sensor was powered by a 12 V DC battery and was placed at a distance outside the chamber. The output of the sensor was connected to a computer via a PICO SCOPE for measurement and to record the UV pulse signals. The signal data were saved in PICO SCOPE files before being transferred into Excel and MATLAB for further analysis. MATLAB was used to remove the noise in the signals to make it easier for pattern identification, and also to find the harmonic distortion of the signals and the frequency component of the signals.

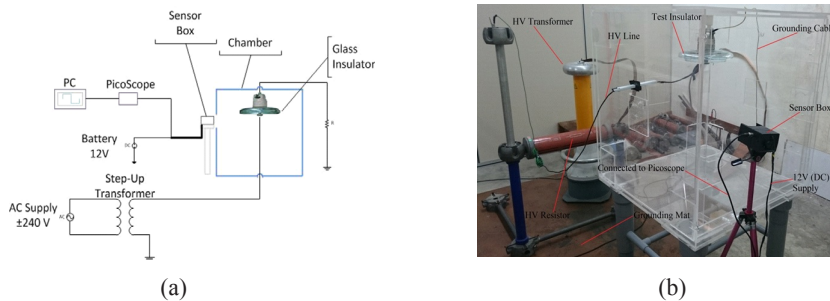


Figure 1. Experimental Setup (a) Schematic diagram (b) Pictorial view

Insulator surface discharge level

In this study, to generate the discharges of various intensities on the surface of the insulator samples, different voltages were applied. Various discharge intensities were simulated to closely mimic service condition as well as processes that lead to flashover of insulator during service. Table 3 depicts the discharge intensities produced in this study due to varied applied voltages. Voltage was applied to the insulator and steadily increased. Once the required discharge intensity level was reached, the applied voltage, UV signal voltages and waveforms were recorded.

Table 3
Classification of Insulator surface discharge intensity levels

Electrical strength discharge level	Description
Hissing	Hissing without any visible discharge
Discharge at pin of the insulators	Hissing sound plus spot discharges at the pin of the insulators
Discharge at cap of the insulators	Louder hissing noise, discharges at both the pin and cap of the insulator samples
Severed discharge	Very loud hissing noise, intense sparking discharge on the pin and cap of the insulator (just prior to flashover)

RESULT AND DISCUSSION

UV pulse signals

The UV signals emitted by the insulator samples during discharge activities were recorded and plotted. Figure 2 shows the UV signal waveform for Group A non-contaminated (0 g/l) insulator samples at various discharge intensity levels.

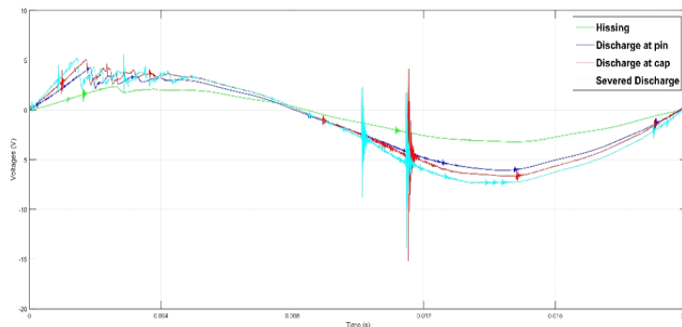


Figure 2. UV signal waveform of non-contaminated Group A insulator samples

The presence of electrical discharge distorts the waveforms thereby creating harmonics. There is a strong correlation between the discharge intensity and UV signal distortion. From Figure 2, it can be seen that the harmonic distortions at the first half cycle of the signals increased when discharge intensity is increased, from hissing to severe discharge. However, in the second half cycle of the waveform, there appears to be a marked difference between the harmonic distortions of the discharge intensities. The hissing and discharges at pin, which were discharges of lesser intensity appeared to have lesser distortions compared with discharges at cap and severe discharge. In addition to the relationship between the discharge intensity and wave distortion, there also appeared to be a relationship between discharge intensity and the amplitude of the sinusoidal waveform. As the surface discharges became increasingly intense, the amplitude of the waveform also increased. Table 4 shows the injected (applied) voltages and the average UV signal peak-to-peak voltages.

Table 4
Voltage Amplitudes of UV signals for non-contaminated Group A insulator samples

Voltages Discharge Intensity levels	Non-Contamination		Light Contamination		Medium Contamination		Heavy Contamination	
	Range Injected Voltage, V_i =(kV)	Average Peak to Peak Voltage, V_{p-p} (V)	Range Injected Voltage, V_i (kV)	Average Peak to Peak Voltage, V_{p-p} (V)	Range Injected Voltage, V_i (kV)	Average Peak to Peak Voltage, V_{p-p} (V)	Range Injected Voltage, V_i (kV)	Average Peak to Peak Voltage, V_{p-p} (V)
Hissing	27 – 35	5.6	20 – 32	6.4	20 – 32	6.3	20 – 31	6.5
Discharge at pin	40 – 50	10.3	42 – 50	11.8	40 – 50	11.0	35 – 48	11.9
Discharge at cap	54 – 56	11.6	50 – 54	12.4	50 – 54	12.1	44 – 49	12.2
Severe	60 – 63	12.5	60 – 63	12.6	60 – 63	12.5	56 – 59	12.2

The distortion and voltage amplitude pattern in Figure 2 and Table 4 were similarly also observed for all cases of the insulator samples investigated in this study.

THD and Fundamental Frequency Component

The measured THD and fundamental frequency component of the UV signal harmonics are presented in Figures 3 and 4 respectively. The THD in this case is the percentages of the sinusoidal signals detected by the UV sensor being disturbed due to the detected UV signal produced by the surface discharges of the insulator samples. On the other hand, the fundamental frequency is the lowest frequency of signals being detected (Nam et al., 2002). From Figure 3, it can be seen that in almost all cases with respect to contamination level for all three insulator sample groups, the THD values increased as the surface discharge intensity increased. The THD values for hissing varied between 5% and 10% while for severe discharges their THD percentages were from 10% and 31%.

Similar patterns were also observed with the fundamental frequency component of the signals as shown in Figure 4. The fundamental frequency components increased as the discharge intensity increased. A large increase is observed in fundamental frequency components from hissing to appearance of a visible discharge at the pin. For transmission line insulators, visible discharges normally originate from the pin as that is the point with the highest electrical stress. However, as the strength of the discharge intensity progresses, the rate of increase in the fundamental frequency component of the UV signal reduces.

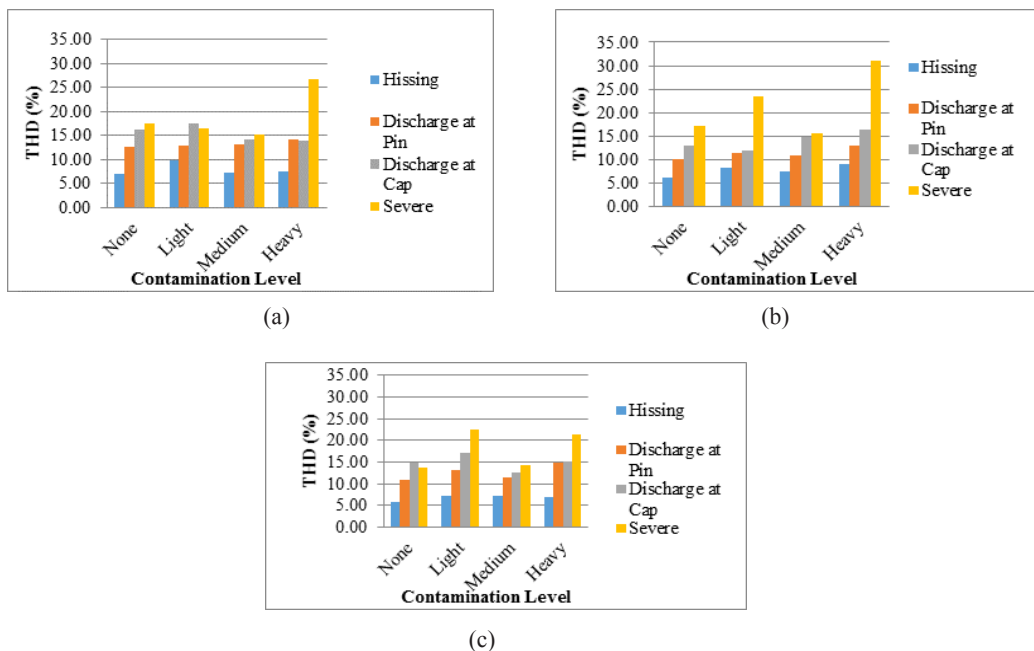


Figure 3. Insulator samples UV signals THD; (a) Group A; (b) Group B; (c) Group C

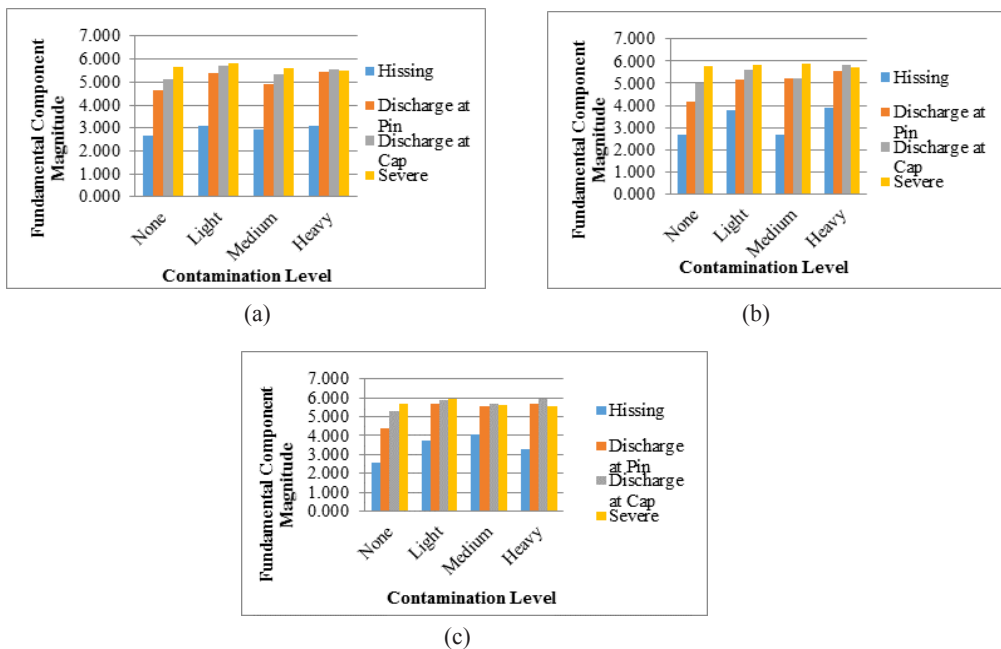


Figure 4. Insulator samples UV signals Fundamental frequency component; (a) Group A; (b) Group B; (c) Group C

CONCLUSION

In this study, the time and frequency components of detected UV signals emitted by insulator surface discharges using UV pulse method has been presented. The signals were analysed under different surface contamination levels and varying degree of ageing. The UV pulse method was able to show a positive correlation between the UV signals' harmonic distortions levels and the surface condition of the insulators. This suggests that the UV pulse method can be a promising technique in monitoring transmission line insulators. Unlike previously used techniques, the UV detection method is non-contact and immune from noise, thus, making it a good tool for monitoring insulators.

ACKNOWLEDGEMENT

The authors gratefully acknowledge the financial support by Universiti Teknologi Malaysia and the Ministry of Education Malaysia under the FRGS grant scheme Vot. nos. 4F398, 4F515, 10H16 and 06H77 to carry out this study.

REFERENCES

- Bashir, N., & Ahmad, H. (2010). Odd harmonics and third to fifth harmonic ratios of leakage currents as diagnostic tools to study the ageing of glass insulators. *IEEE Transactions on Dielectrics and Electrical Insulation*, 17(3), 819-832.

- Chunyan, Z., Huisheng, Y., Hongcai, L., Xiaogen, Y., Junjia, H., Zhenglong, J., . . . Xinjie, Z. (2009). *Using ultraviolet imaging method to detect the external insulation faults of electric device*. Paper presented at the IEEE Conference on Electrical Insulation and Dielectric Phenomena, 2009. CEIDP'09.
- Du, B., & Liu, Y. (2008). *High frequency harmonic components of leakage current for monitoring insulator performance in cold fog*. Paper presented at the 2008 IEEE/PES Transmission and Distribution Conference and Exposition.
- El-Hag, A. H., Jayaram, S. H., & Cherney, E. A. (2003). Fundamental and low frequency harmonic components of leakage current as a diagnostic tool to study aging of RTV and HTV silicone rubber in salt-fog. *IEEE Transactions on Dielectrics and Electrical Insulation*, 10(1), 128-136.
- Gorur, R., Scaffner, D., Vinsan, R., Clarke, W., & Ruff, D. (2005). Utilities Share their Insulator Experiences. *Transmission and Distribution World*, 57(4), 17-27.
- IEC. (1986). *Guide for the Selection of Insulators in respect of Polluted Conditions: IEC*. Bureau Central De La Commission Electrotechnique Internationale.
- IEC. (1991). Artificial Pollution Tests on High-Voltage Insulators to be used on A.C. Systems: IEC. *International Standard IEC*, 507.
- Kim, Y., & Shong, K. (2011). The characteristics of UV strength according to corona discharge from polymer insulators using a UV sensor and optic lens. *IEEE transactions on Power Delivery*, 26(3), 1579-1584.
- Looms, J. S. T. (1988). *Insulators for High Voltages*. England: Peter Peregrinnus Ltd.
- Lu, F., Wang, S., & Li, H. (2010). *Insulator pollution grade evaluation based on ultraviolet imaging and fuzzy logic inference*. Paper presented at the 2010 Asia-Pacific Power and Energy Engineering Conference.
- Lundgaard, L. (1992). Partial discharge. XIV. Acoustic partial discharge detection-practical application. *IEEE Electrical Insulation Magazine*, 8(5), 34-43.
- Markalous, S. M., Tenbohlen, S., & Feser, K. (2008). Detection and location of partial discharges in power transformers using acoustic and electromagnetic signals. *IEEE Transactions on Dielectrics and Electrical Insulation*, 15(6), 1576-1583.
- Nam, S.-R., Kang, S.-H., & Park, J.-K. (2002). An analytic method for measuring accurate fundamental frequency components. *IEEE transactions on Power Delivery*, 17(2), 405-411.
- Suda, T. (1999). *Study on the frequency characteristics of leakage current waveforms of artificially polluted 12t suspension insulators by the clean fog method*. Paper presented at the High Voltage Engineering, 1999. Eleventh International Symposium on (Conf. Publ. No. 467).
- Tsuji, T., Matsumoto, S., Sakata, T., Nakayama, S., Otsubo, M., Honda, C., . . . Noguchi, H. (2005). *Basic study on acoustic noise of polluted insulator and waveform analysis method*. Paper presented at the Proceedings of 2005 International Symposium on Electrical Insulating Materials, 2005. (ISEIM 2005).
- Wang, S., Lv, F., & Liu, Y. (2014). Estimation of discharge magnitude of composite insulator surface corona discharge based on ultraviolet imaging method. *IEEE Transactions on Dielectrics and Electrical Insulation*, 21(4), 1697-1704.
- Zhao, W., Zhang, X., & Jiang, J. (2003). Tip to Plane Corona Discharge Spectroscopic Analysis. *Spectroscopy and Spectral Analysis*, 23(5), 955-957.

A Hermite Interpolated LUT for RF Power Amplifiers

Dinaagaren Selvadurai^{1*}, Roslina M. Sidek², Khalid Al-Hussaini¹ and Borhanuddin M. Ali¹

¹Department of Computer and Communication Engineering, Faculty of Engineering, Universiti Putra Malaysia, 43400 UPM, Serdang, Selangor, Malaysia

²Department of Electrical and Electronic Engineering, Faculty of Engineering, Universiti Putra Malaysia, 43400 UPM, Serdang, Selangor, Malaysia

ABSTRACT

Digital predistortion is one of the most widely used techniques to linearize a power amplifier (PA) to reduce the error vector magnitude (EVM) distortion and spectral regrowth. By far, the lookup table (LUT) predistorters are most frequently used scheme to mitigate the effects of non-linear power amplifier. In this paper, a new algorithm of joint-polynomial LUT predistorter which attains the best linearization performance is proposed. The algorithm employs the hermite interpolation LUT, which has a higher accuracy of interpolation. Simulation results show that the proposed method provides a better rejection of EVM distortion and an improvement of 30-40% of adjacent channel leakage ratio (ACLR) for the wideband code division multiple access at a minimal memory usage.

Keywords: Predistortion, linearization, lookup table, power amplifier, non-linear distortion

INTRODUCTION

One of the most important aspects of wideband digital communication system is the use of complex modulation scheme to increase spectral efficiency. These modulation

schemes possess non-constant envelopes and high peak to average power ratios (PAPR). Transmission of these complex modulation schemes through a power amplifier results in spectral regrowth and low Peak to Average (PA) power efficiency.

Several baseband linearisation techniques have been proposed to resolve the conflict between the linearity and efficiency of PA (Soloveya 2015), and the complex-gain lookup table (LUT) (Teikari et al., 2004), (Feng et al., 2013) based digital predistorter is one of the most commonly used techniques due to its low complexity and fast convergence for adaptation.

ARTICLE INFO

Article history:

Received: 24 August 2016

Accepted: 03 Jun 2017

E-mail addresses:

dinaagarenselva@gmail.com (Dinaagaren Selvadurai),

roslinams@upm.edu.my (Roslina M. Sidek),

khalid@gmail.com (Khalid Al-Hussaini),

borhan@upm.edu.my (Borhanuddin M. Ali)

*Corresponding Author

It has been suggested that a linear interpolation approximation (LUT) improves the accuracy of modelling the inverse PA characteristics (Feng et al., 2013) compared with non-interpolated LUT. However, as the inverse function of the Lin-LUT PA characteristics is not a smooth curve, this would consequently lead to error vector magnitude (EVM) distortion and adjacent channel interference. In this work, a hermite interpolated complex-gain LUT (HMT-LUT) is derived to improve the accuracy of modelling the inverse PA characteristic. This in turn results in better attenuation of EVM distortion and adjacent channel interference hence requiring less LUT entries to be inhabited. The HMT-LUT has been validated to improve the predistorter performance in terms of power spectral density (PSD), adjacent channel leakage ratio (ACLR) and error vector magnitude at a minimal memory usage. The improvement of HMT-LUT is theoretically derived and evaluated through simulations.

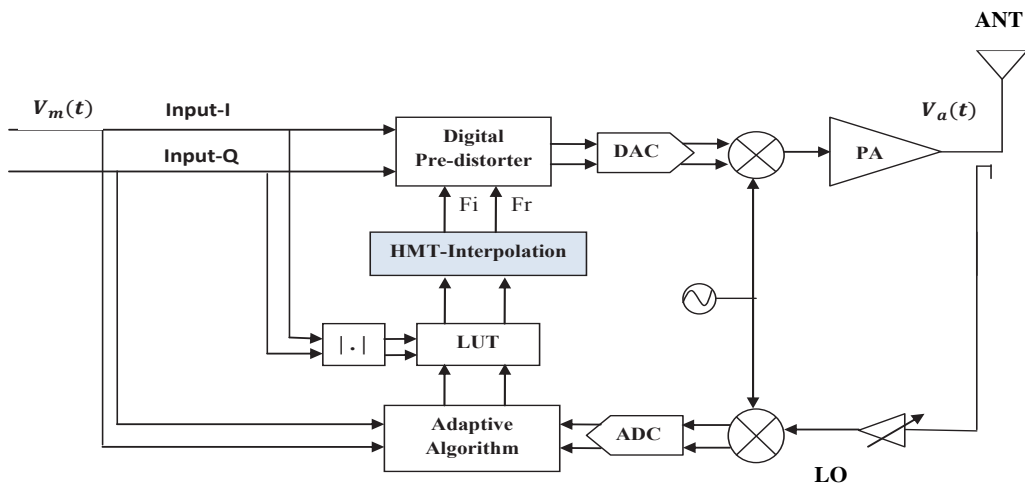


Figure 1. The block diagram of the proposed adaptive DPD system

SYSTEM MODEL ARCHITECTURE

The power amplifier PA has non-linear characteristics both in dynamic and static situations. The static part consists of AM-AM and AM-PM conversion functions. The dynamic part consists of memory effects whereby the output signal is dependent not only on the current input signal but also the input signal at a preceding state. In this brief, the PA is considered as memory-less (Saleh, 1981) whereby V_m (and $V_a(t)$ represents the signal at the input and output of the PA respectively as shown in Figure 1. The input signal, $V_m(t)$ as in Figure 1 is predistorted using the LUT values with hermite interpolation by the predistortion block that operates on the modulated digital baseband signal prior to digital to analog conversion (DAC) and frequency up conversion. Assuming the input signal, $V_m(t)$ is a modulated complex baseband signal which is given as

$$V_m = I + jQ \tag{1}$$

The input signal is fed to the cascade of the baseband digital predistorter (DPD) and power amplifier (PA). The DPD distorts the modulated signal by applying a memoryless non-linearity to produce the predistorted signal $V_d(t)$ as

$$V_d = V_m \cdot f(|V_m|) \tag{2}$$

where the amplitude modulation and complex-gain of predistorter is represented by V_m and $f(\cdot)$, which explains the AM/AM and AM/PM responses of the PA. From here, the output signal of the PA is expressed as

$$V_a = V_d \cdot g(|V_d|) = V_m \cdot f(|V_m|) \cdot g(|V_m| \cdot f(|V_m|)) \tag{3}$$

where V_d and $g|V_d|$ are in a complex form representing the amplitude of the predistorted signal and the complex gain of the amplifier respectively. In the analysis, the amplifier is normalised so the saturation occurs at unit amplitude of its input so the amplitude range of both $|V_m|$ and $|V_d|$ lies within $[0, 1]$. The cascading of PA and DPD eliminates the non-idealities of AM-AM and AM-PM producing a complex linear gain K , where:-

$$K = f(|V_m|) \cdot g(|V_m| \cdot f(|V_m|)) \tag{4}$$

In terms of mathematical convenience, the complex linear gain is normalised to one. From here, the output signal can be written as:

$$V_a = K \cdot V_m \tag{5}$$

The input signal to the DPD is predistorted by means of LUT values and each entry of the LUT is assumed to be optimised at the midpoint of its range. The RLS algorithm (Woo et al., 2007; Varahram et al., 2013) updates the LUT with

$$f_{i+1}^n = f_i^n + \lambda \cdot E_i \tag{6}$$

where λ is the gain vector, f_{i+1}^n and f_i^n are the n th LUT values at time i and $i+1$ respectively and E_i is the error vector at time i defined as the difference between input and output as given by

$$E_i = V_m(t) - V_a(t) \tag{7}$$

HERMITE INTERPOLATED COMPLEX-GAIN LUT METHOD

In a LUT based digital predistorter, each LUT entry is specified at only one single point of the inverse PA characteristics. To have a higher accuracy of estimation on modelling the inverse PA non-linear characteristic, one common method is to increase the number of LUT entries which consequently reduces the quantisation error as shown in (Chung et al., 2007). However, larger LUT entries tend to slower the convergence time and increase the computational complexity. In

order to overcome this drawback, a linear interpolated LUT (Lin-LUT) is proposed in (I. Teikari et al., 2004), (Feng et al. 2013). The Lin-LUT technique employs linear interpolation between the adjacent LUT entries for both predistortion and LUT updates which has been shown to improve performance. An inverse PA characteristic of Lin-LUT technique is shown in Figure 2. The Lin-LUT is proven to be the model that inverses more accurately the characteristics of the PA compared with non-interpolated LUT (Faulkner et al. 1994). However, as the inverse function of Lin-LUT is not a smooth curve as in Figure 2, this would consequently lead to EVM distortion and adjacent channel interference.

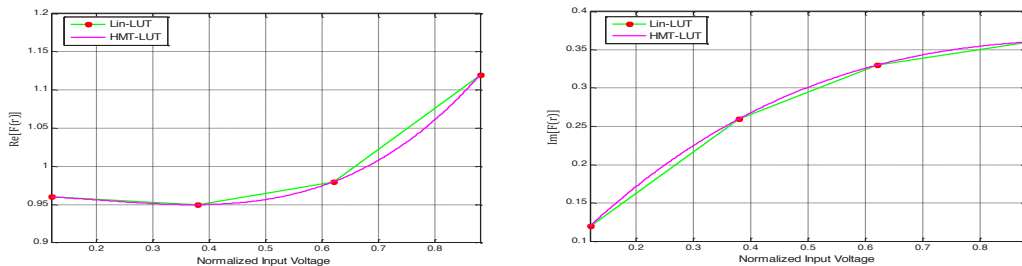


Figure 2. Inverse PA characteristics of Lin-LUT and HMT-LUT

Theoretically, the inverse PA characteristics can be more accurately modelled with high order polynomials. However, the computational complexity introduced by these high-order polynomials does not validate high accuracy. In this paper, a hermite interpolated complex-gain LUT (HMT-LUT) is proposed. Compared with other high order polynomials, HMT-LUT has a lower computational complexity. Additionally, it has a higher accuracy of interpolation compared with Lin-LUT. By employing the Hermite-Interpolation between the adjacent LUT indices (the $n-1$ th, n th and $n+1$ th) which are closest to the input voltage $|V_m|$, the HMT-LUT, entry can be calculated as follows:

$$f(|V_m|) = (H^{n-1}(|V_m|)f_i^{n-1} + H^n(|V_m|)f_i^n + H^{n+1}(|V_m|)f_i^{n+1}) - (H^{n-1'}(|V_m|)f_i^{n-1'} + H^{n'}(|V_m|)f_i^{n'} + H^{n+1'}(|V_m|)f_i^{n+1'}) \quad (8)$$

where f_i^{n-1} , f_i^n and f_i^{n+1} are the $n-1$ th, n th and $n+1$ th LUT values at time i , $f_i^{n-1'}$, $f_i^{n'}$ and $f_i^{n+1'}$ are the first order LUT values of f_i^{n-1} , f_i^n and f_i^{n+1} , and $H^{n-1}(\cdot)$, $H^n(\cdot)$, $H^{n+1}(\cdot)$, $H^{n-1'}(\cdot)$, $H^{n'}(\cdot)$ and $H^{n+1'}(\cdot)$ are the hermite weighing functions that can be approximated as

$$H^{n-1} = \left(1 - 2(V_m - x_{n-1})L^{n-1'}(|V_m|)\right)(L^{n-1}(|V_m|))^2 \quad (9)$$

$$H^n = \left(1 - 2(V_m - x_n)L^{n'}(|V_m|)\right)(L^n(|V_m|))^2 \tag{10}$$

$$H^{n+1} = \left(1 - 2(V_m - x_{n+1})L^{n+1'}(|V_m|)\right)(L^{n+1}(|V_m|))^2 \tag{11}$$

$$H^{n-1'} = (V_m - x_{n-1}) \cdot (L^{n-1}(|V_m|))^2 \tag{12}$$

$$H^{n'} = (V_m - x_n) \cdot (L^n(|V_m|))^2 \tag{13}$$

$$H^{n+1'} = (V_m - x_{n+1}) \cdot (L^{n+1}(|V_m|))^2 \tag{14}$$

where $L^{n-1}(\cdot)$, $L^n(\cdot)$ and $L^{n+1}(\cdot)$ are the lagrange weighing functions that can be approximated as

$$L^{n-1}(|V_m|) = \frac{(|V_m| - x_n)(|V_m| - x_{n+1})}{(x_{n-1} - x_n)(x_{n-1} - x_{n+1})} \tag{15}$$

$$L^n(|V_m|) = \frac{(|V_m| - x_{n-1})(|V_m| - x_{n+1})}{(x_n - x_{n-1})(x_n - x_{n+1})} \tag{16}$$

$$L^{n+1}(|V_m|) = \frac{(|V_m| - x_{n-1})(|V_m| - x_n)}{(x_{n+1} - x_{n-1})(x_{n+1} - x_n)} \tag{17}$$

where $L^{n-1'}$, $L^{n'}$ and $L^{n+1'}$ are the first order lagrange weighing functions and x_{n-1} , x_n and x_{n+1} are corresponding voltage of $n-1$ th, n th and $n+1$ th LUT indices respectively. If the LUT is uniformly spaced, the equations can be simplified as

$$L^{n-1}(|V_m|) = \frac{(|V_m| - x_n)(|V_m| - x_{n+1})}{2T_r^2} \tag{18}$$

$$L^n(|V_m|) = \frac{(|V_m| - x_{n-1})(|V_m| - x_{n+1})}{2T_r^2} \tag{19}$$

$$L^{n+1}(|V_m|) = \frac{(|V_m| - x_{n-1})(|V_m| - x_n)}{2T_r^2} \tag{20}$$

where T_r is the resolution of LUT indices? An inverse PA characteristic of HMT-LUT technique is shown in Figure 2. It can be clearly seen that the usage of hermite interpolation leads to a smooth curve between LUT as it requires more referenced information compared with linear interpolation. Besides, the first order LUT values of HMT-LUT are continuous across the boundary between the adjacent LUT indices (the $n-1$ th, n th and $n+1$ th) which increases the accuracy of estimating the inverse PA characteristics. With the selection of T_r as the order of 2, the divisions can be employed with logic shifters. This in turn results in better rejection of EVM distortion and adjacent channel interference while maintaining similar computational complexity with Lin-LUT.

SIMULATION RESULTS

The proposed algorithm has been evaluated using MATLAB, using Saleh Model’s PA (Saleh, 1981), which possesses non-linear characteristics that can be expressed as

$$K(u) = \frac{\alpha_a u}{1 + \beta_a u^2} \tag{21}$$

$$\phi(u) = \frac{\alpha_p u^2}{1 + \beta_p u^2} \tag{22}$$

where $K(u)$ and $\phi(u)$ are the amplitude and phase corresponding to the non-linear characteristic of the PA. The parameters $\alpha_a = 2.2$, $\beta_a = 0.23$, $\alpha_p = -4.033$, and $\beta_p = 9.104$ are considered in initial simulation which relates to memoryless PA with a gain of 2.16 dB and phase deviation of -22.87° . The simulations are performed using a wideband code division multiple access (WCDMA) signal with a bandwidth of 5MHz. The simulated output spectrums of the linearly amplified input signal (WCDMA) along with the PA under different conditions in terms of power spectral density (PSD) are shown in Figure 3. Spectral regrowth is prominent due to the non-linear characteristics of PA (Cavers, 1999), which consequently increase, the adjacent channel leakage ratio (ACLR). The ACLR is defined as the ratio of the power in the adjacent channel to the transmitted power. The proposed method (HMT-LUT) performs better in terms of linearity compared with non-interpolated LUT and linear interpolated LUT (Lin-LUT), hence reducing the ACLR about 11.8 dBc for the LUT size of 8 entries.

This is expected as HMT-LUT provides an accurate approximation of inverse PA non-linear characteristics and better windowing samples between the LUT entries which requires less LUT to be inhabited.

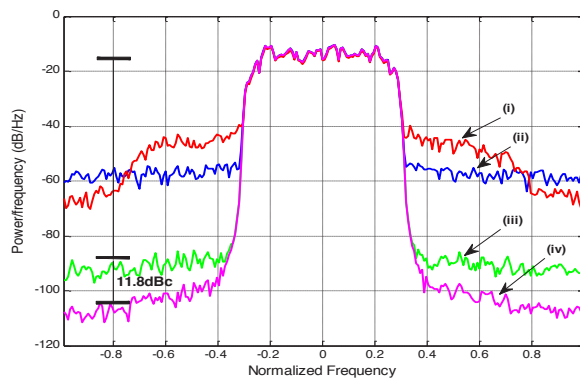


Figure 3. Simulated WCDMA signal spectrum before and after predistortion (i) Without DPD, (ii) DPD without interpolation (iii) DPD with linear interpolation and (iv) DPD with hermite interpolation

To have a similar comparison, the simulation is further assessed in terms of Error Vector Magnitude (EVM) with the same Saleh model PA non-linear characteristics. The EVM is defined as the ratio of power of the error vector to the root mean square (RMS) power of the reference. The result in Figure 4 shows that the HMT-LUT improves the EVM of WCDMA at least by 6 dB for the LUT size of 8 entries with 500 iterations. As the iteration increases, the EVM improves as shown in Figure 4 and summarised in Table I for non-interpolated LUT, linear interpolated LUT (Lin-LUT) and hermite interpolated complex-gain LUT (HMT-LUT) respectively. The proposed method significantly reduces the EVM distortion as the approximation errors introduced by HMT-LUT from modelling the inverse PA characteristics are lower compared with non-interpolated LUT and linear interpolated LUT. As a conclusion, a significant improvement of adjacent channel interference and EVM distortion is observed with the usage of HMT-LUT while maintaining similar computational complexity with linear interpolated LUT (Lin-LUT).

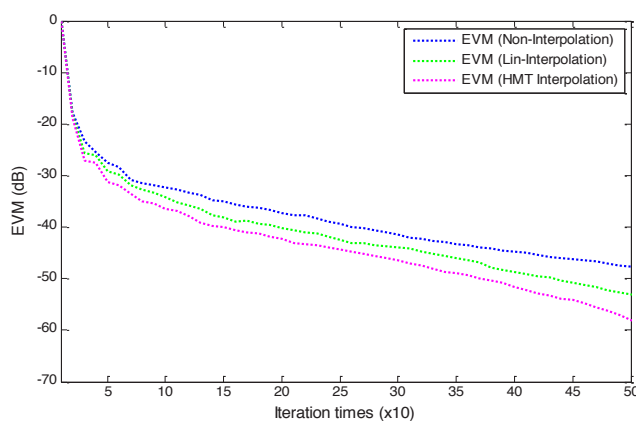


Figure 4. Error Vector Magnitude (EVM) before and after predistortion with different DPD LUT's

Table 1
Simulated EVM of WCDMA signal

Simulated Output Spectrums	8 entries EVM (dB)
Non-Interpolated LUT	-48.82
Linear Interpolated LUT	-52.64
Hermite Interpolated LUT	-58.57

REFERENCES

- Saleh, A. A. (1981). Frequency-independent and frequency-dependent nonlinear models of TWT amplifiers. *IEEE Transactions on communications*, 29(11), 1715-1720.
- Solovyeva, E. B. (2015). Cascade Structure of Digital Predistorter for Power Amplifier Linearization. *Radio Engineering*, 24, 1071-1076.

- Teikari, I., Vankka, J., & Halonen, K. (2006). Baseband digital predistorter with quadrature error correction. *Analog Integrated Circuits and Signal Processing*, 46(1), 73-85.
- Cavers, J. K. (1999). Optimum table spacing in predistorting amplifier linearizers. *IEEE Transactions on Vehicular Technology*, 48(5), 1699-1705.
- Faulkner, M., & Johansson, M. (1994). Adaptive linearization using predistortion-experimental results. *IEEE Transactions on Vehicular Technology*, 43(2), 323-332.
- Varahram, P., Ali, B. M., Mohammady, S., & Sulaiman, N. (2014). Power amplifier linearisation scheme to mitigate superfluous radiations and suppress adjacent channel interference. *IET Communications*, 8(2), 258-265.
- Varahram, P., & Ali, B. M. (2013). Low complexity partial transmit sequence with complex gain memory predistortion in OFDM systems. *Wireless Personal Communications*, 68(4), 1435-1448.
- Chung, S., Holloway, J. W., & Dawson, J. L. (2007, June). Open-loop digital predistortion using Cartesian feedback for adaptive RF power amplifier linearization. In *2007 IEEE/MTT-S International Microwave Symposium* (pp. 1449-1452). IEEE.
- Ba, S. N., Waheed, K., & Zhou, G. T. (2010). Optimal spacing of a linearly interpolated look up table predistorter. *IEEE Trans. Veh. Technol.*, 59, 673-681.
- Feng, X., Feuvrie, B., Descamps, A. S., & Wang, Y. (2013). Improved baseband digital predistortion for linearising PAs with nonlinear memory effects using linearly interpolated LUT. *Electronics Letters*, 49(22), 1389-1391.
- Woo, Y. Y., Kim, J., Yi, J., Hong, S., Kim, I., Moon, J., & Kim, B. (2007). Adaptive digital feedback predistortion technique for linearizing power amplifiers. *IEEE Transactions on Microwave Theory and Techniques*, 55(5), 932-940.

**REFEREES FOR THE PERTANIK
JOURNAL OF SCIENCE AND TECHNOLOGY**

VOL. 25(S) FEB. 2017
Special Edition

Contemporary Issues Towards Smart Sustainable Engineering Solution

The Editorial Board of the Journal of Science and Technology wishes to thank the following:

Afaf Rozan Mohd Radzol
(UiTM, Malaysia)

Ali Khalifa Abdgalil
(College of Industrial Technology Misurata, Libya)

Buba Sani Dahiru
(Federal Polytechnic Mubi, Nigeria)

Fakhrul Zaman Rokhani
(UPM, Malaysia)

Gan Kok Beng
(UKM, Malaysia)

Hafiz Rashidi Ramli
(UPM, Malaysia)

Harikrishnan
(UM, Malaysia)

Haslina Md Sarkan
(UTM, Malaysia)

Hasmaini Mohamad
(UiTM, Malaysia)

Hazlina Selamat
(UTM, Malaysia)

Hidayat Zainuddin
(UteM, Malaysia)

Hiroaki Yamada
(Yamaguchi, Japan)

Ibrahima Faye
(University Petronas, Malaysia)

Ismail Saad
(UMS, Malaysia)

M.H. Shahrokh Abadi
(Hakim Sabzevari University, Iran)

M.M. Aliyu
(UKM, Malaysia)

Mario Alberto Garcia Remires
(UANL, Mexico)

Md Arafatur Rahman
(UMP, Malaysia)

Miszaina Osman
(Unitem, Malaysia)

Mohammad Murthada Othman
(UiTM, Malaysia)

Mohammed Arifuddin Sohel
(MJCET, Malaysia)

Mohd Amrallah Mustafa
(UPM, Malaysia)

Mohd Faisal Ibrahim
(UKM, Malaysia)

Mohd Nabil Muhtazaruddin
(UTM, Malaysia)

Mohd Razali Mohamad Sapiee
(UTEM, Malaysia)

Mohd Tafir Mustaffa
(USM, Malaysia)

Noor Fadzilah Md Sharif
(UPNM, Malaysia)

Norzanah Rosmin
(UTM, Malaysia)

Raja Nor Firdaus Kashfi Raja Othman
(UteM, Malaysia)

Ramizi Mohamed
(UKM, Malaysia)

Rosmiwati Mohd Mokhtar
(USM, Malaysia)

Rozaimi Ghazali
(UteM, Malaysia)

Salah Eldeen Gasim
(Sudan University of Science)

Salmiah Amad
(IIUM, Malaysia)

Sawal Hamid Md Ali
(UKM, Malaysia)

Siti Idzura Yusuf
(UTHM, Malaysia)

Tan Gim Heng
(IUKL, Malaysia)

Zool Hilmi Ismail
(UTM, Malaysia)

Zuhaila Mat Yasin
(UiTM, Malaysia)

UKM - Universiti Kebangsaan Malaysia
UPM - Universiti Putra Malaysia
IUKL - Infrastructure University Kuala Lumpur
USM - Universiti Sains Malaysia
UTM - Universiti Teknologi Malaysia
UNITEN - Universiti Tenaga Nasional
UiTM - Universiti Teknologi Mara
UMP - Universiti Malaysia Pahang
UteM - Universiti Teknikal Malaysia
MJEET - Muffakham Jah College of Engineering and Technology, India
UANL - Autonomous University of Nuevo Leon, Mexico
Untem - Universiti Teknikal Malaysia Melaka
UPNM - Universiti Pertahanan Nasional Malaysia
UTHM - Universiti Tun Hussein Onn Malaysia
IIUM - International Islamic University Malaysia
UMS - Universiti Malaysia Sabah
UM - Universiti Malaya

While every effort has been made to include a complete list of referees for the period stated above, however if any name(s) have been omitted unintentionally or spelt incorrectly, please notify the Chief Executive Editor, *Pertanika* Journals at nayan@upm.my.

Any inclusion or exclusion of name(s) on this page does not commit the *Pertanika* Editorial Office, nor the UPM Press or the University to provide any liability for whatsoever reason.

Pertanika Journals

Our goal is to bring high quality research to the widest possible audience

INSTRUCTIONS TO AUTHORS (Manuscript Preparation & Submission Guide)

Revised: June 2016

Please read the Pertanika guidelines and follow these instructions carefully. Manuscripts not adhering to the instructions will be returned for revision without review. The Chief Executive Editor reserves the right to return manuscripts that are not prepared in accordance with these guidelines.

MANUSCRIPT PREPARATION

Manuscript Types

Pertanika accepts submission of mainly **four** types of manuscripts for peer-review.

1. REGULAR ARTICLE

Regular articles are full-length original empirical investigations, consisting of introduction, materials and methods, results and discussion, conclusions. Original work must provide references and an explanation on research findings that contain new and significant findings.

Size: Generally, these are expected to be between 6 and 12 journal pages (excluding the abstract, references, tables and/or figures), a maximum of 80 references, and an abstract of 100–200 words.

2. REVIEW ARTICLE

These report critical evaluation of materials about current research that has already been published by organizing, integrating, and evaluating previously published materials. It summarizes the status of knowledge and outline future directions of research within the journal scope. Review articles should aim to provide systemic overviews, evaluations and interpretations of research in a given field. Re-analyses as meta-analysis and systemic reviews are encouraged. The manuscript title must start with "Review Article:".

Size: These articles do not have an expected page limit or maximum number of references, should include appropriate figures and/or tables, and an abstract of 100–200 words. Ideally, a review article should be of 7 to 8 printed pages.

3. SHORT COMMUNICATIONS

They are timely, peer-reviewed and brief. These are suitable for the publication of significant technical advances and may be used to:

- (a) report new developments, significant advances and novel aspects of experimental and theoretical methods and techniques which are relevant for scientific investigations within the journal scope;
- (b) report/discuss on significant matters of policy and perspective related to the science of the journal, including 'personal' commentary;
- (c) disseminate information and data on topical events of significant scientific and/or social interest within the scope of the journal.

The manuscript title must start with "*Brief Communication:*".

Size: These are usually between 2 and 4 journal pages and have a maximum of three figures and/or tables, from 8 to 20 references, and an abstract length not exceeding 100 words. Information must be in short but complete form and it is not intended to publish preliminary results or to be a reduced version of Regular or Rapid Papers.

4. OTHERS

Brief reports, case studies, comments, concept papers, Letters to the Editor, and replies on previously published articles may be considered.

PLEASE NOTE: NO EXCEPTIONS WILL BE MADE FOR PAGE LENGTH.

Language Accuracy

Pertanika **emphasizes** on the linguistic accuracy of every manuscript published. Articles must be in **English** and they must be competently written and argued in clear and concise grammatical English. Contributors are strongly advised to have the manuscript checked by a colleague with ample experience in writing English manuscripts or a competent English language editor.

Author(s) **must provide a certificate** confirming that their manuscripts have been adequately edited. A proof from a recognised editing service should be submitted together with the cover letter at the time of submitting a manuscript to Pertanika. **All editing costs must be borne by the author(s)**. This step, taken by authors before submission, will greatly facilitate reviewing, and thus publication if the content is acceptable.

Linguistically hopeless manuscripts will be rejected straightaway (e.g., when the language is so poor that one cannot be sure of what the authors really mean). This process, taken by authors before submission, will greatly facilitate reviewing, and thus publication if the content is acceptable.

MANUSCRIPT FORMAT

The paper should be submitted in one column format with at least 4cm margins and 1.5 line spacing throughout. Authors are advised to use Times New Roman 12-point font and *MS Word* format.

1. Manuscript Structure

Manuscripts in general should be organised in the following order:

Page 1: Running title

This page should **only** contain the running title of your paper. The running title is an abbreviated title used as the running head on every page of the manuscript. The running title should not exceed 60 characters, counting letters and spaces.

Page 2: Author(s) and Corresponding author information.

This page should contain the **full title** of your paper not exceeding 25 words, with name(s) of all the authors, institutions and corresponding author's name, institution and full address (Street address, telephone number (including extension), hand phone number, and e-mail address) for editorial correspondence. First and corresponding authors must be clearly indicated.

The names of the authors may be abbreviated following the international naming convention. e.g. Salleh, A.B.¹, Tan, S.G^{2*}., and Sapuan, S.M³.

Authors' addresses. Multiple authors with different addresses must indicate their respective addresses separately by superscript numbers:

George Swan¹ and Nayan Kanwal²

¹Department of Biology, Faculty of Science, Duke University, Durham, North Carolina, USA.,

²Office of the Deputy Vice Chancellor (R&I), Universiti Putra Malaysia, Serdang, Malaysia.

A **list** of number of **black and white / colour figures and tables** should also be indicated on this page. Figures submitted in color will be printed in colour. See "5. Figures & Photographs" for details.

Page 3: Abstract

This page should **repeat** the **full title** of your paper with only the **Abstract** (the abstract should be less than 250 words for a Regular Paper and up to 100 words for a Short Communication), and **Keywords**.

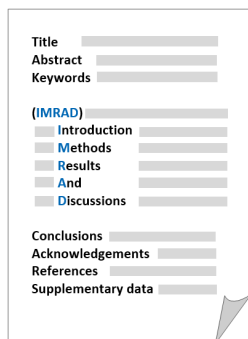
Keywords: Not more than eight keywords in alphabetical order must be provided to describe the contents of the manuscript.

Page 4: Introduction

This page should begin with the **Introduction** of your article and followed by the rest of your paper.

2. Text

Regular Papers should be prepared with the headings *Introduction, Materials and Methods, Results and Discussion, Conclusions, Acknowledgements, References, and Supplementary data* (if available) in this order.



Title _____
 Abstract _____
 Keywords _____
 (IMRAD)
 Introduction _____
 Methods _____
 Results _____
 And _____
 Discussions _____
 Conclusions _____
 Acknowledgements _____
 References _____
 Supplementary data _____

MAKE YOUR ARTICLES AS CONCISE AS POSSIBLE

Most scientific papers are prepared according to a format called IMRAD. The term represents the first letters of the words Introduction, Materials and Methods, Results, And, Discussion. It indicates a pattern or format rather than a complete list of headings or components of research papers; the missing parts of a paper are: Title, Authors, Keywords, Abstract, Conclusions, and References. Additionally, some papers include Acknowledgments and Appendices.

The Introduction explains the scope and objective of the study in the light of current knowledge on the subject; the Materials and Methods describes how the study was conducted; the Results section reports what was found in the study; and the Discussion section explains meaning and significance of the results and provides suggestions for future directions of research. The manuscript must be prepared according to the Journal's instructions to authors.

3. Equations and Formulae

These must be set up clearly and should be typed double spaced. Numbers identifying equations should be in square brackets and placed on the right margin of the text.

4. Tables

All tables should be prepared in a form consistent with recent issues of Pertanika and should be numbered consecutively with Roman numerals. Explanatory material should be given in the table legends and footnotes. Each table should be prepared on a new page, embedded in the manuscript.

When a manuscript is submitted for publication, tables must also be submitted separately as data - .doc, .rtf, Excel or PowerPoint files- because tables submitted as image data cannot be edited for publication and are usually in low-resolution.

5. Figures & Photographs

Submit an **original** figure or photograph. Line drawings must be clear, with high black and white contrast. Each figure or photograph should be prepared on a new page, embedded in the manuscript for reviewing to keep the file of the manuscript under 5 MB. These should be numbered consecutively with Roman numerals.

Figures or photographs must also be submitted separately as TIFF, JPEG, or Excel files- because figures or photographs submitted in low-resolution embedded in the manuscript cannot be accepted for publication. For electronic figures, create your figures using applications that are capable of preparing high resolution TIFF files. In general, we require **300 dpi** or higher resolution for **coloured and half-tone artwork**, and **1200 dpi or higher** for **line drawings** are required.

Failure to comply with these specifications will require new figures and delay in publication.

NOTE: Illustrations may be produced in colour at no extra cost at the discretion of the Publisher; the author could be charged Malaysian Ringgit 50 for each colour page.

6. References

References begin on their own page and are listed in alphabetical order by the first author's last name. Only references cited within the text should be included. All references should be in 12-point font and double-spaced.

NOTE: When formatting your references, please follow the **APA reference style** (6th Edition). Ensure that the references are strictly in the journal's prescribed style, failing which your article will **not be accepted for peer-review**. You may refer to the *Publication Manual of the American Psychological Association* for further details (<http://www.apastyle.org/>).

7. General Guidelines

Abbreviations: Define alphabetically, other than abbreviations that can be used without definition. Words or phrases that are abbreviated in the introduction and following text should be written out in full the first time that they appear in the text, with each abbreviated form in parenthesis. Include the common name or scientific name, or both, of animal and plant materials.

Acknowledgements: Individuals and entities that have provided essential support such as research grants and fellowships and other sources of funding should be acknowledged. Contributions that do not involve researching (clerical assistance or personal acknowledgements) should **not** appear in acknowledgements.

Authors' Affiliation: The primary affiliation for each author should be the institution where the majority of their work was done. If an author has subsequently moved to another institution, the current address may also be stated in the footer.

Co-Authors: The commonly accepted guideline for authorship is that one must have substantially contributed to the development of the paper and share accountability for the results. Researchers should decide who will be an author and what order they will be listed depending upon their order of importance to the study. Other contributions should be cited in the manuscript's Acknowledgements.

Copyright Permissions: Authors should seek necessary permissions for quotations, artwork, boxes or tables taken from other publications or from other freely available sources on the Internet before submission to Pertanika. Acknowledgement must be given to the original source in the illustration legend, in a table footnote, or at the end of the quotation.

Footnotes: Current addresses of authors if different from heading may be inserted here.

Page Numbering: Every page of the manuscript, including the title page, references, tables, etc. should be numbered.

Spelling: The journal uses American or British spelling and authors may follow the latest edition of the Oxford Advanced Learner's Dictionary for British spellings.

SUBMISSION OF MANUSCRIPTS

Owing to the volume of manuscripts we receive, we must insist that all submissions be made electronically using the **online submission system ScholarOne™**, a web-based portal by Thomson Reuters. For more information, go to our web page and [click "Online Submission"](#).

Submission Checklist

1. **MANUSCRIPT:** Ensure your MS has followed the Pertanika style particularly the first four pages as explained earlier. The article should be written in a good academic style and provide an accurate and succinct description of the contents ensuring that grammar and spelling errors have been corrected before submission. It should also not exceed the suggested length.

COVER LETTER: All submissions must be accompanied by a cover letter detailing what you are submitting. Papers are accepted for publication in the journal on the understanding that the article is **original** and the content has **not been published** either **in English** or **any other language(s)** or **submitted for publication elsewhere**. The letter should also briefly describe the research you are reporting, why it is important, and why you think the readers of the journal would be interested in it. The cover letter must also contain an acknowledgement that all authors have contributed significantly, and that all authors have approved the paper for release and are in agreement with its content.

The cover letter of the paper should contain (i) the title; (ii) the full names of the authors; (iii) the addresses of the institutions at which the work was carried out together with (iv) the full postal and email address, plus telephone numbers and emails of all the authors. The current address of any author, if different from that where the work was carried out, should be supplied in a footnote.

The above must be stated in the cover letter. Submission of your manuscript will not be accepted until a cover letter has been received

2. **COPYRIGHT:** Authors publishing the Journal will be asked to sign a copyright form. In signing the form, it is assumed that authors have obtained permission to use any copyrighted or previously published material. All authors must read and agree to the conditions outlined in the form, and must sign the form or agree that the corresponding author can sign on their behalf. Articles cannot be published until a signed form (*original pen-to-paper signature*) has been received.

Please do **not** submit manuscripts to the editor-in-chief or to any other office directly. Any queries must be directed to the **Chief Executive Editor's** office via email to nayan@upm.my.

Visit our Journal's website for more details at <http://www.pertanika.upm.edu.my/home.php>.

HARDCOPIES OF THE JOURNALS AND OFF PRINTS

Under the Journal's open access initiative, authors can choose to download free material (via PDF link) from any of the journal issues from Pertanika's website. Under "**Browse Journals**" you will see a link, "*Current Issues*" or "*Archives*". Here you will get access to all current and back-issues from 1978 onwards.

The **corresponding author** for all articles will receive one complimentary hardcopy of the journal in which his/her articles is published. In addition, 20 off prints of the full text of their article will also be provided. Additional copies of the journals may be purchased by writing to the Chief Executive Editor.



Why should you publish in

Pertanika?

BENEFITS TO AUTHORS

PROFILE: Our journals are circulated in large numbers all over Malaysia, and beyond in Southeast Asia. Our circulation covers other overseas countries as well. We ensure that your work reaches the widest possible audience in print and online, through our wide publicity campaigns held frequently, and through our constantly developing electronic initiatives such as Web of Science Author Connect backed by Thomson Reuters.

QUALITY: Our journals' reputation for quality is unsurpassed ensuring that the originality, authority and accuracy of your work are fully recognised. Each manuscript submitted to Pertanika undergoes a rigid originality check. Our double-blind peer refereeing procedures are fair and open, and we aim to help authors develop and improve their scientific work. Pertanika is now over 38 years old; this accumulated knowledge has resulted in our journals being indexed in SCOPUS (Elsevier), Thomson (ISI) Web of Science™ Core Collection, Emerging Sources Citation Index (ESCI), Web of Knowledge [BIOSIS & CAB Abstracts], EBSCO, DOAJ, ERA, AGRICOLA, Google Scholar, ISC, TIB, Journal Guide, Citefactor, Cabell's Directories and MyCite.

AUTHOR SERVICES: We provide a rapid response service to all our authors, with dedicated support staff for each journal, and a point of contact throughout the refereeing and production processes. Our aim is to ensure that the production process is as smooth as possible, is borne out by the high number of authors who prefer to publish with us.

CODE OF ETHICS: Our Journal has adopted a Code of Ethics to ensure that its commitment to integrity is recognized and adhered to by contributors, editors and reviewers. It warns against plagiarism and self-plagiarism, and provides guidelines on authorship, copyright and submission, among others.

PRESS RELEASES: Landmark academic papers that are published in Pertanika journals are converted into press-releases as a unique strategy for increasing visibility of the journal as well as to make major findings accessible to non-specialist readers. These press releases are then featured in the university's UK and Australian based research portal, ResearchSEA, for the perusal of journalists all over the world.

LAG TIME: The elapsed time from submission to publication for the articles averages 3 to 4 months. A decision on acceptance of a manuscript is reached in 3 to 4 months (average 14 weeks).



Address your submissions to:
The Chief Executive Editor
Tel: +603 8947 1622
nayan@upm.my

Journal's Profile: www.pertanika.upm.edu.my/

Call for Papers 2017-18

now accepting submissions...

Pertanika invites you to explore frontiers from all key areas of agriculture, science and technology to social sciences and humanities.

Original research and review articles are invited from scholars, scientists, professors, post-docs, and university students who are seeking publishing opportunities for their research papers through the Journal's three titles; JTAS, JST & JSSH. Preference is given to the work on leading and innovative research approaches.

Pertanika is a fast track peer-reviewed and open-access academic journal published by Universiti Putra Malaysia. To date, Pertanika Journals have been indexed by many important databases. Authors may contribute their scientific work by publishing in UPM's hallmark SCOPUS & ISI indexed journals.

Our journals are open access - international journals. Researchers worldwide will have full access to all the articles published online and be able to download them with zero subscription fee.

Pertanika uses online article submission, review and tracking system for quality and quick review processing backed by Thomson Reuter's ScholarOne™. Journals provide rapid publication of research articles through this system.

For details on the Guide to Online Submissions, please visit http://www.pertanika.upm.edu.my/guide_online_submission.php

About the Journal

Pertanika is an international multidisciplinary peer-reviewed leading journal in Malaysia which began publication in 1978. The journal publishes in three different areas — Journal of Tropical Agricultural Science (JTAS); Journal of Science and Technology (JST); and Journal of Social Sciences and Humanities (JSSH). All journals are published in English.

JTAS is devoted to the publication of original papers that serves as a forum for practical approaches to improving quality in issues pertaining to tropical agricultural research- or related fields of study. It is published four times a year in *February, May, August* and *November*.

JST caters for science and engineering research- or related fields of study. It is published twice a year in *January* and *July*.

JSSH deals in research or theories in social sciences and humanities research. It aims to develop as a flagship journal with a focus on emerging issues pertaining to the social and behavioural sciences as well as the humanities, particularly in the Asia Pacific region. It is published four times a year in *March, June, September* and *December*.



An Award-winning
International-Malaysian Journal
— CREAM AWARD, MoHE
—Sept 2015





Metal Shape Detection and Evaluation using Giant Magneto Resistance System <i>Norhisam M., M. K. Roslan, Ishak A. and M. N. Hamidon</i>	197
Zero-Padding in DWT Satellite Image Compression <i>Suhaidi Shafie, Halah Saadoon Shihab, Fauzan Ahmad and A. R. Ramli</i>	205
Design of Readout Circuit for Piezoresistive Pressure Sensor Using Nodal Array Approach Reading Technique <i>W. Z. Wan Hasan , F. R. M. Rashidi, M. N. Hamidon and Y. Wahab</i>	215
Transparent Solar Cell Using Spin Coating and Screen Printing <i>A. A. F. Husain and W. Z.Wan Hasan</i>	225
Transmission Lines Modelling based on RLC Passive and Active Filter Design <i>Ahmed Qasim Turki, Nashiren Farzilah Mailah and Ahmed H. Sabry</i>	235
Modelling and Control of Standing Up and Sitting Down Manoeuver <i>A. J. Ishak, M. O. Tokhi, M. S. Al-Quraishi, D. M. Linares and S. K. Ali</i>	243
Silicon Nanowire Interface Circuit for DNA Detection <i>Kamilu Iman Usman, Mohd Nizar Hamidon, Siti Fatimah Abd Rahman and Guan Ling Sim</i>	251
Sensitivity Study of Graphene Nanoribbon with NH ₃ at Room Temperature <i>Mohd Nizar Hamidon, Guan Ling Sim and Kamilu Iman Usman</i>	259
Transformer Incipient Fault Identification Using Depolarisation Current Ratio Index Analysis Technique <i>Mohd Aizam Talib, Nor Asiah Muhamad and Zulkurnain Abdul Malek</i>	267
Tuberculosis Bacteria Counting Using Watershed Segmentation Technique <i>M. K. Hassan, N. F. H. Eko and S. Shafie</i>	275
Analysis of AC - to - DC Uncontrolled Converters Harmonics for Electric Vehicles Applications <i>Shaker M. Khudher, Ishak Bin Aris, Nashiren F. Mailah and R. K .Z. Sahbudin</i>	283
Investigating Insulator UV Signal Frequency Components as Potential Tools for Condition Monitoring of Ceramic Insulators <i>Saiful Mohammad Iezham Suhaimi, Nouruddeen Bashir, Nor Asiah Muhamad and Mohd Aizam Talib</i>	291
A Hermite Interpolated LUT for RF Power Amplifiers <i>Dinaagaren Selvadurai, Roslina M. Sidek, Khalid Al-Hussaini and Borhanuddin M. Ali</i>	299

Development of Power Recovery Circuit for Bio-Implantable Stimulator <i>Mokhalad Khaleel Alghrairi, Nasri Bin Sulaiman, Roslina Bt Mohd Sidek and Saad Mutashar</i>	87
Weakest Bus Frequency Identification of Power System via TFDI <i>Athraa Iessa, Noor Izzri Abdul Wahab and Norman Mariun</i>	97
An FFT Computation Minimisation for an FPGA-Based MCSA while Preserving Frequency Resolution <i>Marut Raksa, Thanaporn Likitjarernkul, Kiattisak Sengchuai, Nattha Jindapetch and Kerkchai Thongnoo</i>	105
Auto-Grasping Algorithm of Robot Gripper Based on Pressure Sensor Measurement <i>Ahmed M. M. Almassri, Chikamune Wada, W. Z. Wan Hasan and S. A. Ahmad'</i>	113
A Programmable CMOS Delay Line for Wide Delay Range Generation and Duty-Cycle Adjustability <i>Bilal I. Abdulrazzaq, Izhal Abdul Halin, Lee Lini, Roslina M. Sidek and Nurul Amziah Md. Yunus</i>	123
Fuzzy-Controlled Humidity Variation by Silica Gel and Nitrogen Gas in an Atmospheric Chamber <i>Ali Ghahraei, Nurul Amziah Md Yunus, Izhal Abdul Halin and Nasri Sulaiman</i>	133
Assessment of Transformer Health Index Using Different Model <i>J. Jasni, A. Azmi, N. Azis, M. S. Yahaya and M. A. Talib</i>	143
Top-oil Temperature Model for Transformers based on Nonlinear Thermal Resistance, Lumped Capacitance and Thermal-electrical Analogy <i>M. H. Roslan, N. Azis, J. Jasni and Z. Ibrahim</i>	151
Effect of Moisture on Electrical Response of Sand and Clay under High Impulse Voltage Applications <i>Chun Lim, Siow, Mohd Syariffuddin, Johari and Chandima, Gomes</i>	161
Generation of Space Vector PWM by Using Arduino Uno <i>Nur Ashida Salim, Muhammad Azizi Kaprowi and Ahmad Asri Abd Samat</i>	171
Analysis of Ground Potential Distribution under Lightning Current Condition <i>Chandima Gomes and Riyadh Z. Sabry</i>	181
EFVD along Porcelain Insulator using the FEM <i>Kian Tsong Ho, Mahdi Izadi and Mohd Zainal Abidin Ab Kadir</i>	189

Contents

Contemporary Issues Towards Smart Sustainable Engineering Solution

Voltage Flicker Estimation Based on Pair of Inter-harmonics Analysis Method <i>Mohd Amran, Mohd Radzi, Zai Peng, Goh and Hashim, Hizam</i>	1
DC-link Capacitor Voltage Regulation with Effort-reduction Fuzzy Logic Control for Three-level Inverter-based Shunt Active Power Filter <i>Nashiren Farzilah, Mailah, Yap Hoon and Mohd Amran, Mohd Radzi</i>	11
The Response of a High Voltage Transformer with Various Geometries of Core Joint Design <i>Omar. SH. Alyozbaky, Maryam. M. Isa, Mohd Zainal Abidin Ab Kadir and Mahdi Izadi</i>	21
RF CMOS Switch Design Methodologies for Multiband Transceiver Applications <i>Veeraiyah Thangasamy, Vinesh Thiruchelvam, Shaiful Jahari Hashim and Noor Ain Kamsani</i>	29
Nonlinear Dynamic Inverse Controller Based in Field Oriented with SVPWM Current Control <i>Settar S. Keream, Ahmed N Abdalla and Mohd Razali Bin Daud</i>	37
Passive Damping Techniques with LCL Filter in Inverter-Grid Connected <i>Erum Pathan and Shamsul Aizam Zulkifli</i>	45
Distinct Position of Chaotic Pulse Trains Observed in Malaysia <i>Muhammad Noh Hamzah and Chandima Gomes</i>	53
Field Evaluation of Magnetic Actuator Driven Switchgear in Malaysia <i>Mohd Dzaki, Mohd Amir and Sanuri, Ishak</i>	61
Lightning Breakdown Voltages of Refined Bleached and Deodorised Palm Oil under Needle-plane Configuration <i>Norhafiz Azis, Yee Von Thien, Robiah Yunus and Zaini Yaakub</i>	69
Analysis of Air Humidity and Temperature for Post Lightning Circumstances <i>Sharifah Sakinah, Tuan Othman, Jasronita, Jasni and Mohd Nazim, Mohtar</i>	79



Pertanika Editorial Office, Journal Division
Office of the Deputy Vice Chancellor (R&I),
1st Floor, IDEA Tower II,
UPM-MTDC Technology Centre
Universiti Putra Malaysia
43400 UPM Serdang
Selangor Darul Ehsan
Malaysia

<http://www.pertanika.upm.edu.my/>

E-mail: executive_editor.pertanika@upm.my

Tel: +603 8947 1622

PENERBIT
UPM
UNIVERSITI PUTRA MALAYSIA
PRESS

<http://penerbit.upm.edu.my>

E-mail : penerbit@putra.upm.edu.my

Tel : +603 8946 8855/8854

Fax : +603 8941 6172

